SLAC-396
UC-414
(E)

A Measurement of the Z^0 Hadronic Branching Fraction to Bottom Quarks and the Charged Multiplicity of Bottom Quark Events Using Precision Vertex Detectors at E_{CM} = 91 GeV*

Dale Steven Koetke

Stanford Linear Accelerator Center
Stanford University
Stanford, California 94309

June 1992

Prepared for the Department of Energy
under contract number DE-AC03-76SF00515

* Ph.D. Thesis

Abstract

Using the precision vertex detectors of the Mark II at the SLC, an impact parameter tag was developed to select a sample of hadronic Z^0 decays enriched in its fraction of bottom quark events. The nominal tagging method requires that there be at least three tracks whose impact parameters are inconsistent with the track having originated at the electron-position interaction point. A tagging efficiency for $b\bar{b}$ events of 50% with a enriched sample purity of 85% was achieved.

This impact parameter tag was used to measure the fraction hadronic Z^0 decays which produce $b\bar{b}$ events, F_b. It is found that

$$\mathrm{F}_b = 0.232^{+0.053}_{-0.045}\,(\mathrm{stat})\,^{+0.025}_{-0.021}\,(\mathrm{syst}).$$

This result is consistent with those found using other tagging methods as well as the Standard Model prediction of 0.217.

The $b\bar{b}$-enriched event sample was also used to measure the difference between the average charged multiplicity of $b\bar{b}$ events and that of all hadronic Z^0 decays,

$$\delta\bar{n}_b = 2.11 \pm 1.82\,(\mathrm{stat}) \pm 0.57\,(\mathrm{syst}).$$

Using previous measurements of the total hadronic charged multiplicity, the corresponding total multiplicity for $b\bar{b}$ events is

$$\bar{n}_b = 23.05 \pm 1.82\ (\mathrm{stat}) \pm 0.60\ (\mathrm{syst}).$$

Subtracting the contribution to the multiplicity from B hadron decays yields the multiplicity of the $b\bar{b}$ non-leading system,

$$\bar{n}_{nl} = 12.04 \pm 1.82\ (\mathrm{stat}) \pm 0.63(\mathrm{syst}).$$

Comparing this non-leading multiplicity to the total hadronic multiplicity data at lower energy supports the hypothesis that the non-leading particle production is independent of the flavor of the inital quarks. This also yields a determination of the average energy fraction of bottom hadrons in Z^0 decays of

$$\langle x_E \rangle_b = 0.619^{+.096}_{-.107}\,(\mathrm{stat})^{+.043}_{-.045}(\mathrm{syst}).$$

Acknowledgments

Many people have contributed to the quality of my experiences during the years I have spent at SLAC and at Stanford. First and foremost, I want to express my sincere gratitude to my advisor, John Jaros. Working under his tutelage for the past six years I have learned a great deal about how to do experimental physics. Participating in the assembly and use of the DCVD has been a great opportunity and valuable learning experience. I am also grateful for John's patience and his guidance. His insight into different solutions and new approaches to solving the problems has been invaluable.

I also owe a debt of gratitude to the members of the *B* Physics Working Group, especially Chris Adolphsen, Don Fujino, Bob Jacobsen, Bruce Schumm, and Steve Wagner who all worked heroically to extract information from a tiny event sample. I have learned much from having had the opportunity to work with each of these people and enjoyed the interaction with them. In particular I want to express my thanks to Bruce, with whom I collaborated on the multiplicity analysis.

Building the DCVD was a large part of my experience here and I want to thank all of those who took part in that project. Specifically, working with Jim Smith on various aspects of this project was both enjoyable and a good chance to learn the physics of wire chambers from a hands-on perspective. Ken Hayes and Jim Alexander also helped me get started on the DCVD by providing guidance on projects which I could squeeze into a busy schedule of classes during my first two years at Stanford.

Of course even the DCVD was part of a much larger detector, and I want to thank all of the Mark II Collaborators for having supported the detector even through the 1990 run.

Throughout my time at SLAC, I have been a member of Martin Perl's group, and am most grateful for his support. Other Group E members, especially Lee Anne Kowalski, Mike Hildreth and Charles Munger and Dave Coward, have been good friends. Thanks for all of the help and the enlightening discussions. Deserving special thanks, however, is Lydia Beers, for everything she has done to make my life at SLAC easier.

Nina Adelman-Stolar has been another good friend and someone who was always willing to help out when the going got tough. Also, thanks to Sylvia and Terry in publications for helping with some of the complicated figures in this thesis.

My six years at Stanford has also allowed me to make many new and dear friends. Keith Martinez, Brian Sterling and Jon Labs made the first-year of graduate school bearable and have been very good friends since then. Living in Escondido Village also provided the opportunity to get to know many new friends, particularly Bruce and Tracy Onsager, and Reinaldo Michelena and Mainlin Suarez. I must also thank a much older friend, Dave Klemz, for providing some of the most fun I have had during my time at Stanford: the yearly ski weeks! Finally, I appreciate the opportunities I had to get away from it all by visiting the Roach family. I'll cherish the time spent at the cabin and the visits to Tres Hombres.

I must also express my deepest thanks for the friendship I have with my family, particularly my mother and father, my brother and my sister. They were always supportive of my endeavors and have provided many of my life's most memorable moments.

Finally, I want to dedicate this thesis to two people: my father and my wife. To my father, I am grateful for having fed my curiosity and guided my learning of the physical world, from my earliest memories through my years in college as both an advisor and a friend. He has set an fine example of what one can achieve as both outstanding educator and researcher.

To my wife, however, I owe the deepest thanks. She has been very supportive of me throughout this endeavour, having to put up with my working strange hours and everything else which is part of being a graduate student. We have known each other for almost a decade now, and her love and companionship through this period have been my life's greatest joy.

Table of Contents

List of Tables

List of Figures

Chapter 1

Introduction

This thesis presents the measurements of several quantities related to the production of bottom quark pairs at the Z^0. The $b\bar{b}$ event enrichment method employed for these measurements used the vertex detector system of the Mark II detector at the SLAC Linear Collider. This system provides very accurate track measurements. In particular, the average impact parameter resolution, including the uncertainty in the e^+e^- interaction point (IP) location, is about 30 μm for high momentum tracks and about 75 μm for tracks with 1 GeV/c of momentum transverse to the beam axis. The property used to identify potential $b\bar{b}$ events is that tracks from B hadron decay will tend to have impact parameters (b) inconsistent with the track having originated at the IP.

The specific technique for selecting a $b\bar{b}$ enriched sample requires that there be at least n_{min} tracks which have an impact parameter significance, b/σ_b, greater than some minimum value S_{min}. Typical values for tags used in this analysis have n_{min} = 3 and S_{min} = 3.0. With a detector of the above resolution, this tag selects $b\bar{b}$ events with an efficiency of 50%. The resulting tagged sample has a $b\bar{b}$ event purity of 85%.

This tagging method was employed to make several measurements. These measurements include,

- the hadronic branching fraction of the Z^0 to bottom quark pairs,
- the non-leading multiplicity in $b\bar{b}$ events, and

- the average energy fraction of bottom hadrons.

The hadronic branching fraction to $b\bar{b}$ events, F_b, is of interest because, with the statistics available to the analysis, it provides a check of the Standard Model couplings to a particular flavor of quark. With larger data samples, a measurement of F_b is sensitive to the top quark mass through electroweak corrections and also to potential sources of new physics. Using the impact parameter tag to measure F_b is also of interest because it will have different sources of systematic error from the other tags used in previous measurements.

With a $b\bar{b}$ enriched sample, the non-leading multiplicity in $b\bar{b}$ events can be determined. The non-leading multiplicity is defined as the average number of the tracks not from the decay of heavy hadrons, namely those tracks which are produced during the fragmentation process. The quantity directly measured in this determination of the non-leading multiplicity, is the difference between the multiplicity of the tagged sample and the multiplicity of the total hadronic sample. The difference between the $b\bar{b}$ event multiplicity and the Z^0 decay multiplicity was then calculated, after accounting for the effects of detector acceptance and bias introduced by the tagging method. The $b\bar{b}$ event multiplicity was determined by adding the multiplicity difference to the average total hadronic Z^0 decay multiplicity as measured by other experiments. The multiplicity of the non-leading system was then extracted by subtracting the B hadron decay multiplicity. The measurement of the multiplicity difference, rather than the $b\bar{b}$ event multiplicity, significantly reduces the sensitivity of the measurement to the systematic errors which affect all types of hadronic events similarly (*e.g.* tracking efficiency, pair production, *etc.*).

The principle purpose of this measurement is as a qualitative check of QCD phenomenology. As explained by QCD, the fragmentation process is governed by a quark and gluon shower and is thus expected to be independent of the flavor of the initial quark. To test this, the non-leading multiplicity measurement can be compared to the total hadronic multiplicity measured at a center of mass energy, which is equal to the energy of the non-leading system. Alternatively, if this flavor independence is assumed, one can extract the energy of the non-leading system by a similar comparison to the multiplicity measurements at lower center of mass energies. The average energy fraction of bottom hadrons, $\langle x_E \rangle_b$, is then determined from this non-leading energy measurement. Although the available event sample precludes a measurement of $\langle x_E \rangle_b$ with errors comparable to the present measurements, this approach has much different systematic errors than the

conventional method of using the momentum spectra of the leptons from semileptonic B decay to determine $\langle x_E \rangle_b$.

This chapter begins with a brief review of the Standard Model and, in particular, the electroweak couplings which govern the decay of the Z^0. The production of $b\bar{b}$ events is discussed along with the various corrections to R_b. The experimental methods used to select enriched $b\bar{b}$ event samples are surveyed, and the impact parameter tagging method used in this analysis is introduced. A summary of the present status of the determination of R_b by other experiments is given and the limiting source of systematic error in these measurements is discussed. Finally, the motivation for the measurement of the non-leading multiplicity is reviewed in more detail and the similar measurements made at PEP and PETRA are summarized.

1.1 The Standard Model

The goal of particle physics is to understand the nature and interactions of the most basic components of matter. The previous 25 years have been ones of great progress toward the achievement of this goal. In particular, the rise and longevity of the *Standard Model*, as a description of the most elementary particles and the forces which govern their behavior, is a testament to this progress.

The Standard Model* incorporates a small number of point-like, spin one-half particles, called *fermions*, to explain the composition of matter. These fermions are divided into two categories, *quarks* and *leptons*, which are each presently believed to contain at least six members (see Table 1–1). The quarks and leptons are divided into three similar generations, with the analogous particle in the next generation having a larger mass than that of the previous generation.

The forces at their most basic level are governed by integral spin particles, called *bosons*. Of the four forces that are known to exist, three have been included in the Standard Model. The *electromagnetic force* is governed by the massless photon (γ). The *weak nuclear force* has three very massive mediating particles, the Z^0, W^- and W^+. One of the ultimate goals of particle physics is the unification of all of the forces into one theory. To this end, the electromagnetic and weak forces were predicted to be different aspects of a single underlying force in the *electroweak theory* of Glashow, Salam and Weinberg.[2] The discovery in 1983 of the Z^0, W^-

* A complete discussion of the Standard Model is beyond the scope of this thesis and only a brief overview of the relevant material is presented herein. There are many very good sources of further information available — see Reference [1].

	Quarks	Leptons
1st generation	up (u) $q = +2/3$	electron neutrino (ν_e) $q = 0$
	down (d) $q = -1/3$	electron (e^-) $q = -1$
2nd generation	charm (c) $q = +2/3$	muon neutrino (ν_μ) $q = 0$
	strange (s) $q = -1/3$	muon (μ) $q = -1$
3rd generation	top (t) $q = +2/3$	tau neutrino (ν_τ) $q = 0$
	bottom (b) $q = -1/3$	tau (τ) $q = -1$

Table 1–1 The known quarks and leptons are listed with their electric charge (q), in units of e. Note that the top quark and the tau neutrino have not been directly observed.

and W^+ at the masses predicted by this theory was the conclusive evidence of its validity.[3]

The theory which explains the strong nuclear force is *quantum chromodynamics* (QCD). In this theory, the strong interactions are governed by the exchange of massless gluons (g) between particles which carry color charge. This color charge has three types, which are called red, green and blue. Of the fermions, only quarks carry color charge. The gluons also carry color charge, however, and thus gluons can interact with themselves, leading to two important consequences. The first is that at small distances, an anti-screening effect occurs which reduces the amount of color charge seen around a quark. This results in the property of *asymptotic freedom*, and implies that at very small distances the quark-quark and quark-gluon forces will be quite weak and the quarks will behave rather like free particles. The second effect is that the color flux lines between the quarks are pulled into a tube due to the gluon-gluon interactions. The inter-quark potential thus rises linearly with the distance between the quarks resulting in *quark-confinement*. Because of quark confinement, quarks are only observed in various bound systems such as *mesons* (a quark-antiquark pair) and *baryons* (three quarks). These mesons and baryons are known collectively as *hadrons*. As the separation between quarks gets quite large the energy stored in the strong field between the quarks becomes large enough to create a quark-antiquark pair from the vacuum. As a result of the

renormalization process, the coupling strength of the strong force varies as a function of energy such that at high energies (the asymptotically free regime), the coupling strength, α_s, is small and thus perturbation theory can be used to calculate the various effects. At lower energy, though, α_s becomes larger and the perturbation theory is no longer of much value. These energies are, however, of critical importance in understanding the production of hadrons from quarks, a process known as fragmentation. Consequently, this process must be described by physically-motivated models, such as those described in Chapter 3.

Finally, gravity is not included in the Standard Model, largely because of theoretical problems in building a suitable theory. This does not pose any difficulty for measurements such as that presented herein, because the strength of the gravitational attraction at the distances considered by the interaction of these elementary particles is far less than that of the other three forces.

1.2 Electroweak Couplings

The electroweak theory is based on an $SU(2)_L \times U(1)$ gauge group and the principle of local gauge invariance. The $SU(2)_L$ is a weak isospin group with a V – A structure such that it only couples to the left-handed fermions (hence the subscript 'L'). The U(1) is the electromagnetic symmetry group, which couples to right and left-handed fermions. Upon mixing the B_μ and W^3_μ fields of the U(1) and $SU(2)_L$ groups, one can generate four massless fields:

$$W^{\pm} = \sqrt{\frac{1}{2}}(W^1 \pm W^2)$$

$$Z_\mu = B_\mu \cos\theta_W + W^3_\mu \sin\theta_W \qquad (1\text{-}1)$$

$$A_\mu = -B_\mu \cos\theta_W + W^3_\mu \sin\theta_W .$$

These fields correspond to the $W^{\pm}$, Z^0 and γ gauge bosons, respectively. The process by which the mass of the $W^{\pm}$ and Z^0 is generated is the Higgs mechanism. This involves introducing a complex Higgs doublet from which three of its four degrees of freedom are used to provide the extra degrees of freedom necessary to form massive bosons. The remaining degree of freedom generates a scalar particle, the Higgs boson, which has not yet been discovered.

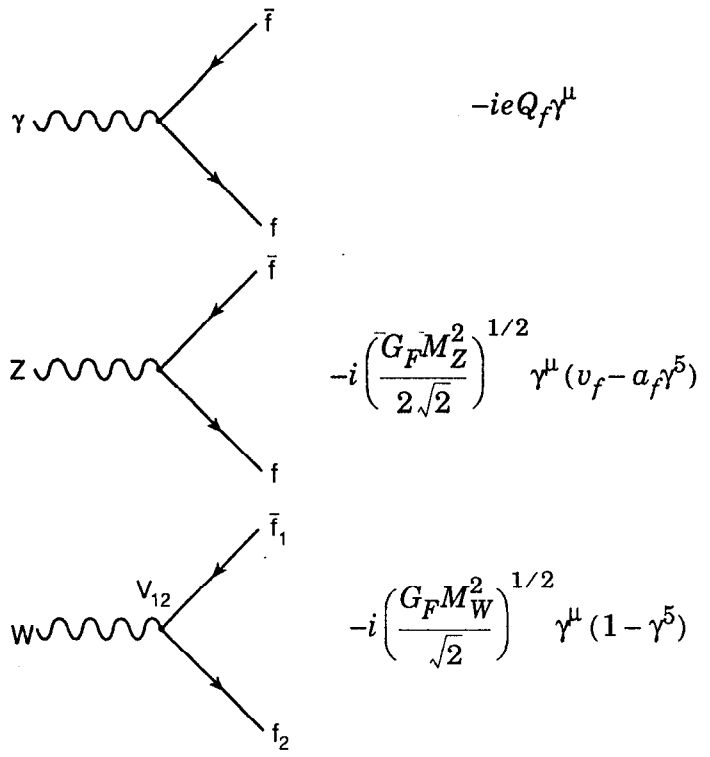

Figure 1–1 Feynman diagram vertex factors for the neutral and charged electroweak interactions.

The electroweak couplings between the fermions and the gauge bosons are given by the Feynman diagram vertex factors in Figure 1–1. These factors are written in terms of the vector and axial vector couplings, defined for a fermion of type f as

$$v_f = 2(T_f^{3L} - 2Q_f \sin^2\theta_W) \tag{1-2}$$

$$a_f = 2T_f^{3L} \tag{1-3}$$

where Q_f is the electric charge in units of the positron charge, and T_f^3 is the projection of the weak isospin onto the z-axis. The values of these constants are given in Table 1–2. It is also interesting to note that the $Z^0 f\bar{f}$ vertex factor can be re-written in a form which clearly exhibits the right and left-handed contributions:

$$-i\left(\frac{G_F M_Z^2}{2\sqrt{2}}\right)^{1/2}\gamma^\mu(v_f - a_f\gamma^5) = -i\left(\frac{G_F M_Z^2}{2\sqrt{2}}\right)^{1/2}\gamma^\mu[R_f(1+\gamma^5) + L_f(1-\gamma^5)], \tag{1-4}$$

Fermion type	Q_f	T_f^{3L}	a_f	v_f
u, c, t	+2/3	1/2	1	$1-\frac{8}{3}\sin^2\theta_w \approx 0.38$
d, c, b	–1/3	–1/2	–1	$-1+\frac{4}{3}\sin^2\theta_w \approx -0.68$
ν_e, ν_μ, ν_τ	0	1/2	1	1
e, μ, τ	–1	–1/2	–1	$-1+4\sin^2\theta_w \approx -0.06$

Table 1–2 The electric charge, the z-component of the weak isospin, and the axial-vector and vector couplings for the quarks and leptons in the electroweak theory. For right-handed fermions, $T_f = 0$. The numerical values for the vector coupling strengths are calculated for $\sin^2\theta_w = 0.231$.[4]

where,

$$R_f = \frac{1}{2}(v_f - a_f) = -2Q_f \sin^2\theta_W$$

$$L_f = \frac{1}{2}(v_f + a_f) = 2T_f^3 - 2Q_f \sin^2\theta_W.$$

There is one more small complication: the weak eigenstates of the quarks are different from their mass eigenstates. The left-handed eigenstates, namely those which participate in the charged-current interactions, are related by a 3×3 unitary, complex matrix known as the Kobayashi-Maskawa matrix.[5] By convention, the charge –1/3 quarks are chosen to be related by this matrix such that the weak eigenstates (primed) are given in terms of the mass eigenstates (un-primed) by

$$\begin{pmatrix} d'_L \\ s'_L \\ b'_L \end{pmatrix} = \begin{pmatrix} V_{ud} & V_{us} & V_{ub} \\ V_{cd} & V_{cs} & V_{cb} \\ V_{td} & V_{ts} & V_{tb} \end{pmatrix} \begin{pmatrix} d_L \\ s_L \\ b_L \end{pmatrix}. \tag{1-5}$$

This matrix has four free parameters: three angles and one complex phase.

1.3 Bottom Quark Production at the Z^0 Resonance

The production of quarks through electron-positron annihilation proceeds via two primary channels as illustrated in Figure 1–2. The cross section to produce hadronic events generally falls off as $1/s$ (where $s = E_{cm}^2$) in the energy region where the photon-exchange diagram dominates. At the center of mass energy around the mass of the Z^0, there is very large resonance. One can characterize the

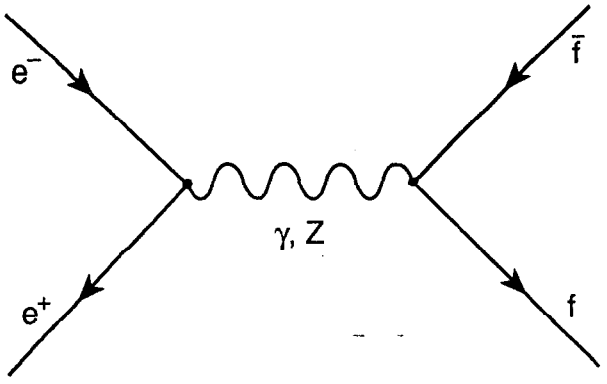

Figure 1–2 Electron-positron annihilation to an electroweak boson and the subsequent decay into a fermion-antifermion pair.

size of a resonance by comparing it to the point cross section for muon production, $\sigma_{pt} = 4\pi\alpha^2/3s$. The ratio of the cross section for producing hadronic events to σ_{pt} is referred to as R. At $E_{cm} = m_Z$, R is approximately 2900 (after correcting for the ~30% effect of initial state radiation).[6] This analysis is based on data from electron-positron annihilations at a center of mass energy of about 91 GeV.

1.3.1 Branching Fraction of the Z^0 to Fermions

The partial width of the Z^0 decay into a fermion-antifermion pair can be calculated in the Born approximation, given the vertex factors from Figure 1–1. The amplitude for this decay is

$$\boldsymbol{M}_{Z\to f\bar{f}} = -i\left(\frac{G_F M_Z^2}{2\sqrt{2}}\right)^{-1/2} \varepsilon_\mu^\lambda \, \bar{f}\gamma^\mu (a_f - v_f\gamma^5) f, \tag{1-6}$$

where ε_μ^λ is the polarization vector of the Z^0, and f and $\bar{f}$ are the fermion and antifermion spinors. The partial width for a two-body decay is given by:

$$\Gamma(Z^0 \to f\bar{f}) = \frac{1}{64\pi^2}\frac{s\beta}{M_Z^3}\int \left|\boldsymbol{M}_{Z\to f\bar{f}}\right|^2 d\Omega_{cm}, \tag{1-7}$$

where β is the speed of the fermion, equal to $\sqrt{1-4m_f^2/s}$. Thus, the resulting partial width for massless quarks is:

$$\Gamma(Z^0 \to f\bar{f}) = n_c\frac{G_F M_Z^3}{24\sqrt{2}\pi}(a_f^2 + v_f^2) = \frac{1}{2}n_c(a_f^2 + v_f^2)\,\Gamma_Z^0, \tag{1-8}$$

where n_c is a color factor which is 3 for quarks and 1 for leptons. In the last part of the expression $\Gamma_Z^0 = \Gamma(Z^0 \to \nu\bar{\nu}) \approx 0.17$ GeV.

The hadronic branching fraction of the Z^0 into a $b\bar{b}$ pair is defined as

$$F_b = \frac{\Gamma(Z^0 \to b\bar{b})}{\Gamma(Z^0 \to \text{hadrons})}. \tag{1-9}$$

In the absence of the production of additional flavors beyond bottom, the denominator is just the sum of the partial widths of the Z^0 to decay into the five flavors of quarks:

$$\Gamma(Z^0 \to \text{hadrons}) = \Gamma_u + \Gamma_d + \Gamma_s + \Gamma_c + \Gamma_b. \tag{1-10}$$

The tree level partial widths and hadronic branching fractions are given in Table 1–3.The total width of the Z^0 is about 2.5 GeV; the total hadronic width is about 1.7 GeV.

Fermion type (per channel)	$\Gamma(Z^0 \to f\bar{f})$	$\frac{\Gamma(Z^0 \to f\bar{f})}{\Gamma(Z^0 \to \text{had})}$
u, c	0.29 GeV	17%
d, s, b	0.37 GeV	22%
ν_e, ν_μ, ν_τ	0.10 GeV	—
e^-, μ^-, τ^-	0.17 GeV	—

Table 1–3 Estimates of the tree level, massless fermions partial widths and branching fractions, calculated for M_Z = 91.1 GeV and $\sin\theta_w$ = 0.231.[4] The coupling strengths used are given in Table 1–2.

The measurement of the branching fraction involves selecting the $b\bar{b}$ events from the *udsc* events with some known efficiencies, because in a given sample of Z^0 decays, F_b is calculated from the ratio of the number of $b\bar{b}$ events to the total number of events. Methods for selecting a sample of $b\bar{b}$ events are introduced in Section 1.4. The details of relating F_b to the fraction of events tagged as $b\bar{b}$ are found in Chapter 6.

1.3.2 Corrections to the Tree Level Branching Fraction

There are a number of corrections to this massless-quark, Born approximation calculation of the partial width. The first of these is the mass of the quark which is produced. With a non-zero mass, Equation (1-8) becomes

$$\Gamma(Z^0 \to f\bar{f}) = n_c \frac{G_F M_Z^3}{24\sqrt{2}\pi} \beta \left[\beta^2 a_f^2 + \left(\frac{3-\beta^2}{2} \right) v_f^2 \right]. \tag{1-11}$$

For bottom quarks at the Z^0, this correction is about –1.2%.

QCD Corrections

The radiation of soft gluons from the final state quarks is the source of the largest corrections due to QCD. To first order, the effect of these corrections is equivalent to the substitution into Equation (1-11) of [7]

$$a_f^2 \to a_f^2 \left\{ 1 + \frac{4}{3}\alpha_s \left[\frac{\pi}{2\beta} - \left(\frac{19}{10} - \frac{22}{5}\beta + \frac{7}{2}\beta^2 \right) \left(\frac{\pi}{2} - \frac{3}{4\pi} \right) \right] \right\} \tag{1-12}$$

$$v_f^2 \to v_f^2 \left\{ 1 + \frac{4}{3}\alpha_s \left[\frac{\pi}{2\beta} - \left(\frac{3+\beta}{4} \right) \left(\frac{\pi}{2} - \frac{3}{4\pi} \right) \right] \right\}. \tag{1-13}$$

In these expressions, the strong coupling constant α_s is given by [8]

$$\alpha_s(\mu) = \frac{12\pi}{(33-2n_f)\ln(\mu^2/\Lambda^2)} \left[1 - \frac{6(153-19n_f)\ln[\ln(\mu^2/\Lambda^2)]}{(33-2n_f)^2 \ln(\mu^2/\Lambda^2)} \right], \tag{1-14}$$

where μ is the energy scale, n_f is the number of quarks with mass less than μ and Λ is the QCD scale parameter. As $\beta \to 1$, these correction factors approach the same value of $(1+\alpha_s/\pi)$, which for a value of $\alpha_s = 0.123$ produces a correction of about 4%. Second and third order corrections have been calculated in the massless quark limit and are believed to be less than 1%.[9] Because this correction affects all quark flavors similarly, measuring the branching ratio instead of the partial width significantly reduces the contribution from this correction and the associated uncertainty in the value of α_s.

QED Corrections

In an analogous fashion to the QCD corrections discussed above, corrections due to pure QED process such as photon radiation and exchange between the final fermions can also be calculated. The result is a multiplicative correction factor of $(1+3\alpha Q_f^2/4\pi)$ for the partial width.[10] For bottom quarks this correction is

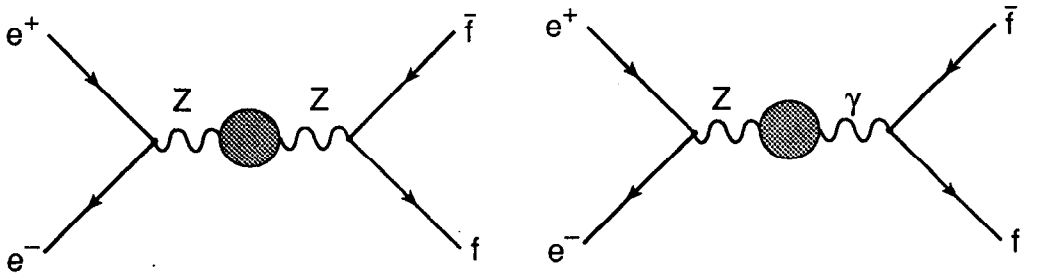

Figure 1–3 Examples of oblique corrections, including the γ-Z mixing diagram.

0.019%. The largest correction, that for the charged leptons, is 0.17%. Photon radiation from the initial state electron and positron reduces the peak cross section by ~30% as noted previously. Its affect on the partial widths, however, is only ~3%. Both of these QED corrections cancel in the branching ratio.

Electroweak Corrections

The genuine electroweak corrections can be divided into two categories: the corrections to the propagators via vacuum polarization diagrams (oblique corrections — see Figure 1–3) and the corrections to the final state vertex. The oblique corrections can be calculated using formalism such as that of Kennedy and Lynn[11] which allows the calculation of these corrections to all orders. These corrections are essentially the same for all flavors of quarks. The vertex and fermion self-energy corrections have been calculated by a number of authors.[12][13][14] They are of particular interest because $Z^0 \to b\bar{b}$ events have vertex and self-energy contributions from the yet unseen top quark. This is the case because the Kobayashi-Maskawa matrix element V_{tb} is expected to be approximately unity. The diagrams which contribute to the top quark coupling are shown in Figure 1–4. These additional contributions actually reduce the dependence of $\Gamma(Z^0 \to b\bar{b})$ on the top mass relative to that of $\Gamma(Z^0 \to d\bar{d})$ because of cancellations between the oblique and vertex corrections.[13][15][16] Specifically, the m_t^2-dependence of the branching fraction that results from the oblique corrections almost entirely cancels with that from the vertex diagrams. This leaves a term proportional to $\ln(m_t^2/M_Z^2)$ which, depending on the top mass, can be twice as large as original oblique correction. This logarithmic term also has the opposite sign than that of the oblique correction (see Figure 1–5). A very thorough compilation of the expected effects on the partial widths can be found in Reference [13]. Because of these additional top quark contributions to the vertex diagrams, the study of the $Z^0 \to b\bar{b}$ channel provides a tool with which one can

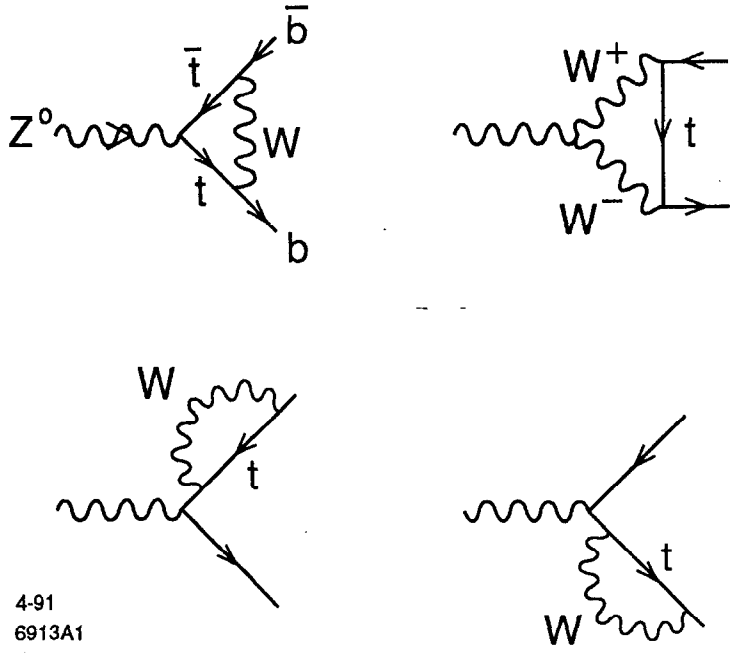

Figure 1–4 Contributions to the Z^0-$b\bar{b}$ vertex from the top quark.

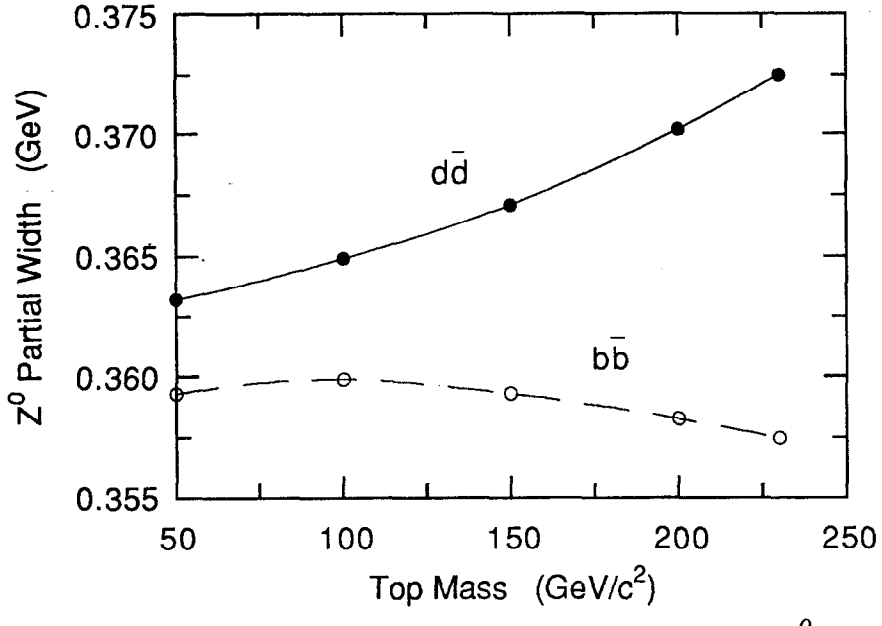

Figure 1–5 The dependence of the partial widths of the Z^0 to decay to down and bottom quark pairs. The points were calculated by W. Hollik for M_Z = 91 GeV/c^2 and a Higgs mass of 100 GeV/c^2. The lines are an interpolation between these points.[13]

attempt to separate the effects due to the top quark from those due to other new physics (see Section 1.3.3).

Finally, it should be noted that the variation of mass of a neutral Higgs boson, which is predicted to be present in the minimal Standard Model, has a very small effect on the partial width (less than 10 MeV).

1.3.3 Contributions from Exotic Phenomena

There are a number of mechanisms beyond the minimal Standard Model, which can affect the branching fraction to $b\bar{b}$. These extensions to the Standard Model include the possibility of additional Z bosons, the supersymmetry theory and the addition of a second Higgs doublet without all of the supersymmetric contributions. Djouadi *et al.* have presented a consistent strategy for disentangling these extensions from the $Zb\bar{b}$ vertex itself which involves measuring several quantities at accuracies requiring a very large event sample.[15]

Extra Z Boson: the Z'

In higher dimensional symmetry groups favored by Grand Unified Theories, it is possible to generate additional weak vector bosons.[17] Direct searches for the Z' with couplings similar to that of the Z at hadron colliders have set lower limits on the mass at 173 GeV/c^2 (UA1, 90% C.L.), 180 GeV/c^2 (UA2, 90% C.L.) and 412 GeV/c^2 (CDF, 95% C.L.).[18] Also, given a particular choice of symmetry group, indirect limits can be set on Z' mass given the Z, W and top quark masses.[19] The effects of the presence of a Z' on the partial width to $b\bar{b}$ is considered in Reference [15] and can vary significantly depending on the assumptions as to the source of the new boson.

Second Higgs Doublet

Although one Higgs doublet is required to generate the mass of quarks and bosons, more doublets are possible. This produces a pair of charged Higgs scalars which would lead to a number of new vertex diagrams shown in Figure 1–6(a). The effect of these additional diagrams on F_b has been calculated and is shown in Figure 1–7.[16] Again, precision measurements may make it possible to determine the presence of an additional Higgs doublet.

Supersymmetry

Supersymmetry (SUSY) is an attempt to resolve the vast difference in mass scales between the 10^{16} GeV mass scale of Grand Unified Theories and the much lighter mass scales of the Z and W around 100 GeV.[20] In unifying the treatment of the quark, leptons and gauge bosons, SUSY requires that every fundamental

particle have a supersymmetric partner with the same charge and color, but with a spin which differs by 1/2. The resulting partners of the quarks and leptons are the spin 0 squarks and sleptons. Similarly, the photon, *Z*, *W*, gluon and Higgs are paired with the photino, zino, wino, gluiono and higgsino, respectively, all of which have spin 1/2. Additionally, a second Higgs doublet is also required by SUSY. At the present, there has been no experimental observation of any of these partners.[8][21] Some of the diagrams containing these new particles, which will contribute to modifying F_b, are shown in Figure 1–6. The net result of these new diagrams on F_b has been calculated.[15][16] The result of Boulware and Finnell for a particular minimal SUSY model is shown as a function of the top quark mass in Figure 1–7.* The central line in this figure is the prediction of the minimal Standard Model and the upper line is the minimal supersymmetric model. Even for a very large top mass, the difference between these curves is about 1%, which is about the same magnitude as the variation in the minimal Standard Model for the reasonable range of top mass. However, with the combination of other precision measurements (such as the Z and W masses) and a precise determination of F_b it may be possible to find indirect evidence of supersymmetry and untangle it from the effects of the top quark.

1.4 Experimental Methods for Identifying *b* Events

In order to study properties of *B* hadrons, it is necessary to select an event subset which is enriched with $Z^0 \to b\bar{b}$ events. In particular, the goal of the tagging algorithm is both to tag the $Z^0 \to b\bar{b}$ events efficiently and have a high $Z^0 \to b\bar{b}$ purity in the tagged sample of events.

The B hadron has several properties which are relevant to tagging $Z^0 \to b\bar{b}$ events. These include,

1. *B* hadrons have much larger mass than other hadrons;[8]
2. *B* hadrons tend to be produced from fragmentation with a substantial fraction of the beam energy (~0.7);[22][23][24]
3. The mean lifetime of *B* hadrons is about 1.3 psec,[8][25] which with the rather hard fragmentation and the high energy at the Z^0, corresponds to a decay length of ~2 mm. Furthermore, because of the small value of V_{ub},[26] *B* hadrons decay almost exclusively into *D* hadrons which also

* As noted by Boulware and Finnell[16] their result for the supersymmetric contributions to the $Zb\bar{b}$ vertex differs in sign from that of Djouadi *et al.*[15] The latter find that the contribution of the charged Higgs and true supersymmetric contributions have the same sign, whereas the former find these to have the opposite sign.

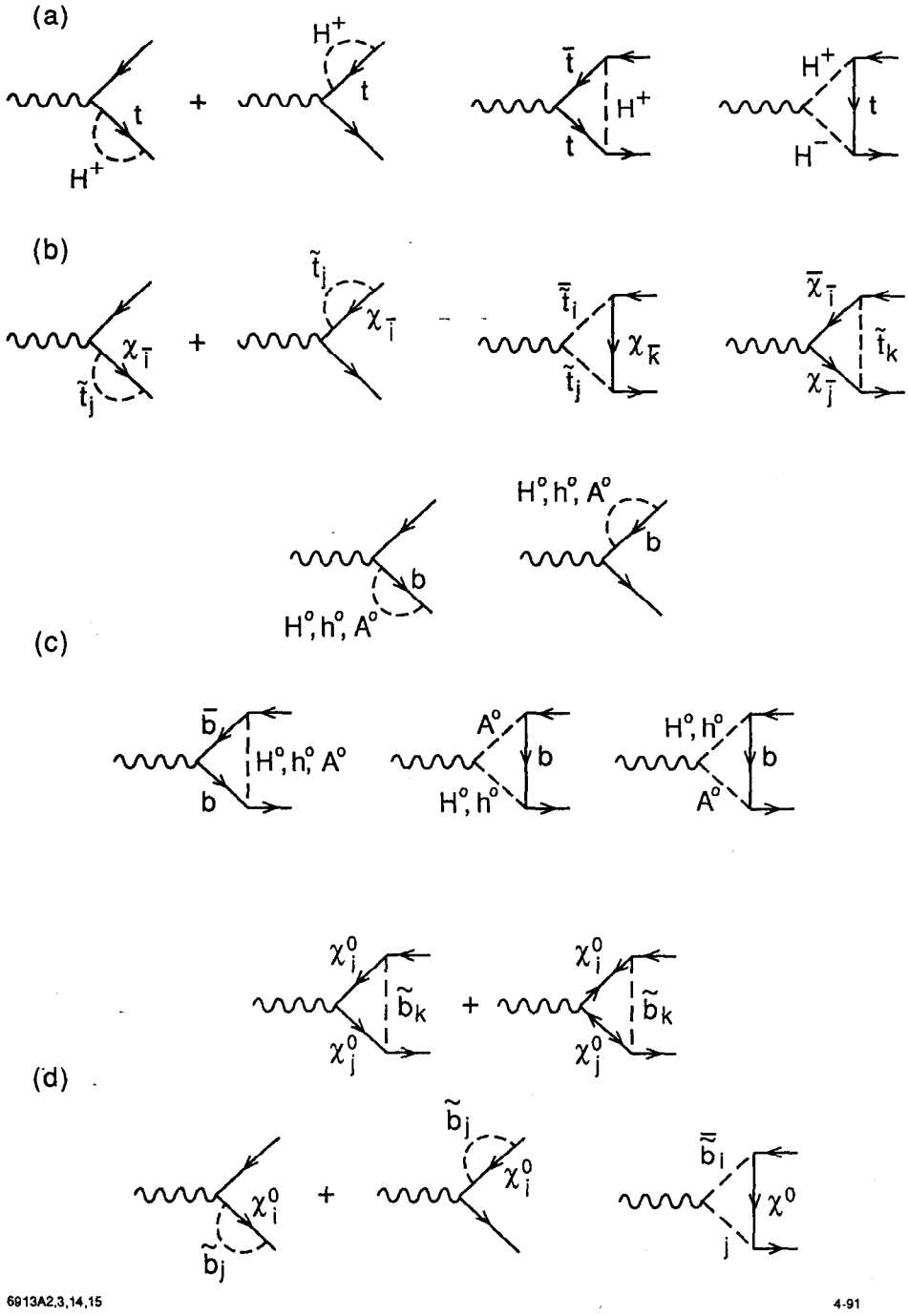

Figure 1–6 Supersymmetric contributions to bottom quark production from Z^0 decay: (a) charged Higgs, (b) charginos (χ), (c) neutral scalars, and (d) neutralinos.[16] The charginos and neutralinos are, respectively, the mixtures of the charged and neutral gauginos and higgsinos.

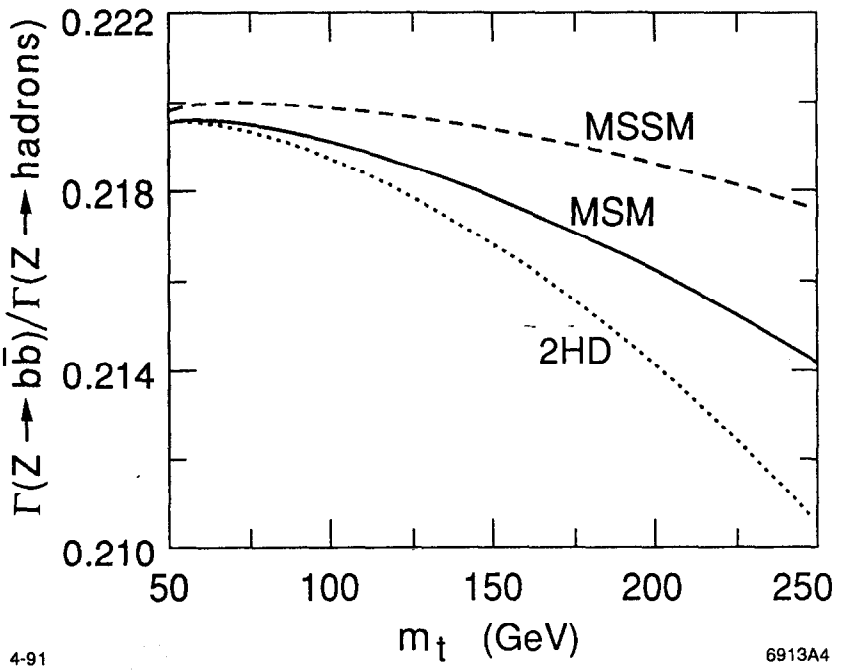

Figure 1–7 The dependence of the branching fraction of the Z^0 to bottom quarks for several models: the minimal Standard Model (MSM), the addition of a second Higgs doublet (2HD), and the minimal supersymmetric model (MSSM), as calculated by Boulware and Finnell.[16] The MSSM calculation assumes tanβ = 1 (relative size of the vacuum expectation values of the two Higgs doublets), M = 50 GeV (W-ino mass matrix parameter), μ = 30 GeV (coupling between the two Higgs fields), and *m(top squark)* = $M(H^+)$ = 100 GeV. This combination of values was chosen to illustrate a maximal effect.

have significant lifetimes, ranging from 0.4 to 1.0 psec, depending on the type of D.[8]

As described below, the high p and p_T lepton tag and the boosted sphericity product tag use these first two properties, which imply that tracks from B decay will tend to have a large total momentum (p) and also a large momentum component in the direction transverse to the event axis (p_T).

The third property of the B hadron decay implies that $Z^0 \rightarrow b\bar{b}$ events will have a rich vertex structure, which distinguishes them from *uds* and to some extent charm events. Figure 1–8 illustrates this vertex structure for a typical light quark and $b\bar{b}$ event. Indications of this vertex structure are potentially resolvable with state-of-the-art tracking detectors. Figure 1–9 shows the same events as Figure 1–8, except that the tracks have been reconstructed after detector

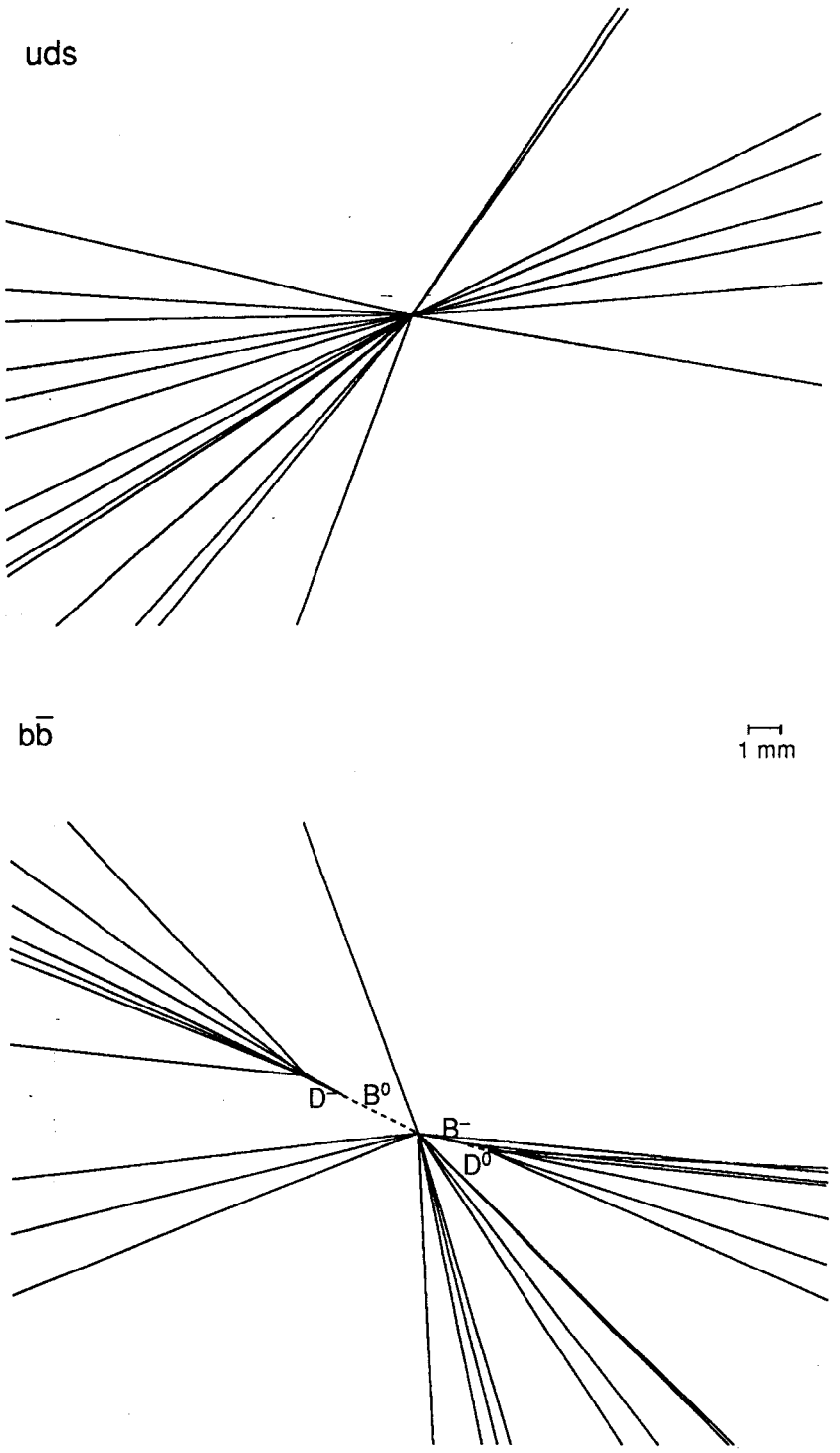

Figure 1–8 Monte Carlo events showing the generated particle trajectories. The upper event is a light quark event and the lower is a bottom quark event, showing the B and D decay vertices.

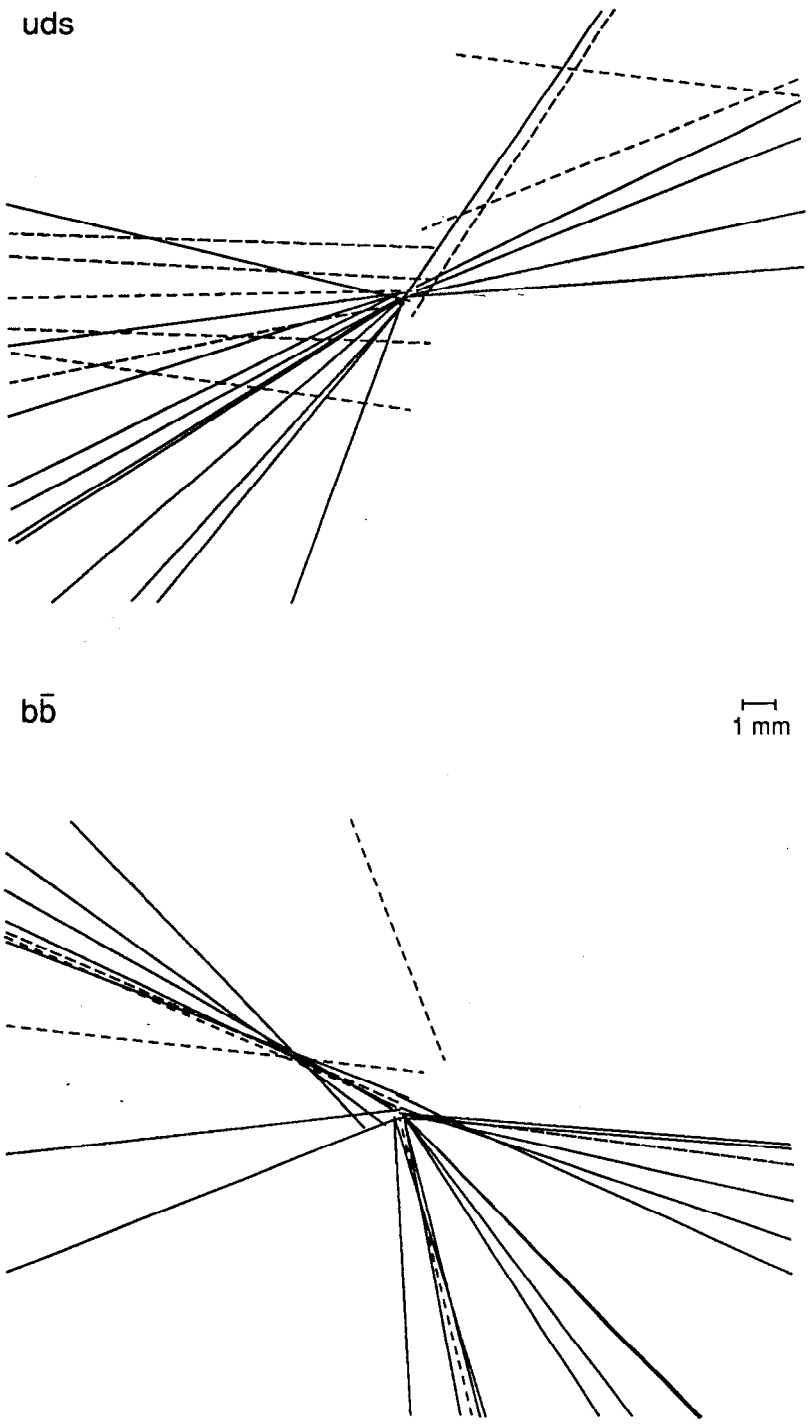

Figure 1–9 Monte Carlo events showing the tracks reconstructed after the Mark II detector simulation. The upper event is a light quark event and the lower is a bottom quark event. These are the same events as shown in Figure 1–8. The tracks represented as dashed lines failed track quality cuts.

simulation. Note that the vertex structure is now significantly more difficult to discern. Because of this, no attempt has been made to tag $Z^0 \to b\bar{b}$ events by fully reconstructing these vertices, primarily because of its low efficiency. Instead, the analyses use properties of the tracks which emanate from the secondary and tertiary vertices. At PEP and PETRA, the introduction of vertex detectors permitted new algorithms to be used to select $b\bar{b}$ events based on the positions of potential secondary vertices. The tag used in this analysis is also based on the use of precision tracking detectors, except that the algorithm only looks for tracks inconsistent with having originated from the location of the e^+e^- annihilation and does not do any fits for secondary vertices.

1.4.1 Lepton Tag

The high p and p_T lepton tag has been used by numerous groups to isolate $b\bar{b}$ events at PEP and PETRA, and more recently at the SLC[27] and LEP.[22][23][24] For the lepton tag, one searches for leptons from the semileptonic decay of the B hadron, $B \to Dl\nu$, requiring these leptons to have a large p and p_T. Typical cuts for selecting only the leptons from B decay, such as those used by OPAL,[24] are $p > 4.5$ GeV and $p_T > 1$ GeV. The branching fraction can then be extracted from the number of events which pass these criteria. Alternatively, the lepton p and p_T spectra can be fit using Monte Carlo predicted p and p_T distributions for all of the sources of leptons.

1.4.2 Boosted Sphericity Product Tag

The boosted sphericity product tag, originally developed by TASSO[28] and used at LEP by DELPHI,[29] uses the shape of the events to select a $b\bar{b}$-enriched event sample. Specifically, $b\bar{b}$ events will, because of the large B mass, tend to be less collimated than *udsc* events. The event-shape variable sphericity, S, is used to quantify this difference in event shape. It is defined as

$$S = \frac{3}{2}\min\left(\frac{\sum_i \left|\vec{p}_i \times \hat{S}\right|^2}{\sum_j \left|\vec{p}_j\right|^2}\right), \tag{1-15}$$

where the sum i is over tracks and the unit vector $\hat{S}$ is that which minimizes the momentum sum.

The algorithm consists of calculating the sphericity separately in each hemisphere defined by the plane perpendicular to the event sphericity axis, after

boosting the tracks in each hemisphere to the rest frame of the average B hadron (TASSO used β=0.74 at E_{cm} = 35GeV and DELPHI used β=0.96 at 91 GeV). The product of the jet sphericities, S_1S_2, is then used to separate the $b\bar{b}$ sample. TASSO used a fixed cut requiring that $S_1S_2 > 0.18$ to select the enriched event sample which it used for B lifetime measurements. DELPHI has fit the S_1S_2 spectrum between 0.1 and 0.5 to a pair of Monte Carlo predicted S_1S_2 distributions for $b\bar{b}$ and *udsc* events weighted by the fraction of $b\bar{b}$ events.

1.4.3 Vertex Detector-Based Tags: PEP and PETRA

Algorithms were developed at PEP and PETRA which used information from their vertex detectors as indicators of $b\bar{b}$ events. P. Weber[30] developed a vertex search algorithm used with the Mark II at PEP. This algorithm initially fit all of the tracks in an event to a common vertex, removing those tracks necessary to achieve a fit probability of some minimum value. Secondary vertices were then sought in the events and $b\bar{b}$ candidate events selected with the requirements that the vertex contain at least four tracks, have a positive decay length, and lie close to the expected flight path as determined by the thrust axis.

The TASSO Collaboration[31] developed an enrichment method that did not attempt to reconstruct a multitrack B decay vertex, but instead fit a vertex using each track pair. Each of these vertices were assigned a weight based upon distance to the beam spot, and the angle between the momentum sum of the tracks in the vertex and the line connecting the two-track vertex to the beam position. These individual vertex weights were then summed, either by event or jet, and a fixed cut was used to select the $b\bar{b}$-enriched event sample.

1.4.4 Impact Parameter Tag

Instead of fitting tracks to vertices, the tag used by this analysis simply looks for tracks which are inconsistent with the electron-positron interaction point (IP).* The IP used in this analysis is one which is determined with a fitting algorithm on an event-by-event basis. The variable used to measure the distance of a track from the IP is the impact parameter, b (see Figure 1–10). However, the resolution with which the impact parameter can be measured for a given track may vary significantly with the track's momentum and angle, and the number of position measurements associated with that track. Thus, it is useful to use the impact parameter

* The details of this algorithm and the use of impact parameters are discussed in subsequent chapters. For more information on impact parameters and the impact parameter measurement resolution of the tracking detectors refer to Chapter 4. For the specifics of the tagging method see Chapter 5.

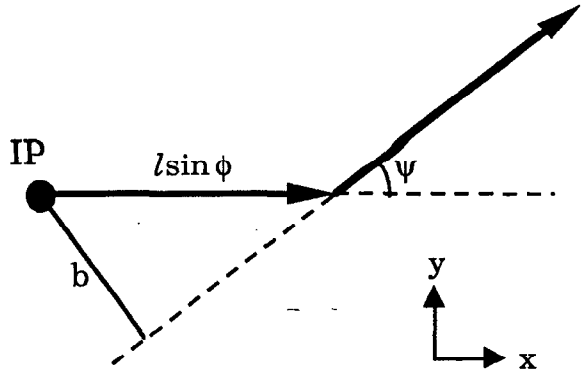

Figure 1–10 Definition of the impact parameter b. For a parent particle which traveled a distance l at an angle ϕ with respect to the beam axis, and then decayed into a daughter at an angle ψ from the parent's direction, the projection of the impact parameter into the plane perpendicular to the beam axis is given by $l\sin\psi\sin\phi$. The projection of the impact parameter is used because the precision vertex detectors only measure the tracks in this plane.

significance, b/σ_b, where σ_b is the expected impact parameter resolution. The tagging algorithm then requires an event (or hemisphere) to have a minimum number of tracks of some minimum impact parameter significance. A typical tag requires at least three tracks with $b/\sigma_b > 3.0$. To further increase the signal-to-noise ratio of the tracks with large significance, the impact parameters are given an algebraic sign which is positive if the vector from the IP to the point where the track crosses the thrust axis makes an acute angle with respect to the track direction. The result of this is that most of the tracks from B decays have positive impact parameters, while tracks from *udsc* events are distributed more symmetrically about $b = 0$. The distribution of impact parameter significance as predicted by the Monte Carlo whose impact parameter resolution was tuned to that in the data is shown in Figure 1–11.

1.4.5 Other Tags

Other types of hybrid tags are also possible which incorporate a number of event properties to achieve statistically powerful tags. A multidimensional algorithm has been explored by ALEPH[32] and DELPHI[33] using Monte Carlo simulation. The use of neural networks also has been investigated by DELPHI[34] and used to measure the branching fractions to different flavors of events. The major drawback of these methods is the evaluation of the systematic error with such a complicated algorithm.

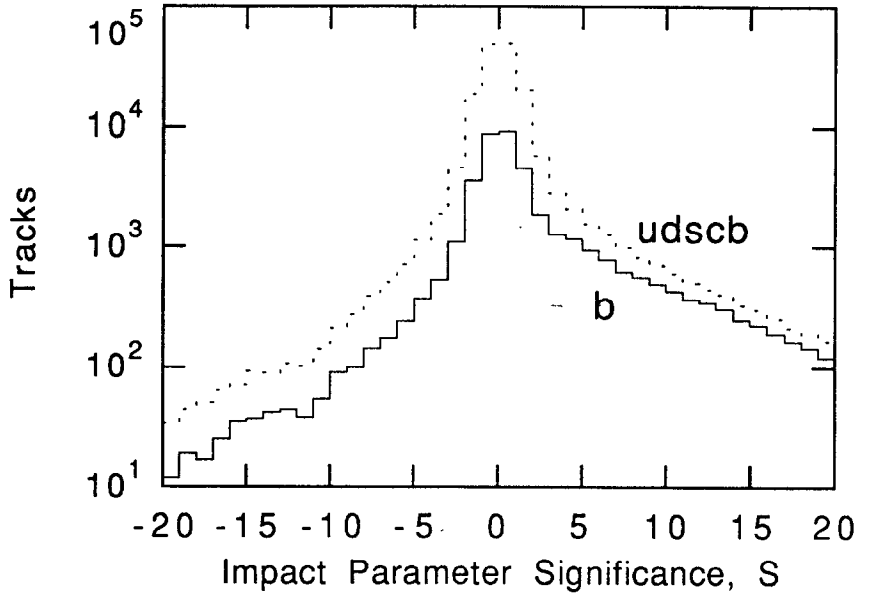

Figure 1–11 The impact parameter significance distributions for all flavors of hadronic events and the bottom flavor events. The asymmetry is the result of applying a sign to the impact parameter with the thrust axis. Note that the tracks from b events are the dominant contribution to the tracks with a positive impact parameter.

1.5 Measurements of the Branching Fraction to b Quarks

The measurement of the hadronic branching fraction of the Z^0 to decay into $b\bar{b}$ is well motivated for a number of reasons. With the statistics presently available, this provides a check of the Standard Model prediction for the Z^0 couplings to b quarks. When larger event samples are available, the increased sensitivity makes this an interesting window on the top quark as well as various possibilities of new physics as discussed in Sections 1.3.2 and 1.3.3 While this measurement has been done by a number of collaborations, the use of an impact parameter tag to measure F_b is potentially interesting because of the different sources of systematic error from the methods employed in the previous measurements.

All of the experiments at SLC and LEP have measured quantities related to F_b. A summary of these measurements and their quoted results is given in Table 1–4. Four experiments, Mark II,[27] ALEPH,[22] L3[23] and OPAL,[24] have used lepton tags and DELPHI[29] used the boosted sphericity product tag.

Experiment	Method	Quantity quoted
Mark II[27]	lepton tag (e & μ)	$F_b = 0.23^{+0.10+0.05}_{-0.09-0.04}$
ALEPH[22]	lepton tag (e & μ)	$F_b = 0.220\pm0.016\pm0.024$
L3[23]	lepton tag (e & μ)	$\Gamma_b = 385\pm7\pm22$ MeV
OPAL[24]	lepton tag (μ)	$F_b \cdot Br(B \to lX) = 0.0226\pm0.0007\pm0.0013$
DELPHI[29]	boosted sphericity product	$F_b = 0.209\pm0.030\pm0.031$

Table 1–4 Measurement of F_b and quantities related to F_b by the experiments at the SLC and LEP. The errors are statistical and systematic, respectively. To get their value for F_b, Mark II, ALEPH and L3 used 0.11 ± 0.01, 0.102 ± 0.010 and 0.117 ± 0.006 respectively as the B decay semileptonic branching ratio.

To compare the results of the lepton tag measurements, it is useful to compare the quantity which is actually measured with this tag, namely the product of F_b and the branching fraction of the B hadron to leptons, $F_b \cdot Br(B \to lX)$. In order to convert the L3 value for Γ_b into F_b, their measured hadronic width of the Z^0, to which they normalized their result for Γ_b, of 1742 ± 19 MeV[35] is used to yield $0.221\pm0.004\pm0.012$ (where the 19 MeV error on the total hadronic width was removed in quadrature). The value of $F_b \cdot Br(B \to lX)$ is then extracted using the same value of $Br(B \to lX)$ that was used by each experiment to calculate F_b. The $F_b \cdot Br(B \to lX)$ measurements are given in Table 1–5.

Experiment	$F_b \cdot Br(B \to lX)$
Mark II (e & μ)	$0.025^{+0.011+0.006}_{-0.088-0.005}$
ALEPH (e & μ)	$0.0224\pm0.0016\pm0.0010$
L3 (e & μ)	$0.0259\pm0.0005\pm0.0007$
OPAL (μ)	$0.0226\pm0.0007\pm0.0013$
Weighted Average	$0.0248\pm0.0004\pm0.0005$

Table 1–5 The SLC and LEP measurements of the product of the hadronic branching fraction to b quarks and the branching ratio of the B hadron to leptons.

To determine an average value for F_b, the common systematics among the lepton tags of the B decay semileptonic branching ratio must be properly handled. As mentioned previously, the lepton tags actually measure the product of F_b and the branching fraction of the B hadron to leptons, $F_b \cdot Br(B \to lX)$, so in order to combine the lepton tag results, the weighted average of the product will be taken and then converted to F_b afterward. The resulting average value is given in Table 1–5.

To determine a value for F_b, a value of $Br(B \to lX)$ must be chosen. There is some question of what value of $Br(B \to lX)$ to use. ALEPH, for instance, has used the value from CLEO and ARGUS measurements at the $\Upsilon(4s)$,[36] where only $B_{u,d}$ mesons are studied, whereas the Mark II and L3 use values measured at higher energies. There appears to be a significant difference between these results, the former being 0.102±0.007 and the latter being 0.117±0.006. The branching ratios measured at PEP, PETRA and LEP are used for calculating the following average value of F_b because the mixture of various B hadron species at these energies more properly represents that at the Z^0. This results in an average of

$$F_b(\text{lepton tags}) = 0.212 \pm 0.003 \pm 0.012$$

where the error includes the uncertainty in $Br(B \to lX)$. Averaging this with the DELPHI result yields,

$$F_b(\text{world average}) = 0.212 \pm 0.003 \pm 0.011.$$

The Standard Model predicts a value of $F_b = 0.217$.[13] Despite the contribution from the DELPHI measurement, the systematic uncertainty in this value is dominated by the uncertainty in $Br(B \to lX)$, which suggests that other measurements not depending on tagged leptons — such as the impact parameter significance tag — would be beneficial.

1.6 Measuring the Non-leading Multiplicity in b Quark Events

The high $b\bar{b}$-purity sample of impact parameter tagged events can also be used to measure other properties of $b\bar{b}$ events. The average charged multiplicity of $Z^0 \to b\bar{b}$ events, $\bar{n}_b$, is pursued in this analysis.

1.6.1 Theoretical Interest

The primary purpose of this measurement is a qualitative check of QCD phenomenology as observed in the fragmentation process. The framework of QCD provides that, at high energy, multiple particle production is governed by gluon fragmentation, which is triggered by the disruption of the vacuum by the color charge of the leading quark. As such, the fragmentation process is expected to be independent of the initial quark flavor. It has been suggested[37][38] how this expectation can be tested by measuring $\bar{n}_b$, subtracting off the well-known average B meson decay multiplicity, $\bar{n}_B$, and determine the *non-leading* multiplicity,

$$\bar{n}_{nl} = \bar{n}_b - \bar{n}_B. \tag{1-16}$$

The non-leading multiplicity can then be compared to the total multiplicity of e^+e^- annihilation at the center of mass energy equal to the average energy available to the non-leading system in $Z^0 \to b\bar{b}$ events. This is shown graphically in Figure 1–12(a). This average non-leading energy can be expressed as

$$\langle E_{nl} \rangle = E_{cm}(1 - \langle x_E \rangle) \tag{1-17}$$

where E_{cm} is the center-of-mass energy and $\langle x_E \rangle$ is the average energy fraction carried off by the heavy hadron,

$$x_E = \frac{2E_{had}}{E_{cm}}. \tag{1-18}$$

Conversely, as shown in Figure 1–12(b), it was also suggested that one can determine $\langle x_E \rangle$ by a measurement of $\bar{n}_{nl}$ by assuming that the multiplicity of the non-leading system is indeed independent of the flavor of the initial quark flavor.

1.6.2 Previous Measurements

The measurement of $\bar{n}_b$ ($\bar{n}_c$), in the case of $e^+e^- \to \gamma^* \to b\bar{b}$ ($c\bar{c}$) decays at PEP and PETRA energies, has been published by the Mark II,[37] DELCO,[39] TPC[40] and TASSO,[41] so a measurement at E_{cm} = 91 GeV is well motivated. Table 1–6 shows the measured values of $\bar{n}_b$. The Mark II and TPC analyses also make the comparison of the non-leading multiplicity to lower energy total multiplicity data, both finding that their $\bar{n}_{nl}$ is consistent with the total multiplicity measurements, within their experimental uncertainty. The Mark II and TASSO analyses also reverse the measurement to determine average fragmentation information. The Mark II measured $\langle x_E \rangle$ in the manner described above, while TASSO used the $\bar{n}_b$ distribution to determine $\langle z_b \rangle$ by a comparison with Monte Carlo predictions. Each

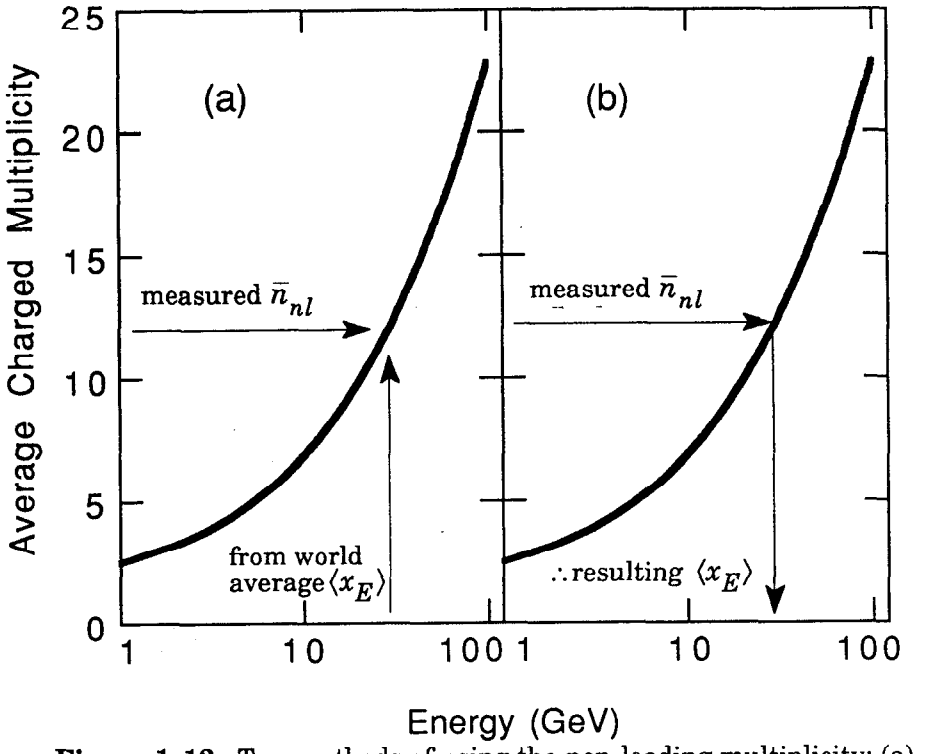

Figure 1-12 Two methods of using the non-leading multiplicity: (a) a test of the independence of the fragmentation process on the flavor of the initial quark by comparing a measured non-leading multiplicity, $\bar{n}_{nl}$, and its average non-leading energy to total multiplicity at lower E_{cm}; (b) the determination of $\langle x_E \rangle$ from the measured non-leading multiplicity by assuming the flavor independence. In both figures, the line represents the world's average measurement of the total charged multiplicity.

of the PEP and PETRA measured values of $\bar{n}_b$ can be used to make the comparison with the lower energy total multiplicity by use of an average decay multiplicity for the bottom or charm heavy hadron.

In making these comparisons a number of corrections were studied to make the comparison as relevant as possible. These corrections include:

- heavy quark correction, which removes the effects of heavy quarks in the lower energy total multiplicity data;
- leading particle correction, which removes the effect of the leading particles in light quark events;
- x_E-distribution correction, which accounts for the distribution of the non-leading energy and the non-linear relationship between multiplicity and energy.

experiment and heavy quark type	tagging method	E_{cm} (GeV)	$\bar{n}_b$ or $\bar{n}_c$
Mark II $(b\bar{b})$[37]	lepton tag	29	16.1±1.1
Mark II $(c\bar{c})$[37]	lepton tag	29	13.2±1.0
DELCO $(b\bar{b})$[39]	lepton tag	29	14.32±0.92
TPC $(b\bar{b})$[40]	lepton tag	29	16.7±1.0
TPC $(c\bar{c})$[40]	lepton tag	29	13.5±0.9
TASSO $(b\bar{b})$[41]	vertex tag	35	15.96±1.43
TASSO $(b\bar{b})$[41]	vertex tag	42.1	17.02±1.98

Table 1–6 The b or c event multiplicities $\bar{n}_b$ or $\bar{n}_c$ measured at PEP and PETRA are given with their total statistical and systematic error. Also given is the method used to select the subset enriched in b or c events. DELCO, TPC and TASSO measured the multiplicity in the thrust hemisphere opposite the tagged hemisphere, whereas Mark II used the entire event multiplicity.

It can be seen in Figure 1–13 that the overall agreement between the non-leading multiplicity measurements and lower energy multiplicity is indeed good and a similar point at E_{cm} = 91 GeV would be advantageous in demonstrating further agreement. These corrections, and the comparison with them appropriately applied, are discussed in all their detail in Section 7.6, "Comparison with Data at Lower C.M. Energy," on page 217.

The measurement which is performed in this analysis has a number of advantages over earlier measurements. Firstly, by measuring the non-leading multiplicity at a significantly higher center-of-mass energy than earlier experiments, the corresponding non-leading energy (~30 GeV) is on the continuum, well away from any resonances, and is in a region where the total multiplicity has been accurately measured by many of the PEP and PETRA experiments. Also, the use of the impact parameter tag avoids systematic difficulties of the high p and p_T lepton tags alluded to by J. Chrin.[42] Finally, the measurement of $\langle x_E \rangle_b$ in this fashion is an important independent check on $\langle x_E \rangle_b$ measured using the lepton momentum spectrum from semileptonic B decay.

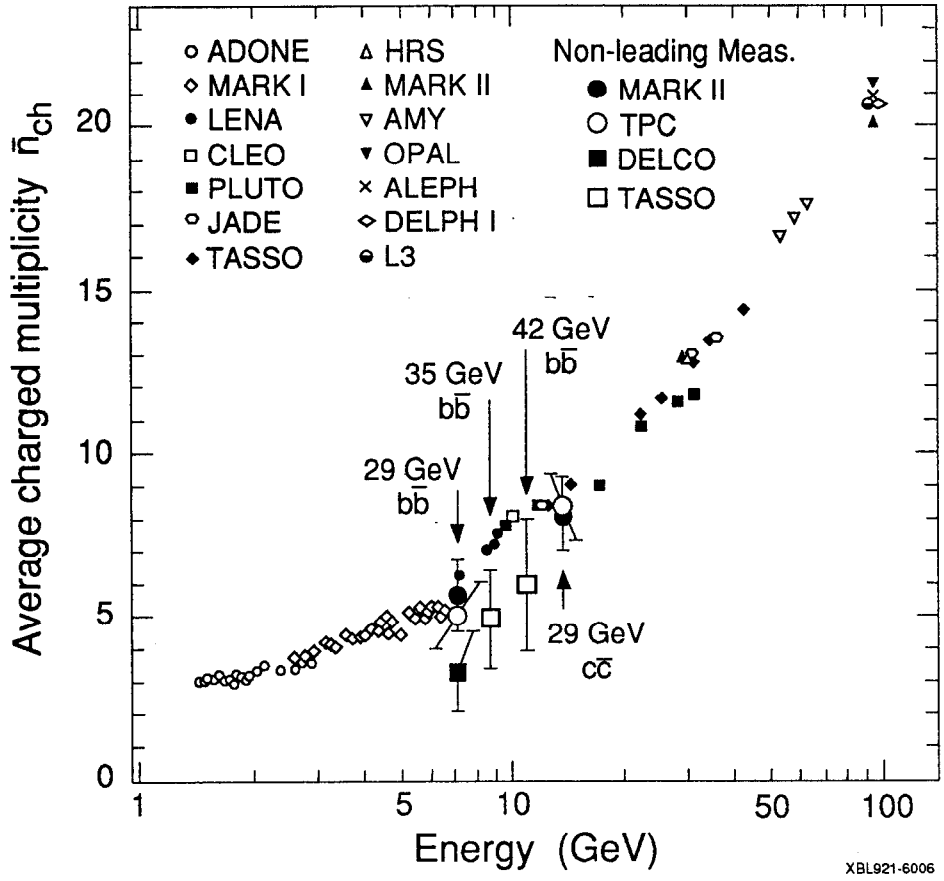

Figure 1–13 The comparison between the non-leading multiplicity at the corresponding non-leading energy, and the total multiplicity at a given center of mass energy. The center of mass energies at which the non-leading multiplicities were measured are indicated. The non-leading energy for a measurement of the *b* event multiplicity at a center-of-mass energy of 91 GeV is about 30 GeV.

Chapter 2

Experimental Apparatus

The heart of the Stanford Linear Accelerator Center (SLAC) is the linear accelerator (LINAC) which accelerates electrons up to very high energies.[44] Constructed between 1962 and 1966, the LINAC originally provided electrons for a very productive fixed target experimental program. This program included the deep inelastic scattering experiments which demonstrated the quark nature of the proton and neutron.[45] In the early 1970's SLAC built its first electron-positron storage ring, SPEAR, where the charm quark[46] and tau lepton[47] were discovered. In the late 1970's the PEP storage ring was built to collide electrons and positrons at still higher energies. Finally in the mid-1980's the SLAC Linear Collider (SLC) was constructed to provide electron-positron collisions at high enough energies to produce the weak boson, the Z^0. To detect the produced particles, we use the Mark II detector, which was originally used at SPEAR and PEP. It was extensively upgraded at PEP in preparation for its move to the SLC and upgraded still further at the SLC.

2.1 The SLAC Linear Collider

The SLC is unique among electron-positron colliders now in use, in that it is a single pass collider, not a storage ring.[48] An important motivation behind the concept of a linear collider is an economic one. The cost associated with electron circular accelerators varies as the square of the energy of the machine, whereas a

linear accelerator's costs varies linearly with the energy.* Thus the linear collider concept is the only one which will be financially reasonable for the next generation of high energy electron-positron colliders and the SLC is a prototype for the study of linear colliders.

The SLC uses the LINAC to accelerate both the e^- and e^+ beams up to an energy of 47 GeV. At the end of the linac the beams are sent into opposite arcs which bend them around in order to collide them together head-on (see Figure 2–1). Three bunches of particles are accelerated simultaneously, two e^- bunches and one e^+ bunch. The purpose of the second e^- bunch is for producing the e^+ bunch for the next accelerator cycle. At two-thirds of the way down the accelerator, this extra e^- bunch is deflected out of the accelerating tube and directed onto a tungsten target. Here the ensuing electromagnetic shower produces the positrons which will be sent to the beginning of the LINAC and accelerated along with two new e^- bunches.

In order to maximize the luminosity of the accelerator, and thus the production of Z^0s, it is essential that the beams be compressed to a very small transverse size when they collide at the interaction point (IP). To achieve this it is essential that the beams be very well tuned coming from the LINAC. Damping rings, near the beginning of the LINAC, reduce the transverse emittance of the beams through synchrotron radiation. Just before the beams reach the IP, the Final Focus system compresses the transverse size of the beams from about 1 mm to only a few microns. After the collision, the beams go out through the opposite final focus where they are diverted toward beam dumps.

The SLC produced it's first recorded Z^0 on 11 April 1989. In the remainder of that year, the Mark II detector recorded 528 events. In the fall of 1989 the SLC was shut down for upgrades both to the accelerator and the Mark II detector, which included the installation of the vertex detectors. The SLC began running in 1990 with a test run during January in which 37 Z^0 events were produced and then ran through the summer to produce 257 more events. As the analysis in this thesis requires the precision tracking provided by the vertex detectors, only the 294 events

* These cost scaling rules can be illustrated with the following argument. In a storage ring design, the majority of the cost scales as the size of the ring. However, the RF power required to compensate for the sychrotron radiation scales differently. The energy loss per orbit due to synchrotron radiation is proportional to E^4/R, where E is the machine energy and R is its radius. Thus the cost will be a sum of two terms: costs which scale linearly with the size of the ring (magnets, excavation, *etc.*) and those due to the RF system. The total cost, C, can be expressed as $C = \alpha R + \beta E^4/R$. Differentiating this with respect to R and setting the derivative to zero to optimize the cost performance yields the result that the cost of a storage ring scales as E^2. In contrast the cost of a linear machine scales linearly with energy. More detailed information can be found in Reference [49]

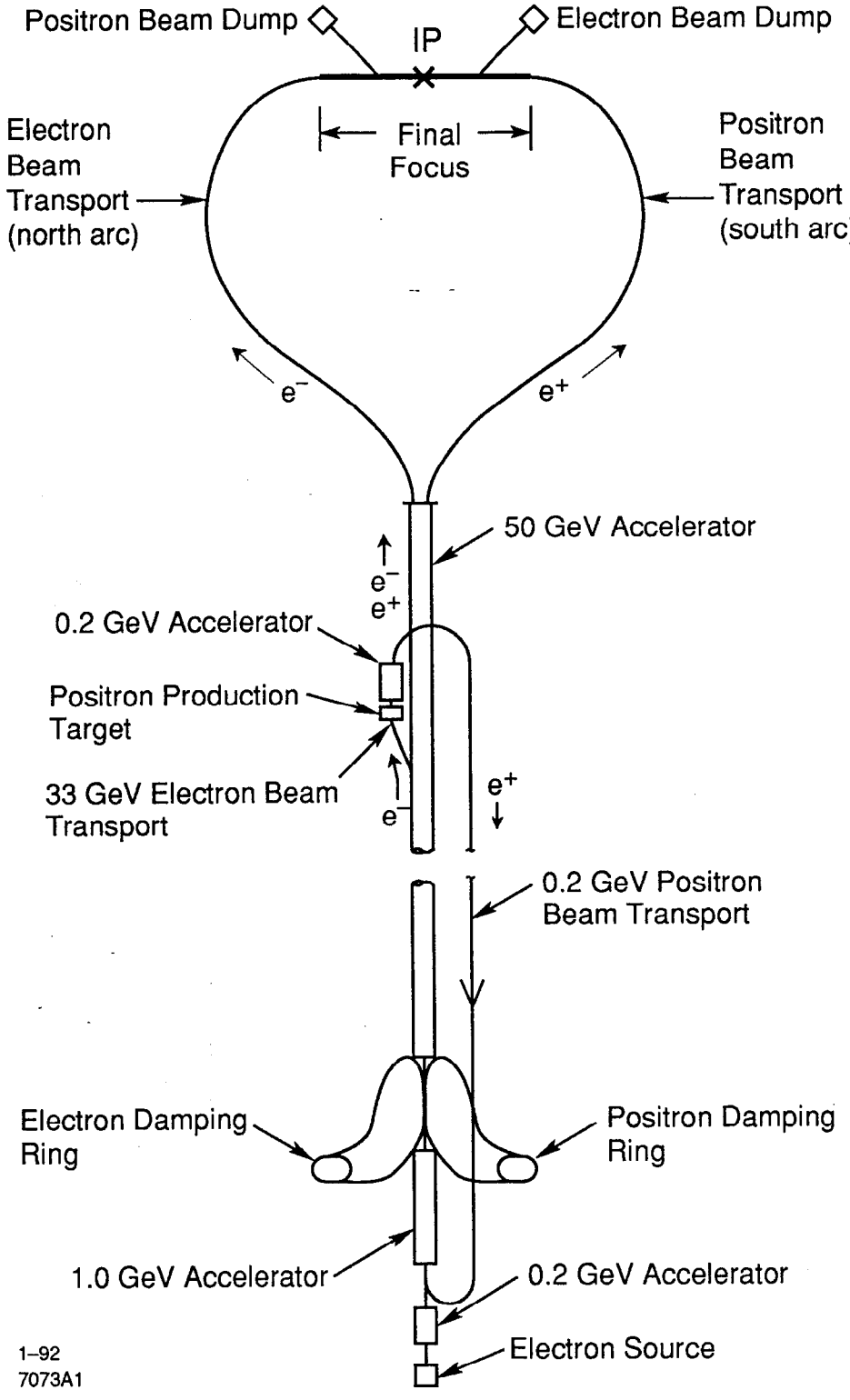

Figure 2–1 A schematic layout of the SLC.

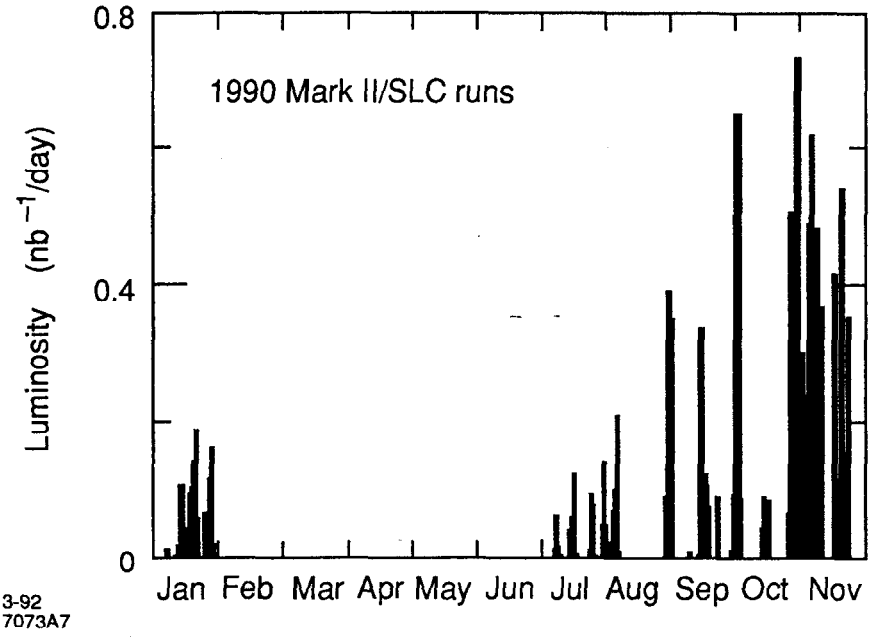

Figure 2–2 The daily luminosity delivered to the Mark II by the SLC during the 1990 runs.

taken during the 1990 runs are used here. The average center of mass energy for the 1990 runs was measured to be 90.93±0.01±0.04 GeV.[50] The luminosity recorded by the Mark II during 1990 is shown in Figure 2–2. From July through October, the focus of the run was on SLC machine physics studies, particularly improvement of performance parameters such as the repetition rate and raising the beam currents. With these improvements, instantaneous luminosity as high as 3 to 4 Z^0 events per hour was achieved.

2.2 The Mark II Detector

The Mark II is a solenoidal spectrometer which was based on the first e^+e^- detector at SLAC, the Mark I. The detector was first used at SPEAR from 1978 to 1979, and later at PEP from 1981 to 1984. In preparation for its move to the SLC, the detector was substantially upgraded with the additional of several new detector components, most notably a new central tracking detector. The upgraded detector was tested at PEP with a run during 1985 and 1986. The Mark II was moved to the SLC collider hall in 1986 and started operations there in 1987. Finally, in the fall of 1989, the vertex detectors were installed for the final Mark II runs during 1990.

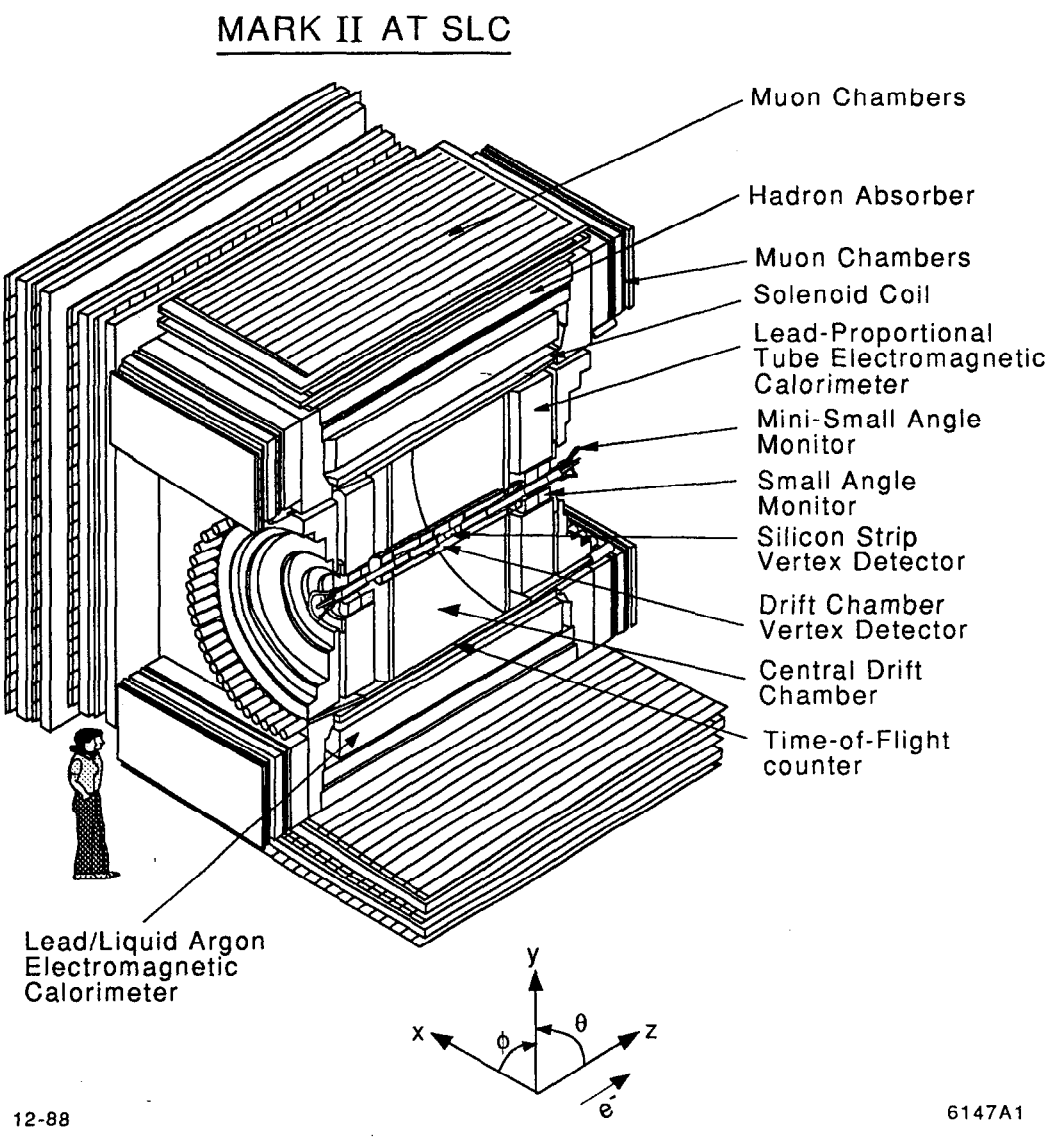

Figure 2–3 A cut-away view of the Mark II detector systems in place for the 1990 runs at the SLC with the definition of the Mark II coordinate system.

2.2.1 Detector Overview

As shown in Figure 2–3, the Mark II has a series of detecting layers which surround a central beam pipe that brings the e^- and e^+ beams into the IP located at the center of the detector. From the IP, particles whose trajectories are not at small angles with respect to the beam pipe will go through the beam pipe, then into the detector systems. These are introduced roughly in the order a particle would pass through them. As the tracking detectors are the primary tool in this analysis, they are discussed in more detail, along with the event trigger, data acquisition and

energy measurement, in the following sections. Reference [51] contains an extensive description of the upgraded Mark II detector.

Beam Pipe

The beam pipe used by the Mark II during 1990 is an aluminum vacuum chamber with a copper coating on the inner surface. In order to get detectors as close as possible to the IP, the radius is only 25 mm.

Silicon Strip Vertex Detector

The Silicon Strip Vertex Detector (SSVD) is a three layer silicon strip detector located just outside of the beam pipe. The radii of the three detector layers are 29, 33 and 37 mm from the beam axis. The primary function of the SSVD is to provide a very accurate track measurement close to the IP in order to accurately measure the track impact parameter.

Drift Chamber Vertex Detector

The Drift Chamber Vertex Detector (DCVD) is a 38 layer drift chamber divided axially into 10 jet cells. The strengths of the DCVD are providing very accurate track position measurements, particularly for locating the correct hits for a given track in the SSVD and for rejecting spurious tracks detected by the outer detector.

Central Drift Chamber

The Central Drift Chamber (CDC) is a large 72 layer drift chamber, extending out to a radius of 1.52 m and having an active length of 2.3m. The initial track finding is done in the CDC, where closely spaced tracks have the greatest separation. Furthermore, its lever arm provides a very accurate angle measurement necessary for good impact parameter determination with high momentum tracks. By measuring the charge deposited on each of the layers in the CDC, it also provides a measurement of the energy loss by a given particle (dE/dx), which when combined with a momentum measurement can aid the identification of electrons.

Time-of-Flight System

The time-of-flight system (TOF) is used primarily for particle identification and detection of cosmic rays. It consists of 48 blocks of 4.5 cm thick plastic scintillator that extend axially for 3.0 m along the outside edge of the CDC. A phototube is placed at each end. The system's measured average time resolution is 220 psec. Combined with the dE/dx information from the CDC, a 2σ separation is possible between π and K up to a momentum of 10 GeV/c and between K and p up to 2 GeV/c.

Solenoidal Magnet Coil

The Mark II solenoid is a conventional coil which provides the nominal magnetic field of 4.75 kG. The thickness is 1.3 radiation lengths and the field uniformity is held to 3% in the tracking volume. The field has been mapped as a function of z and r with an error of <0.1% for use in the tracking fitting programs. The absolute scale of the field during data runs is measured with a pair of Hall probes positioned on the ends of the CDC which provide field-normalization to <0.1%.

Liquid Argon Electromagnetic Calorimeter

The primary calorimeter of the Mark II detector is a lead-liquid argon sampling calorimeter. It is comprised of eight modules arranged in an octagonal barrel outside of the solenoid magnet. Except for small gaps between the modules, it covers the polar angle range from 47 to 133 degrees, which corresponds to 64% of the total solid angle. Each module has a stack of 18 lead strips each of 2 mm thickness which are oriented in different directions to aid in assigning energy to a particular track. The total amount of material in the calorimeter is 14.1 radiation lengths for normal incidence. These strips are separated by 3 mm gap filled with liquid argon in which the ionized argon atoms drift in a 12 kV/cm electric field to the readout strips. The energy resolution has been measured at PEP to be $\sigma_E/E = [(3.3\%)^2 + (13.3\%)^2/E]^{1/2}$, where E is in GeV.

Endcap Calorimeter

The endcap calorimeter increases the solid angle coverage of the Mark II electromagnetic calorimetry by covering the region from 15 to 45 degrees from the beam axis. This system consists of a lead/proportional tube stack of 36 layers, for a total of 18 radiation lengths. In conjunction with the liquid argon calorimeter, 86% of the solid angle is covered with full electromagnetic calorimetry. During the Mark II upgrade run at PEP in 1985, the end-cap energy resolution was measured to be $\sim 22\%/\sqrt{E}$, where E is measured in GeV.

Muon Detector System

The Muon Detector System is comprised of four alternating layers of steel hadron absorbers and planes of proportional tubes. Some of these absorbers also serve as the flux return for the magnet. The solid angle coverage is 45% at the outermost layer. There are about 1.2 nuclear interaction lengths inside of the muon system and about 6 more in the muon system. The efficiency of the muon system is greater than 85% for muons in the fiducial volume of the detector with a momentum greater than ~1.8 GeV/c. The Muon Upgrade Detectors, which are located along the

faces of the detector above and below the beam pipe, add about 15% more solid angle coverage. There are 1.8 nuclear interaction lengths of lead before the first layer of proportional tubes and 1.2 nuclear interaction lengths of steel between that and the second layer of proportional tubes.

Luminosity Monitors

The Small-Angle Monitor (SAM) and Mini-Small-Angle Monitor (Mini-SAM) are designed primarily to precisely measure the integrated luminosity by counting small-angle Bhabha events. The SAM and Mini-SAM cover angular ranges of 50 to 160 mrad and 15 to 25 mrad, respectively. The SAM consists of nine layers of drift tubes for tracking and six layers of a lead/proportional tube sandwich which form a sampling calorimeter. The Mini-SAM is composed of six layers of plastic scintillator interspersed between a total of 15 radiation lengths of tungsten slabs.

2.2.2 The Central Drift Chamber

In upgrading the Mark II detector for operations at the SLC, a new drift chamber was constructed to replace the drift chamber used at SPEAR and at PEP prior to 1986. The new Central Drift Chamber (CDC)[51][52] was designed to provide large solid angle coverage, high momentum resolution in the solenoidal magnetic field, and good pattern recognition and track finding required in the narrow, high multiplicity jets at E_{cm} = 91 GeV.

There are a number of very good papers on the principles of drift chambers. For a general introduction to the concepts of drift chambers see any of those suggested in Reference [53]. A more detailed and especially informative article is the 1977 paper by F. Sauli.[54]

2.2.2.1 Design

The CDC is designed in a modified jet cell configuration in which there are 12 concentric layers of jet cells (superlayers), with each jet cell containing 6 sense wires (see Figure 2–4). Within a cell, the sense wires are spaced at 8.33 mm intervals and are staggered by ±380 μm from the centerline of the cell in order to aid pattern recognition by being able to determine locally through which side of the cell a particular track passed. Potential wires are placed between the sense wires so that the gain and drift field can be independently controlled. There are two guard wires on each end of the row of sense wires to provide a more uniform drift field in the center of the cell. The width of the cell at its center is 3.3 cm which was constrained by the desire to minimize the effect of diffusion and thus achieve the best double-track separation.

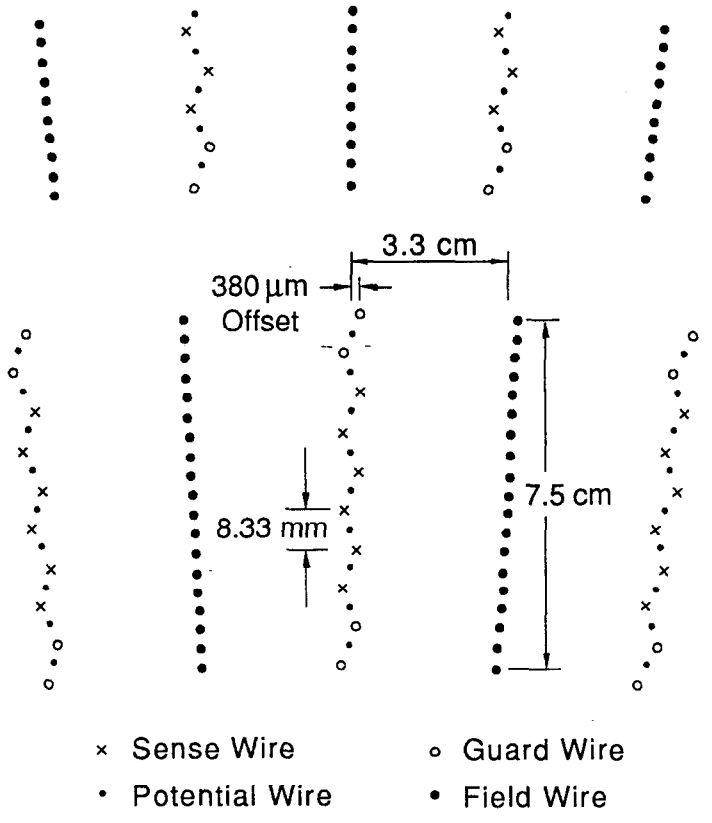

Figure 2–4 Wire pattern for a cell in the Central Drift Chamber.

The 12 superlayers consist of alternating layers of axial and stereo wires. The stereo layers are at ±3.8° angles with respect to the axis of the detector. Each superlayer has 10 more cells than the superlayer inside of it, ranging from 26 to 136 cells. As shown in Figure 2–5, this results in the cells being staggered with respect to each other, ensuring that a track will never pass through the entire detector into regions where the resolution could be degraded (for instance near the wire planes). The minimum distance between superlayers is 2.5 cm, including the effect of the stereo layers being at a smaller radius in the center of the chamber. The active length of the chamber is 2.30 m and it extends radially from 0.192 m to 1.519 m.

The mechanical design of the CDC consists of two aluminum endplates held apart by a 2 mm thick beryllium inner core and a 12.5 mm thick outer shell. Each row of wires within a cell are positioned with Delrin feedthroughs which are located on the endplate by pinning to three precisely machined holes. The accuracy of the wire positioning is expected to be ±35 μm. The contributions to this value are the

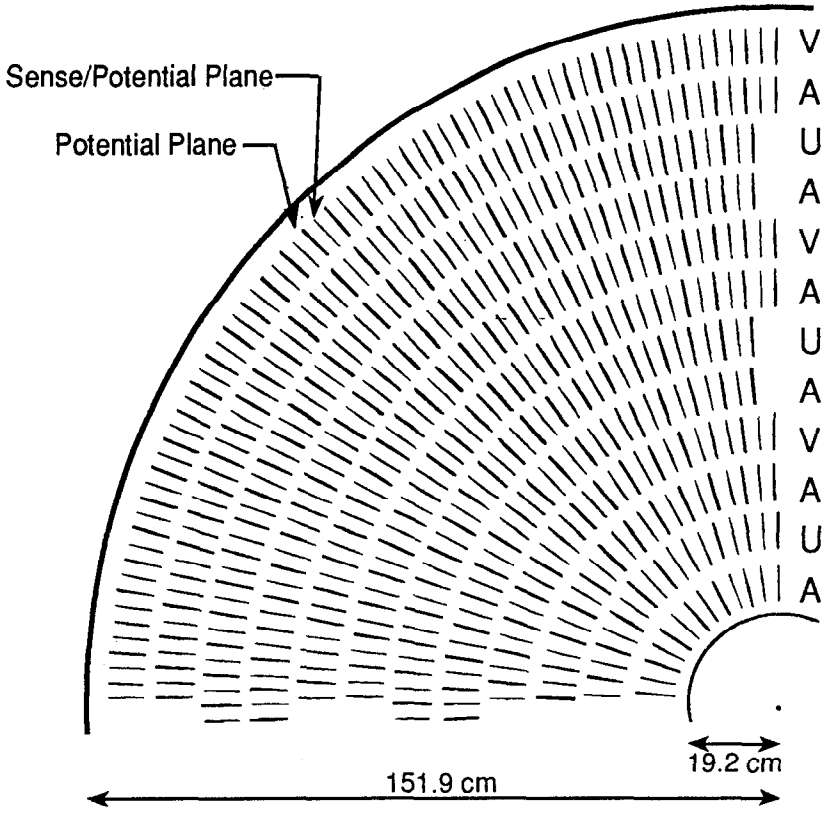

Figure 2–5 The layout of cells in the CDC. The letters indicate axial layers (A) and stereo layers at ±3.8° (U and V). Each layer has 10 more cells than the layer inside of it. Figure 2–4 shows the detailed wire pattern of each cell.

machining and placement of the endplates (25 μm), feedthrough machining and placement (15 μm), and wire sag and electrostatic deflection (10 μm).

2.2.2.2 Electronics

A schematic diagram of the CDC electronics is shown in Figure 2–6. The first stage is the preamplifiers, which are based on a Plessey SL560C chip, and is mounted on the endplates of the detector. The preamplifier gain is 25. The postamplifiers provide an additional gain of 100, pulse shaping, and two output signals: a discriminated timing signal and a pulse-shape signal.[55] The drift times are digitized by LeCroy 1879 Time-to-Distance Converters (TDC's), which are located in FASTBUS crates. They have achieved time resolutions of less than 1 ns. This timing signal is also used in the trigger, which is described later. The analog pulse height signals are digitalized using 100-MHz, 6-bit Flash Analog-to-Digital Converters (FADC's) based on the TRW 1029J7C chip and which are housed on SLAC-built FASTBUS boards.[57] The readout from the TDC's and the FADC's to

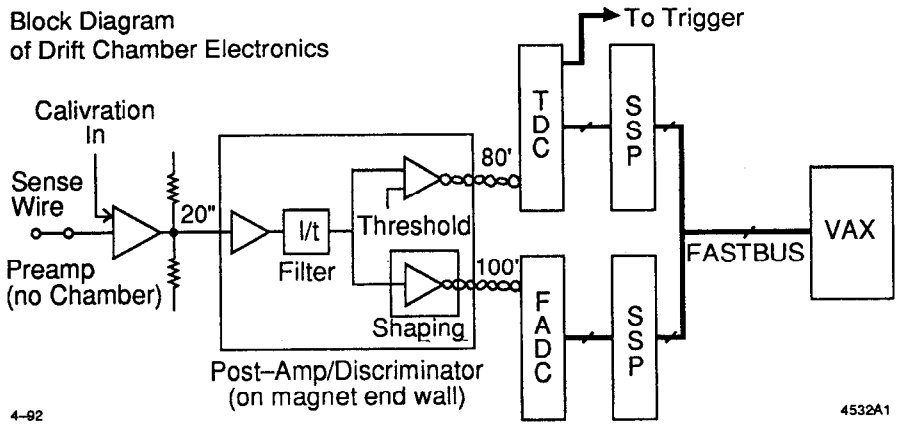

Figure 2–6 Schematic diagram of the CDC electronics.

the VAX 8600 host computer is controlled by programmable FASTBUS modules, the SLAC Scanner Processors (SSP's).[55]

2.2.2.3 Operation

The high voltage system provides graded voltages to the field wires through a resistor-divider chain, in which the center wire typically has about –4.5 kV, the potential wires are at -1.5 kV, the guard wires at -0.2 kV and the sense wires at ground. The copper skins which line inner and outer cylinders are typically at –2.5kV.

The chamber gas is composed of 89% Argon (Ar), 10% carbon-dioxide (CO_2) and 1% methane (CH_4), a mixture which is often referred to as "HRS gas". The pressure is just slightly higher than atmospheric pressure, which results in a gain of 2×10^4. The drift field with the above voltages is 900 V/cm. This corresponds to a drift velocity which is saturated at about 52 μm/ns.*

2.2.2.4 Track Finding

The first step of the track finding algorithm[59] is to group the individual position measurements, or hits, within each cell into track segments which are required to have at least three of the six possible hits. These segments are then combined into tracks first by using only the axial track segments and then adding the stereo information later. Pairs of the axial segments are then combined using a $\chi 2$ test requiring that they be consistent with belonging to a single track, with an arbitration algorithm to assign clusters to closely spaced tracks in a manner to

* This gas mixture has a saturated drift velocity at rather low fields beyond E/p of about 300 V/cm/atm (see Reference [56]).

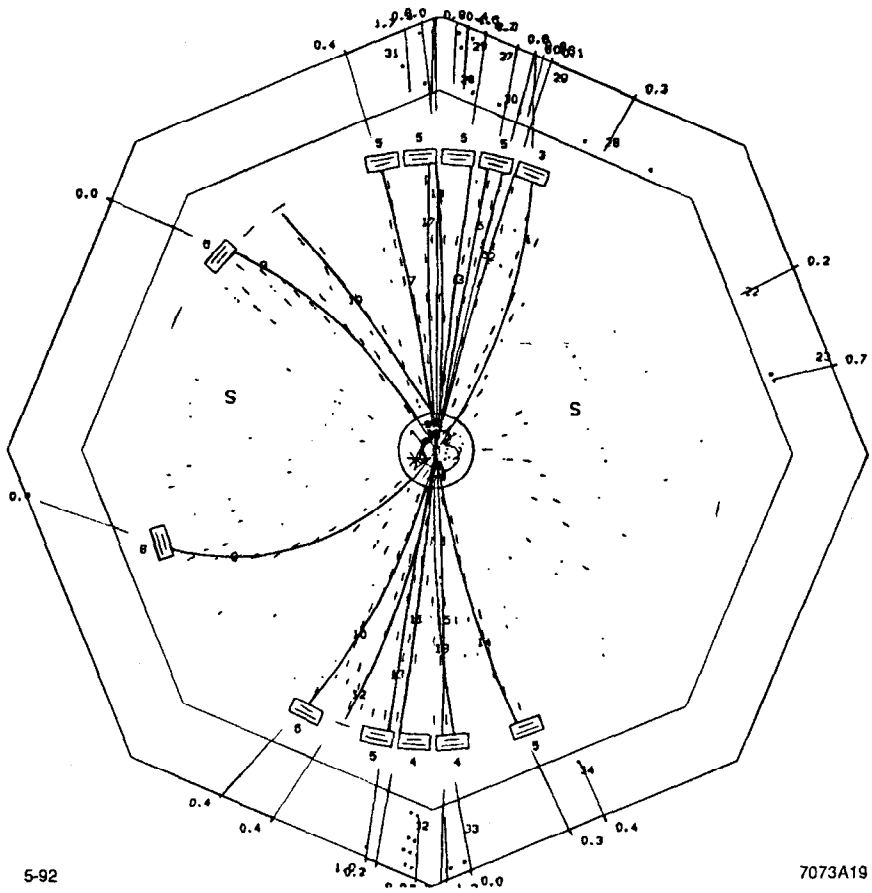

Figure 2–7 A typical event as recorded by the CDC. Also shown are the time-of-flight hits and the tracks detected in the liquid argon calorimeter.

minimize the overall χ^2. To add the stereo information, if a track has two or more stereo segments which can be unambiguously associated with that track, a χ^2 test is used to join the rest of the stereo segments. The remainder of the stereo segments are assigned to a track by using a smaller error for the stereo segments. Segments which are assigned to more than one track are arbitrated to only one of the tracks. Finally, the hits belonging to these tracks are then passed to a track fitting routine. Figure 2–7 shows a typical hadronic event with the fitted tracks.

The track fitting routine SARCS6[60] is based on a least-squares fit which determines the track trajectories in terms of five track parameters:

1. the tangent of the dip angle of the track from the beam axis, $s = \tan\lambda$, where $\lambda = \frac{\pi}{2} - \theta$,
2. the curvature of the track, $\kappa = 1/p\cos\lambda = 1/p_{xy}$ (where p is the track momentum),

3. the angle of the track projection in the xy plane at the track's point of closest approach to the origin, φ_0,
4. the radial distance to the point of closest approach of the track to the origin, δ_{xy}, and
5. the distance parallel to the z-axis to the point of closest approach of the track to the origin, δ_z.

The track fit also calculates the 5×5 error matrix relating these five track variables, accounting for a number of factors such as non-uniformity of the magnetic field, energy loss and multiple scattering. The multiple scattering inside the chamber is taken into account using the approximate formulas calculated by R. Gluckstern.[61] The use of these formulas to handle multiple scattering saves a vast amount of processing time by reducing the size of the matrix to be inverted in the track fit. Ordinarily, including multiple scattering in the track fit would mean having to invert a 72×72 matrix, but with these approximate formulas the problem is reduced to a 5×5 matrix inversion.

2.2.2.5 Position Resolution and Efficiencies

The drift times for hits in the CDC are determined by the information from the TDC. Using the FADC information, a time-slewing correction can be added which compensates for variation in the timing signal as a function of the signal pulse height. A particularly useful quantity to study which uses all of the information in a cell is the difference of triplet residuals for the inner and outer three sense wires:

$$[(t_1+t_3-2t_2)-(t_4+t_6-2t_5)]/8,$$

where t_i is the drift time for one of the six sense wires in a drift cell. Due to the staggering of the sense wires, the resulting distribution has a double peak structure which contains information about the position resolution, the wire stagger and can be used to monitor the changes in the drift velocity (see Figure 2–8).

The position resolution can also be measured by comparing the individual hits with respect to the fit of the track to which they are assigned. This method includes various systematic effects which are not studied by the local residuals such as the relative positions of superlayers. Figure 2–9 shows the track resolution as a function of drift distance. With the time-slewing correction, the average position resolution is about 170 μm.

The FADC's are of particular assistance to the tracking performance for their ability to resolve closely spaced hits. Various scanning algorithms that utilize the pulse shape information have an 80% efficiency for separating hits which are

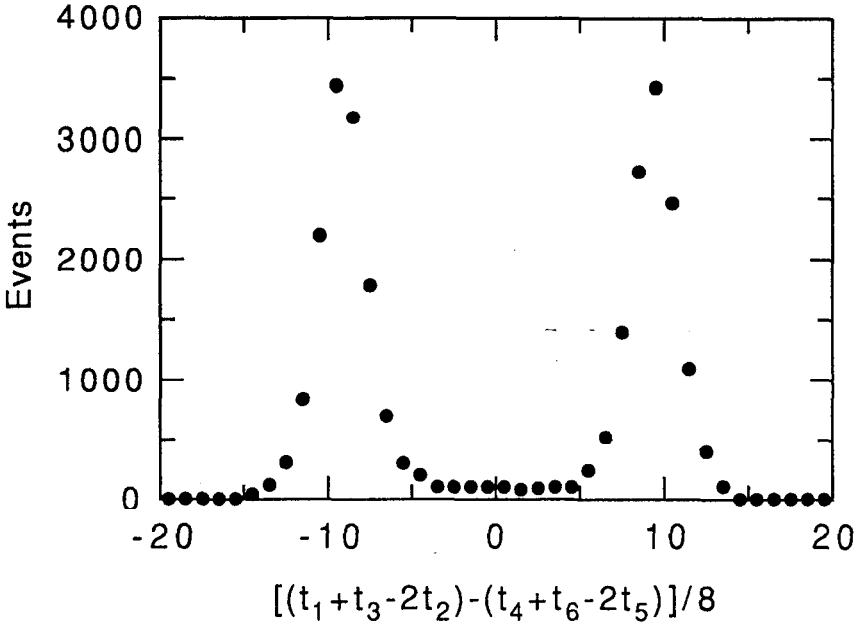

Figure 2-8 Double peaked distribution of drift times for the staggered wire in a CDC cell.[52]

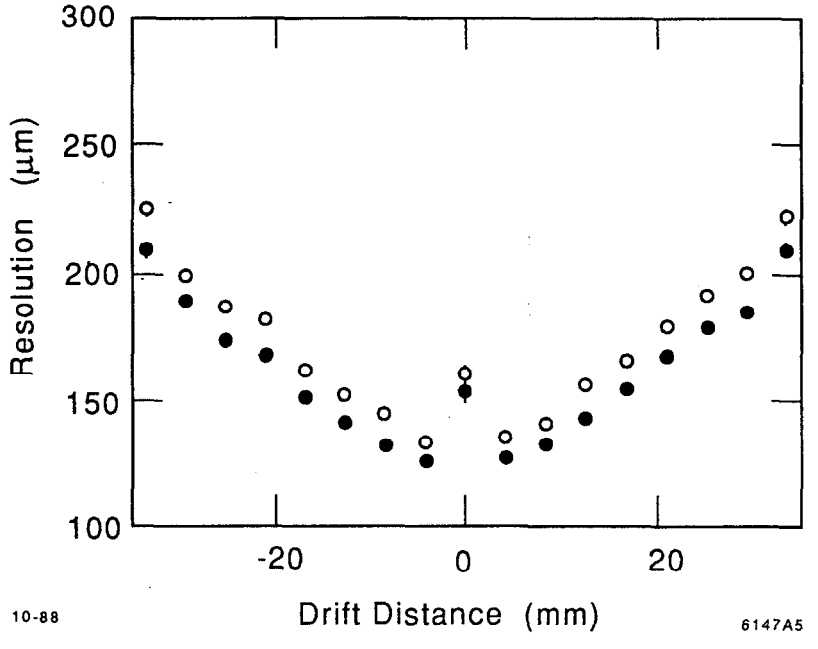

Figure 2-9 The CDC position resolution as a function of drift distance. The closed (open) circles are with (without) the FADC time-slewing correction.[51]

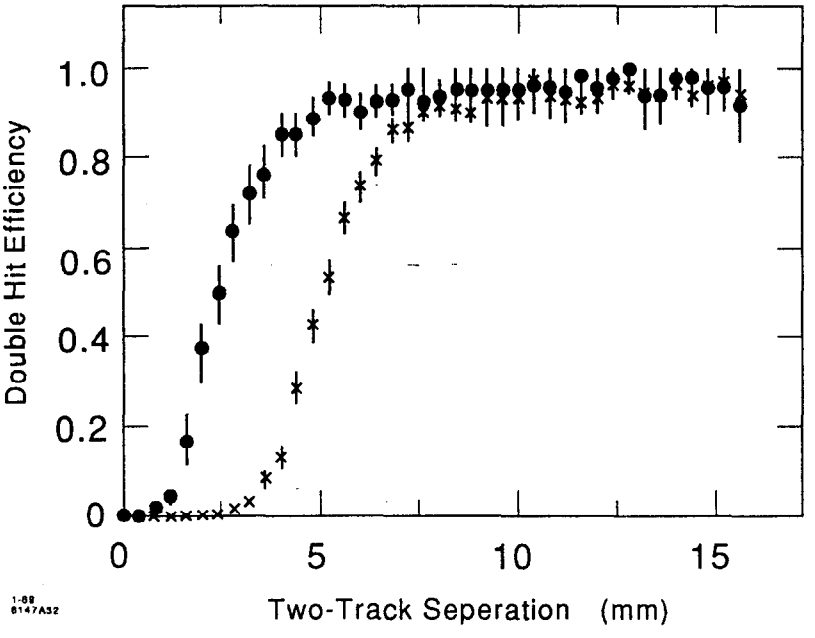

Figure 2–10 The double hit efficiency is plotted as a function of the separation of the two tracks using the TDC (×'s) and the FADC pulse height information (closed circles).[51]

3.8 mm apart, whereas with the TDC's alone, this is 6.4 mm. Figure 2–10 shows the double-hit efficiency as a function of the hit separation with and without the FADC information.

The CDC hit finding efficiencies have been studied and tuned in the Monte Carlo to reflect that which is observed in the data. In order to allow for efficiency correlations of the wires within a particular layer, the efficiencies are parameterized as single layer and superlayer efficiencies, which are shown in Figure 2–11 and Figure 2–12. The particularly lower efficiency in superlayer 12 is primarily due to high voltage problems in that layer which necessitated running at lower voltages at various times. The overall track finding efficiency has been measured in low multiplicity events at PEP to be approximately 99%. It is estimated that the track finding efficiency is greater than 95% for high multiplicity events at SLC energies. Figure 2–13 shows the distributions of the measured track finding efficiency for Bhabha events at PEP and Monte Carlo estimates of the efficiency in hadronic events at the SLC.[62] Below a $|\cos\theta|$ of 0.8 the efficiency is essentially flat with values which are essentially unity. The loss of efficiency at large values of $|\cos\theta|$ is well understood, as illustrated in Figure 2–14. The behavior and small p_{xy} is also well modelled by the Monte Carlo (see Figure 2–15). Nonetheless, to avoid these

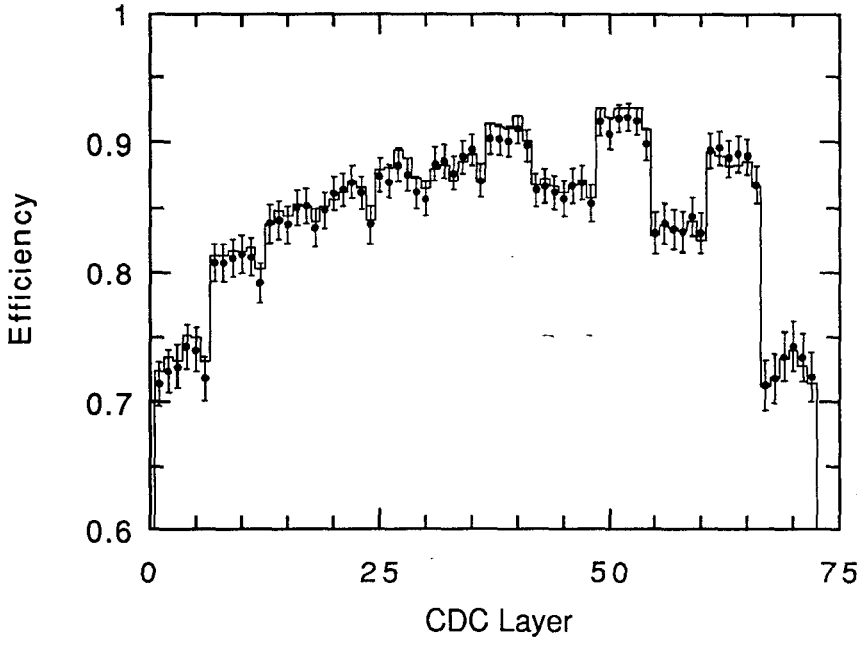

Figure 2–11 The single layer hit efficiencies in the CDC as measured in the 1990 hadronic data sample. The line is the Monte Carlo as tuned to the data.

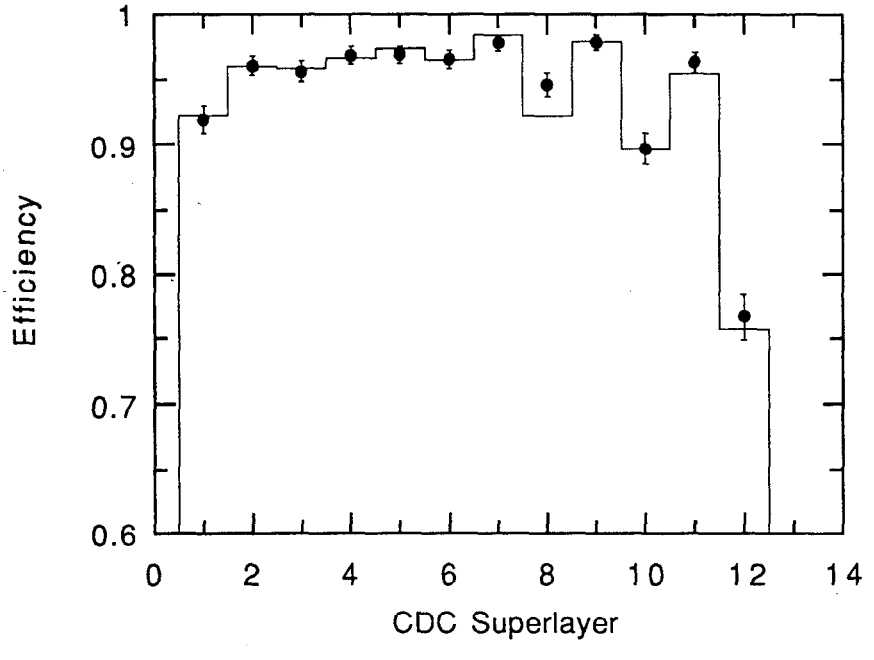

Figure 2–12 The superlayer efficiencies in the CDC as measured in the 1990 hadronic data sample. The line is the Monte Carlo which was tuned to the data.

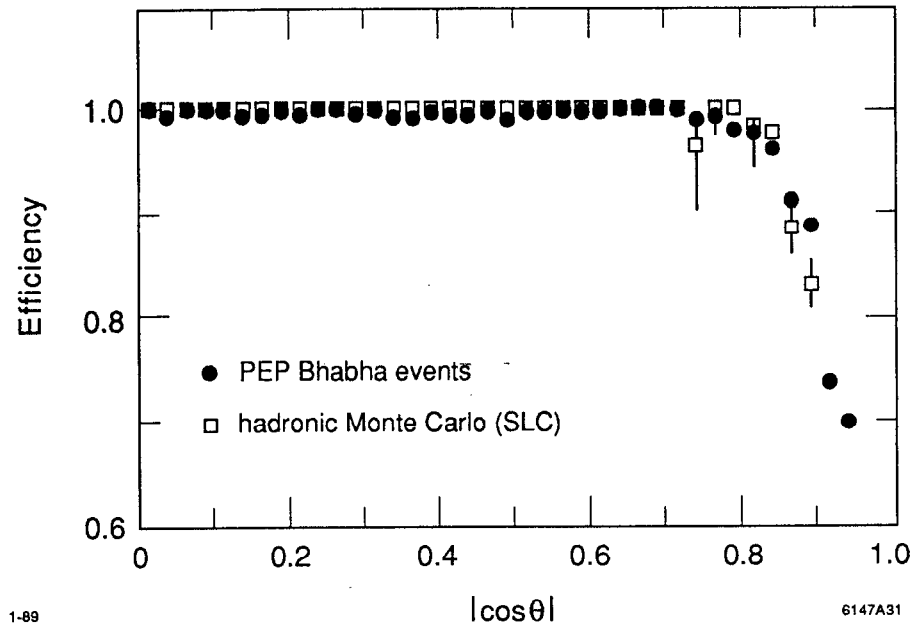

Figure 2–13 CDC track finding efficiency as a function of cos θ, as measured by Bhabha events detected with the Mark II Upgrade detector at PEP and as estimated using a hadronic Monte Carlo at SLC energies.

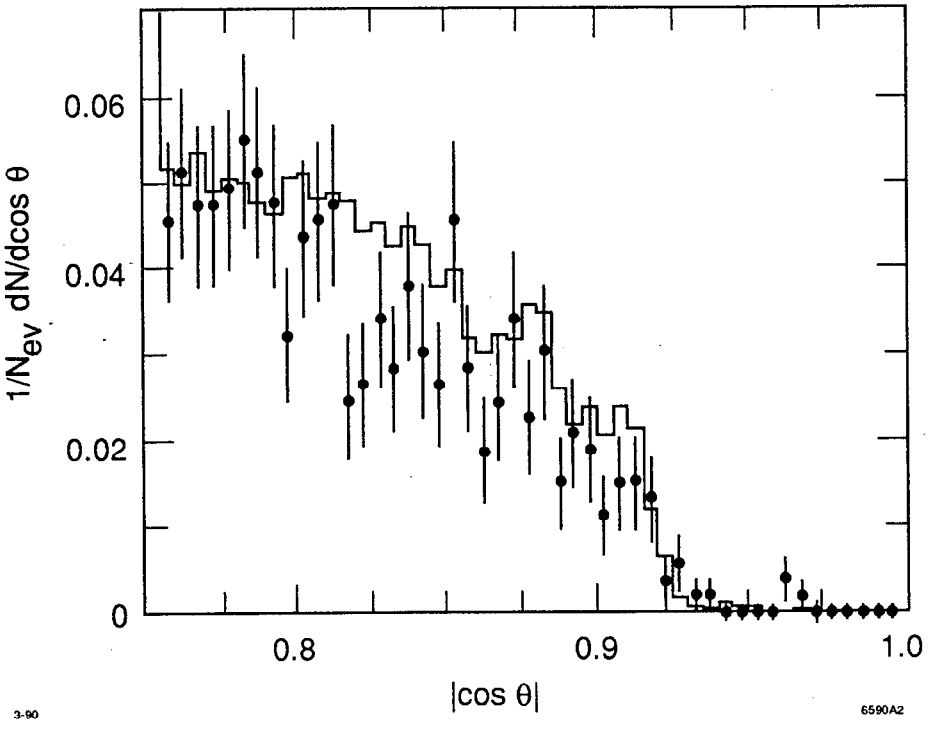

Figure 2–14 The distribution of tracks in the 1989 data set at large polar angles in the CDC.[62] The data is represented by points and the Monte Carlo by the line. The Monte Carlo is normalized to the number of events in the data.

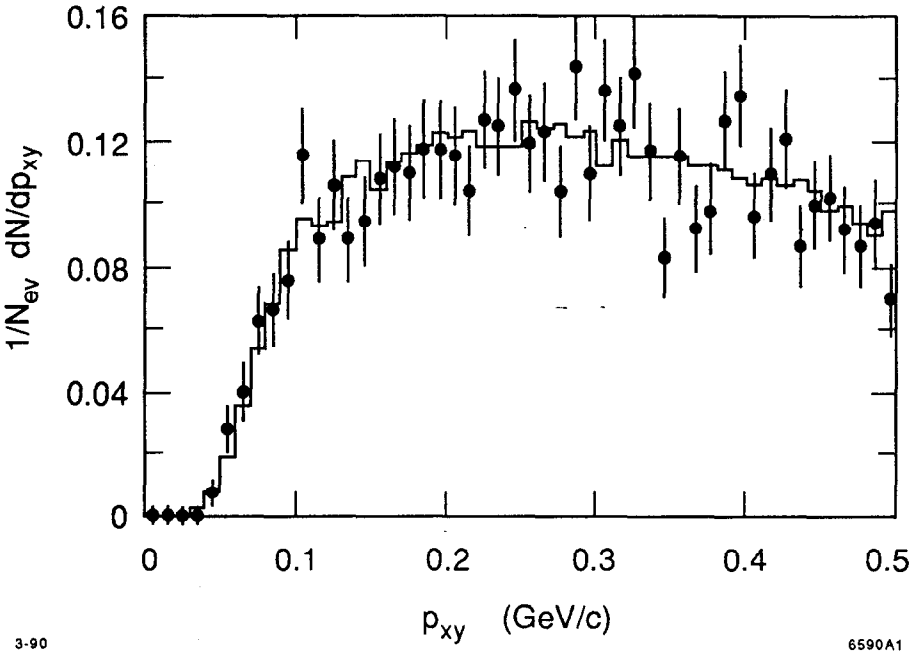

Figure 2–15 The distribution of tracks in the 1989 data set at small transverse momenta in the CDC.[62] The data is represented by points and the Monte Carlo by the line. The Monte Carlo is normalized to the number of events in the data.

regions of lower efficiency in the subsequent analyses, tracks are required to have $|\cos\theta| < 0.8$ and $p_{xy} < 0.15$ GeV/c. A data and Monte Carlo comparison of the distributions of the number hits per track is shown in Figure 2–16.

The large number of position measurements over a radial distance of about 1.3 m in the CDC provides an accurate measurement of the sagitta of a track in the axial magnetic field, and hence determination of the component of the momentum perpendicular to the beam axis. The momentum resolution was measured at PEP, and verified with muon events at the SLC, to be[63]

$$\frac{\sigma(p_{xy})}{p_{xy}} = \sqrt{(0.0046 p_{xy})^2 + (0.019)^2}\ , (p_{xy} \text{ in GeV/c})$$

where the first term is the intrinsic resolution and the second term is due to multiple scattering effects.

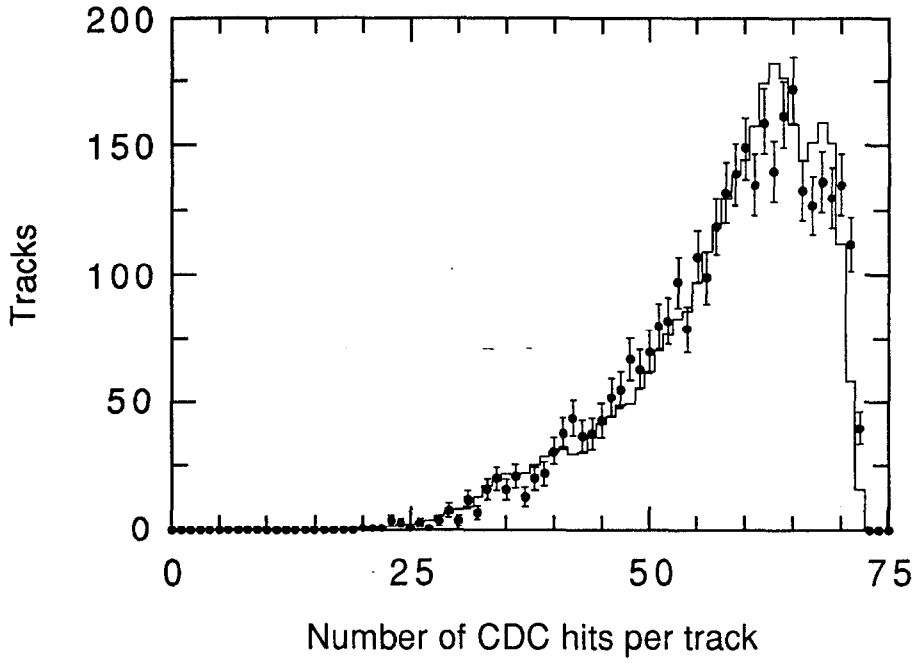

Figure 2–16 The distribution of the number of CDC hits per track for the data (points) and Monte Carlo (line). These tracks are required to have $|\cos\theta| < 0.8$ and $p_{xy} > 0.15$ GeV/c (refer to Figure 2–14 and Figure 2–15).

2.2.3 The Drift Chamber Vertex Detector

The Drift Chamber Vertex Detector (DCVD) is a high precision drift chamber designed to provide the high precision tracking necessary for the study of heavy quark decays at SLC energies. Of particular concern was that the detector be able to measure track trajectories with high resolution even in dense jets. In order to achieve the best possible resolution, it was necessary to control a wide spectrum of systematic effects, including the precision of the mechanical design and the physical environment inside the chamber such as the drift field, gas pressure and temperature. The development and initial studies of the DCVD are described in a number of references.[64][65][66]

2.2.3.1 Design

The layout of the DCVD is based on a jet cell geometry as illustrated in Figure 2–17. The active volume of the detector extends radially from 5.3 to 16.5 cm and has a total length of 48 cm. There are 10 jets cells in azimuth, each tilted at about 15° with respect to the radial direction from the chamber center, namely the beam axis. This feature resolves the ambiguity regarding which side of the cell a track passed, because the wrong tracks will be projected several centimeters away

from the beam axis. It is also useful to determine drift velocity by studying tracks which cross between cells and ensures that tracks from the interaction point are never entirely in a region near a wire plane where the chamber performance is degraded.

The cells contain 40 sense wires, spaced at 2.9 mm intervals, of which the central 38 are instrumented. The sense wires alternate with potential wires and there are grid planes at 1.8 mm from the sense plane on either side. Opposite the sense plane is the 59 wire cathode plane which is located between 1.44 and 5.08 cm from the sense plane at the innermost and outermost sense wires. A summary of the wire properties is given in Table 2–1.

To control the field quality near the inner and outer edges of the chamber, edge field wires with varying potential are used. All of the wires are parallel to the beam axis. Additionally, there are three types of field shaping electrodes used to grade the

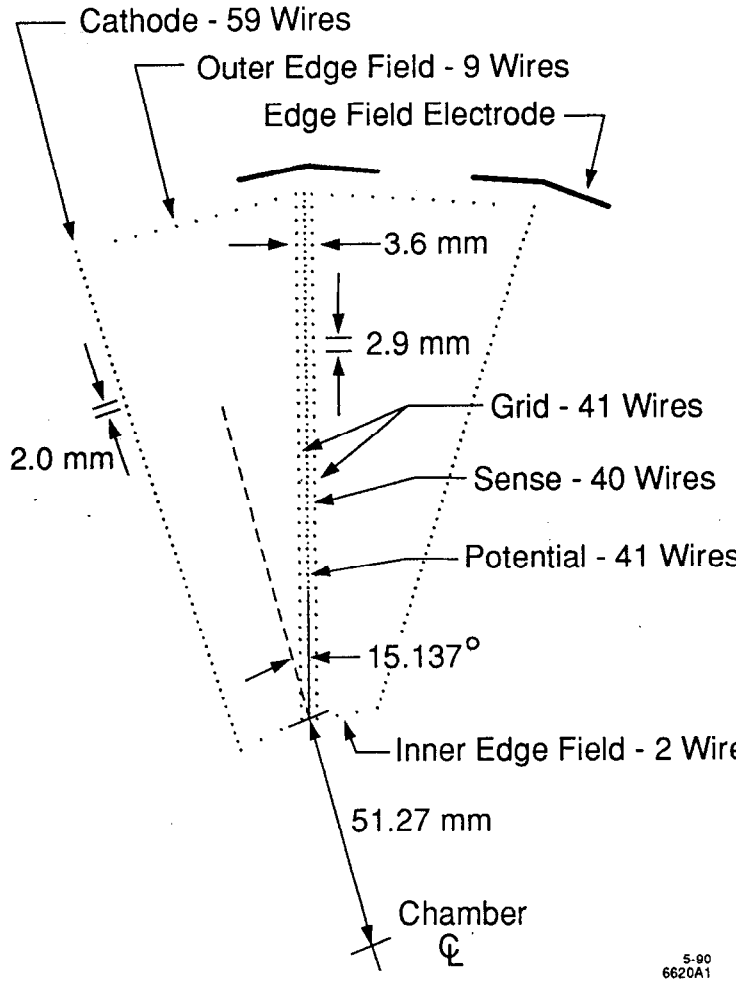

Figure 2–17 The DCVD jet cell design.

Wire Type	Number per plane	Diameter	Material
Sense	40	20 μm	tungsten
Potential	41	150 μm	Cu/Be
Grid	41	150 μm	Cu/Be
Cathode	59	225 μm	Cu/Be
Inner Edge Field	2	150 μm	Cu/Be
Outer Edge Field	9	150 μm	Cu/Be

Table 2–1 Wire characteristics for the various types of the wires in the DCVD. All of the wires are coated with a thin layer of gold.

field and improve its quality near the edges of the cell. There are conducting surfaces ("skins") bonded to kapton which is epoxied onto the inner and outer pressure cylinders. There are also twenty 'V' shaped edge field electrodes ("angel wings") between the wires and the outer skin. With the nominal operating voltages given in Table 2–2, this cell design produces drift fields which vary by <1% for all but a few of the wires near the cell edge.

System	Voltage (V)
Sense Wire	+2500
Potential Wire	0
Grid Wire	–480
Cathode Wire	–7900 to –2300
Outer Edge Field Wire	–6300 to –2300
Inner Edge Field Wire	-1500 & –440
Outer Skin	–6500
Inner Skin	–1600
Angel Wings (sense)	–1600
Angel Wings (cathode)	–6800

Table 2–2 Nominal operating voltages for 2 atm gas pressure. The angle wings by the sense and cathode planes are at different voltages.

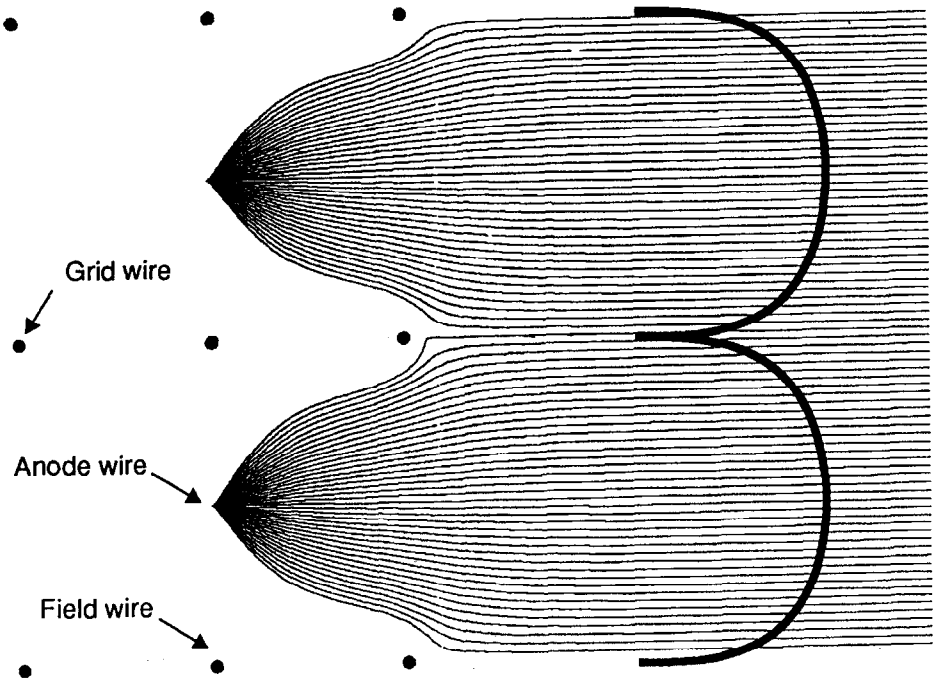

Figure 2–18 Electron drift trajectories in the region near the anode and grid planes. The heavy line is the line of constant drift time (isochrone).

Figure 2–18 shows the electron drift trajectories for a cell which employs a grid plane on either side of the sense plane. The primary advantage of the grid plane is the improved isochrony of the charge as a track traverses the region where charge will drift to the sense wire. It also aids in improving the electrostatic stability of the sense wire and in reducing cross-talk between adjacent channels.

To control the systematics which result from imperfections in the placement of the wires in the chamber, a novel approach was taken to positioning the wires. Instead of each wire position being individually determined by the location of a feedthrough on the end of the chamber, the planes of wires were attached as a unit to foundations made of Macor, a machinable ceramic with very good dielectric characteristics. In this fashion, the positions of the wires within a plane could be measured and their position within the chamber characterized by relatively few parameters. This modular design is illustrated in Figure 2–19. Each cell has two Macor foundations to hold the grid, cathode and edge field wires plus a much smaller stainless steel and Macor foundation to hold the anode wires. In the chamber, each of these are attached to an aluminum endplate held apart by 1.3 mm

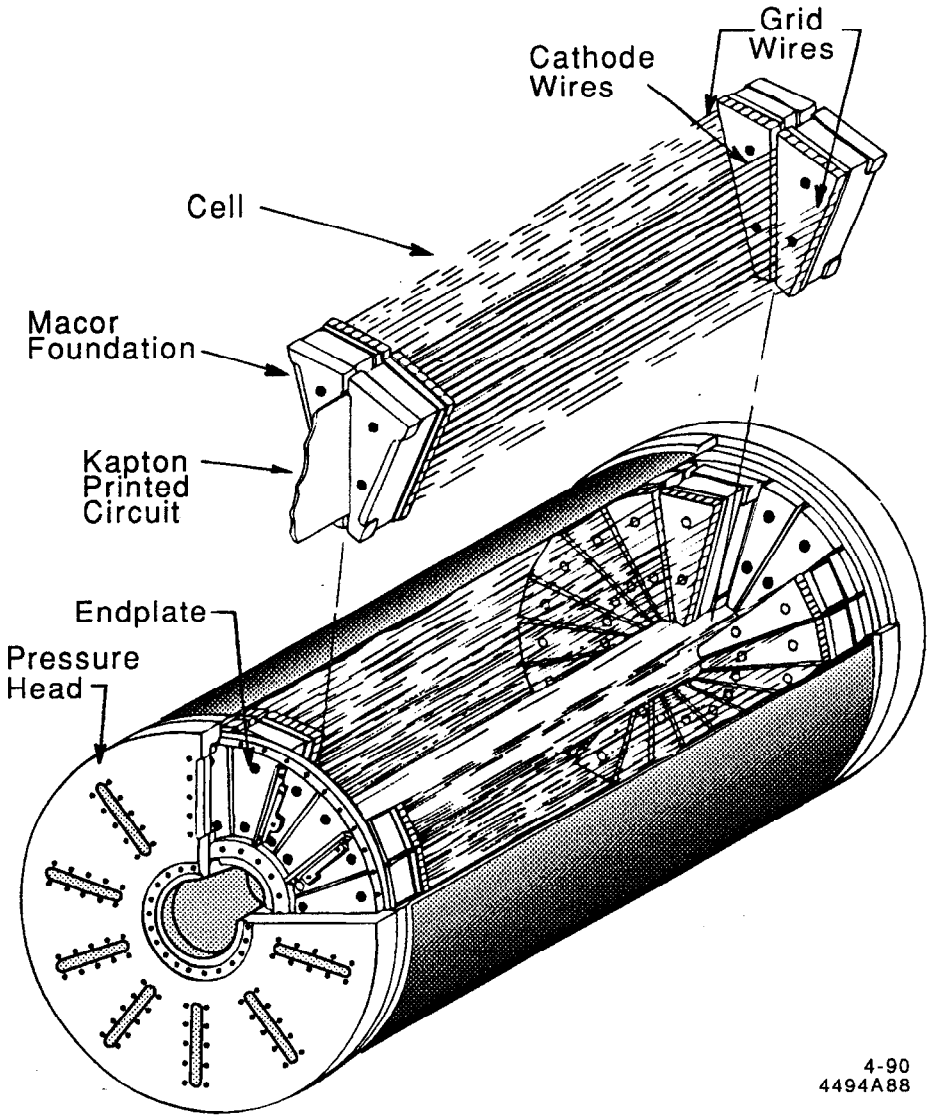

Figure 2–19 Mechanical assembly of the DCVD, illustrating the modular assembly of the cells on the Macor foundations.

thick beryllium inner and a 2.3 mm thick aluminum cylinders, which also serve as the pressure vessels.

The position of each of these foundations with respect to the endplate of the chamber is determined using a positioning system based upon a precision bearing which rests between a pair of two opposing conical sockets located in the foundation and the chamber endplate (see Figure 2–20). The first set of sockets were epoxied into a precision machined, steel template known as the master gage, which served as the definition of the relative positions of the sockets for foundations which would attach to one end of the chamber. To transfer the positioning from one system to the foundations or the chamber endplates, the master gage was bolted onto pieces

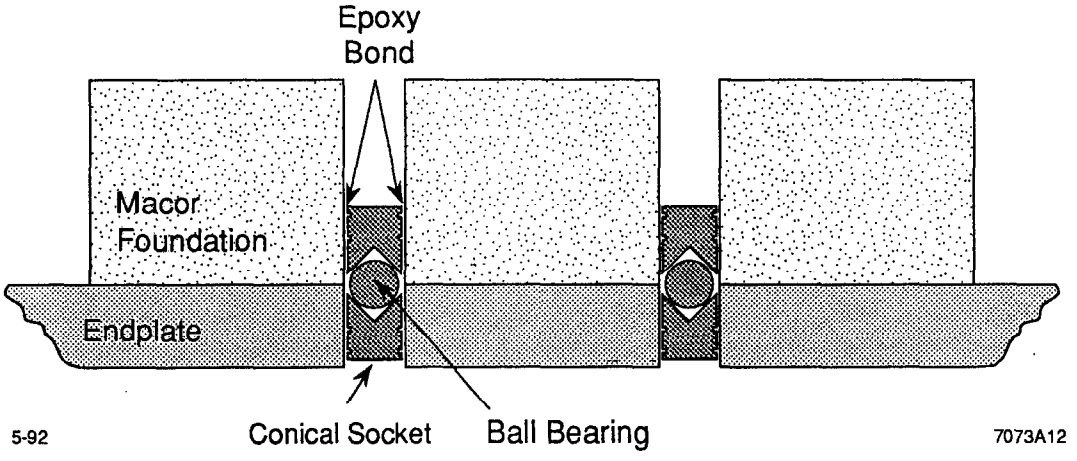

Figure 2–20 Cross sectional view of the ball-and-socket system used to locate the Macor foundations within the chamber.

requiring positioning sockets, and the sockets were glued into this piece — their position determined not by the hole in the piece, but rather by the socket position on the master gage. To affix sockets into the pieces whose sockets were set with the master gage, a second gage, the mirror gage, was used. This is a mirror-image duplicate of the master gage, and had its socket positions set from the master gage. It must be noted that this system of alignment does overconstrain the system and so care must be taken when epoxying the sockets. Nonetheless, it produces mating pairs whose positions are reproducible to ~1 μm.

The wires were positioned onto the Macor foundations using a system of granite blocks to which the socket positions of the master and mirror gages had been transferred. The wire planes were wound to the desired tension onto very precise copper-clad Invar* cylinders and lowered over the foundation and epoxied to that foundation. Note that the wires do not contact the Macor itself, but are bonded to it by a thin layer of epoxy. Thus, the wire position within a plane is largely determined by the accuracy of these Invar cylinders. As part of the wire bonding apparatus, a traveling microscope was built which allowed the wire positions within planes to be accurately surveyed for quality control. The wire position measurements for a plane of sense wires is shown in Figure 2–21 from which it is evident that the wires can be located within a plane to only a few microns.

The electrical connection to the wires are made via a solder connection to flexible kapton printed circuits. Pressure/high voltage feedthroughs have been

* Invar is an iron-nickel alloy with a low thermal expansion coefficient.

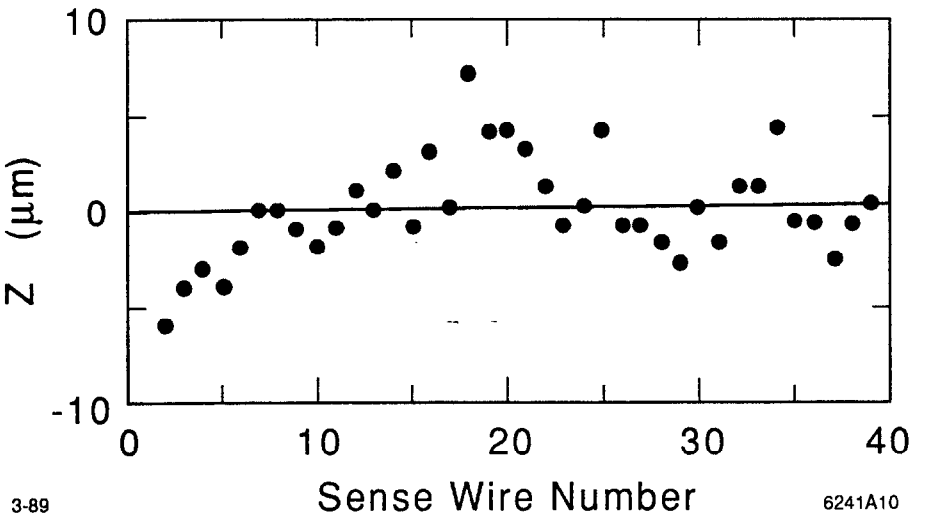

Figure 2–21 Measured deviations for wires within a completed sense wire plane.

expoxied onto these kapton circuits which form the gas seal at the pressure head (see Figure 2–22).

To position the sockets in the endplates of the detector, the master and mirror gages were used to transfer the socket positions to the opposing endplates. The angular position of the socket was determined by an Ultradex Model B precision dividing head, to which the endplate was attached. The master and mirror gages were mounted onto the endplates and a system of precisely cut granite blocks were used to align the endplates with respect to each other on the beryllium central core The endplates were then expoxied to the central core. This method achieved endplates which are parallel to within ±25 μm and have a relative rotation of less than ±40 μrad. The final positioning accuracy of the wires is illustrated in Figure 2–23. This demonstrates that the gaps between the sense and grid planes are the nominal 1.8 mm to within a tolerance of ±25 μm for all but one of the twenty gaps.

2.2.3.2 Gas and Temperature Control Systems

The chamber gas is a mixture of 92% carbon-dioxide (CO_2) and 8% ethane (C_2H_6). The ethane is added to provide quenching by absorbing photons from the electron avalanche at the sense wire before the photons could reach the cathode and extract photo-electrons. The gas is at an absolute pressure of 2 atm and the drift field is E/P = 0.77 kV/cm/atm. With this field, the drift velocity is well in the unsaturated regime in which the drift velocity is linearly proportional to the

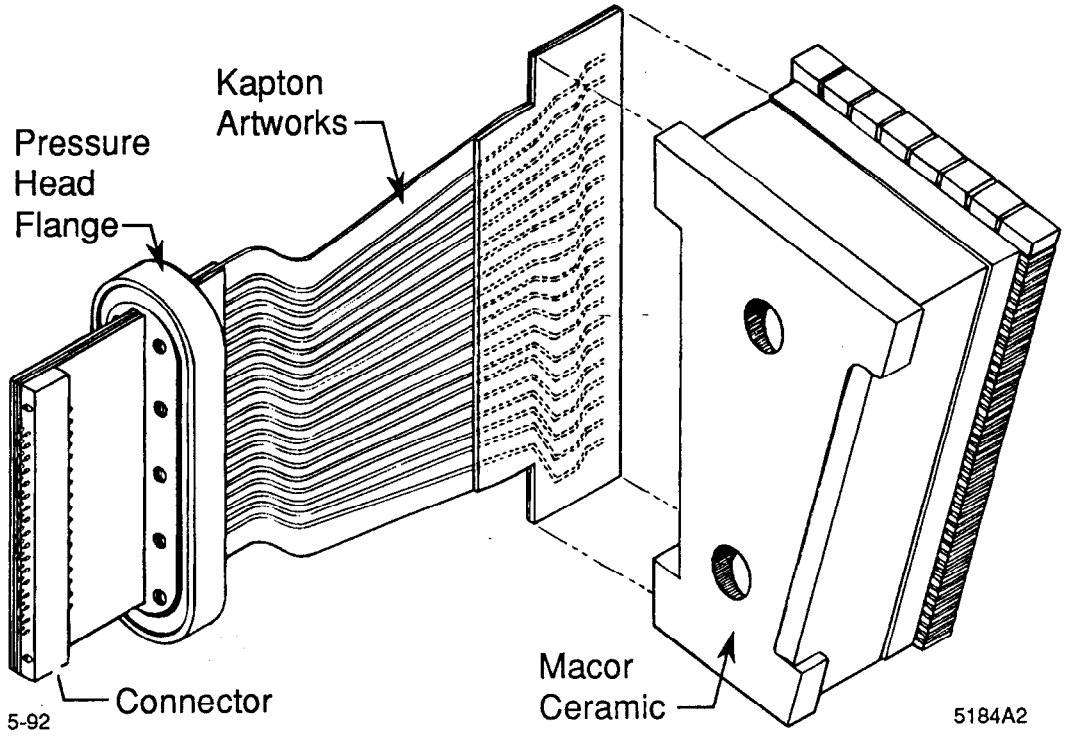

Figure 2-22 A schematic view of the Macor foundation, the kapton printed circuit and the pressure/high voltage feedthrough.

reduced drift field. This makes the drift-time relationship dependent on precise knowledge of any non-uniformities of the drift field. However, these operating conditions are potentially beneficial because this gas mixture is a *cool gas*, meaning that it exhibits electron diffusion which is near its thermal lower limit. Furthermore, cool gases typically have much slower drift velocities, in this case v_d = 5.7 μm/ns. A consequence of operating in this unsaturated regime is that the control of physical conditions inside the chamber such as the pressure, temperature, and composition of the chamber gas and the electric drift field is of particular importance. The drift field control is discussed in the next section. A more complete discussion of the gas studies and these control systems can be found in Appendix B.

The gas system is non-recirculating and uses commercially-made gas mixtures, which are purchased in large quantities in order to assure a constant gas composition. It is important that the amount of electronegative component to the gas in the chamber be as small as possible in order to minimize the charge lost at longer drift distances. This requires that the gas supplied by the vendor be of high

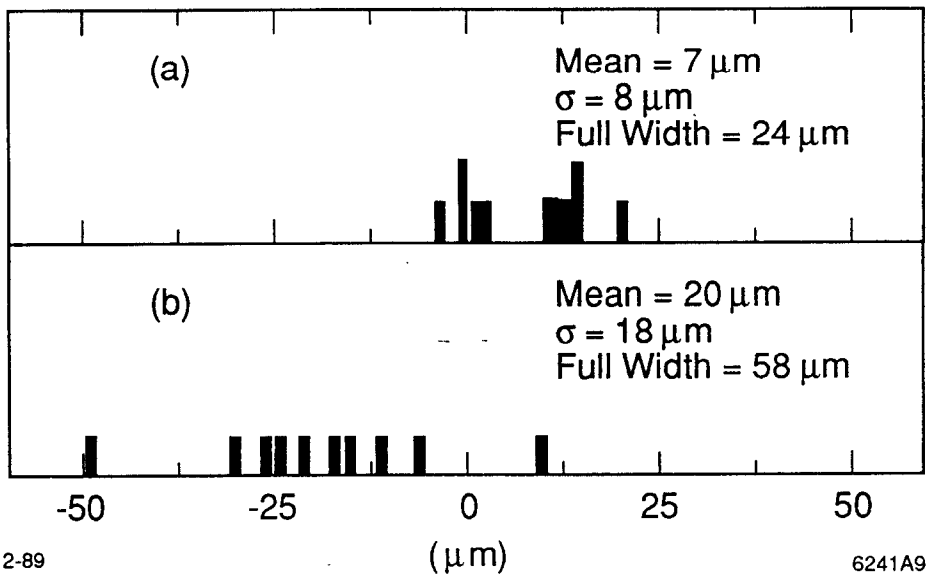

Figure 2–23 Deviation of the sense plane/grid plane gap from the nominal 1.8 mm for grid planes (a) whose Macor foundations do not support cathode planes and (b) for those foundations which also support cathode planes.

purity and that the DCVD gas system not admit atmospheric oxygen. Oxisorb was used to remove all but about 0.2 ppm of O_2 from the gas from the tube trailer, which typically had 1–2 ppm of O_2 when entering the gas system. The gas composition was monitored to a relative accuracy of 0.1 ppm O_2 by a Teledyne Model 316 Oxygen Analyzer and to the level of 0.01% ethane by a Teledyne Model 325 Thermal Conductivity Analyzer. The pressure was measured by a Barocell pressure sensor and controlled to the level of 7×10^{-4} atm by an electronic feedback system, the Datametrics Type 1501 Controller.

The gas temperature was also controlled by an electronic feedback system which maintained an average temperature of 28.15±0.05° C. This system recirculates water through a closed loop system from a 15 liter reservoir to the chamber, where the water is sent through 0.25″ aluminum tubing which has been attached to the pressure heads on either end of the chamber and the outer shell of the DCVD. The beryllium inner core is the only section of the chamber whose temperature is not actively controlled. The temperature of the water in the reservoir is controlled by a HAAKE N 2-R Digital Cryostat. The temperature monitoring system uses an array of 48 thermistors placed on and around the chamber. The temperature measured from these thermistors are sent to the VAX host computer where a feedback program adjusts the temperature setting of the cryostat. As it is not actively

temperature controlled, the inner core exhibited temperature fluctuations of ±0.15° C and the temperature variation between the inner core and outer shell was less than 0.35° C.

2.2.3.3 High Voltage System

Because the chamber is used in an unsaturated regime, the drift velocity depends linearly on the drift field, and thus it is crucial to precisely monitor and control the field voltages supplied to the chamber. To achieve this, great care was taken in both the assembly of the high voltage components such as the resistor-divider chains, and in the choice of voltage monitoring equipment.

A single high voltage supply powers the ten resistor-divider chains from which the cathode wire and edge field wires are supplied. The remainder of the voltages are controlled by separate supplies. These supplies are controlled from a feedback system on the VAX host computer, which sends information via CAMAC to the power supplies. The high voltage for the DCVD is measured to an accuracy of a few parts in 10^4 using a FLUKE Model 8506A digital multimeter which itself has a 5 ppm accuracy, and the resulting measurement sent in digital form to the VAX. This system is illustrated schematically in Figure 2–24.

Excess current in the cathode system is monitored by comparing the voltage differences from near the top and bottom of the resistor-divider chain with a reference chain. The other systems monitor current at the power supply. If excess current is detected, the chamber protection system is activated and within a few milliseconds the high voltage systems in the chamber are connected to 80 MΩ discharge resistors.

The voltages have been monitored during running and show that the extended stability of the cathode high voltage supply is 0.03%. The anode high voltage supplies were stable over the same period to 0.3%.

During the 1990 data run, there were often rather severe backgrounds in the DCVD (see Section 2.2.3.6). The high level of backgrounds led to some high voltage problems within the chamber. During periods of high backgrounds, it was not uncommon for the sense wires in one of the cells to begin drawing excessive current and eventually trip off the protection circuits. The damage was only temporary and could be fixed by leaving the sense wire high voltage at 1000 V for a period of several hours. Although the cause of this was never conclusively determined, one possibility is that charge was building up, perhaps in the gap between Macor foundations, which had an RC time constant of roughly an hour. Studies of the cells adjacent to that with the lowered sense show no detectable degradations in

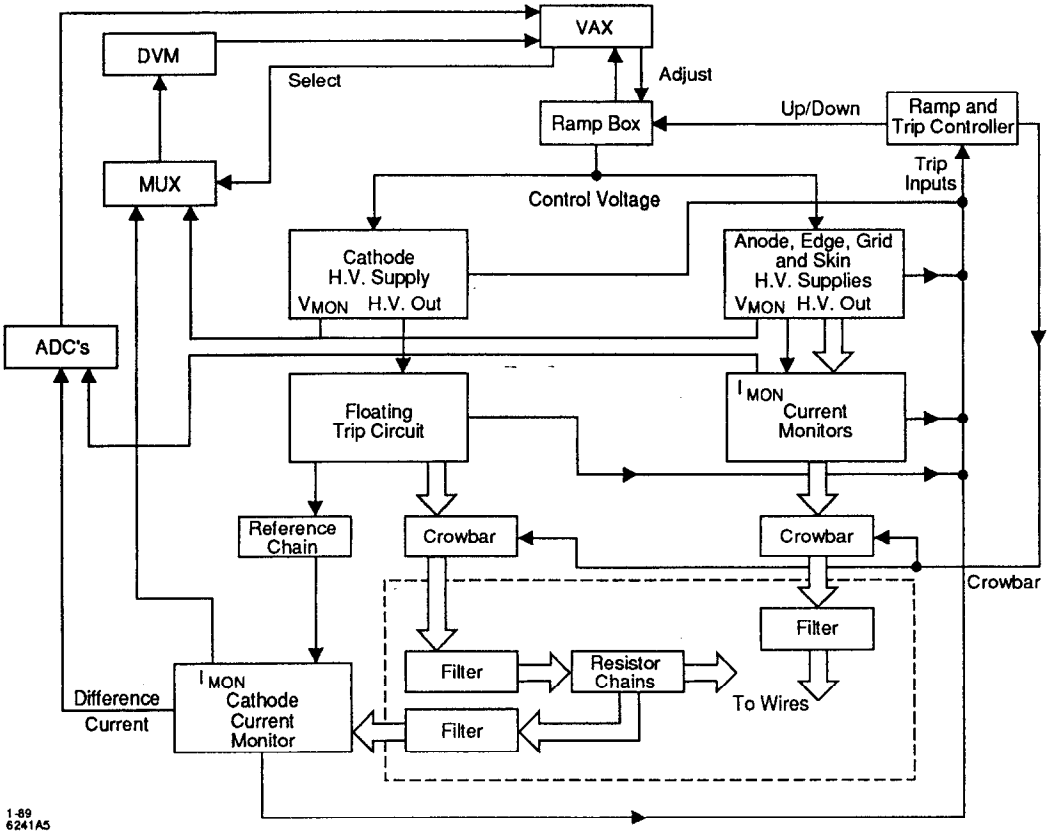

Figure 2–24 A schematic diagram of the DCVD high voltage system.

chamber performance as measured in terms of the single hit and cosmic miss distance resolutions.

2.2.3.4 Electronics

The signals from the sense wires are fed into 38-channel preamplifier cards which are mounted on the ends of the chamber. Each channel contains a fast, charge sensitive hybrid amplifier with a 40 nsec integration time. The preamplifiers are connected to postamplifiers by 30 feet of standard 50 Ω cable. The postamplifiers, located just outside the Mark II magnet iron, contain a pole-zero filter which compensates for the integration of the preamplifier and removes the $1/t$ ion tail. The postamplifiers are connected to 6-bit 100 MHz Flash ADC's with a memory depth of 1024 bins.[67] These 16-channel FADC's reside in two FASTBUS crates in the Mark II data acquisition building. The data is read from the FADC modules into SLAC Scanner Processors[55] (SSP's), one of which is located in each FASTBUS crate. The SSP's provide hit recognition, time and change measurement, zero-suppression and formatting for the raw and processed data. The overall gain

has been set such that the root-mean-square thermal noise is about half of one FADC count.

2.2.3.5 Hit and Track Finding Algorithms

A differential hit finding algorithm[68] is used to locate hits in the FADC data. This algorithm aids in separating closely spaced hits where the second hit is on the tail of the first. In such cases, a fixed threshold algorithm would have less tendency to find the second hit as the pulse height may not yet have dropped below the threshold. The differential algorithm steps through the 1024-bin digitalized pulse train bin by bin, forming the difference between the sum of three adjacent bins and the three following bins. The leading edge is flagged if this difference exceeds a threshold which decreases slightly with drift distance in order to account for the effects of diffusion and attenuation. A trailing edge is flagged when the difference of the sums is negative for two consecutive bins. A further cut is made which requires the integrated pulse height of the hit be larger than a second threshold in order to reduce the number of smaller fake hits from late arriving clusters. The time assigned to each hit is then calculated as,

$$t = \frac{\sum_i (\alpha)^i p_i \cdot t_i}{\sum_i (\alpha)^i p_i}, \qquad (2\text{-}1)$$

where i is the bin number counting from the bin at the leading edge of the hit, p and t are the pulse height and time of the i^{th} bin and $\alpha < 1$ is a constant which varies linearly with the drift distance and is adjusted to optimize the resolution. This form is useful because a typical pulse has a fast risetime which is determined by diffusion, ion statistics and electronics. In contrast, the much longer trailing edge is dominated by the non-isochrony of the cell and the late-arriving clusters and so contains less useful time information. The performance of this algorithm on closely spaced tracks is discussed in Section 2.2.3.8.

The pattern recognition algorithm which identifies charged tracks in the DCVD employs two stages to achieve maximum track finding efficiency.[69] In the first stage, track segments in the DCVD are sought using a *curvature module* approach.* This approach searches through regions of constant azimuthal angle, ϕ, and curvature, κ, looking for a collection of hits with the same ϕ and κ. The algorithm is

* This is named after the hardware curvature modules employed in the trigger system (see Section 2.2.8, "Trigger System," on page 84).

designed to be fully efficient for tracks with $p_{xy} > 250$ MeV/c and a distance of closest approach to the origin, δ_{xy}, of less than 4 mm. These segments are further refined by adding and subtracting hits based on the residuals to a fit of the hits to a circular arc in the xy plane. Occurrences of ten or more hits are then considered track segments.

The next step is to attempt to join these track segments to the tracks found in the CDC. To do this, a χ^2 is formed between the CDC track and DCVD segments with an arbitration procedure for closely spaced tracks. This χ^2 is involves the match of the three track fit parameters in the xy plane (δ_{xy}, ϕ and κ) with an additional term to allow for scattering in the material between the two detectors. Hits on segments for which a matching CDC track is not found are then used in the second stage of the algorithm.

This stage begins by using the tracks found in the CDC for which no DCVD hits were found and extrapolating the track into the DCVD, then looking for the nearest hit starting in the outermost layer. The process continues layer-by-layer, adding each hit to the track if it passes a χ^2 cut and recalculating the track parameters.

These methods are complementary, particularly in hadronic events. The first stage is particularly adept at finding hits in dense jets and regions of many spurious hits caused by the backgrounds in hadronic events (see Section 2.2.2.5). It is, however, not efficient for the lowest momentum tracks or tracks with large impact parameters. These are tracks which can be more readily found with the second stage algorithm. The major drawbacks of this part of the algorithm, and the impetus of using the other stage first, is that this algorithm can become confused when tracks are closely spaced or the track passes through a region of high backgrounds. This happens when a few wrong hits are associated with the track, forcing the track fit off of the correct trajectory and making it unlikely that subsequent correct hits will be added.

Once the DCVD hits have been associated with the tracks found in the CDC, the full set of CDC and DCVD hits are refit using the SARCS6 least-squares fitting routine (see Section 2.2.2.4). There are regions in the jet cell in which the electric field has non-uniformities which are not fully modelled in the time-distance relation, and consequently, it is chosen to discard the hits from these regions prior to the track fit. (Investigation of these effects is considered more thoroughly in Sections 2.2.3.7 and 2.2.3.8.) To this end, it is required that a hit not be on the innermost two or outermost four wires, whereas the hit finding algorithms use layers 3 through 36. Hits which are further than 20 cm from the center of the

chamber also are removed. Finally, hits which are within 2 mm of the sense plane or 3 mm of the cathode plane have their resolution inflated in order to minimize their effect on the track fit.

In addition to the five conventional track parameters, a sixth parameter is included in the fit which allows a kink in the track due to multiple scattering in the material between the detectors. The multiple scattering inside the chambers due to the gas and wires is taken into account by modifying the resulting error matrix according to the formalism of R. Gluckstern.[61] It should be pointed out that this formalism does not strictly apply in this case, as it assumes that the scattering region contains equally-spaced measurements of the same resolution. However, Monte Carlo studies have demonstrated this formalism is satisfactory in this case, particularly because of the large number of layers.

2.2.3.6 Backgrounds

Data recorded during the 1990 SLC run showed that there was a significant amount of beam-related background in the DCVD. Figure 2–25 shows the hits detected by the DCVD in a typical random-trigger event from this run. The

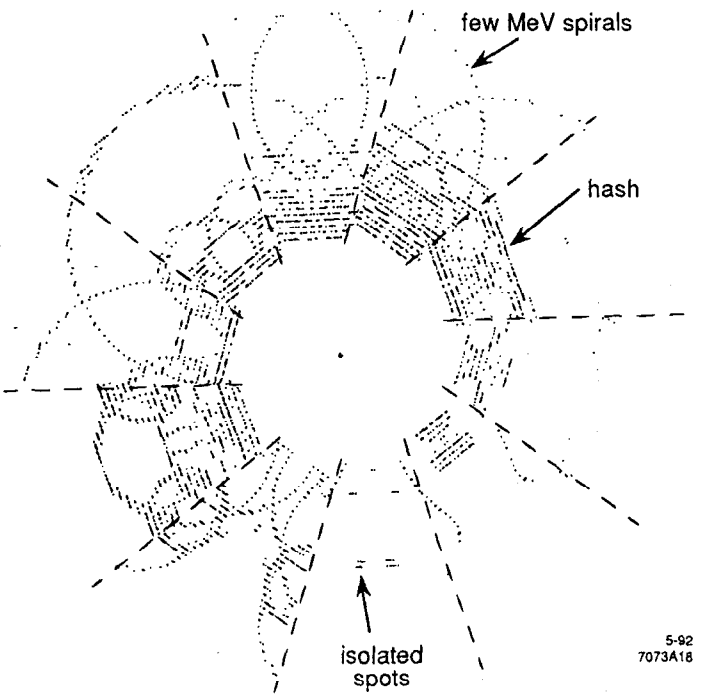

Figure 2–25 A typical random trigger event illustrating the level of backgrounds in the DCVD. The DCVD hit occupancy in this event is 20%. Note that each hit is shown on either side of the sense plane because locally it can not be determined from which side of the sense plane the hit originated.

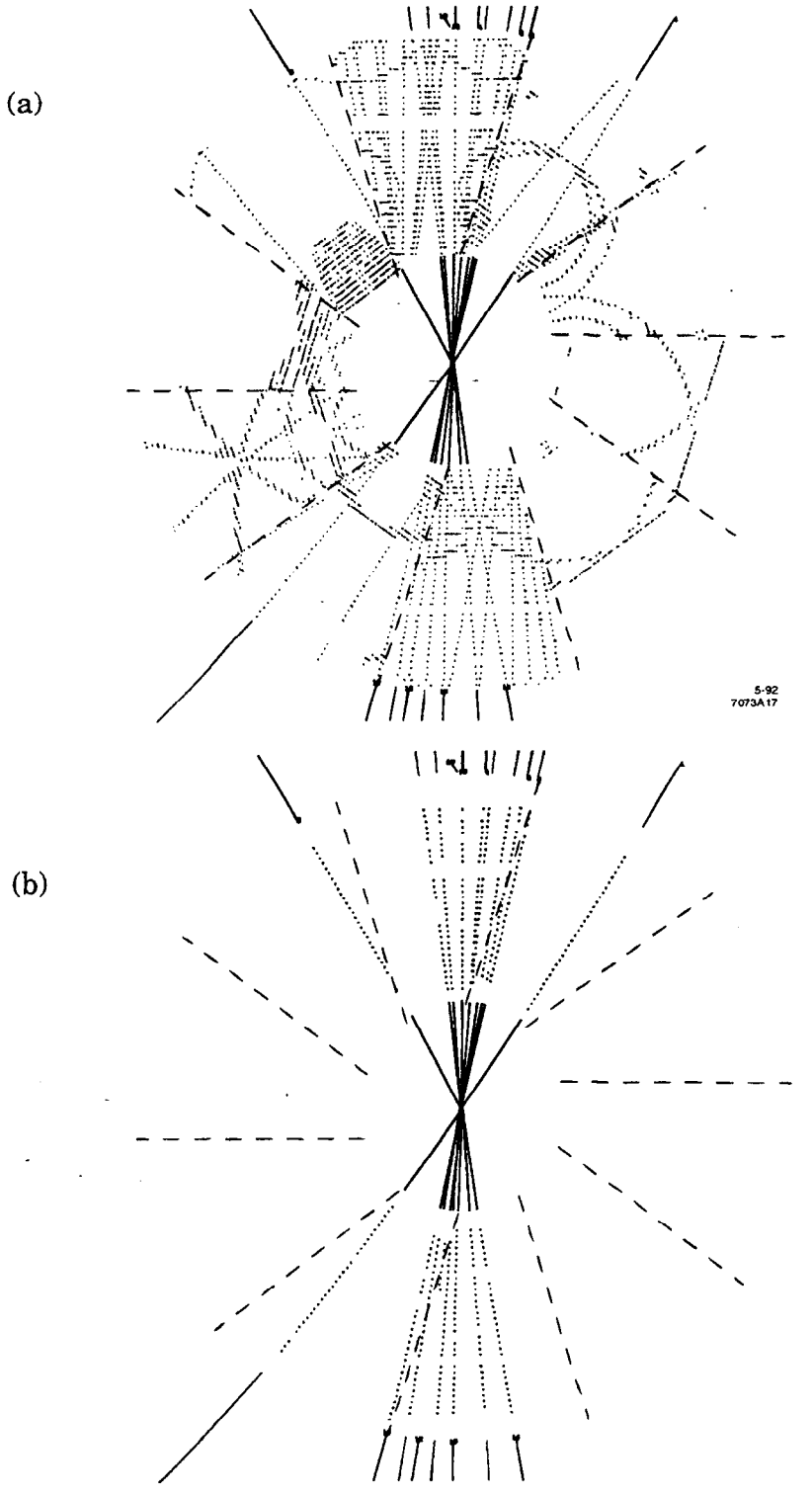

Figure 2–26 A typical hadronic event in the DCVD showing: (a) all detected hits, and (b) those hits assigned to tracks. This event has an occupancy of about 23%. In the upper plot each hit is shown on either side of the sense plane because of the local left-right ambiguity.

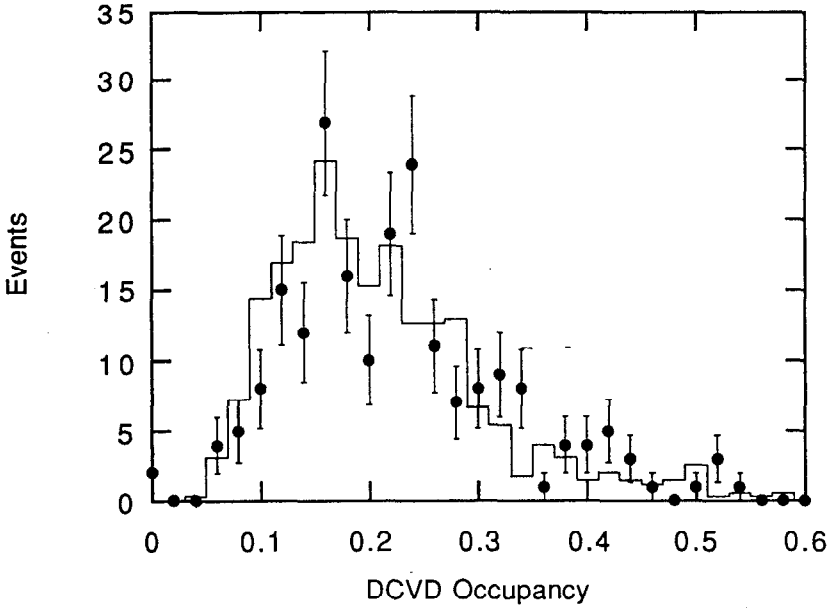

Figure 2–27 The DCVD occupancy observed in hadronic events. This does not account for events during which one or more DCVD cells was off. The points are the data and the line is the Monte Carlo with mixed background as described in Section 3.4.

background consists primarily of several distinct types. The spirals are electrons from photon conversions produced with a few MeV/c of momentum in the xy plane. The hash which is typically found in the inner layers is thought to be caused by a large number of very low energy particles, potentially produced from electromagnetic showers. Finally, the smaller spots due to photon conversions in the gas volume. Figure 2–26 illustrates the backgrounds in a hadronic event. As illustrated by this event, the DCVD hit finding algorithms nonetheless prove sufficiently robust to adequately reconstruct the tracks despite this level of background.

The level of backgrounds in the DCVD was characterized in terms of the occupancy, which is defined as the fraction of physical FADC bins in the chamber included in the found hits. The levels varied greatly, with most hadronic events having occupancies of about 20%, though events were observed with occupancies >50% (see Figure 2–27). The event illustrated in Figure 2–26 is typical in another fashion, which is that the backgrounds tend to be most severe at smaller radii, as illustrated in Figure 2–28. The backgrounds in the CDC are minimal in the 1990 data. (During the 1989 running, the CDC had significantly worse backgrounds which were reduced because of new masking and the material in the DCVD.) The

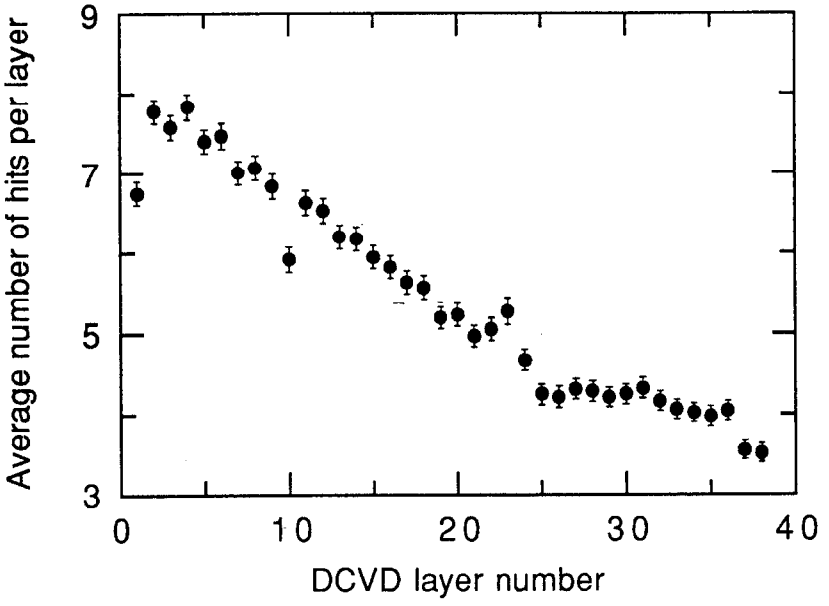

Figure 2–28 Number of hits observed per DCVD layer as a function of the layers number, illustrating the increased backgrounds at the inner layers.

SSVD also saw much less background than the DCVD, despite its much smaller radius. This is quite simply a result of the much smaller active volume of the SSVD.

2.2.3.7 Time-Distance Relation

In order to achieve the optimum resolution it is necessary to carefully study the relation between the drift time of a hit and the distance which it had drifted, called the *time-distance relation.*[70] As mentioned previously, the DCVD is operated in the unsaturated regime, such that the drift velocity varies linearly with E/P. Thus, understanding drift fields in the cell is crucial.

The first step in understanding the electric field is an analytic solution for the strength of the field along a line from a sense wire perpendicular to the sense plane. This solution, though calculated for an infinite wire plane array, describes the field to an accuracy of about 0.1% in the center of the jet cell, based upon comparison with a detailed electrostatics simulation. Using published data of the drift velocity in CO_2 as a function of E/P,[71] and scaling these results up by 10% based on our measurements in order to account for the addition of 8% ethane, a first-order time distance relation was derived (see Figure 2–29). For tracks which are not parallel to the sense plane, the electrons are assumed to drift in a direction perpendicular to the sense plane until they are at a radius of 1.78 mm from the sense wire. From

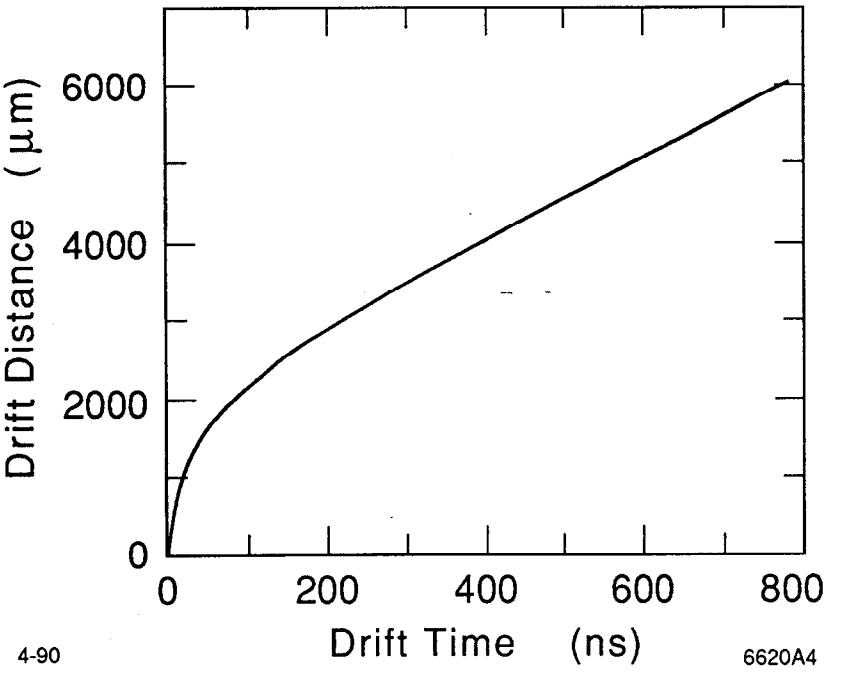

Figure 2–29 Time-distance relation as calculated from the analytic electric field calculation. Beyond 6 mm the drift velocity is assumed to be constant.

that point, the electrons are assumed to drift toward the sense wire radially. This radius is chosen to match the line of constant drift time based on the electrostatic simulation. The same time-distance relationship shown in Figure 2–29 is used for tracks not parallel to the sense plane, except that the drift distance is taken to be the length of this modified trajectory. The 4.75 kG magnetic field tilts the drift trajectories slightly by the Lorentz angle of 18.2 mrad.

To account for the perturbation of the electric field near the edges of the jet cell, a full electrostatic simulation was used to generate corrections to the first-order analytic model. This correction is based on a comparison of the electric field calculated by the simulation for all drift distances and wires in the DCVD jet cell. The resulting correction to the drift distance is shown in Figure 2–30 as a function of drift distance and wire number. The level of this correction can be as large as 10% for the wires on the extreme inner and outer edges of the cell. A smaller correction is also applied which accounts for tracks which are not parallel to the sense plane.

Finally, cosmic ray events have been used to refine the time-distance relation further. This is done by assuming a functional form which includes terms up to third order in the signed drift distance and wire number, then with a global 22-parameter fit, minimizing the residuals of the cosmic tracks. For this study, the

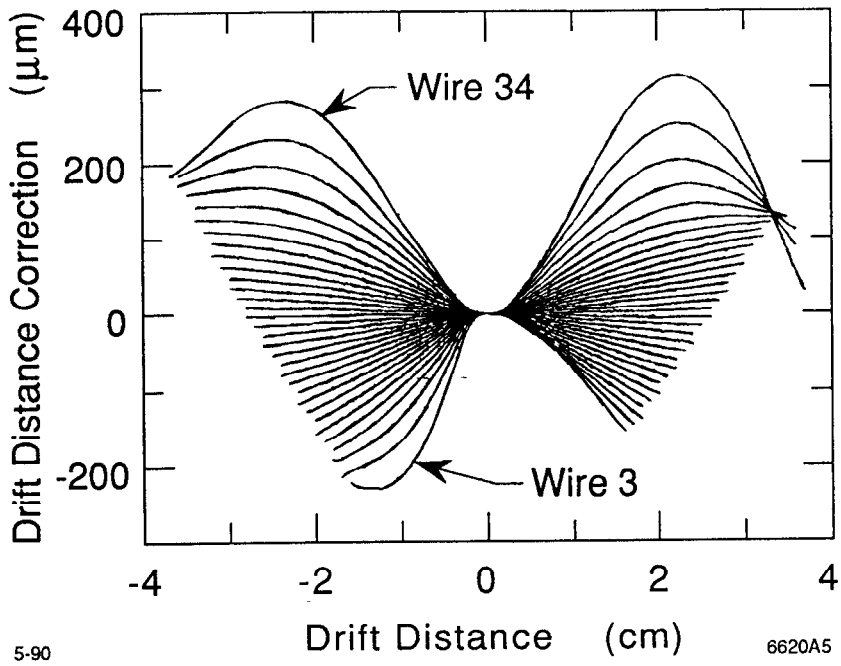

Figure 2–30 The drift distance correction to the first-order analytic model, as calculated by the full electrostatic simulation, is shown as a function of drift distance for the various DCVD layers.

cosmic rays are required to have $p_{xy} > 5$ GeV/c and a distance of closest approach to the chamber center in the xy plane which is less than 2.5 cm. Furthermore, the two halves of the cosmic ray are fit to a single trajectory. The results demonstrate that there are variations, which are less than 50 μm for all but the outermost layers, that were not included by the electrostatic correction. The results of this empirical correction are shown in Figure 2–31. A similar, but lower dimensional fit to the DCVD residuals in the cosmic events was used to determine the physical alignment of the DCVD with respect to the CDC.

2.2.3.8 Position Resolution and Efficiencies

The DCVD position resolution was studied primarily with the aid of track residual distributions. The track residual, δ, is defined as the difference between the hit location for a given layer and the position predicted for that layer by the track fit. It is expected that the resolution should be the sum of two terms in quadrature. The first is an intrinsic term which is related to the intrinsic gas properties (ionization statistics and amplification) and the hit timing strategy. The second term is due to the diffusion of the electron pulse. For a particular choice of chamber gas, the amount of diffusion depends on the square-root of the drift time,

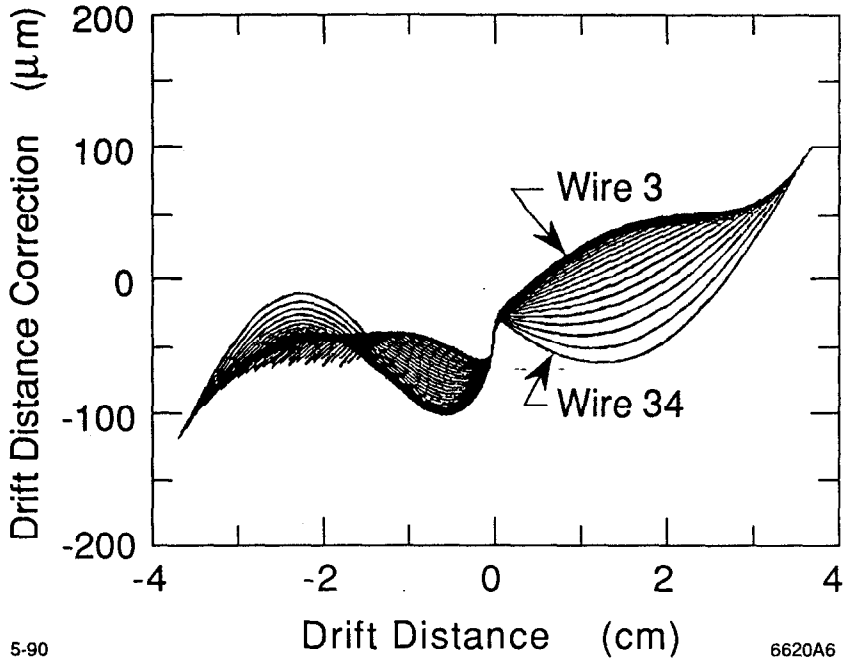

Figure 2–31 The empirical correction to the time-distance relation based on cosmic ray studies.

or for a constant drift velocity, the drift distance. The position resolution is thus expressed as

$$\sigma_x^2 = \sigma_{int}^2 + \sigma_{diff}^2 \cdot D \tag{2-2}$$

where σ_{int} and σ_{diff} are the intrinsic and diffusion coefficients, and D is the drift distance. The residual distributions were studied using tracks with $p_{xy} > 1$ GeV/c. The rms widths were calculated with a cut requiring that the normalized residuals, δ/σ_δ, be less than 4 to prevent the widths from being dominated by the tails.

Figure 2–32 shows the variance of the residual distributions binned as a function of drift distance for cosmic ray data taken during 1990. A fit to this data yields,

$$\sigma_x^2 = (12.4 \pm 0.8\ \mu\text{m})^2 + (40.2 \pm 0.3\ \mu\text{m})^2 \cdot D, \tag{2-3}$$

where D is in units of cm. There is potentially a small systematic shift toward poorer resolution than is found by the fit at large drift distances. However, this region is sparsely populated with hits compared to lower drift distances and thus has less statistical strength in the fit.

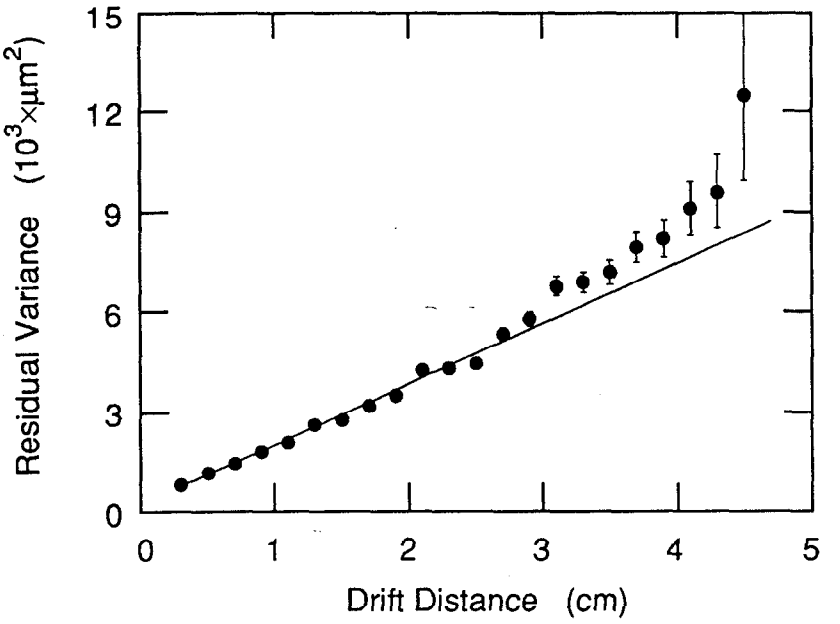

Figure 2–32 The DCVD resolution as a function of drift distance for cosmic events, and a linear fit to these points.

Of more concern is the resolution in hadronic events. This was studied in a similar fashion using track residuals. It was found that the resolution of hits in hadronic events depends not only on the drift distance but also on the layer in the DCVD (see Figure 2–33). It was found empirically that this dependence could be parameterized adequately with a simple dependence on the layer number, L:

$$\sigma_x^2 = \sigma_{int}^2 + \sigma_{diff}^2 \cdot D + \sigma_{layer}^2 \cdot (19 - L). \tag{2-4}$$

Binning the residuals in terms of drift distance and layer number, the above functional form was used to fit the residual variances. The result is:

$$\sigma_x^2 = (28.4 \pm 0.8\ \mu m)^2 + (43.0 \pm 0.5\ \mu m)^2 \cdot D + (7.58 \pm 0.2\ \mu m)^2 \cdot (19 - L), \tag{2-5}$$

where the drift distance, D, is in units of cm. This function can be more readily understood by viewing it graphically, as done in Figure 2–34. From this, it is evident that compared to the resolution of cosmic events, the hadronic event position resolution is significantly degraded at the inner layers, but is very nearly the same as cosmics at the outer layers.

There are primarily two explanations for the poorer resolution at the inner layers. One is that at the inner layers the hits from closely spaced tracks will be more likely to overlap and thus potentially affect the measured time of the latter

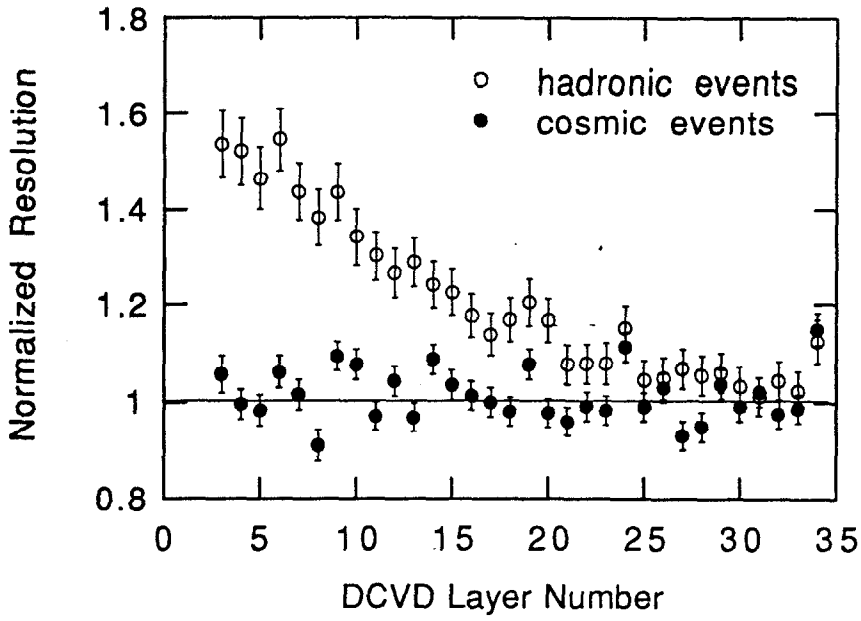

Figure 2-33 Normalized residuals as a function of wire number for cosmic events and hadronic events of all drift distances. In this plot, the hadronic residuals were normalized with the values calculated for cosmic events, Equation (2-3).

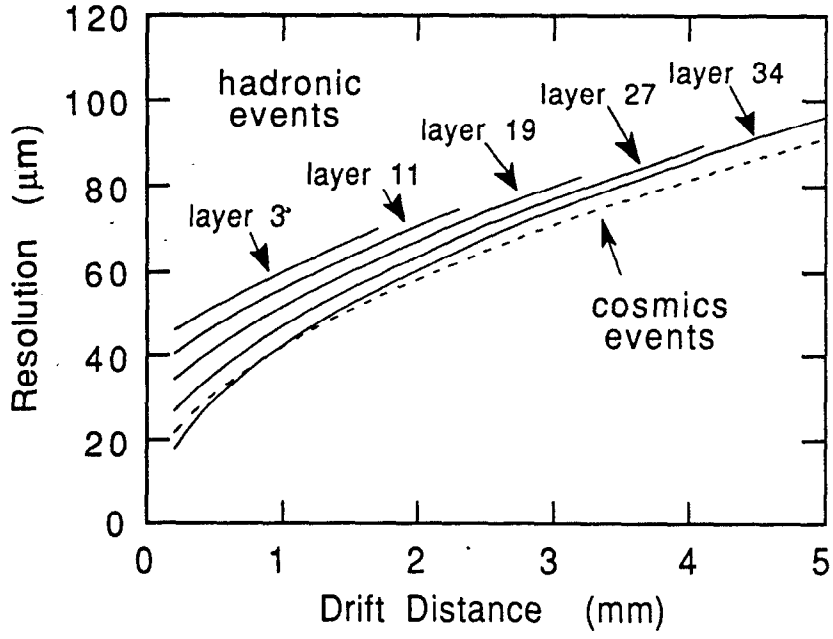

Figure 2-34 The fit resolution as a function of drift distance for hadronic events and cosmic events.

hit. The other possibility is that it is simply related to backgrounds, which as shown in Section 2.2.3.6 are more severe at the inner layers.

To determine the source of the degraded resolution, the Monte Carlo was employed. Specifically, the resolution measured in the Monte Carlo with full detector simulation can be compared for three different sets of Monte Carlo events: muon-pair events, hadronic events with no beam-related background added and hadronic events with the beam-related backgrounds similar to those observed in the data.* The muon pairs in the Monte Carlo show no dependence on the DCVD layer number, as similarly cosmic events did not. The hadronic events with no background have only a slight dependence on the layer number. For these events, there is a fractional resolution difference between the inner and outer layers of 10% at a small drift distance of 2 mm (where the fractional effect of wire dependence is most acute). The hadronic events with the backgrounds applied show much more layer dependence, with the same fractional difference of 55%. Thus it is clear that the majority of the resolution degradation is in fact due to the presence of backgrounds, with only a fairly small contribution from the closely spaced tracks.

The resolution also exhibits a dependence on the polar angle of the track, θ. The length of the track segment from which charge will drift to a particular sense wire will increase as $(\sin\theta)^{-1}$. The average amount of deposited charge will increase accordingly. Thus, the statistics will improve and the resolution with which the pulse time is determined should vary as $(\sin\theta)^{-1/2}$. As illustrated in Figure 2–35, this was indeed found to be the case, and a correction was applied to the resolution to account for this. The correction is $1.057/\sqrt{\sin\theta}$, where the constant is chosen to leave the overall resolution unchanged.

The resolution and time-distance relation were also investigated in some of the potentially problematic regions of the jet cell. Hits which were within 2 mm of the sense plane or 3 mm of the cathode plane were effectively removed from the track fit by inflating the errors assigned to these hits. This was done because the resolution was measured to be significantly worse in these regions than the rest of the cell, since the time-distance relation does not fully account for all of the variation in the field. The position of the hit along the axis of the chamber is also of interest because of the possibility of electric field variations near the ends of the chamber. It was found that hits with $|z| > 20$ cm show some adverse affects in their time-distance relation and the resolution, and thus are not used. The slope of the

* See Section 3.4, "Detector Simulation," on page 102 for information describing the treatment of Monte Carlo hits and backgrounds.

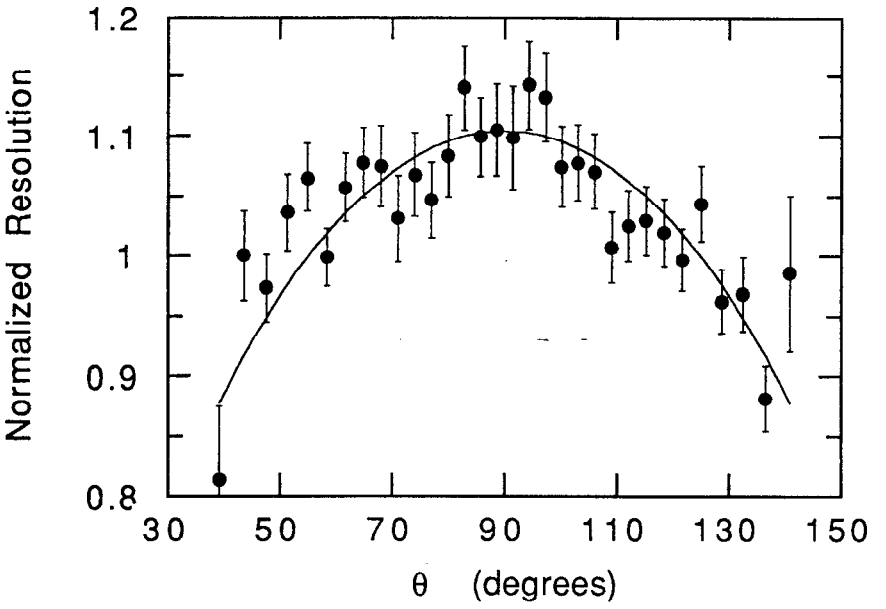

Figure 2–35 The normalized resolution as a function of the polar angle of the track. The line is a fit with a $(\sin\theta)^{-1/2}$ dependence.

track with respect to the sense plane was also investigated. It was found that the corrections in the time-distance relation are adequate and that no resolution degradation is observed.

The double hit resolution was investigated[68] first with the use of a pulse library containing a large sample of pulses from cosmic events. By superposing the pulse trains from different cosmic ray tracks with various separations, the efficiency with which the second hit is found can be studied. It is found that even with hits separated by as little as 400 μm, the efficiency of detecting the second hit is nearly unity (see Figure 2–36). There is however some loss of efficiency until the separation is about 1500 μm because of the effects of the first pulse on the measured time of the second pulse. The fake hit rate has been investigated using cosmic ray data and shows that, as illustrated in Figure 2–36, beyond 700 μm from the first hit the fake hit fraction drops below 10%. Finally, closely spaced tracks in hadronic events have also been used to study the double track resolution and the results are consistent with those determined above.

The hit finding efficiency has been studied and tuned for the best agreement with the data. In the Monte Carlo generation, a single value of the hit efficiency was used to characterize all the sense wires in the detector. Assigning the input efficiency to 0.95 yielded the best data/Monte Carlo agreement. The measured layer-by-layer efficiency varies with the layer number particularly due to the effects of

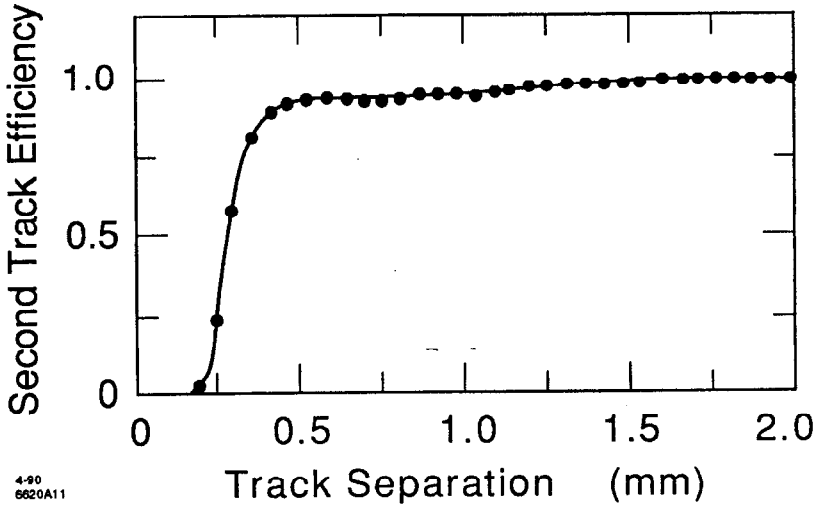

Figure 2–36 The efficiency to detect a second hit as a function of the separation of the tracks at this layer.

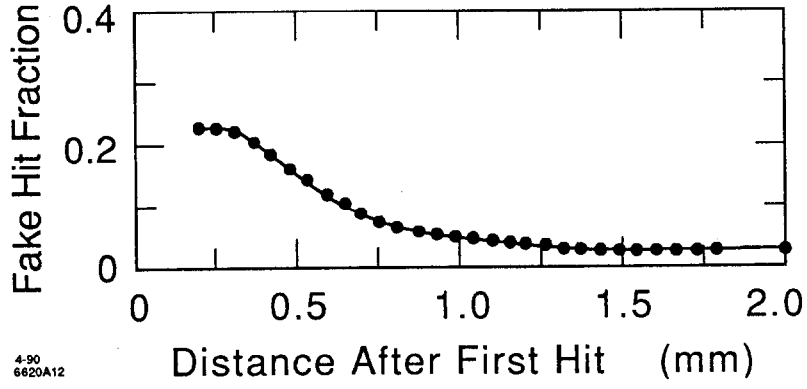

Figure 2–37 The fake hit fraction measured in cosmic events as a function of the distance from the first hit.

higher backgrounds in the inner layers (see Figure 2–38). The distribution of the number of DCVD hits assigned to tracks found in the CDC is shown in Figure 2–39. The general agreement between the data and Monte Carlo is good, although the data has a less-peaked structure. This produces a slightly lower average in the data (21.7±0.2 hits per track) than is predicted by the Monte Carlo (22.2 hits per track).

2.2.4 The Silicon Strip Vertex Detector

The innermost tracking detector, the Silicon Strip Vertex Detector (SSVD), was designed to provide several very high precision measurements of the produced tracks at a location as close as possible to the e^+e^- interaction point. This allows very precise determination of the track impact parameter especially for those tracks

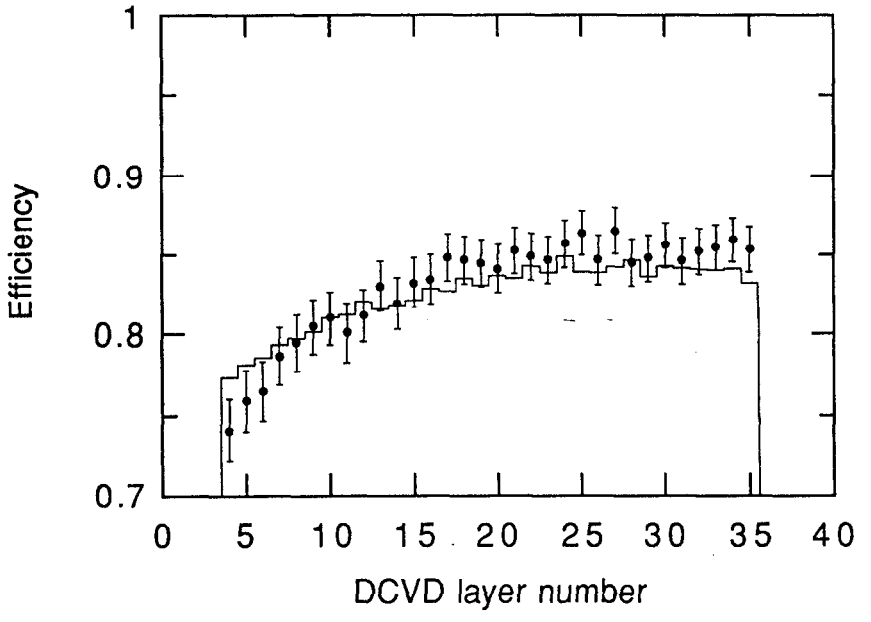

Figure 2–38 The DCVD measured hit efficiency as a function of the layer number for the data (points) and the Monte Carlo (line).

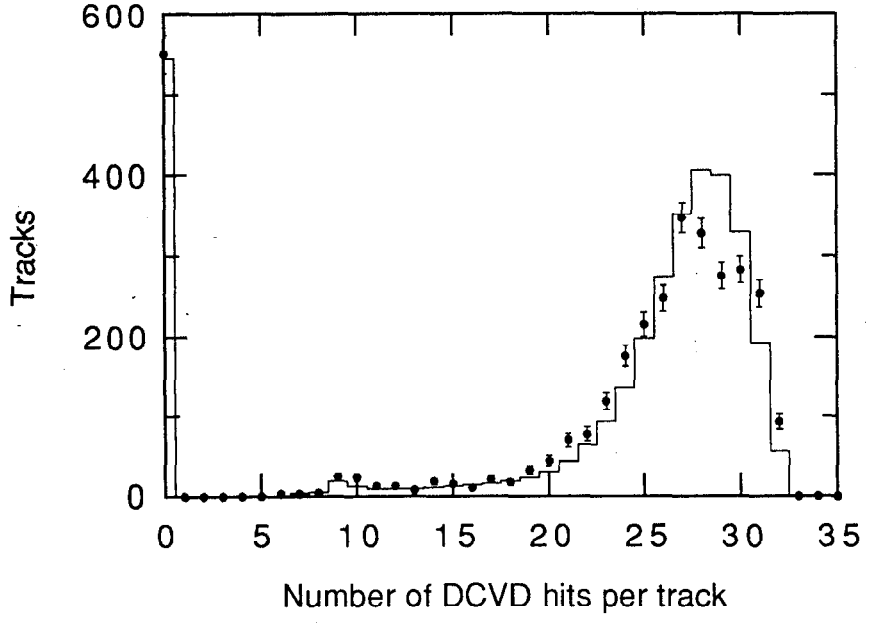

Figure 2–39 The distribution of the number of DCVD hits per track for the data (points) and Monte Carlo (line). These tracks are required to have $|\cos\theta| < 0.8$, $p_{xy} > 0.15$ GeV/c, $|z| < 1.5$ cm, $|b| < 1.5$ cm and $N_{CDC} \geq 25$. Many of tracks with no found DCVD hits were in cells which had their sense voltage lowered due to high voltage problems.

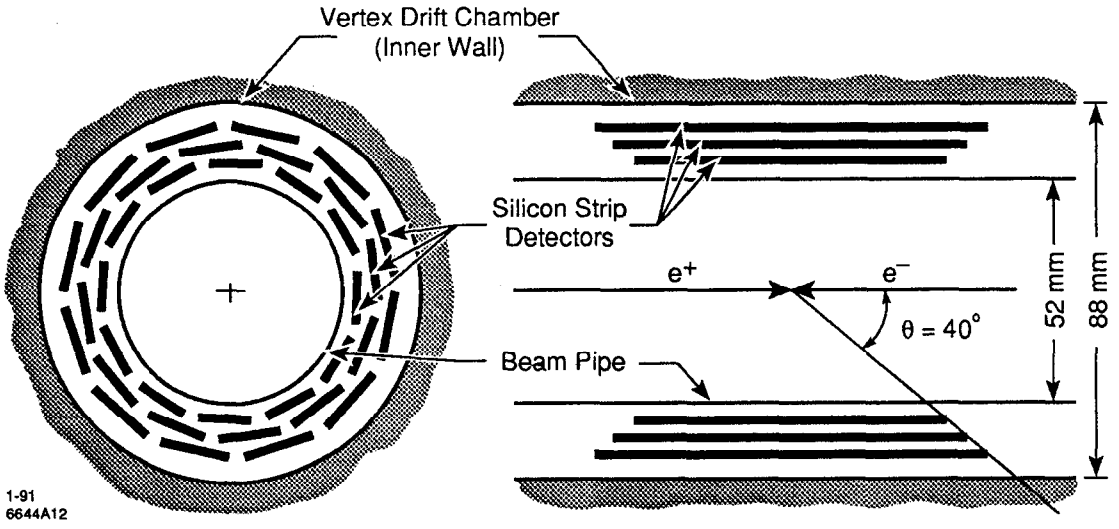

Figure 2–40 Schematic layout of the Silicon Detector Modules in the SSVD.

Layer	Radius	Active Length	Pitch
1	29.4 mm	72 mm	25 μm
2	33.7 mm	82 mm	29 μm
3	38.0 mm	90 mm	33 μm

Table 2–3 Geometric properties of the Silicon Detector Modules used in the three layers of the SSVD.

with high momentum. The design and performance of the SSVD is extensively described elsewhere. In particular, the reader may wish to refer to References [72] and [73] for greater detail than is presented here.

2.2.4.1 Design

The SSVD is designed of 3 layers from 29 to 37 mm from the beam axis. Each layer is comprised of 12 of the Silicon Detector Modules (SDM's), as illustrated in Figure 2–40. Each SDM has 512 axial strips with differing pitches depending on the layer. The average SDM thickness is 314 μm of silicon, which when combined with a small cable beneath the detector is about 0.55% of a radiation length. Table 2–3 summarizes the details for each of the three detecting layers in the SSVD.

The detector is made from two identical halves to facilitate assembly onto the beam pipe (see Figure 2–41). Each half of the detector is held against the beam pipe with a set of three copper springs with a 3 mm sapphire ball to assure that no

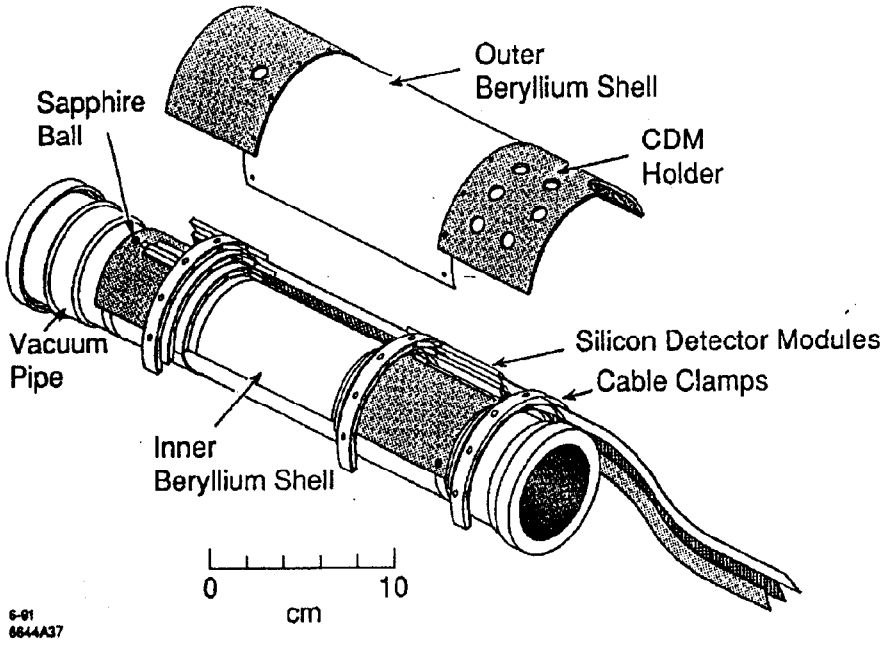

Figure 2–41 Mechanical assembly of the one half of the SSVD.

electrical connection is made to the beam pipe. The SDM's are inserted in aluminum end pieces, held apart by half-cylindrical beryllium shells of a 250 μm thickness. The modules were held in place by spring mounts in the end pieces to assure that the modules remain in the same position even through temperature fluctuations as large as 15° C in 30 minutes. Finally, the cables leading from the SDM's were clamped firmly to prevent them from affecting the detector placement.

2.2.4.2 Electronics

The first stage of the readout electronics utilizes 128-channel custom-designed VLSI Microplex chips[74] mounted outside the active region on both ends of the detectors. The SDM's are connected to driver/receiver modules which pulse the power to the detectors in order to minimize the power dissipation, and provide the timing signals to the Microplex chip readout. The readout is controlled by nine microprocessor-controlled ADC's, the so-called "Brilliant Analog-to-Digital Converters" or BADC's.[75] These devices controlled the analog multiplexing of the Microplex signals, digitized the signals and analyzed the results. The BADC's performed a pedestal subtraction and a common-mode correction, and then stored the resulting pulse heights. A second pass through the data then allowed a cluster finding algorithm to select channels with significant pulse height information by requiring that a sum of pulse heights over three strips be larger than the sum of the

thresholds for those three strips. Three strips are used for finding clusters because given that a track from the IP will cross a strip at an angle of less than 200 mrad in the xy plane, this is the maximum number of strips which can have a signal generated by a single track. The pulse height information for the five strips around the center of the cluster are then sent to the VAX host computer to be saved in the event record.

The SSVD functioned quite well in general with relatively few failed channels. There were two cases in which an entire cell was rendered inoperable due to failed cables. One of these modules was lost for the entire run and the other for slightly more than half. Aside from this, only 1.6% of the remaining channels failed during the run due to defects in the detector or problems with the electronics.

2.2.4.3 Hit Finding and Track Fitting

Hits were defined at a contiguous series of detector strips with a corrected pulse height of at least $1.5\sigma_i$, where σ_i is the rms noise of each individual strip. Additionally, it was required that at least one strip have a pulse height of at least $5\sigma_i$ and that the cluster contain no bad strips. The point at which the particle traversed the module is then given by a weighted mean of the strips in the cluster. For closely spaced tracks, the algorithm splits the clusters into two separate clusters if there is a pulse height dip of more than $1.5\sigma_i$ within the original cluster, provided that each half have at least one strip have a pulse height of at least $5\sigma_i$. The pulse height of the strip dividing the two half clusters is split evenly between them. It is expected that this algorithm should work well for tracks separated by 2 or more strips. On average only 1% of tracks are affected by merged clusters due to the high granularity of the detector.

The process of matching the clusters found on the SSVD layers to the tracks measured in the CDC and DCVD begins by extrapolating the track through the SSVD and looking at all combinations of hits within ±1 mm of the track projection. This rather simple algorithm works because there are only three layers and the backgrounds are low, thus keeping the combinatorics reasonable. The final set of hits for each track is decided upon by a χ^2 test. Table 2–4 illustrates the agreement of the fraction of tracks with different numbers of hits between that found in the data and the Monte Carlo with the full detector simulation.*

The information from the SSVD hits assigned to a track is then combined with the track fit information from the CDC and DCVD to form an 8×8 covariance

* The Monte Carlo detector simulation is described in Chapter 3.

number of SSVD hits per track	fraction of tracks	
	data	Monte Carlo
0	8.0±0.6%	7.0%
1	14.4±0.8%	13.4%
2	54.0±1.5%	55.2%
3	23.5±1.0%	24.5%

Table 2–4 The fraction of tracks with various numbers of SSVD hits per track. The cuts on the tracks are all of the 'vertex quality cuts' described in Section 4.4 on page 128 (exclusive of the cut on the number of SSVD hits) which are designed to be selected high quality tracks.

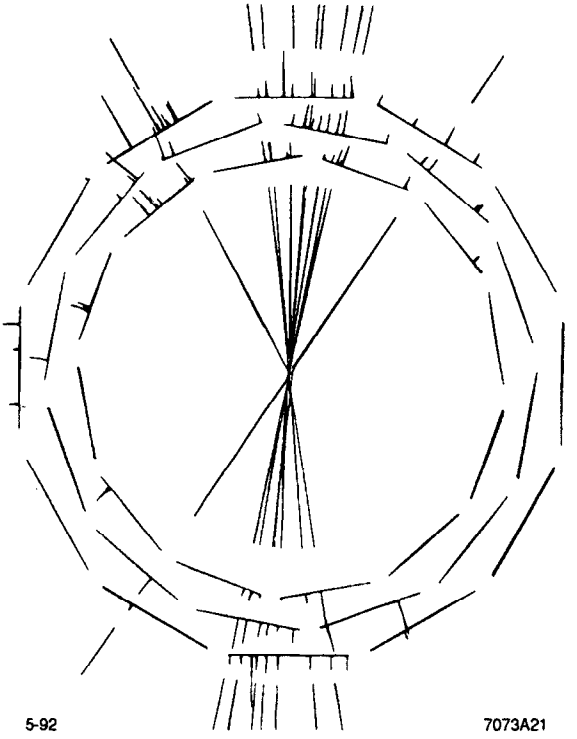

Figure 2–42 A hadronic event recorded in the SSVD. The height each hit is proportional to its pulse height. This is the same event as displayed in the DCVD in Figure 2–26.

matrix. This matrix is comprised of two parts. There is the 5×5 covariance matrix from the SARCS6 fit to the CDC and DCVD measurements and a 3×3 matrix for the SSVD hits which includes the correlations between layers due to multiple scattering.[73] Figure 2–42 shows a typical hadronic event recorded in the SSVD.

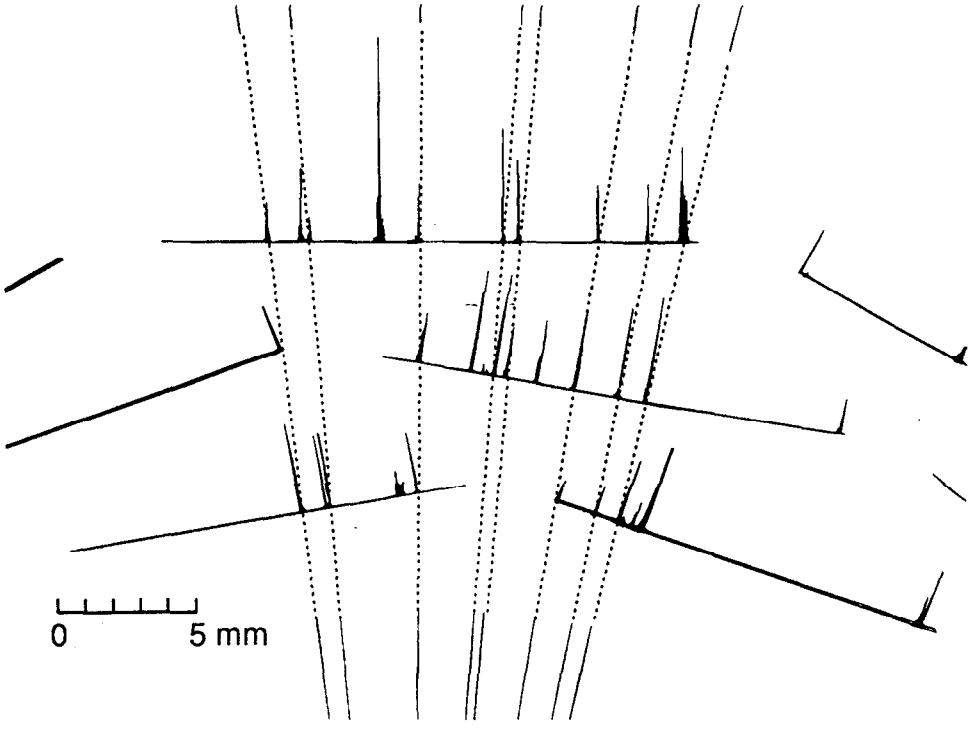

Figure 2–43 An illustration of the SSVD hit matching onto tracks from CDC and DCVD. The hits in the SSVD are shown with their pulse heights. The fitted tracks are denoted by the lines.

The ability of SSVD hits to matched with the track projections from the CDC and DCVD is illustrated in Figure 2–43.

2.2.4.4 Alignment

The local alignment of each SDM relative to the end pieces of the detector is described by seven parameters. There are three angles and two displacements along the x and y directions as illustrated in Figure 2–44. The offset in the z direction is not considered as all of the strips are axial. Additionally there are parameters to account for the possibility of a bow and twist in the module. The global alignment of each of the halves of the SSVD can be characterized by the same set of three angles and a displacement along the x and y directions.

The local alignment of the SSVD, namely the alignment of each of the detector modules relative to each other was attempted using several different approaches. Before the SSVD was installed into the DCVD, an optical alignment and an alignment using x-rays[77] to survey the detector were done. It was hoped that it would only be necessary to do a global alignment of each half of the detector with respect to the DCVD and CDC using detected tracks. Upon taking data in the

SSVD, it became clear that this was not the case. These alignments did not position the modules with respect to each other within the required accuracy. As both of the alignments are potentially quite accurate, it remains unknown why the alignments did not describe the installed detector. Possible explanations include systematic problems in these measurements or motion of the modules during installation. The precise cause notwithstanding, the situation required that tracks be used for both the global and local alignments. During the run, the motion of the SSVD with respect to the DCVD was monitored by the Capacitive Displacement Monitor (CDM).[76] This system was comprised of a series of capacitive sensors mounted on the inside of the DCVD inner core and on the outside of the SSVD. The observed motion was incorporated, but the magnitude of the effects were small compared to the sensitivity of the global alignment.

The global and local alignment procedures start with the projections of the tracks as fit by the CDC and DCVD, from which are calculated the residuals, ξ_i, in each of the SSVD layers in which a hit was assigned to this track. Note that since the SSVD hits are assigned to tracks from the CDC and DCVD based on the best hit/track matches, this procedure will be iterative. A series of variables are formed using these residuals:

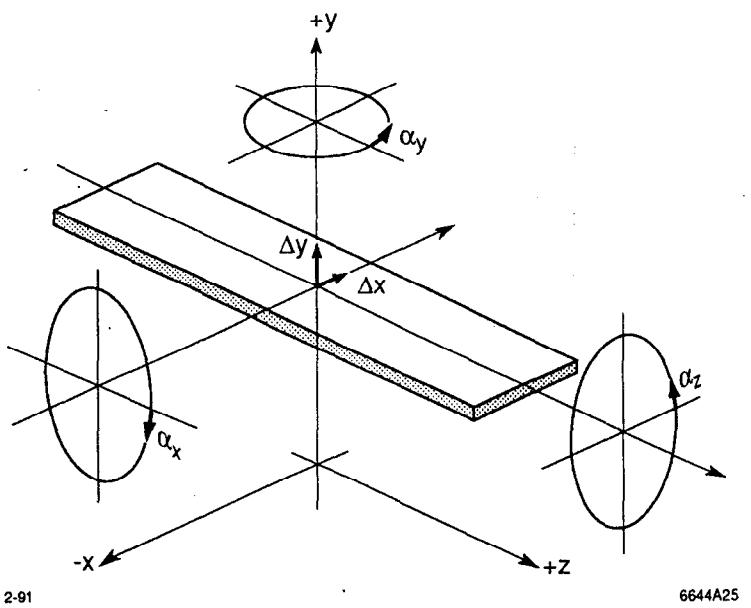

Figure 2–44 Definition of the local alignment variables Δx, Δy, α_x, α_y and α_z.

- for tracks with hits in layers j and k:

$$\Delta b_{jk} = (\xi_j + \xi_k)/2 \tag{2-6}$$

$$\Delta \phi_{jk} = (\xi_j - \xi_k)/\Delta r_{jk} \tag{2-7}$$

- for tracks with SSVD hits in three layers:

$$\Delta b_{123} = (\xi_1 + \xi_2 + \xi_3)/3 \tag{2-8}$$

$$\Delta \phi_{123} = (\xi_1 - \xi_3)/\Delta r_{13} = \Delta \phi_{13} \tag{2-9}$$

$$\Delta \delta = (\xi_1 - 2\xi_2 + \xi_3)/2 \tag{2-10}$$

The five global alignment constants per detector half are then determined by minimizing the sum of the squares of each of the variables divided by its variance using a sample of about 2100 tracks with $p_{xy} > 0.5$ GeV/c. The local alignment was similar except that it determined a subset of the seven local alignment parameters for each of the modules. This subset included the radial offsets Δx and Δy and the yaw angle α_y The sensitivity to the remaining local parameters was small and the x-ray alignment results were used for these values. The level of improvement provided by the local alignment is illustrated using the triplet residual, Δ, defined as the difference between the track fit with only the SSVD hits in the first and third layers (using curvature and z information as determined by the outer chambers) and the position of the SSVD hit in layer two. The mean triplet residual as a function of the azimuthal angle around the chamber is shown in Figure 2–45.

2.2.4.5 Position Resolution and Efficiency

The position resolution of the SSVD can be studied using the triplet residual, Δ, as defined above. A distribution of Δ for tracks with $p > 1$ GeV/c is shown in Figure 2–46. A fit to the width of this Gaussian yields a width of 8.7 μm, which corresponds to an average resolution per layer of $\sigma = 8.7/\sqrt{3/2} = 7.1$ μm. This, however, is an average over three layers with different strip pitches (25, 29 and 33 μm). The Monte Carlo with the full detector simulation reproduced the observed average resolution remarkably well. This Monte Carlo assumes intrinsic resolution of 5, 6 and 7 μm for the three layers. It also includes effects from beam-related backgrounds and the uncertainty in SSVD alignment, which effectively add 3 μm and 2.5 μm in quadrature to the resolution, respectively.

The hit finding efficiency was investigated by looking at tracks with two or more hits. A straight line between the hits was defined and if the line crossed a third

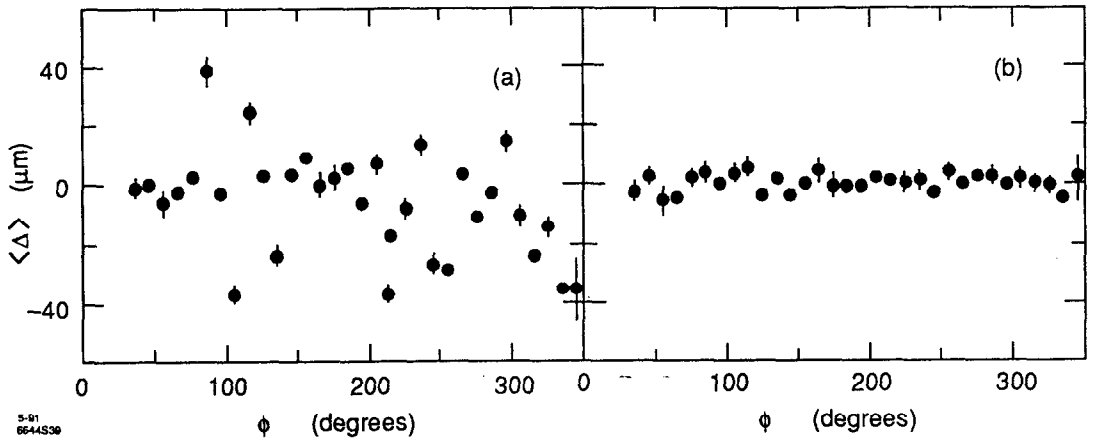

Figure 2–45 Mean triplet residual, Δ, as a function of the azimuthal angle, ϕ, (a) before and (b) after the local alignment. Each point corresponds to a different set of three overlapping modules. The lack of points between 0 and 36° is the result of the dead module in that region.

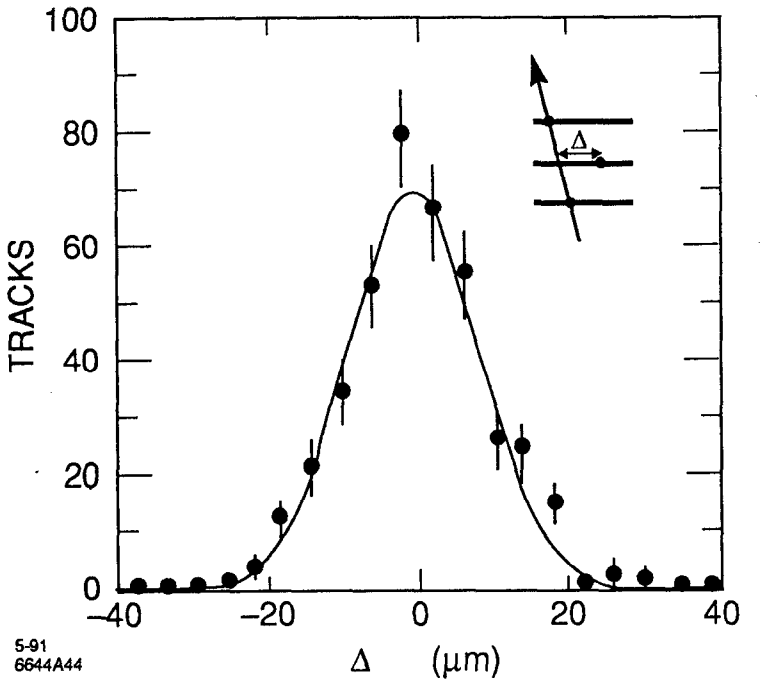

Figure 2–46 Distribution of triplet residuals observed in the data (points) and the Monte Carlo with the full detector simulation (line), for tracks with at least 1 GeV/c of momentum.

module farther than 10 strips from any know bad strips a hit was sought in that layer. To avoid problems from close tracks it was required that the track in question be at least 15 mrad from any other track. Furthermore, each hit was required to be at least 30 strips from any other hit to reduce effects from background hits. Of 731

pairs of hits satisfying the above requirements, 730 had a hit located within three strips of the predicted location, corresponding to a hit finding efficiency of 99.9±0.1%.

2.2.5 The Beam Pipe

The beam pipe used for the 1990 Mark II run has a diameter of 25 mm in order to get the inner detecting layers as close as possible to the interaction point. The central section of the beam pipe, which spans the entire angular acceptance of the tracking detectors, is made from a 0.483 mm thick aluminum tube with a 0.025 mm coating of copper to aid in the absorption of low energy photons. The beam pipe also contains two "wire flippers" for measuring beam profiles in the vertical and horizontal directions.[78] These wire flippers hold carbon fiber wires which can be inserted into and retracted from the beam axis. These wire flippers are 0.80 mm of aluminum and cover about 11% of the solid angle in the region given by $|\cos\theta| < 0.8$. The beam pipe assembly is shown in Figure 2–47.

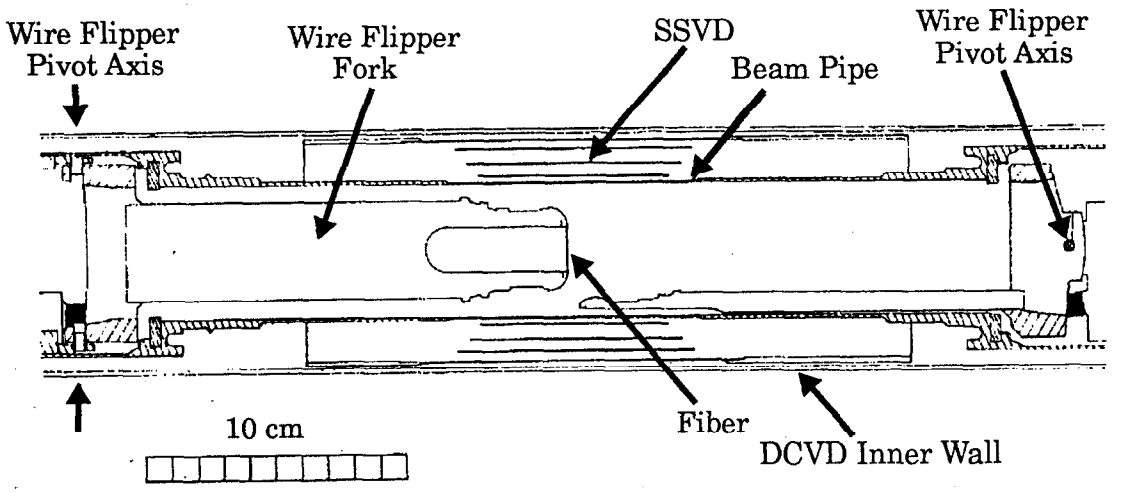

Figure 2–47 Beam pipe and wire flipper assembly.

2.2.6 Tracking Detector Summary

Table 2–5, below, has a summary of the primary dimensions and performance parameters of the tracking detectors. Table 2–6 lists the material present in the different detectors, which will be important in the performance of the tracking detectors which is the subject of later chapters.

2.2.7 Extraction Line Spectrometers

The energy of the beams at the interaction point is determined using a pair of precision spectrometers housed in the extraction lines of the SLC (refer to

Parameter	CDC	DCVD	SSVD
Number of layers	72	38	3
Active inner radius (cm)	19.2	5.3	2.94
Active outer radius (cm)	151.9	16.5	3.80
Active length (cm)	230	48	7.2–9.0
$\lvert\cos\theta\rvert$ acceptance (all layers)	0.60	0.82	0.77
Average resolution (μm)	185	61	7.1
Double track resolution (μm)	~4000	~400	~60
Double track resolution (mrad)	~5	~4	~2
Number of readout channels	5832	380	18432

Table 2–5 A summary of some of the parameters for the three tracking detectors.

Item	Radius (mm)	Thickness (% R.L.)
wire flipper	23.7	0.90
beam pipe	25.0	0.75
SSVD inner shell	27.6	0.11
SSVD layers (3)	29.4–38.0	0.55/each
SSVD outer shell	41.0	0.11
DCVD inner shell	45.0	0.86
DCVD gas & wires	50–170	0.72
DCVD outer shell	177	5.93
CDC inner shell	190	0.95
CDC gas & wires	190–1520	2.12

Table 2–6 A list of the location and number of radiation lengths of the material present in the tracking detectors. Note that the wire flipper only covers 11% of the azimuthal acceptance. The amount of material was studied using tracks, and these values reflect small corrections to the nominally measured values (within the measured errors). See Section 4.5.2, "Multiple Scattering-Limited Resolution," on page 138.

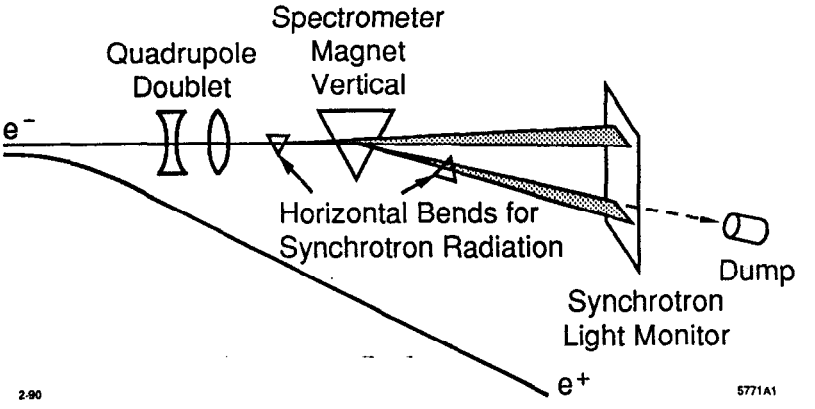

Figure 2–48 A schematic diagram of the Extraction Line Spectrometer.

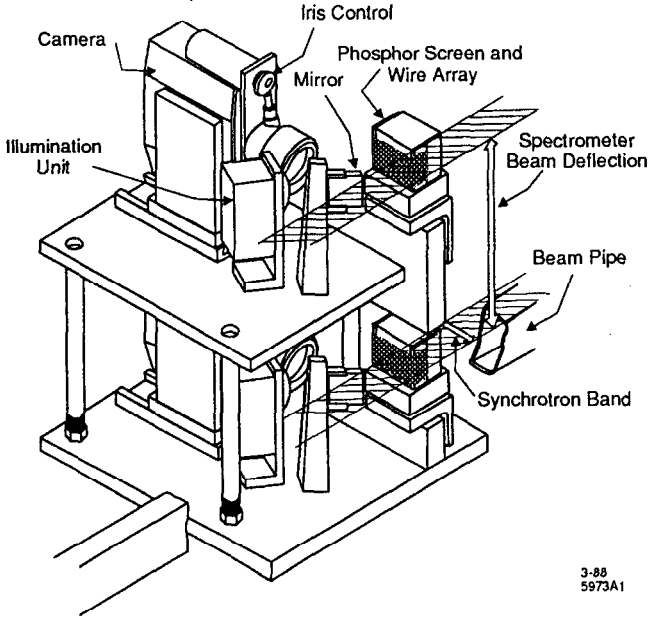

Figure 2–49 The Phosphorescent Screen Monitor for detecting the synchrotron beams from the Extraction Line Spectrometer.

Figure 2–1 on page 31). The schematic layout of the Extraction Line Spectrometers[79] is shown in Figure 2–48. The e^- or e^+ beams are directed through a vertical bend magnet whose field has been carefully mapped and are monitored throughout the run. Before and after this vertical bend are horizontal bend magnets which produce swaths of synchrotron radiation. The principle device used for detecting the synchrotron radiation was the Phosphorescent Screen Monitor (PSM) This is illustrated in Figure 2–49. The PSM has a target for each of the synchrotron beams which is an array 100 μm wires at a 500 μm spacing and a phosphorescent

screen to emit light when struck by the synchrotron beams. The wire positions and the spot on the phosphorescent screen due to the striking synchrotron beam are recorded by a camera, whose output is digitized for processing. This system has achieved an absolute $e^{\pm}$ beam energy measurement accuracy of ±35 MeV.

2.2.8 Trigger System

The trigger system selects events which are to be stored on magnetic tape for future analysis. There are three different triggers for selecting hadronic and leptonic events. These triggers use information from different detector systems and provide a level of redundancy sufficient to be fully efficient for triggering on hadronic events. There are also two special purpose triggers for selecting cosmic ray events and events at random beam crossing intervals. Information from these trigger systems is passed to the VAX host computer via the Master Interrupt Controller (MIC).

Charged Particle Trigger

This trigger uses CDC and DCVD to locate track patterns entirely in hardware using coarsely segmented hit information. The trigger for the 1990 runs used nine layers of the CDC and three layers of the DCVD. In the CDC, the basic unit used in this pattern finder was a jet cell. A cell was considered to be hit if at least four of the six wires had TDC information. In the DCVD, the information from the postamplifiers was divided into eight time bins for the trigger. These hit patterns were loaded into shift registers and transferred to hardware curvature finding modules to identify the hit patterns (see Figure 2–50). Each module searches for tracks in a given range of curvature and typically require 10 layers to define a track. Tracks within 10° of each other are considered one track. The total number of detected tracks is passed to the MIC for a trigger decision.

Calorimetry Energy Trigger

The calorimetry energy trigger searches for events of interest by matching certain pre-selected event topologies to the detected events. The information from the Liquid Argon Calorimeter and Endcap Calorimeters are used for a Total Energy Deposition (TED) trigger, which sums energy seen by both calorimeters. Signals in the SAM and mini-SAM are used to form a low-angle Bhabha trigger for luminosity monitoring. This is accomplished with the aid of the programmable Memory Logic Modules which interfaces with MIC.

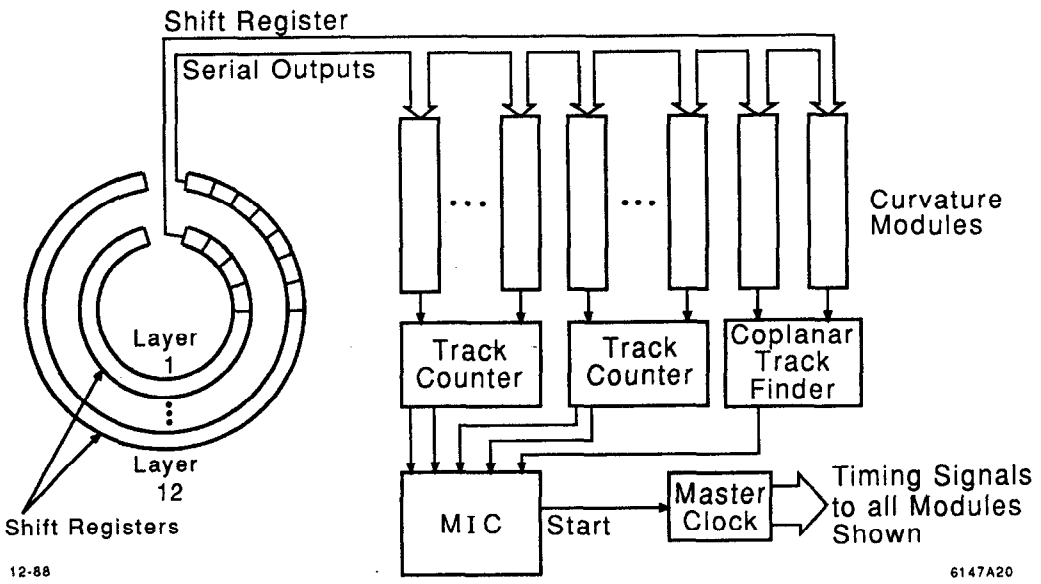

Figure 2–50 Block diagram of the charged particle trigger.

SSP-Based Software Trigger (SST)

The SST[80] was designed to improve upon the TED trigger by processing the energy information with programmable FASTBUS modules, the SLAC Scanner Processors (SSP's).[55] This provided a great deal of flexibility in optimizing the trigger algorithms compared to a hardware trigger. The calorimeter information is read into LeCroy 1885N FASTBUS ADC's and then summed into clusters by the SSP's. The trigger algorithms can then sum this information into towers which point back toward the IP and compare the results to expected patterns to make the trigger decision.

Cosmic Trigger

The cosmic trigger is used to identify cosmic ray events either between beam crossing or during dedicated cosmic ray runs. These events are useful for detector studies such as those previously discussed in the chapter. The events can be selected with either the normal charged trigger or by the Coplanar Track Finder (CTF) which is designed specifically to look for back-to-back tracks. The CTF uses two curvature modules to estimate the azimuthal angle of the track and returns a positive result to MIC if the tracks are within about ~11° of each other.

Random Trigger

Finally, there is a random trigger to select and record events on random beam crossings. This aids in monitoring the beam-related backgrounds and including their effects in the Monte Carlo detector simulation.

2.2.9 Data Acquisition System

The data acquisition system of the Mark II[51] reads the data from each of the detectors systems through CAMAC and FASTBUS systems and sends it to the VAX 8600 host computer. The on-line programs running on the VAX then merges the data records and stores them in the appropriate order onto magnetic tape. The VAX is also responsible for environmental and performance monitoring of parts of many detectors. The CAMAC system reads out a variety of instrumentation modules and the BADC's.[75] The FASTBUS system reads out through a master SSP[55] which controls the SSP's placed in each FASTBUS crate for reading out the TDC's or FADC's in that crate.

The data acquisition system is operated for each bunch crossing of the SLC. This introduces no dead-time because of the low 120 Hz repetition rate of the SLC. If a trigger detects a valid event, the data acquisition system reads out the CAMAC system and starts the read-out process of the FASTBUS system.

Chapter 3

Monte Carlo Simulation

In order to extract results about the physical processes underlying observed data, a Monte Carlo simulation is employed. Specifically, in the following analyses the Monte Carlo will be used to calculate the efficiencies for the tagging algorithm and the relations between the observed and the produced (or corrected) multiplicity. The Monte Carlo can be divided into two equally important parts: the models which generate the four-vectors of the particles from the electron-positron annihilation, and the algorithms for simulating the effects of the detectors in which we observe the tracks.

3.1 Electron-Positron Interaction Overview

The process through which hadrons are produced in electron-positron annihilation can be divided into a number of distinct processes, illustrated in Figure 3–1. The first process is initial state photon radiation, which affects the amount of energy available in the following annihilation. The probability of a hadronic event with a radiated photon of a given energy is the product of the probability to radiate a photon of that energy and the probability to produce a hadronic event at the reduced center of mass energy. At the Z^0 pole, initial state radiation is suppressed because the cross section is lower on either side of the pole. Above the Z^0 pole, however, this effect enhances the radiation such that many

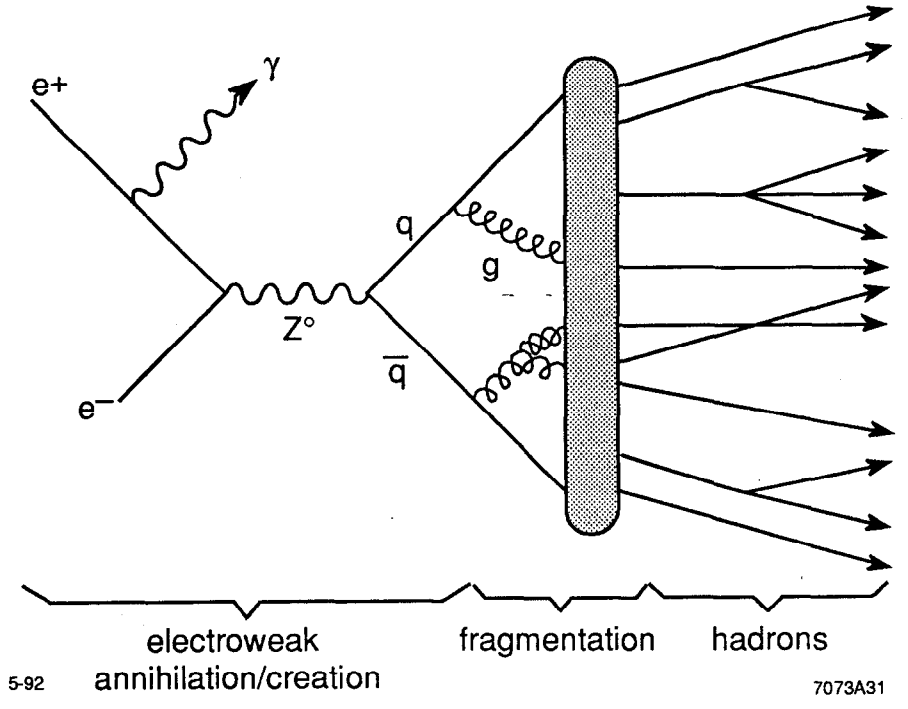

Figure 3–1 Schematic illustration of an e^+e^- annihilation event.

events will radiate the amount of energy required to reduce the center of mass energy to the Z^0 mass.

The annihilation of the electron-positron pair into the Z^0, and its decay into a quark pair is of course governed by the electroweak force. As discussed in Chapter 1, this process is calculable and has been studied in detail.

The radiation of gluons from the initial quarks and the conversion of these quarks and gluons into hadrons is dealt with in the fragmentation process. For reasons discussed in Section 3.2, this process is not calculable. Consequently one must employ physically-motivated models to handle the hadronization process.

Some of these produced hadrons decay via electromagnetic, weak or strong processes. Of particular importance in this analysis is the weak decay of the bottom and charm flavor hadrons, such as $B \rightarrow D + X$ which is discussed further in Section 3.3. Finally, the particles are observed in the detectors.

3.2 Fragmentation Models

The methods which are employed to calculate the effects of the strong force vary depending on the energy of the quarks. At high quark energies, the strong coupling constant, α_s, is much less than unity. For instance at the Z^0, the Mark II has

measured α_s to be $0.123 \pm 0.009 \pm 0.005$.[81] The consequence of this for perturbative calculations is that the effects of the increasingly complicated and numerous diagrams with more gluon vertices will tend to yield smaller corrections as the order of the diagrams in α_s increase. Thus, in principle, the calculations may be terminated at the order for which yields the accuracy desired. In practice, however, this calculation becomes extremely complex with the increasing order of α_s, and presently only those diagrams up to $O(\alpha_s^2)$ have been calculated.[82]

At lower energies, around 1 GeV, the strong coupling constant becomes larger than unity. Consequently, the perturbative approach becomes useless, as each succeeding level of diagrams can produce corrections of the same order as the $O(\alpha_s)$ diagrams. These low energies are of critical importance, however, because it is here that the quarks and gluons hadronize. It is precisely to cope with this low energy regime that the models of fragmentation were developed. A number of different fragmentation models have been developed. Reference [83] reviews the present status of these models.

3.2.1 Lund Monte Carlo

For this analysis, we use the Lund Monte Carlo (JETSET version 6.3).[84] We have elected to use the parton shower model to generate the final state quarks and gluons, and string fragmentation to combine these into hadrons.

The parton shower model[85] is a QCD cascade model in which partons are produced in a quark-gluon shower analogous to an electromagnetic shower. A leading log approximation is employed to determine the 'branching' during the shower process. The final state at the end of the shower is mostly comprised of gluons. This model was introduced into the Lund Monte Carlo to better reproduce the behavior expected at energies higher than those of PEP and PETRA. At those energies, the 2-, 3- and 4-parton states produced by matrix element methods were generally regarded as sufficient, though some evidence pointed to the limitations of that approach.[86] The parton shower method generates showers by the three possible branchings: $q \to qg$, $g \to gg$ and $g \to q\bar{q}$ (see Figure 3–2). The probability for each of these branchings is given by

$$dP_{a \to bc} = \frac{\alpha_s(Q^2)}{2\pi} \frac{dm_a^2}{m_a^2} P_{a \to bc}(z)\, dz \qquad (3\text{-}1)$$

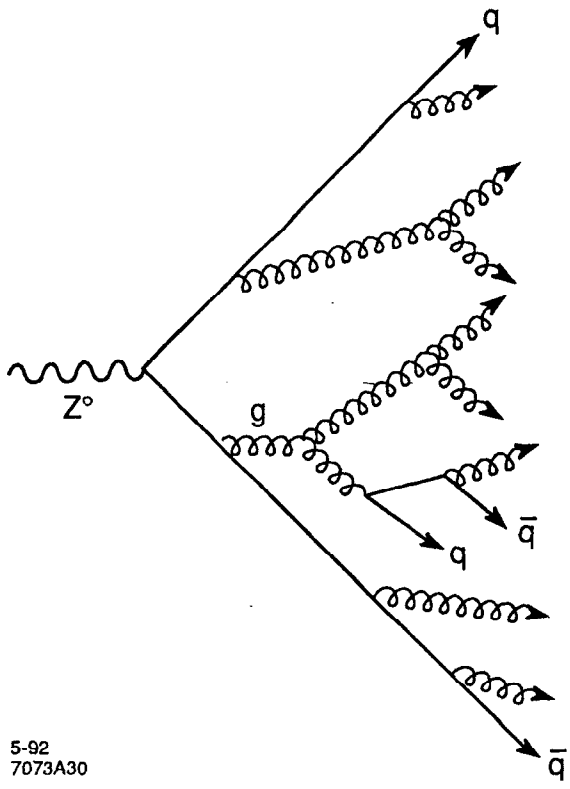

Figure 3–2 Parton shower evolution process.

where m_a is the mass of the parton a, z is the energy fraction E_b/E_a in the center of mass frame of the event, $Q^2 = z(1-z)m_a^2$ and α_s is calculated from the first-order expression:

$$\alpha_s(Q^2) = \frac{12\pi}{(33-2n_f)\ln(Q^2/\Lambda^2)}, \tag{3-2}$$

where n_f is the number of quark flavors and Λ is the QCD scale parameter.

The functions $P_{a\to bc}(z)$ are given by the Altarelli-Parisi splitting functions:[87]

$$\begin{aligned} P_{q\to qg}(z) &= \frac{4(1+z^2)}{3(1-z)} \\ P_{g\to gg}(z) &= \frac{6(1-z(1-z))}{z(1-z)} \\ P_{g\to q\bar{q}}(z) &= \frac{(z^2+(1-z)^2)}{2} \end{aligned} \tag{3-3}$$

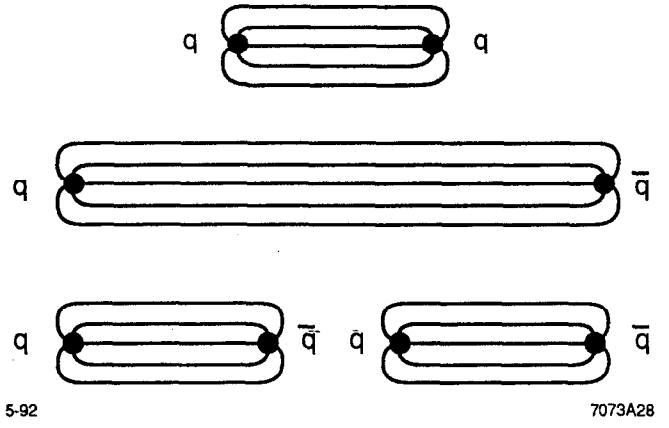

Figure 3–3 The color flux lines stretched between a pair of quarks until there is enough energy to produce a new quark pair from the energy of the color field.

In the leading log approximation, there is a coherence effect between Feynman diagrams which is equivalent to an angular ordering, meaning that the opening angle for a parton branching cannot occur an angle larger than that of the previous branching. The angular ordering is imposed as an additional constraint on the value of z and the masses.

The initial partons are produced substantially off-shell and the parton shower is continued until the virtuality of all of the partons reach a cut-off value which is fixed at m_{min} for gluons and $m_q + \frac{1}{2}m_{min}$ for quarks (where m_q is the constituent quark mass). Typical values of m_{min} are ~1 GeV.

Once the parton shower is finished, the partons are formed into hadrons using the Lund string fragmentation model.[88] String models are based on the idea that because of the coupling between gluons, the strong force flux lines between partons will tend to be close together, forming a narrow flux tube, or string. If this string is assumed to be uniform along its length, this leads to a potential which depends linearly on the length of the string. The energy density of the string, κ, is about 1 GeV/fm (0.2 GeV ^{2}). As the partons stretch the string, the energy stored in the string increases until it is sufficient to create a new quark-antiquark pair (see Figure 3–3). It is possible with the Lund model to have strings with additional gluons from the parton shower on the string connecting the quark and antiquark. Due to the momentum of these gluons, they will appear as kinks in the string connecting the quarks.

Baryons are formed either by production of diquarks[89] or by the popcorn mechanism.[90] In the former method, diquarks are allowed to be produced from a single breaking of the string. These diquarks can then combine with the quarks on the ends of the string to form baryons. The latter method involves the production of two or more $q\bar{q}$ pairs, of a different color than the $q\bar{q}$ on the end of the string, from which different combinations of baryons (B) and mesons (M), such as $B\bar{B}$, $BM\bar{B}$, $BMM\bar{B}$, *etc.*, can be formed. In practice, the probability for all but the first two combinations is very small in the Lund model. These baryon production models require numerous parameters, which characterize diquark production, strange diquarks, spin-1 diquarks, the relative probability of $B\bar{B}$ to $BM\bar{B}$, and strange quark suppression factors for the quarks which make of the meson, M, and the quark shared between the B and $\bar{B}$.

A string usually breaks when the quark and antiquark at each end of the string are about 1–5 fm apart. The quarks must be produced at a separation large enough such that the energy required to generate the quark's mass and transverse momentum is removed from the field. The quantum mechanical tunneling probability for the quarks to be produced with a particular transverse mass m_T is proportional to

$$\exp\left(-\pi m_T^2/\kappa\right) = \exp\left(-\pi m^2/\kappa\right)\ \exp\left(-\pi p_T^2/\kappa\right). \tag{3-4}$$

Locally the transverse momentum, p_T, is balanced between the $q\bar{q}$ pair. This equation also implies the suppression of heavy flavor production: strange quark production is reduced by a factor of about 0.3 while charm reduced by about 10^{-11} relative to the up and down quarks. Consequently, charm and bottom quarks do not participate in the soft fragmentation. In the Lund Monte Carlo, the generated parton p_T distribution is described by a Gaussian whose width, σ_0 is a tunable parameter. Similarly, the suppression of $s\bar{s}$ production relative to $u\bar{u}$ and $d\bar{d}$, and the production of pseudo-scalar to vector particles are also input parameters.

The longitudinal fragmentation is expressed in terms of the fraction of energy which the quark passes on to a meson. The Lorentz invariant variable used is chosen to be

$$z = \frac{(E+p_L)_{hadron}}{(E+p)_{quark}}, \tag{3-5}$$

where p_L is the momentum along the original quark direction. The probability of a quark pair to form a meson of transverse mass m_T with a particular value of z, is given by the Lund symmetric function,[91]

$$f(z) \propto \frac{1}{z} z^{a_1} \left[\frac{1-z}{z}\right]^{a_2} \exp\left[\frac{-bm_T^2}{z}\right], \tag{3-6}$$

where the a_i are quantities which may depend on the flavor of the quarks which together define the hadron and b as flavor independent. This form was developed in order to ensure a left-right symmetry so that the fragmentation process will yield the same results regardless of the end of the string chosen as the starting point. In practice, it is normally assumed that the a_i are the same

$$f(z) \propto \frac{(1-z)^a}{z} \exp\left[\frac{-bm_T^2}{z}\right]. \tag{3-7}$$

Thus, $f(z)$ depends only on two parameters (a and b). Note that this function $f(z)$ is not the probability of a primary hadron being produced in a particular event with a given z, but rather it is the probability used each time a string is broken producing a new quark pair. The former quantity, $D(z)$, is a combination of the $f(z)$ functions folded together according to the ordering along the string.

3.2.2 Heavy Quark Fragmentation

The large mass of the charm and bottom quarks compared with the light quarks requires that effects of flavor-dependent fragmentation be included in these events. Compared to light quarks, the fragmentation of heavy quarks is expected to be much harder, meaning that the distribution of energy carried away by the hadron containing the heavy quark favors larger values of z.[92] This hard fragmentation has been observed for both charm and bottom events at PEP and PETRA[42][93] and at LEP.[22][23][24][94][95] The most common parameterization for the probability of heavy hadrons being produced with a particular value of z is given by the Peterson function.[94] A phenomenological picture of the heavy quark fragmentation process of $Q \rightarrow H + q$, where $H = Q\bar{q}$ is illustrated in Figure 3–4. The Peterson function was derived on the assumption that the amplitude for this process is proportional the reciprocal of the energy transfer $\Delta E = E_H + E_q - E_Q$. If this is expanded in

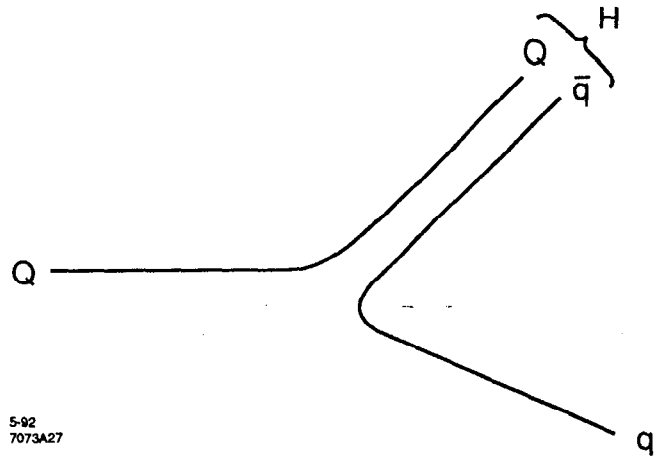

Figure 3–4 A phenomenological diagram of the fragmentation of a heavy quark, Q, into a hadron, H, and an antiquark.

terms of the particle masses, and a $1/z$ term is included to account for the effect of longitudinal phase space, then the result is:

$$D_Q(z) \propto \frac{1}{z\,[1-1/z-\varepsilon_Q/(1-z)]^2}, \tag{3-8}$$

where the parameter ε_Q is given by the ratio of the light to heavy quark transverse masses:

$$\varepsilon_Q = \frac{m_T^2(\text{light quark})}{m_T^2(\text{heavy quark})} \tag{3-9}$$

A plot of this function is shown in Figure 3–5. Because heavy quark production in soft fragmentation is almost entirely absent, the fragmentation probability function $f(z)$ is just the same as $D_Q(z)$, unlike for *uds* events.

A caveat which should be noted in the use of the fragmentation functions for heavy quarks is that there are two slightly different definitions of z (and ε) which can be used.[42] The definition by the Monte Carlo during the fragmentation is the primordial value of z:

$$z_{pri} = \frac{(E+p_L)_{hadron}}{(E+p)_{unfragmented\ system}}, \tag{3-10}$$

where the unfragmented system includes the heavy quark as well as other nearby quarks. The other definition is known as the reconstructed value, z_{rec}, and is

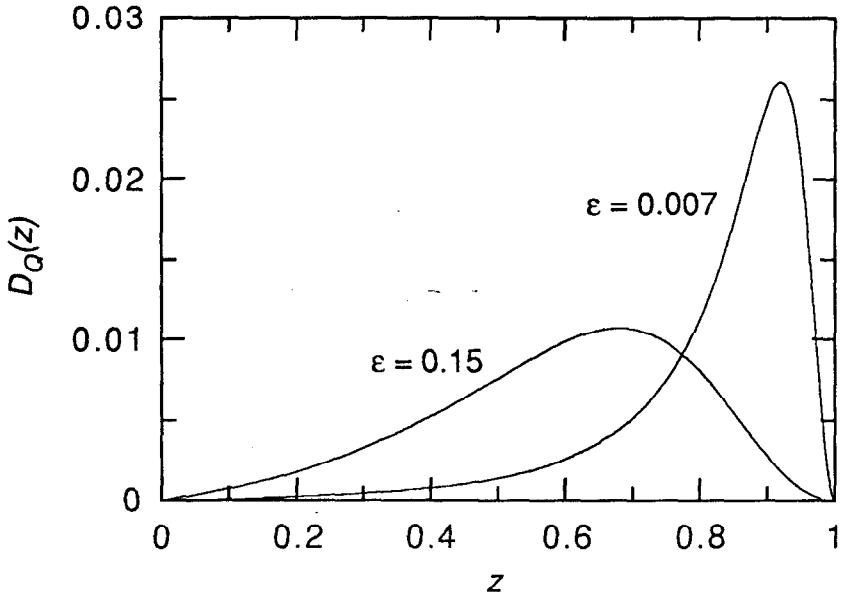

Figure 3–5 The Peterson fragmentation function for ε of 0.15 and 0.007, which yield an average z of 0.59 and 0.82 respectively.

defined by Equation (3-5). This value is favored for comparison among different experiments as it is model independent. Finally, it should be noted that the while the Peterson function is adequate for use as the input to the Monte Carlo, one should use caution when fitting (corrected) z_{rec} distributions for a number of reasons, including the possibility of events with a hard gluon having $z_{rec} > 1$, a feature which is not accommodated by the Peterson function.[6][42]

Guided with the results found by Chrin,[42] the values of ε_c and ε_b used by the Peterson function for describing the longitudinal fragmentation of charm and bottom quarks to hadrons are 0.15 and 0.007, when the parton shower model is employed. These correspond to averages of the Peterson function of 0.67 and 0.83, respectively. With these values as input to the Monte Carlo, the average values for the quantity $x_E = 2E_{had}/E_{cm}$ are $\langle x_E \rangle_c = 0.41$ and $\langle x_E \rangle_b = 0.68$.

3.2.3 Monte Carlo Tuning

The Lund Monte Carlo fragmentation parameters which are used in this analysis are the result of tuning the Monte Carlo with Mark II data at PEP (E_{cm} = 29 GeV), which if the Monte Carlo properly treat the energy dependency, are expected to be valid at the Z^0.[97] As illustrated in the following section, the Monte Carlo with this tuning is in fact a reasonable description of the data. More

recent high-statistics studies at LEP have shown no major sources of disagreement between various versions of the Lund Monte Carlo and their larger data sample.[102]

Table 3–1 gives a partial list of the parameters used in the Monte Carlo. Parameters not included in this table, such as the various baryon production parameters,* should be assumed to be the default parameters in JETSET version 6.3.[84]

3.2.4 Hadronic Event Properties

Using the 528 event sample recorded by the Mark II in 1989, the global properties were studied and it was found that a Monte Carlo with this tuning is a good model for describing the data.[62][98] The events in these plots were selected with a standard set of cuts for selecting hadronic events which is described in Section 4.3. A small number of cuts were made on the tracks used, chief among them that the track have $|\cos\theta|$ of less than 0.82 and that the projection of momentum in the plane perpendicular to the beam axis be at least 300 MeV/c. Two useful event shape parameters are the thrust and sphericity. The thrust, T, is defined as

$$T = \max\left(\frac{\sum_i \vec{p}_i \cdot \hat{T}}{\sum_j |\vec{p}_j|}\right), \tag{3-11}$$

where $\hat{T}$ is the unit vector which maximizes the sum of its dot product with each of the track momenta. The sphericity, S, is a similar quantity, except that it is quadratic in momentum. It is defined as

$$S = \frac{3}{2}\min\left(\frac{\sum_i |\vec{p}_i \times \hat{S}|^2}{\sum_j |\vec{p}_j|^2}\right), \tag{3-12}$$

where the unit vector $\hat{S}$ minimizes the momentum sum. Figure 3–6 shows the agreement of the thrust and sphericity distributions between the data and Monte Carlo for the 1989 Mark II data sample. In addition to the Monte Carlo model used in this analysis (Lund 6.3) these show, for comparison, the results of other Monte Carlo models: the Weber 4.1,[99] the Caltech-II 86[100] and Lund's JETSET 6.3 using a matrix element parton generation.[84]

* The baryon production parameters are in PAR(1) through PAR(7) in COMMON LUDATE.

	Name	Description	Variable name	Value
Lund Parton Shower	Λ_{LLA}	QCD scale	PARE(21)	0.4 GeV
	m_{min}	virtuality cut-off for further parton evolution	PARE(22)	1.0 GeV
Lund String Fragmentation	$\sigma_o(p_T)$	width of parton p_T distribution	PAR(12)	0.23 GeV/c
	P(*s*)/P(*u*)	$s\bar{s}$ suppression relative to $u\bar{u}$ and $d\bar{d}$	PAR(2)	0.30
	$\left.\frac{V}{PS+V}\right\|_{u,d}$	fraction of vector *u* and *d*-flavor meson production	PAR(8)	0.50
	$\left.\frac{V}{PS+V}\right\|_{s}$	fraction of vector *u* and *d*-flavor meson production	PAR(9)	0.60
	$\left.\frac{V}{PS+V}\right\|_{c,b}$	fraction of vector *u* and *d*-flavor meson production	PAR(10)	0.75
Lund Symmetric Fragmentation Function (*uds*)	*a*	*uds* fragmentation parameter	PAR(31)	0.45
	b	*uds* fragmentation parameter	PAR(32)	0.90
Peterson Fragmentation Function (*c* and *b*)	ε_c	*c* fragmentation parameter	PAR(44)	0.15
	ε_b	*b* fragmentation parameter	PAR(45)	0.007

Table 3–1 Some of Lund Monte Carlo (JETSET version 6.3) parameters used in this analysis. The variable name refers to the location of this variable in the Lund programs LUDATE and LUDAT1 common blocks[84].

The more detailed jet structure of the events can be investigated with jet finding algorithms such as the JADE clustering algorithm (YCLUS).[101] This algorithm starts with each of the tracks being considered to be a jet and then combines them, beginning with the pairs that will yield the smallest value of the parameter $y \equiv m_{ij}/E_{vis}$, the ratio of the invariant mass to the total visible energy. This process continues until all pairs have y larger than some value y_{cut}. For a range of y_{cut}

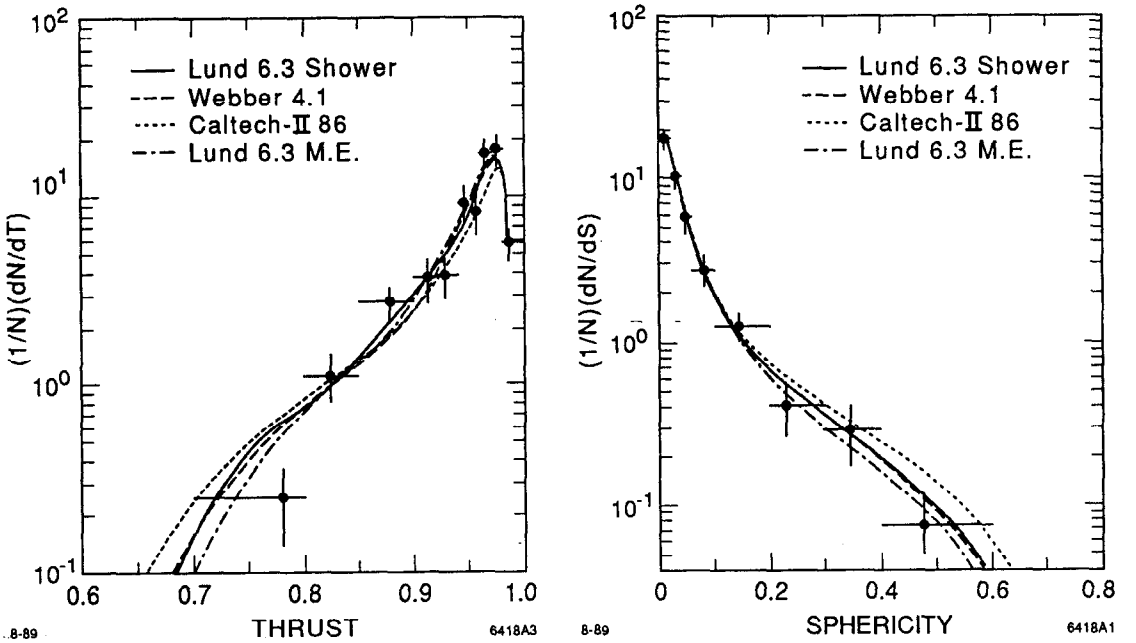

Figure 3–6 Corrected distributions of the thrust and sphericity for the events in the 1989 data sample.

values, the fraction of events with a given number of jets can be calculated and compared between data and Monte Carlo, as is shown in Figure 3–7(a). Another method of using this algorithm is too look at the value of y at which the event forms only two jets. The resulting differential distribution, $D_2(y)$, is illustrated in Figure 3–7(b).

Inclusive track distributions can also be investigated. The detected charged multiplicity distribution is shown in Figure 3–8. The distribution of the fraction of tracks with $x = 2p/E_{cm}$ is shown in Figure 3–9. The momentum projected into the plane perpendicular to the sphericity axis is another way to view the jet nature of the events. This momentum is shown in Figure 3–10 as the component in the plane of the event ($p_{\perp in}$) and that out of the plane of the event ($p_{\perp out}$).

These various plots, illustrating the global event properties, the jet production properties and the inclusive track properties, all confirm that within the statistics of this measurement, the Lund Monte Carlo tuned at PEP energies shows excellent agreement with that observed data at 91 GeV.

3.3 Heavy Hadrons in the Monte Carlo

As noted in Table 3–1, charm and bottom mesons are produced from Z^0 in the ratio of 3:1 vector (D^* and B^*) to pseudoscalar (D and B). With a B^*–B mass

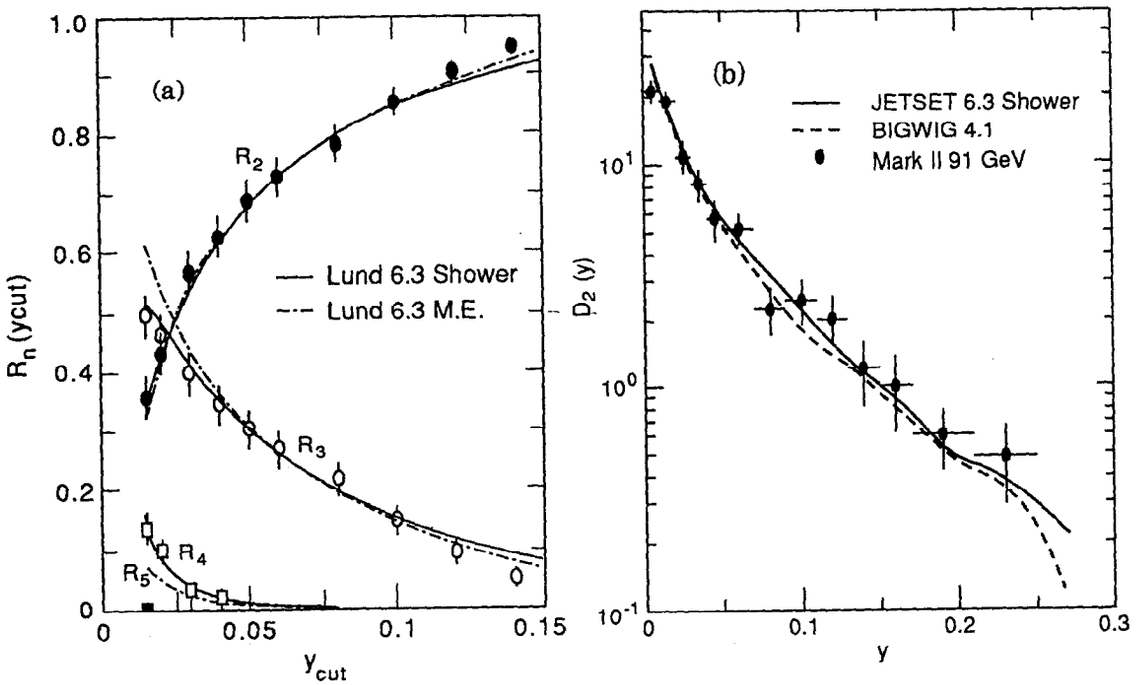

Figure 3–7 Jet distributions: (a) integral distribution of the number of events as a function of y_{cut}, and (b) the differential distribution of the y value for which an event goes from 3 to 2 jets.

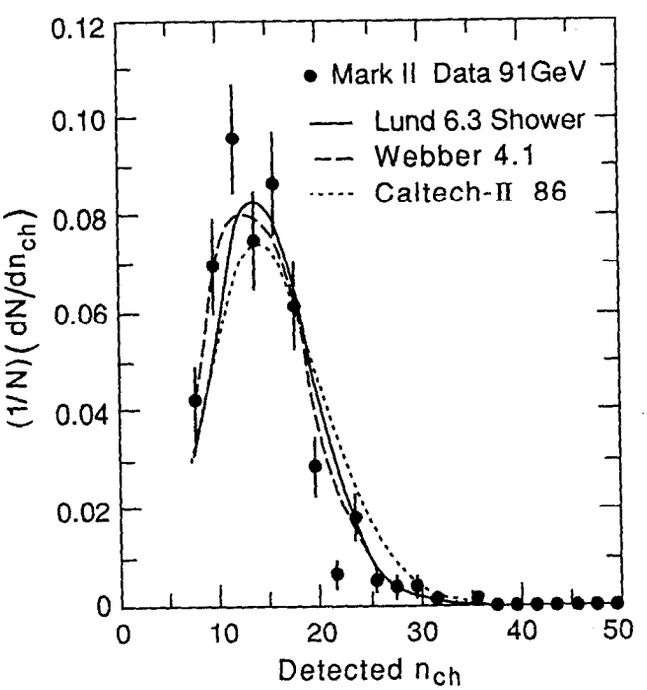

Figure 3–8 Distribution of the number of detected tracks per event passing the fiducial cuts observed in the data and as predicted by several Monte Carlo models.

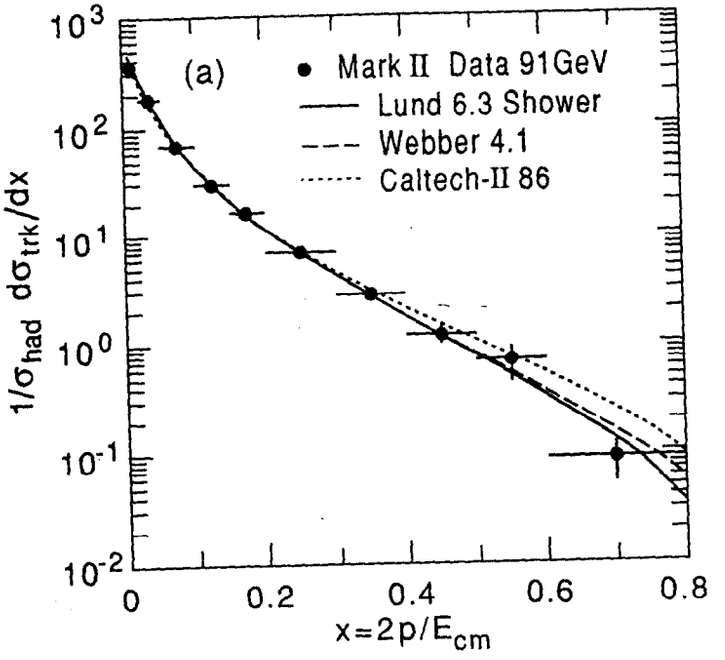

Figure 3–9 Distribution of the scaled momentum.

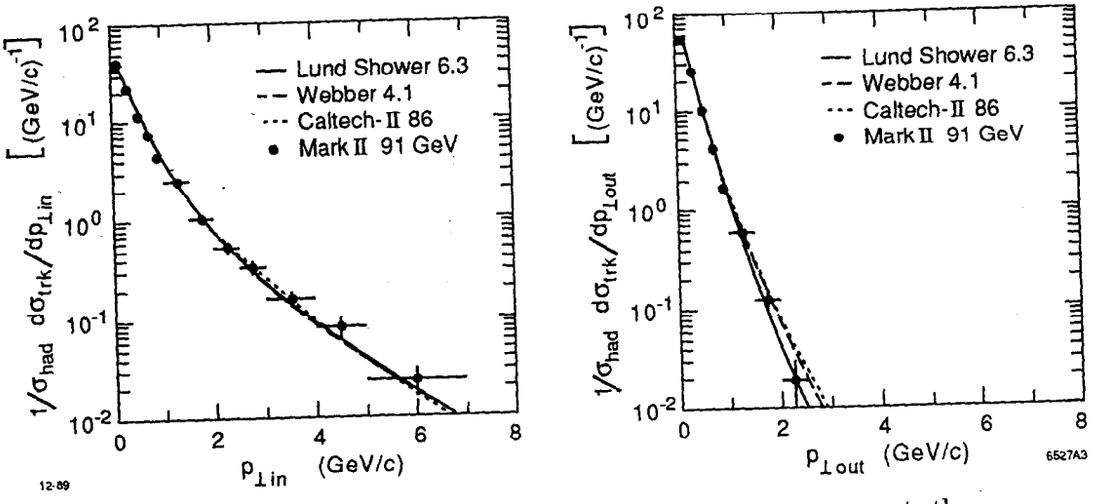

Figure 3–10 The two projections of the momentum transverse to the sphericity axis: the projection in and out of the event plane.

difference of ~50 MeV, the B^* mesons all decay electromagnetically to a B meson.[8] The D^* mesons decays both hadronically and electromagnetically, however the possible hadronic decay modes are different for neutral and charged D's:[8]

$D^{*0} \to D^0 \gamma$	45±6%	$D^{*+} \to D^+ \gamma$	18±4%
$D^{*0} \to D^0 \pi^0$	55±6%	$D^{*+} \to D^+ \pi^0$	27.2±2.5%
$D^{*0} \to D^+ \pi^-$	not allowed	$D^{*+} \to D^0 \pi^+$	55±4%

Note that the D^{*0} is not allowed, by conservation of energy, to decay into the charged pion. This results in an asymmetry of the produced charged and neutral D mesons, despite the fact that the mesons are produced in equal numbers of charged and neutral varieties. All other excited hadrons such as the heavy strange mesons, D_s^* and B_s^*, and spin $\frac{3}{2}$ baryons are decayed to the ground state mesons electromagnetically by the Monte Carlo. The ground state heavy strange mesons comprise 13% (12%) of all heavy flavor baryons for charm and bottom mesons, respectively. The heavy flavor baryons comprise 9% of the heavy hadrons for both charm and bottom.

The Monte Carlo then decays the ground state heavy flavor hadrons weakly by the emission of a virtual $W^{\pm}$ boson. The simplest diagram for the decay of heavy hadrons is the spectator diagram shown in Figure 3–11. The lifetimes for the various charm hadrons has been well measured for each type:[8]

$\tau(D^0) = 0.421 \pm 0.010$ psec	$\tau(D^+) = 1.062 \pm 0.028$ psec
$\tau(D_s) = 0.445^{+0.035}_{-0.029}$ psec	$\tau(\Lambda_c) = 0.191^{+0.017}_{-0.013}$ psec

These lifetimes vary quite significantly, a fact which is not predicted by the spectator model. These lifetime differences are believed to arise from interferences between diagrams and diagrams with interactions involving the spectator quark such as annihilation and W-exchange. The Monte Carlo generation used values equivalent to these, with the exception of the Λ_c whose lifetime was 0.10 psec.

The situation is different in the case of average bottom hadrons. The lifetime of the admixture of bottom hadrons produced at PEP, PETRA and LEP has been reasonably well measured,[8][25] but considerably less constraint exists for the separate species of bottom hadrons.* Hence, the Monte Carlo decays all of the bottom hadrons with the same lifetime given by the average bottom hadron

* The present status of the separate B lifetime measurements is discussed in more detail in Section 6.3.1 on page 180.

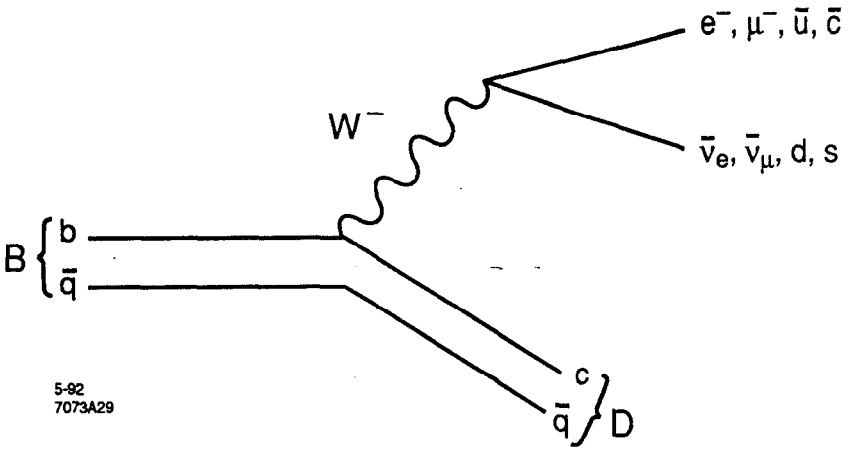

Figure 3–11 The spectator diagram for the decay of a hadron containing a heavy quark (in this example *b*) into a W^- which in turn decays into a charged-lepton and neutrino or a quark-antiquark pair.

lifetime. This is not expected to be a cause for concern as the lifetime difference among the bottom hadrons is expected to be significantly less than that observed for charm hadrons. We use a value of 1.24 psec in the Monte Carlo generation.

The weak decays of the charm and bottom hadrons in the Monte Carlo are handled somewhat differently. The decays of the D^0 and $D^{\pm}$ are handled primarily through explicit decays which have been measured or are good educated guesses of the correct branching fractions. The other charm and bottom baryons are decayed to quarks via a V – A matrix element, and then the resulting quarks are allowed to fragment like a jet system. For semileptonic decays it is assumed that the spectator system always collapses into a single hadron.

3.4 Detector Simulation

In order to relate the physical parameters of interest to the observed data, a detector simulation is employed. This allows one to study the effects of these parameters on events which are similar in nature to those we observe with the actual detectors. This detector simulation follows the generated tracks through the detectors and leaves hits at the appropriate locations. The tracking detectors are divided into layers for the detector simulation, corresponding to the material and measurement locations in each apparatus. As a particle enters each layer, probabilities are calculated for it to interact with the material in that layer and to generate a detected hit there. The effects included in this manner are multiple Coulomb scattering, nuclear scattering, energy loss, photon conversions and the

efficiency for a hit to be generated. In each of the detectors, the simulation allows all of the same reconstruction code to be used on the Monte Carlo events as is used the real data events. In the DCVD, for instance, the FADC data is simulated by placing hits from a large library of detected hits at a position determined using an inverse of the measured time-distance relationship. Nearby hits will have their pulse height information summed together. The SSVD uses a Landau distribution to determine pulse heights in each strip, accounting for the track angle. Effects such as diffusion between strips, Gaussian noise and strip-to-strip coupling are also included.

Additionally, the beam-related backgrounds observed in the data were added to the detector simulation. To do this, a set of events which were recorded by a random trigger were selected by requiring that they be near in time to a recorded Z^0 event. The raw hits in these random events were then 'mixed' onto the hits generated for tracks by the Monte Carlo. In the CDC, all of the recorded hits in Monte Carlo and background data events were combined. Closely spaced hits in a CDC jet cell were treated using the measured double-hit efficiencies to decide whether the latter hit is found. The latter hit time resolution is also degraded depending on its proximity to the prior hit. For the DCVD and SSVD, the inclusion of backgrounds was performed by adding the pulse heights of the generated Monte Carlo event and random event. In the DCVD this pulse height addition was done on a bin-by-bin basis through all of the FADC record. Similarly, for the SSVD, the pulse heights from each strip in the background event were added to the appropriate strip in the Monte Carlo event.

In the SSVD, the effects of uncertainty in the local and global alignment are also included in the detector simulation. This uncertainty is a result of alignment process which used the limited sample of hadronic tracks.* Incorporating these uncertainties into the Monte Carlo was accomplished by running the same alignment routines on Monte Carlo event samples of the same number of events as our data sample. The resulting imperfect alignment constants were then used in the track reconstruction code for the Monte Carlo events.

A significant improvement to the detector simulation was made by the implementation of a better model for multiple Coulomb scattering in the detector simulation. The original method would change the particle's direction as it passed through each scattering layer according to a Gaussian distribution whose width was

* See Section 2.2.4.4 on page 77 for information on the SSVD alignment.

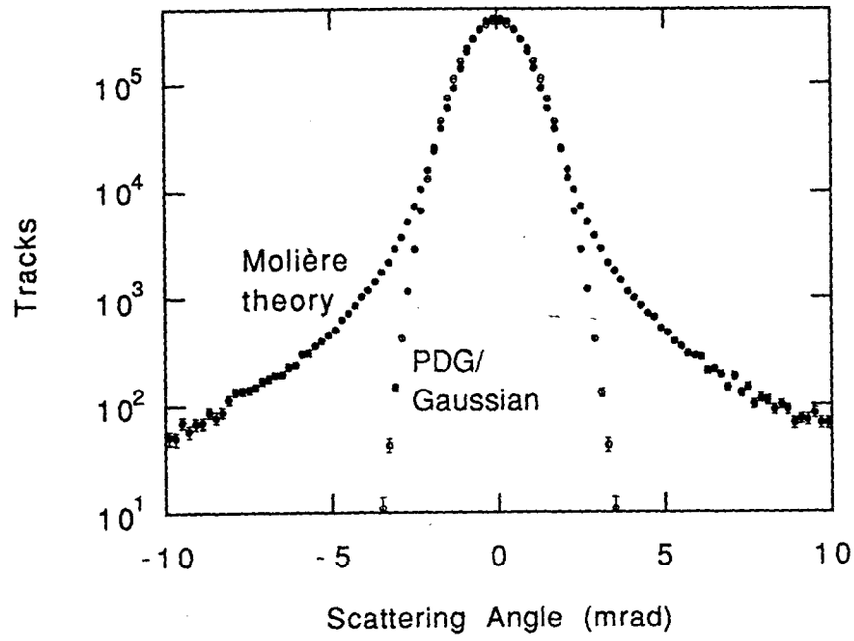

Figure 3–12 The multiple scattering angle distribution for the Molière theory as calculated by the subroutine MLR, and a Gaussian assumption using the Particle Data Group's Equation (3-13) as the width of the distribution. This particular example is calculated for a pion of momentum 1 GeV/c which is normally incident on 500 μm of silicon (which corresponds to 0.53% of a radiation length).

specified, in limit of small angle scattering, by the standard multiple scattering formula as given by the Particle Data Group:[103]

$$\Phi_{ms} = \frac{13.6\text{MeV}}{\beta cp}\sqrt{\frac{x}{X_0}}\left[1 + 0.038\log\frac{x}{X_0}\right], \qquad (3\text{-}13)$$

where x is the material thickness and X_0 is the radiation length of the material.*

There are two problems with this approach. First, the scattering layers in the Monte Carlo detector simulation can be comprised of very little material, such that it can be below the range of the validity of the standard formula ($10^{-3} < x/X_0 < 100$ for all Z). Second, this method does not properly introduce the tails from occasional large-angle scatters (plural and single scattering) which are actually present in the multiple scattering process. To do this, the Molière scattering theory[104] was employed using the MLR subroutine in the CERN Program Library (CERNLIB).[105] Figure 3–12 compares the predicted multiple scattering angle

* See Section 4.1.3 on page 116 for more information on multiple Coulomb scattering and the use of this equation.

distribution for a track passing through a particular scattering layer using a Gaussian formula and using the Molière scattering theory. The effects of this change on the track measurement will be discussed further in Section 4.5.2, "Multiple Scattering-Limited Resolution," on page 138.

Chapter 4

Tracking System Performance

In order to extract results from the observed data it is essential to accurately model the detector in the Monte Carlo, which requires that the performance of the detector elements be well understood. Of particular concern for the subsequent analyses is the tracking detector system, namely the CDC, DCVD and SSVD. This chapter contains a study of the performance of the combination of the three tracking detectors. The performance of the detectors individually was discussed in Chapter 2.

The tracking system characteristics of primary importance in the following analyses are the

- impact parameter resolution, and
- track finding and reconstruction efficiency,

both of which are addressed in this chapter. The impact parameter resolution is of primary importance for determining the efficiency and purity of the enrichment method used for selecting $Z^0 \to b\bar{b}$ events. This method, the impact parameter significance tag, is discussed in Chapter 5 and its application to measure the hadronic branching fraction of the Z^0 to $b\bar{b}$ events in Chapter 6. The tracking efficiency is also important, particularly for the multiplicity measurements described in Chapter 7.

4.1 An Introduction to Track Impact Parameter

The *impact parameter* of a track is the distance of closest approach to some reference point, namely the distance perpendicular from a track's trajectory. In this case the reference point is the interaction point (IP) where the e^- and e^+ beams nominally collide.

4.1.1 Impact Parameter Definition

If a particle created at the IP lives for a time t, its decay length is then given by $l = \gamma\beta ct$, where $\beta = v/c$ (the particle's speed relative to the speed of light) and $\gamma = E/mc^2$ (the particle's energy divided by its mass). If this particle decays, then the impact parameter of the daughter with respect to the IP, as projected into the plane perpendicular to the beam axis (the xy plane), is given by

$$b = l\sin\psi\sin\phi = \gamma\beta ct\sin\psi\sin\phi. \quad (4\text{-}1)$$

In this equation, ϕ is the polar angle from the beam axis and ψ is the angle of the daughter direction with respect to that of the parent, as illustrated in Figure 4–1. Because the tracking detectors have primarily axial segmentation, in subsequent usage the terms 'impact parameter' (b) and 'decay length' (l) will refer to the projection of the three-dimensional lengths into the plane perpendicular to the beam axis.

An interesting feature of the impact parameter is that as the parent particle becomes highly relativistic, the impact parameter becomes insensitive to the parent particle's momentum. This is seen as the cancellation between the decay length,

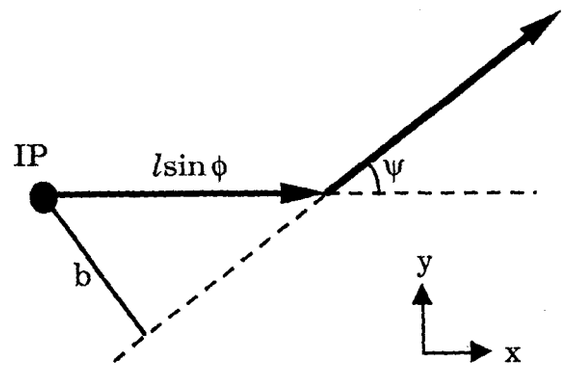

Figure 4–1 Definition of the variables involved in calculating impact parameters. The parent particle traveled a distance l and then decayed into a daughter which travels at an angle ψ from the parent's direction.

which increases with higher momentum, and the decay angle, which decreases with higher momentum. To illustrate this in the limit that the daughter particle's mass is small compared to its momentum in the parent's center-of-mass (CM) frame, consider a track which decays at an angle ψ_{cm} in the parent particle's CM frame. In the frame in which we observe the daughter particle, this corresponds to the angle ψ, given by

$$\sin\psi = \frac{\sin\psi_{cm}}{\gamma(1+\beta\cos\psi_{cm})} \; ; \; 0 < \psi_{cm} < \pi. \; ^{*} \tag{4-2}$$

This relation is a consequence of the fact that the daughter's momentum parallel to the parent's will be Lorentz boosted, whereas the transverse momentum is Lorentz invariant. Inserting this into the expression for b in Equation (4-1), the γ terms cancel, yielding

$$b \approx \frac{\beta ct \sin\phi \sin\psi_{cm}}{(1+\beta\cos\psi_{cm})} \approx c\beta t \sin\phi \tan\tfrac{1}{2}\psi_{cm} \; ; \; 0 < \psi_{cm} < \frac{\pi}{2}, \tag{4-3}$$

where the last expression is a further approximation assuming that $\beta \approx 1$ in the denominator.

The level to which the impact parameters of daughter tracks from B decays are insensitive to the B momentum at the Z^0 resonance can be seen in Figure 4–2. This figure shows, as a function of B hadron momentum, the average impact parameter divided by the proper decay length, $c\tau$, of the B hadron for all charged tracks from B decay. Also shown is the expected spectrum of B hadron momenta. Both of these were calculated by the LUND Monte Carlo at E_{cm} = 91 GeV.[†] From this example, one can see that at such high center-of-mass energy, the impact parameter of the daughter track is indeed only sensitive to the parent B hadron momentum for those tracks from the decay of the B's which received very little energy during the fragmentation process. Furthermore, because the fragmentation to B hadrons is quite hard, the number of tracks from these low momentum B hadrons is small. For example, only 23% of the tracks are from a B hadron of a momentum for which $\langle b/c\tau \rangle$ is below 0.9 of is high B momentum plateau.

* Equation (4-2) has been frequently noted without reference to the $p_{daughter} \gg m_{daughter}$ limit in the parent's rest frame. This may be a result of the fact that this has often been mentioned in the context of tagging leptons from B decay. In this case, a massless approximation is clearly valid for electrons due to their small mass, while the momentum spectrum, which will be harder for both muons or electrons than for hadrons from B decay, will further justify the equation's validity in semi-leptonic decays.

† See Chapter 3 for more information on the Monte Carlo used in this analysis.

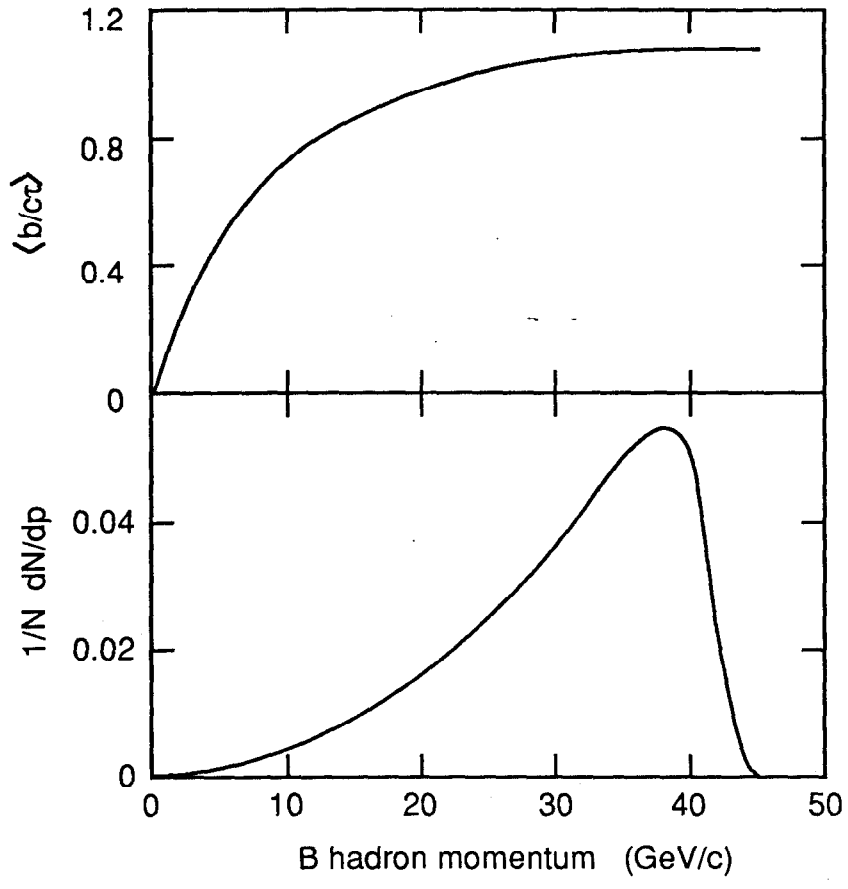

Figure 4–2 In the upper plot, the average of the impact parameter divided by the lifetime of the B hadron is shown as a function of the momentum of the B hadron. Below is the expected spectrum of B hadron momentum.

4.1.2 Impact Parameter Signing

Impact parameters can be made more useful if they are given an algebraic sign based upon the apparent origin of the track, particularly for heavy quark events. The sign applied will be negative if the track appears to come from behind the interaction point and positive otherwise. This definition is referred to as the *physically-signed impact parameter.* This method of applying an algebraic sign is useful because all of the B decay products are swept forward by the B's large boost into the hemisphere defined by the B direction for B hadrons with a momentum of at least 8 GeV/c. Because a majority of hadronic events have a general back-to-back jet nature, the first step is to determine the axis of the event, which approximates the direction of the original partons, as given by a event or jet axis. Since the event

axis is a good approximation for the B direction, the majority of the tracks from B decay will be given the same algebraic sign.

4.1.2.1 Event and Jet Axis Algorithms

The *thrust axis* is defined as the unit vector $\hat{T}$ which maximizes the thrust, T, defined as

$$T = \max\left(\frac{\sum_i \vec{p}_i \cdot \hat{T}}{\sum_j |\vec{p}_j|}\right), \tag{4-4}$$

where the sum of the momenta $\vec{p}_i$ is taken over all of the charged tracks. The value of the thrust varies from 0.5 in the case of a very isotropic event to 1.0 for an event with narrow back-to-back jets. A nice feature of the thrust axis is that because it depends linearly on momentum, it is *infrared safe*.[106] This means that the thrust will be unchanged if one particle decays into two collinear particles. This thrust axis can then be used to divide the event into two *thrust hemispheres* defined by the plane perpendicular to the thrust axis. In heavy quark events, the thrust axis approximates the direction of the heavy hadrons in the majority of the events. The angular difference between the thrust axis and the direction of the B hadrons is shown in Figure 4–3 as determined by the LUND Monte Carlo. It is seen that the thrust axis does reasonably approximate the actual B direction in most cases although there are broad tails. The source of these tails is primarily events in which either one or both of the B hadrons has fairly little energy, such as the case when a hard gluon has been radiated. This produces multi-jet events in which the B hadron momenta are not back-to-back and thus the thrust axis cannot accurately reconstruct the directions of both B hadrons.

The use of other event axes was also studied. In particular these were the sphericity axis and jet axes using two different algorithms: a scaled invariant mass algorithm[101] and a momentum cluster algorithm[107]. The sphericity axis unit vector $\hat{S}$ is defined by

$$S = \frac{3}{2}\min\left(\frac{\sum_i |\vec{p}_i \times \hat{S}|^2}{\sum_j |\vec{p}_j|^2}\right) \tag{4-5}$$

and, as it depends on the square of the momentum, will be more strongly affected by high momentum tracks. The value of the sphericity, S, will range from 0 for

narrow 2-jet events to 1 for events with an isotropic distribution of tracks. Unlike the thrust axis, it's quadratic dependence on the momentum means that it is not co-linear safe. Despite these differences, the sphericity axis yielded results which are virtually the same as those for the thrust axis.

The cluster algorithm YCLUS starts with each of the particles being considered to be a jet and then combines these, beginning with the pairs that will yield the smallest value of the parameter $y \equiv m_{ij}/E_{vis}$, the ratio of the invariant mass to the total visible energy. This process continues until all pairs have y larger than some value y_{cut} which typically ranges from 0.02 to 0.10. The LCLUS algorithm similarly begins with each particle being considered its own jet. It then combines these beginning with that pair with the smallest value of

$$D = \sqrt{\frac{2|p_i|^2|p_j|^2(1-\cos\theta_{ij})}{(|p_i|+|p_j|)^2}}, \tag{4-6}$$

until all of the jets are above a cut-off, D_{join}. This cut-off was tuned at E_{cm} = 30 GeV to be 2.5 GeV, and scales to a value of 7.9 GeV at 91 GeV.[62] Both of the jet algorithms more accurately reconstructed the B hadron direction than did

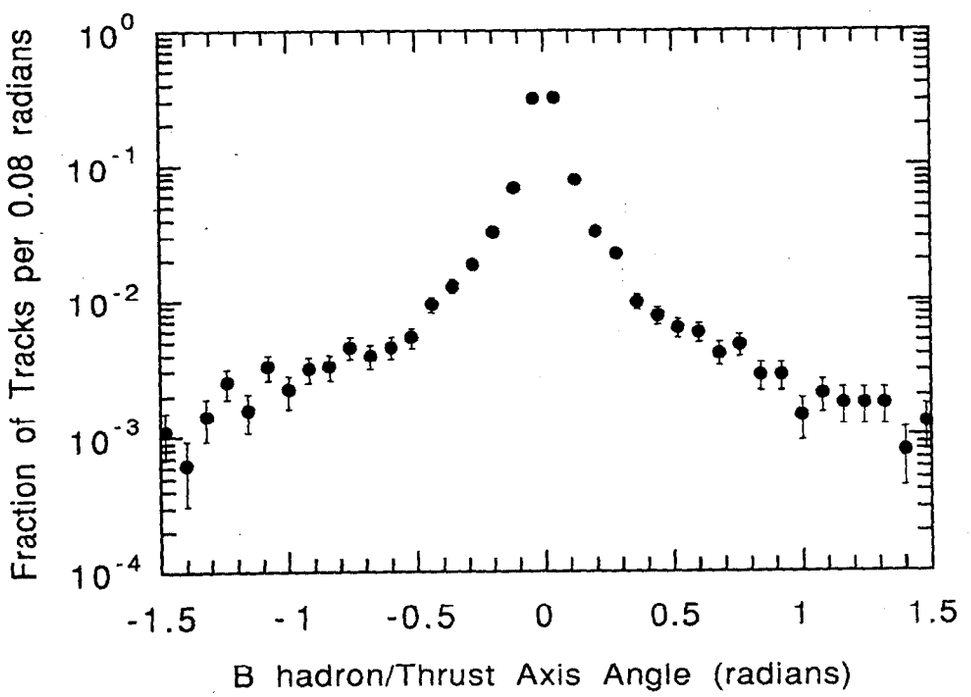

Figure 4–3 Angular separation between the thrust axis and the B hadron directions as determined by the Monte Carlo.

the thrust or sphericity axes. This is to be expected as a significant fraction of events have hard gluon radiation. However, these events retrieved from the tail of the B hadron direction/thrust axis distribution by using a jet algorithm will be those in which the B had fairly low momentum. As a result, the decay products will also have low momentum which will make them more difficult to use in identifying $b\bar{b}$ events and thus there is negligible change in the tag characteristics. (See the next chapter for a discussion of the tagging method.)

4.1.2.2 Determination and Analysis of the Impact Parameter Sign

The sign of the impact parameter is determined in the following manner: if the track crosses the thrust axis in the same thrust hemisphere as the track, then $b > 0$, otherwise $b < 0$. This is illustrated in Figure 4–4. This definition is useful because all of the B decay products are swept forward by the B's large boost into the hemisphere defined by the B direction for $p_B > 8$ GeV. Since the B direction is fairly well approximated by the thrust axis, the majority of the tracks from B decay will have $b > 0$.

Negative impact parameter tracks will come from a number of sources. In all types of hadronic events, the impact parameters of tracks from the IP will be smeared due to the finite resolution of the detectors. This will result in the typical Gaussian-like distribution around $b = 0$. There are also a number of other

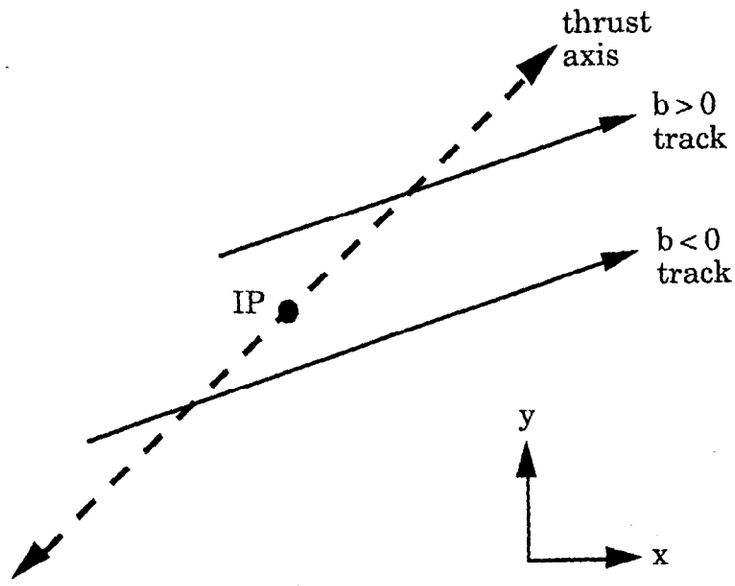

Figure 4–4 The method for assigning an algebraic sign to the track impact parameters using the event thrust axis is illustrated here.

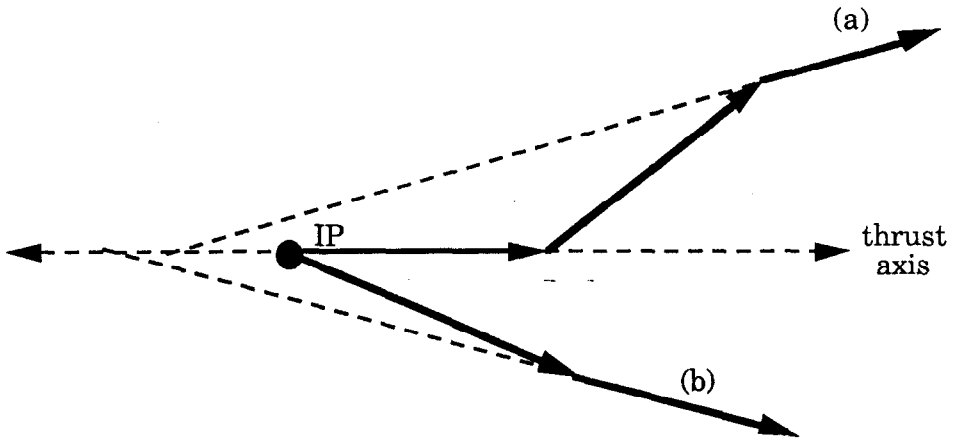

Figure 4–5 Some of the mechanisms for tracks from a long-lived parent being assigned a negative impact parameter when using the thrust axis to determine the sign: (a) tertiary decays, and (b) a misalignment between the thrust axis and the parent particle.

possibilities for generating negative impact parameter tracks particularly for tracks resulting from the decay of long-lived particles (bottom, charm and strange-flavored hadrons). As illustrated in Figure 4–5, these sources include:

- actual backward going tracks, which should be only a few, as most of the decay products will be swept forward along the parent's direction;
- secondary decays such as $B \rightarrow D \rightarrow X$ where the lifetime of the second generation particle (*i.e.* the D) allows the decay vertex at which the daughter X is produced not to lie on the B direction;
- instances in which the thrust axis and parent direction are not well aligned, for instance $b\bar{b}$ events with a hard radiated gluon or tracks from K_s^0 decay.

The level to which each of these contribute for the particles from B hadron decay at the Z^0 can be quantified using the Monte Carlo. Figure 4–6(a) shows the generated impact parameters with respect to the actual IP, for tracks from prompt B decay,* where the actual B-direction has been used to apply the impact parameter sign. Thus the only source of the negative impact parameter tracks are actual backward going decays which are indeed a small fraction (2.1%). A fairly small result is expected, because as pointed out earlier, only tracks from the few very low momentum B hadrons can decay into the hemisphere opposite the B direction. As shown in Figure 4–6(b), when all of the tracks from B decay are included, such as

* In this context, "prompt B decay tracks" are those tracks resulting directly from a B decay, and not from subsequent decays (of a D or K, for instance). This latter set of tracks will be referred to as the "non-prompt B decay tracks."

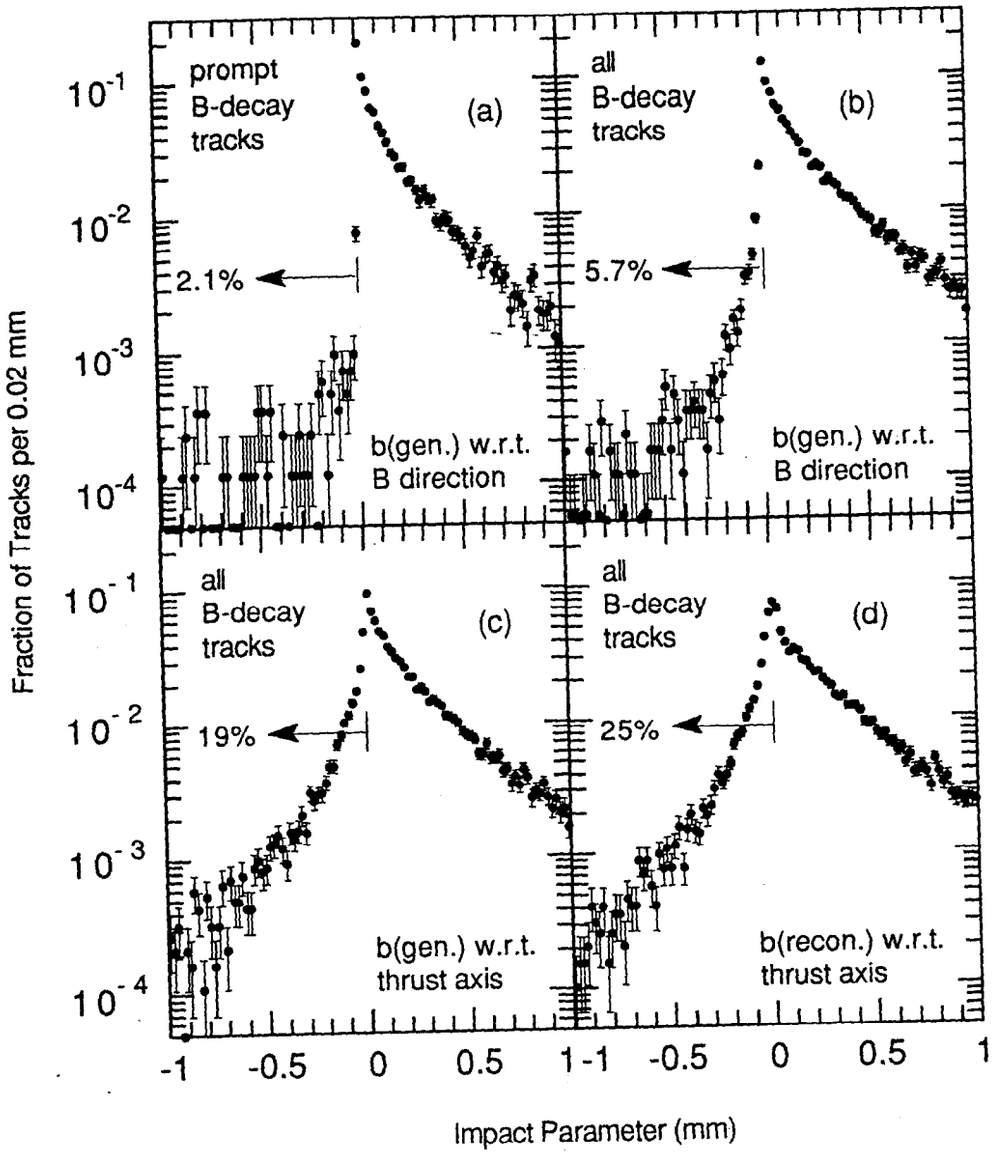

Figure 4–6 These plots illustrate the level that various effects contribute to producing negative impact parameters for tracks from B decay: (a) the impact parameters of the *generated* prompt B decay tracks using the B hadron direction to determine the sign; (b) impact parameters for all of the generated tracks from B decay (including tertiary decays such as $B \rightarrow D \rightarrow X$); (c) impact parameters of the generated tracks which are signed using the thrust axis; (d) the impact parameters of the *reconstructed* tracks, again using the thrust axis. The thrust axis used is that determined with the reconstructed tracks. The tracks used in these plots were all reconstructed by the tracking algorithms and are required to have passed a series of track quality cuts (see Section 4.4 on page 128).

tracks from a tertiary D decay vertex, the fraction of the tracks which are given negative impact parameters using the actual B direction is still small (5.7%), but slightly larger than the fraction in prompt B decay. This increase in the fraction of negative impact parameter tracks is the consequence of the fact that tracks from tertiary decay vertices may have negative impact parameters, as illustrated in Figure 4–5. To observe the effects of using the thrust axis instead of the B direction to sign the impact parameters, Figure 4–6(c) shows the generated impact parameters for all tracks from B decay, now using the thrust axis found with the reconstructed tracks. The effect is to double the fraction of tracks with negative impact parameters to 21%. Finally, the effect of detector resolution is included by using the impact parameter reconstructed with the tracking algorithms from the full detector simulation. The reconstructed impact parameter is also with respect to an IP which is determined for each event using a fit of these reconstructed tracks (see Section 4.2 on page 123). These detector effects show the level to which fluctuations of a track's impact parameters cause them to be assigned a negative impact parameter, as illustrated in Figure 4–6(d). The effect of the detector resolution produces slightly more $b < 0$ tracks, causing a total of 25% of the tracks from B decay to be assigned negative impact parameters. There is another interesting effect, which is the narrower central peak compared with the other distributions. This is an artifact of the use of the event-by-event fit IP, which will tend to pull towards the small impact parameter tracks which are included in the fit.

The effects of this impact parameter signing method on the different flavors of events is illustrated in Figure 4–7 which shows the distribution of reconstructed impact parameters. For *uds* events, this distribution has a generally Gaussian shape, with only slight tails from strange particle decays (K_s^0 and Λ). In contrast, $c\bar{c}$ events have a more asymmetric distribution due to the finite lifetime of charmed hadrons, although the positive tail is significantly larger for $b\bar{b}$ events owing primarily to their longer lifetime. Both of the heavy quark events have a significant fraction of their tracks which are from the primary vertex, such as those from fragmentation, which form a central core to the distribution.

4.1.3 Impact Parameter Resolution

Because of the finite resolution of any tracking detector, the measurement of the impact parameter for a track will have associated with it some level of uncertainty.

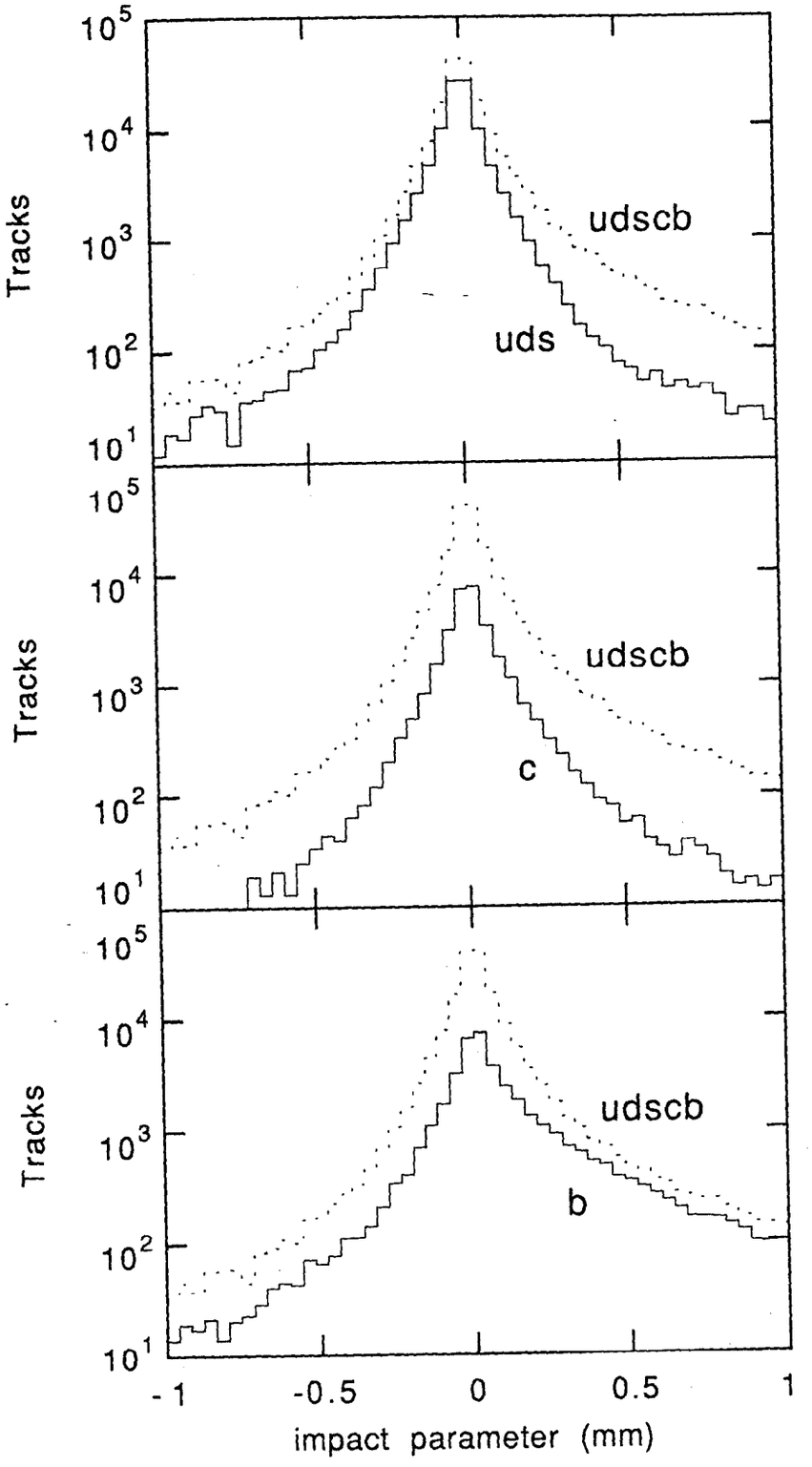

Figure 4–7 The reconstructed impact parameter distributions for different flavors of events as predicted by the Monte Carlo.

Understanding the impact parameter resolution function is important in order to properly model the detectors by the Monte Carlo simulation.

The impact parameter resolution has contributions from two primary sources: the resolution of the measured track extended to its point of closest approach to the IP, σ_{TR}, and the uncertainty in the actual interaction point, σ_{IP}, which is discussed in Section 4.2. The impact parameter resolution is thus related to the sum in quadrature of these two terms,

$$\sigma_b \propto \sqrt{\sigma_{TR}^2 + \sigma_{IP}^2}. \tag{4-7}$$

The uncertainty of the track measurement can be expressed in terms of two components, one which represents the intrinsic detector resolution, σ_{int}, and a second which accounts for the multiple Coulomb scattering of low momentum tracks, σ_{ms}. The resulting relation is

$$\sigma_{TR}^2 = \sigma_{int}^2 + \sigma_{ms}^2. \tag{4-8}$$

4.1.3.1 Intrinsic Resolution Term

For tracking detectors which are composed of a series of n equally spaced position measurements of resolution, σ_0, extending from an inner radius of r_i and to an outer radius of $L + r_i$ from the IP, the intrinsic resolution is given by

$$\sigma_{int} = \frac{\sigma_0}{\sqrt{n}} \sqrt{1 + 3\frac{n-1}{n+1}\left[\frac{L+2r_i}{L}\right]^2}. \tag{4-9}$$

One can see several trends from this expression which can in general be extrapolated to more complicated detector systems where such a straightforward expression can not as easily be obtained. First, the track resolution varies essentially as $n^{-1/2}$ which would of course be expected from statistics, so it is beneficial to have many position measurements. Second, the best resolution is achieved by minimizing the inner radius, r_i, and maximizing the lever arm, L.

Equation (4-9) is not valid for the entire detector system containing detectors of widely varying resolution and spacing, particularly with the advent of silicon vertex detectors which usually have only a few layers of very high position resolution. As is the case for the Mark II, when a silicon detector is used in conjunction with lower

resolution outer detectors one can imagine that the intrinsic resolution may roughly be expressed as

$$\sigma_{int}^2 = \sigma_0^2 + (r_0\sigma_\varphi)^2 \tag{4-10}$$

where σ_0 and r_0 are the average position resolution and radius of the silicon detector and σ_φ is the angular resolution of the outer tracking detectors which provide an accurate angular measurement for most tracks. As will be discussed latter, for very low momentum tracks, the best measurement of the angle is made within the SSVD itself.

4.1.3.2 Multiple Scattering Resolution Term

At low momentum, the measurement accuracy of a track is limited by the multiple Coulomb scattering as it passes through the material in the beam pipe and the detectors. If, as was the case in the past, the beam pipe and inner wall of the vertex detector were the dominant source of material, then the multiple scattering contribution to the track resolution would be

$$\sigma_{ms} = \frac{r_{pipe}}{\sin\theta} \cdot \Phi_{ms}(\vec{p}, x_{pipe}) \tag{4-11}$$

where, r_{pipe} is the beam-pipe/inner wall radius, θ is the dip angle to the beam axis and Φ_{ms} is the related to the width of the scattering angle distribution for a track of momentum $\vec{p}$ and beam pipe thickness of x_{pipe} (see Figure 4–8)

In general, this multiple scattering angular distribution is well described by the Molière theory which has been investigated in numerous papers[104] and is incorporated into the Monte Carlo detector simulation (see Section 3.4 on page 102). In order to develop some intuitive feel for the effects multiple scattering, an approximate formalism can be used. For small-angle scattering however, the angular distribution is roughly Gaussian in nature. Thus it has become commonplace to approximate the angular distribution as a Gaussian distribution of width Φ_{ms}. This width was first approximated as[108]

$$\Phi_{ms} = \frac{E_c}{\beta c p}\, z\sqrt{\frac{x}{X_0}}, \tag{4-12}$$

where E_c is a constant with units of energy, p, βc and z are the momentum, speed and charge of the particle, x is the material thickness and X_0 is the radiation length of the material. (A radiation length is defined as the "mean distance over which a high energy electron loses all but $1/e$ of it's energy by bremsstrahlung"[25] and very

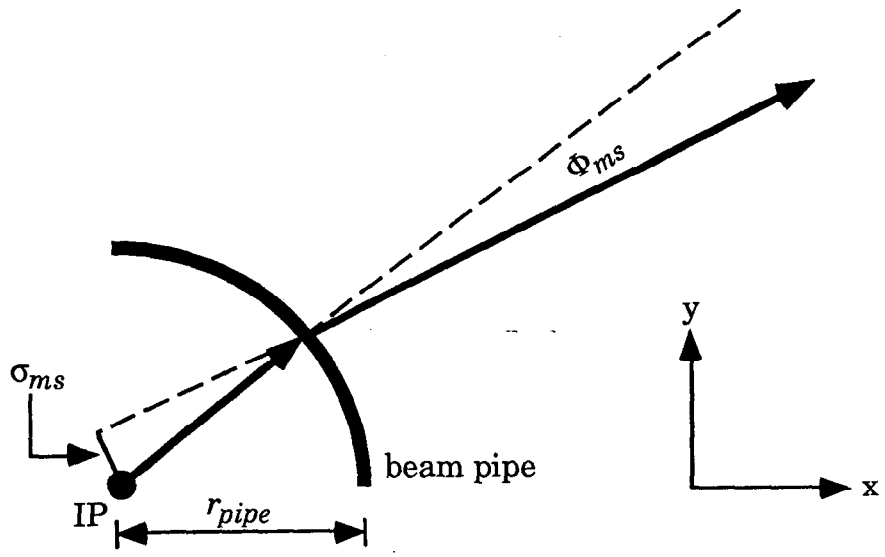

Figure 4–8 A simplified view of multiple scattering where the dominant source of scattering is the beam pipe/inner detector wall before the detectors. The amount of additional error in the measurement of impact parameter due to this scattering is the product of the rms scattering angle, Φ_{ms}, and the distance from the IP, $r_{pipe}/\sin\theta$ where θ is the dip angle.

roughly depends on the atomic number of the material from which the particle is scattering as Z^{-2}.)

Later it was shown that the width of the scattering angle distribution could be much better approximated by an additional dependence on the material thickness which led to a new formula:[109]

$$\Phi_{ms} = \frac{E_c}{\beta cp}\, z\sqrt{\frac{x}{X_0}}\left[1 + C\ln\frac{x}{X_0}\right]. \tag{4-13}$$

The most recent determination of the constants for Equation (4-13) has been done in Reference [110] and yields

$$\Phi_{ms} = \frac{13.6\text{MeV}}{\beta cp}\, z\sqrt{\frac{x}{X_0}}\left[1 + 0.038\log\frac{x}{X_0}\right] \tag{4-14}$$

Upon comparison to Molière theory, it is seen that this width is the same as the width of the central 98% of the Molière distribution to an accuracy of 11% for a range of scatterer thicknesses of $10^{-3} < x/X_0 < 100$ for all Z.

In the cylindrical geometry of the Mark II, the amount of material through which a track traverses varies with the polar angle as $x_0/\sin\theta$ where x_0 is the

thickness of that layer. Thus, the resulting contribution of the multiple scattering to the track extrapolation resolution can be written by substituting this last equation into Equation (4-11),

$$\sigma_{ms} = r_{pipe} \cdot \frac{13.6\text{MeV}}{\beta cp\,(\sin\theta)^{3/2}}\, z\sqrt{\frac{x_0}{X_0}}\left[1+0.038\log\frac{x_0/\sin\theta}{X_0}\right]. \tag{4-15}$$

This illustrates the general dependence of the multiple scattering term on the track momentum and direction,

$$\sigma_{ms}(p,\theta) = \frac{\sigma^{o}_{ms}}{p\,(\sin\theta)^{3/2}} \tag{4-16}$$

where the weak dependence of the logarithmic term on $\sin\theta$ has been ignored and it is assumed that $\beta \approx 1$.

4.1.3.3 Total Track Resolution

The Mark II tracking detector system is actually more complex than the models presented in the previous two sections, but the results of these models will provide some guidance when working with the real system. In particular, the track resolution is expected to have the form

$$\sigma^2_{TR} \approx \sigma^2_{int} + \left[\frac{\sigma^{o}_{ms}}{p\,(\sin\theta)^{3/2}}\right]^2 \tag{4-17}$$

which was derived assuming all of the scattering comes from the beam pipe or first measurement layer. In actuality, there is substantial scattering material throughout the detectors. Thus, the calculation of σ_{TR}, from the error matrix of the track, as determined by the track fitting programs (see Chapter 2) will be more complex than Equation (4-17). Different approaches are taken to include the effects of multiple scattering in this fit. In the CDC and DCVD, multiple scattering is accounted for both by allowing a kink in the track fit between the chambers and with a correction term to account for material in the tracking volume, as derived by Gluckstern[61]. This correction is not strictly valid in our case, as it is derived for detectors with equally spaced layers of equal spatial resolution, but it nonetheless works satisfactorily. In the SSVD, the multiple scattering is handled properly by its inclusion in the covariance matrix for the full track fit.[73]

Figure 4–9(a) shows the calculated track resolution at the distance of closest approach to the IP as a function of $[p\,(\sin\theta)^{3/2}]^{-1}$ for a collection of Monte Carlo

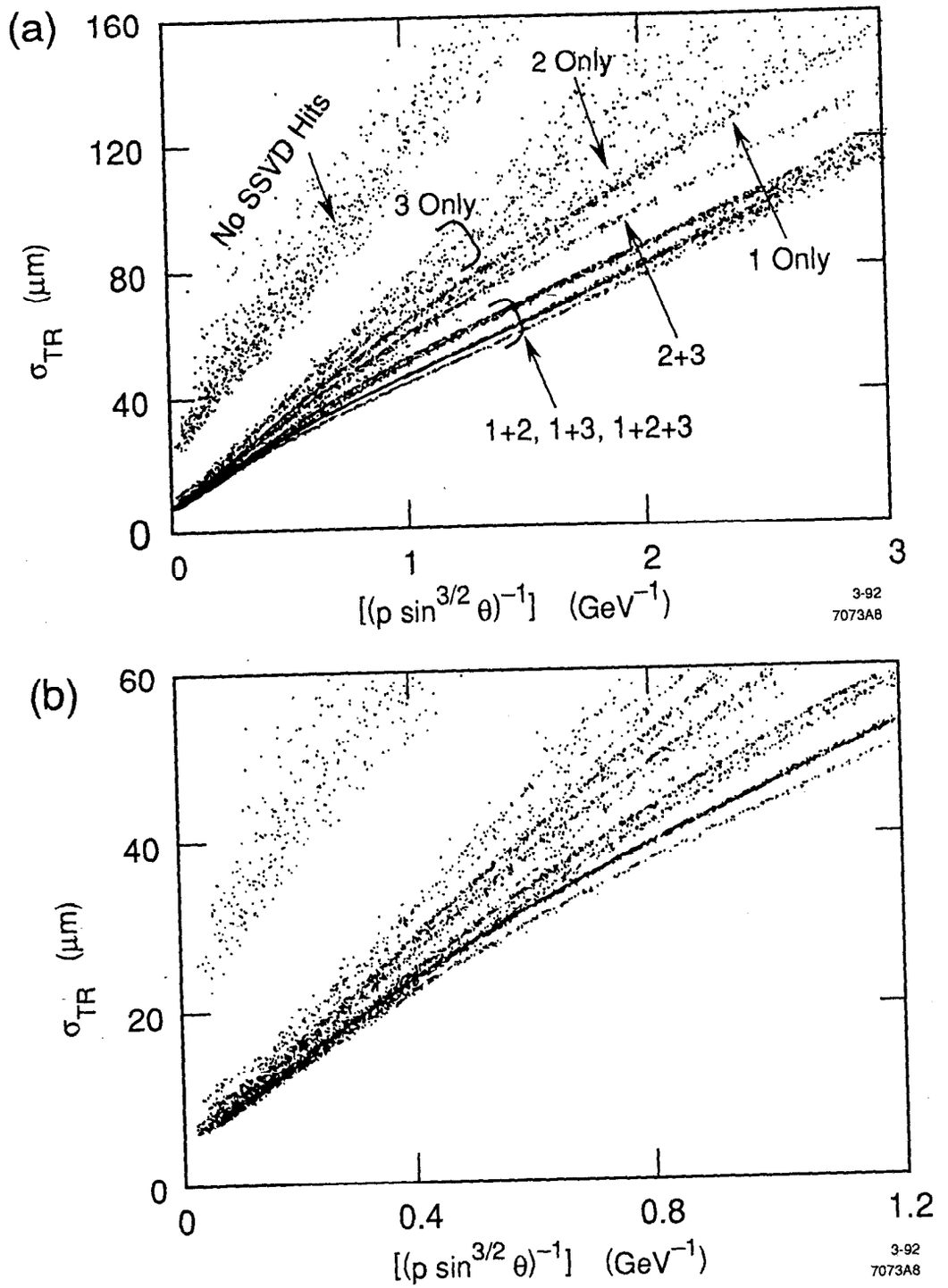

Figure 4–9 The calculated impact parameter resolution of the full CDC, DCVD and SSVD tracking system is shown as a function of the track momentum. These points were calculated for a collection of Monte Carlo tracks using the position measurements determined with data for each detector.

tracks using the position resolution measurements discussed in Chapter 2. The tracks included in this figure must have passed a general series of cuts, most importantly that there be at least 25 (15) position measurements in the CDC (DCVD). The tracks with no found SSVD position measurements are clustered in the upper left of the plot, namely they have the worst resolution for a given momentum. This is due primarily fact that the track must be extrapolated back toward the IP over a longer distance and through more scattering material. Those tracks with only one position measurement in the SSVD are to the right of the CDC/DCVD-only tracks and are separated by the layer in which the SSVD hit occurred, again due to the same argument as above. These tracks with no more than one SSVD position measurement have their impact parameter determined in essentially the same manner as high momentum tracks: the angle of the track is determined by the CDC and DCVD while the track is fixed to a point near the IP essentially by the SSVD or DCVD, depending on whether a SSVD hit was found. The resolution for each combination of hits is spread over fairly broad bands because of the various combinations of CDC and DCVD hits as well as the polar angle of the track.

Tracks with two or more hits in the SSVD have even better resolution, as can be expected, and separate clearly into bands depending on the combination of the three SSVD layers which have position measurements on the track (*i.e.* 1+2, 1+3, 2+3 or 1+2+3). What is different about the low-momentum track resolution determined for these tracks is that the polar angle of the track is determined almost solely by the SSVD. This is because the scattering material between the SSVD and DCVD degrades the extrapolation of the track from the CDC and DCVD as the track momentum is lowered, until at momenta lower than 2-3 GeV, the SSVD can itself measure the angle of the track better than the CDC and DCVD, despite its very small lever arm. As the track momentum increases, the effect of multiple scattering is diminished and the greater lever arm of the outer chambers provides a better angle determination. Graphically this can be seen in Figure 4–9(b). The slope of the resolution dependence on the momentum is shallower at low momentum than at larger momentum where the angle information from the CDC and DCVD becomes useful, providing a better measurement of the track.

4.2 Interaction Point Determination

Recall that the impact parameter resolution as given in Equation (4-7), contains contributions from the track measurement accuracy as well as the knowledge of the

interaction point. A particularly advantageous feature of the SLC is the very small size of the beam spots at the interaction point, where the beams have a diameter of less than 5 microns. In contrast, a storage ring typically has significantly larger beam spots. In the case of LEP, these are about 20 microns in the vertical plane and 150–200 microns in the horizontal plane. Although the beam spots are less than 5 microns in diameter, the knowledge of their position with respect to the tracking [112]detectors must still be determined. While instrumentation in the SLC final focus provides some information as to the relative position of the beams, the determination of the absolute beam position necessitates using Z^0 events. As described below, this is done using hadronic events and fitting for a vertex using a subset of the tracks which best match to this vertex. The resulting fit vertex position can either be applied on an event-by-event basis or as an average over groups of events. This latter option is discussed in Section 4.7.

4.2.1 Interaction Point Finding Algorithm

The interaction point finding algorithm involves building up a vertex by sequentially adding tracks to the vertex fit which have the highest probability of having originated in a common point. Specifically, the algorithm begins with the four tracks that have the smallest impact parameters to a seed interaction point location. The four combinations of three of these tracks are then fit to a vertex in the xy plane and the χ^2 probability for those tracks to form a vertex calculated. The combination with the largest probability is then taken as the initial vertex to which other tracks will be added.

To add more tracks to the vertex, each of the remaining tracks is individually fit to a vertex with the three tracks found in the initial vertex fit and the χ^2 probability of that vertex calculated. The additional track which yields a vertex of the largest χ^2 probability is then permanently added to the vertex. The process is then repeated with the remaining tracks, individually fitting a vertex with each additional track and the tracks already assigned to the vertex, then again permanently keeping the track with the highest χ^2 probability in the vertex. The process of adding tracks to the fit vertex is then terminated when none of the additional tracks yield a vertex of a χ^2 probability greater than 0.01.

Using all detected tracks as candidates for the vertex, as will be standard when using an event-by-event determined vertex, the resulting fit vertex typically has an error ellipse with a semi-major axis (σ_x) of 30–60 μm and a semi-minor axis (σ_y) of 5–15 μm, for an aspect ratio of roughly 5:1. The direction of the semi-major axis is

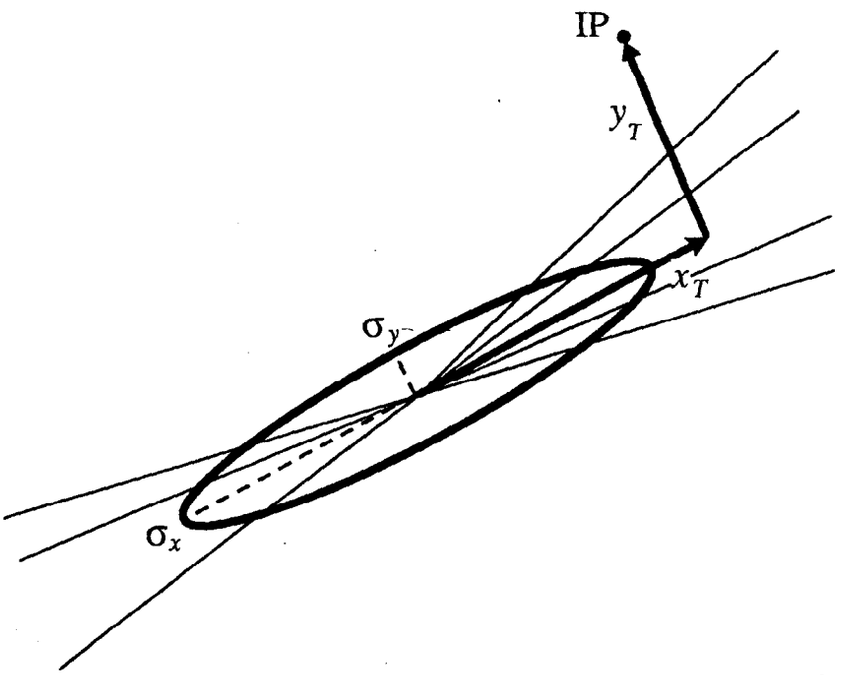

Figure 4–10 Definitions of the variables used in studying the interaction point fit results.

usually fairly parallel to the thrust axis. On average, about 60–70% of the detected tracks are used in vertex, which is about 14 tracks in the data. In $b\bar{b}$ events, about one fewer tracks are, on average, are included in the vertex fit. The fraction of the tracks from a B hadron decay which are included in the fit decreases roughly linearly from about 68% for a decay length less than 1 mm to about 55% for a decay length of about 10 mm. This level to which these tracks affect the fit is discussed below. This algorithm successfully finds an interaction point location with three or more tracks for all events which pass the event selection cuts (see Section 4.3).

Useful quantities to use in studying the vertex fit results are the distance perpendicular (y_T) and parallel (x_T) to the major axis, between the fit and assumed vertex position. These variables are illustrated in Figure 4–10. Expected distributions for y_T as calculated by the Monte Carlo are shown by event flavor in Figure 4–11. It can be seen that the y_T distribution for $c\bar{c}$ events is only slightly wider than that for *uds* events and neither has very significant non-Gaussian tails. The $b\bar{b}$ events have a notably broader y_T distribution than *uds* or $c\bar{c}$ events. A wider distribution for $b\bar{b}$ events would be expected for a number of reasons. First, on average, fewer tracks are included in the fit vertex in $b\bar{b}$ events than in *udsc* events. Furthermore, a broader tail might also be expected as there will be some

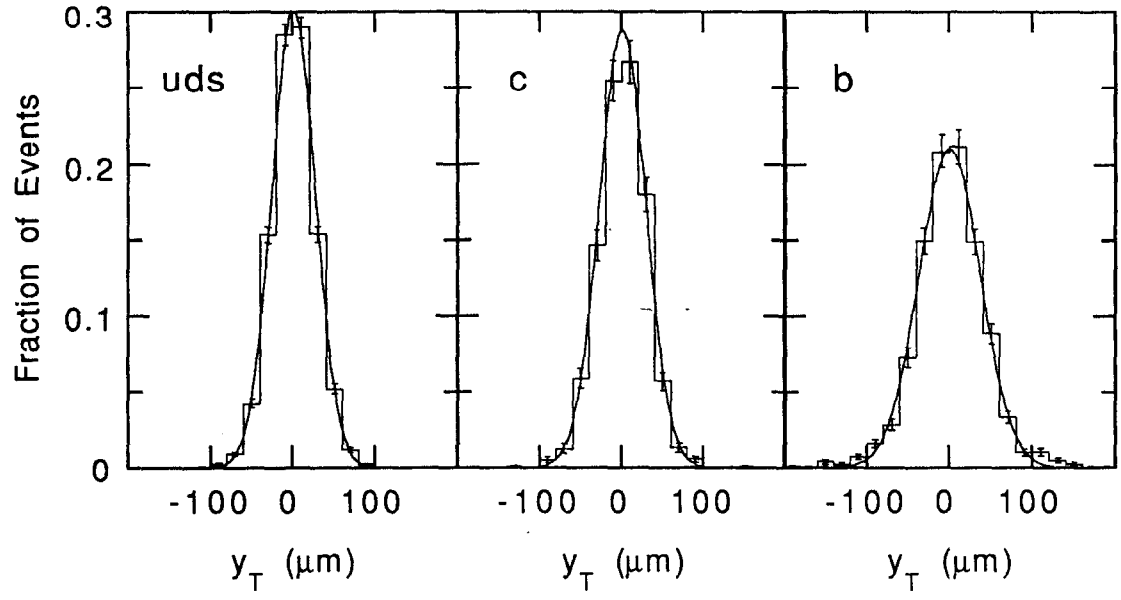

Figure 4–11 *Monte Carlo predictions of y_T distributions for different flavors of events with 25 μm of IP motion in the Monte Carlo. All events which pass the event selection cuts (see Section 4.3) are included in these plots.*

instances where the fitting algorithm found a secondary vertex rather than the primary one, particularly when the B hadrons decay with a short lifetime. These effects combine to make the y_T distribution ~40% wider than that for the lighter quark species. However, the lack of a very large tail indicates that in the vast majority of the events, the vertex finding algorithm is doing quite well even in multi-vertex events. The distributions between the actual and found vertex along the major axis of the error major axis of the error ellipse, x_T, shown in Figure 4–12. As is the same for the y_T distribution, the x_T distribution is broader for the $b\bar{b}$ events, in this case by about 20%.

It is interesting to note that the error assigned to the vertex ellipse underestimates the actual error with which the vertex is determined. This can be seen when the Monte Carlo is studied with no generated IP motion. The average error along the minor axis is 12 μm while the y_T distribution has a Gaussian fit width of 18 μm and a standard deviation of 26 μm. The source of this discrepancy and the non-Gaussian tail is largely due to tails in the impact parameter distribution which are not accounted for in the impact parameter resolution assigned to a given track. These impact parameter tails and the treatment of them in the Monte Carlo will be discussed later in Section 4.5.

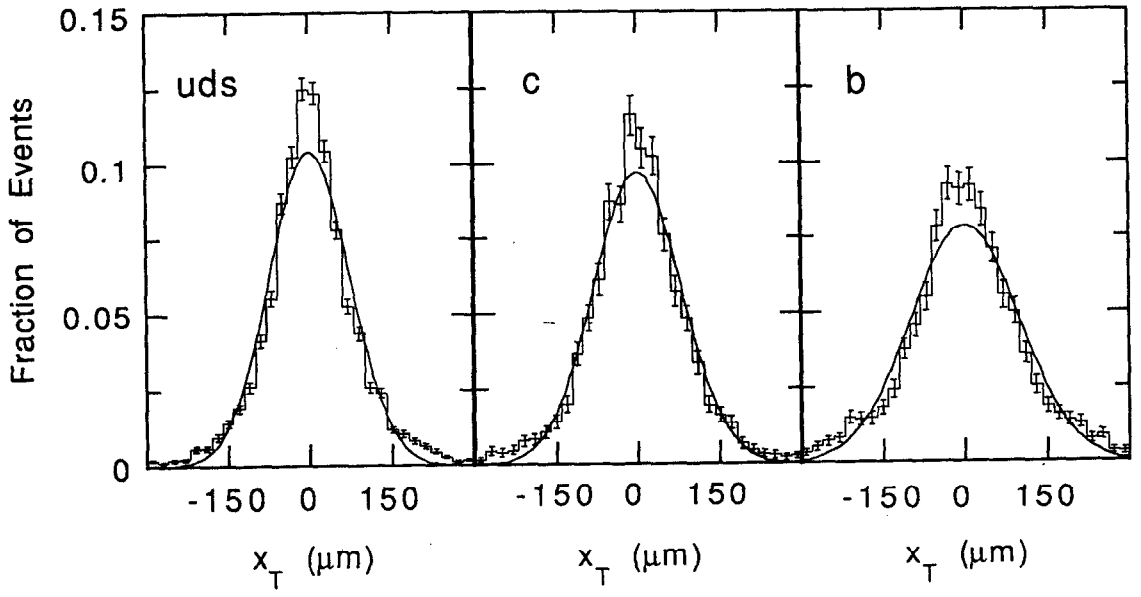

Figure 4–12 Monte Carlo predictions of x_T distributions for different flavors of events with 25 μm of IP motion in the Monte Carlo. All events which pass the event selection cuts (see Section 4.3) are included in these plots

4.3 Event Selection Cuts

The event selection cuts first require that the event pass a standard set of cuts which select hadronic events and reduce the background from e^+e^-, $\mu^+\mu^-$, $\tau^+\tau^-$ events and random background events. These cuts are:

- At least 7 tracks must be in the nominal fiducial volume. Specifically, these tracks must satisfy the following four minimal requirements.
  1. The calculated angle of the track with respect to the beam axis must satisfy $|\cos\theta| < 0.8$ such that the tracks are well inside the active regions of the tracking detectors.
  2. The projection of the track's momentum into the plane perpendicular to the beam axis, p_{xy}, must be greater than 0.150 GeV/c.
  3. The distance of closest approach in the z-direction of the track to the nominal interaction point must satisfy $|z_m| < 15$ mm.
  4. The number of hits associated with the track in the CDC tracking must be at least 25 of the 72 possible.

- The sum of the observed charged and neutral visible energy must be at least half of the center-of-mass energy, where charged tracks are assigned the mass of a pion. Specifically, this requirement is

$$E_{vis} = \sum_{i}^{n_{ch}} \sqrt{p_i^2 + m_\pi^2} + \sum_{i}^{n_{neu}} E_i \; > \; 0.5 E_{cm}.$$

These cuts select 80.0% of the hadronic events with a very small non-hadronic background of less than 0.1%. In the 1990 data sample, 220 events pass these cuts.

An additional cut was made to ensure that the events are oriented in the central region of the detector where the tracking detectors are located:

- The angle of the thrust axis calculated using the charged tracks which pass the above cuts only, must satisfy $|\cos\theta_{thrust}| < 0.7$.

This cut reduces the event-to-event fluctuations with negligible loss of statistical power in the analyses to be discussed later. After this cut, the event-selection efficiency is 70.4%, and in our data sample 196 events remain.

4.4 Vertex Quality Track Cuts

Once hadronic events are found, a subset of the tracks within these events are selected whose impact parameter resolution will be thoroughly studied. These *vertex quality* tracks will later be used to tag $b\bar{b}$ events. Initially, it is required that each track pass the four minimal track cuts used in the event cuts. Additionally, a track must satisfy the following requirements that ensure accurate impact parameter determination:

5. The number of hits found on the track in the DCVD must be at least 15 of 32 possible.
6. Similarly, the number of hits found in the track in the SSVD must be at least 1 of 3 possible.
7. The error on the extrapolation of the track back to the interaction point including multiple scattering, σ_{TR}, must be less than 200 μm.

To reduce the number of tracks with large impact parameters which come from non-$b\bar{b}$ sources, in particular those from K_s^0 or Λ decays, multiple Coulomb scattering and nuclear interactions, it is also required that:

8. The impact parameter of the track, with respect to an interaction point which is fit on an event-by-event basis, must satisfy $|b| < 2$ mm.

A total of 2330 tracks in the 220 events pass the cuts which select hadronic events, and 2176 tracks in the 196 events pass all of the event selection cuts (namely the hadronic cuts and the cut on the polar angle of the thrust axis) are found in the 1990 data sample. To maximize the statistical power, the former sample of tracks will be used to study the impact parameter resolution. Table 4–1 gives the fraction of tracks remaining after each cut is applied in order, as estimated by the Monte Carlo.

track cut	% passed
1. $\|\cos\theta\| < 0.8$	92.8%
2. $p_{xy} > 0.15$ GeV	87.0%
3. $\|z_m\| < 15$ mm	79.`%
4. $N_{CDC} \geq 25$	78.9%
5. $N_{DCVD} \geq 15$	62.9%
6. $N_{SSVD} \geq 1$	56.4%
7. $\sigma_{TR} < 200$ μm	55.5%
8. $\|b\| < 2$ mm	52.3%

Table 4–1 The fraction of the reconstructed tracks passing each of the multiplicity track quality cuts for events which pass the hadronic event cuts, but not necessarily the additional cut on the thrust axis dip angle.

4.5 Impact Parameter Resolution Studies

With the above set of high quality tracks defined, it is essential to understand their impact parameter well, since this serves as the basis of the tagging algorithm to select a sample of predominantly $b\bar{b}$ events. This is the case because the Monte Carlo will be used to predict the tagging efficiencies, and thus understanding and properly modelling the impact parameter resolution are critical to an accurate detector simulation.

The impact parameter resolution can be studied in a number of ways, including the use of cosmic rays, lepton pair events and hadronic events. While the first two can provide a straightforward method for determination of the resolution, the use of hadronic events poses some difficulties. In particular, it is these events which will be used in the subsequent analyses of the $Z^0 \rightarrow b\bar{b}$ fraction and the $b\bar{b}$ event

multiplicity both of which use a tag to identify $b\bar{b}$ events which is based on the track impact parameter. Thus, care must be taken not to allow the resolution studies to be biased by assumptions about the quantities to be measured. The primary method used to achieve this independence relies on the use of the physically signed impact parameter, which causes the tracks from B decay and other long lived hadrons to have predominantly positive impact parameters, whereas the tracks from the primary decay vertex will be smeared equally to have positive and negative impact parameters by the finite detector resolution (see Section 4.1.2). Hence, using only those tracks with $b < 0$ will significantly reduce the dependence of the resolution on the tracks from B decay. The level to which this is achieved is discussed later in Section 4.5.3.

4.5.1 Intrinsic Resolution

To study the intrinsic performance of the tracking detector system it is desirable to use high momentum tracks which are insensitive to effects from multiple scattering.

4.5.1.1 Cosmic Ray Events

High energy cosmic ray events provide a good source of events for the study of intrinsic resolution by fitting the two halves of the cosmic ray separately and then looking at the *miss distance*, namely the difference between the extrapolation of the two halves of the track back to the center of the detector. Extensive use was made of cosmic rays by the CDC and DCVD. However, the SSVD electronics are operated in a pulsed mode and thus its livetime is too small to accrue a useful number of cosmic events. A distribution of the miss distance as measured by the CDC and DCVD for cosmic rays with a momentum of at least 15 GeV is shown in Figure 4–13. The Gaussian fit to this distribution gives a width of 55 μm which corresponds to an error on the track resolution of $\sigma_{TR} = 55/\sqrt{2} = 39\ \mu m$. This is about 60% higher than would be expected by calculating the expected resolution using the measured local resolutions for the detectors (as discussed in Sections 2.2.2.5 and 2.2.3.8) presumably due to systematic effects. Although this demonstrates the possibility for improved resolution for these two detectors, this resolution is more than adequate to locate the position measurements on the SSVD for the final impact parameter determination in Z^0 events.

4.5.1.2 Intrinsic Resolution in Hadronic Events

To study the intrinsic performance of the detectors in the hadronic data, a subset of the tracks were chosen which passed the vertex quality track cuts as

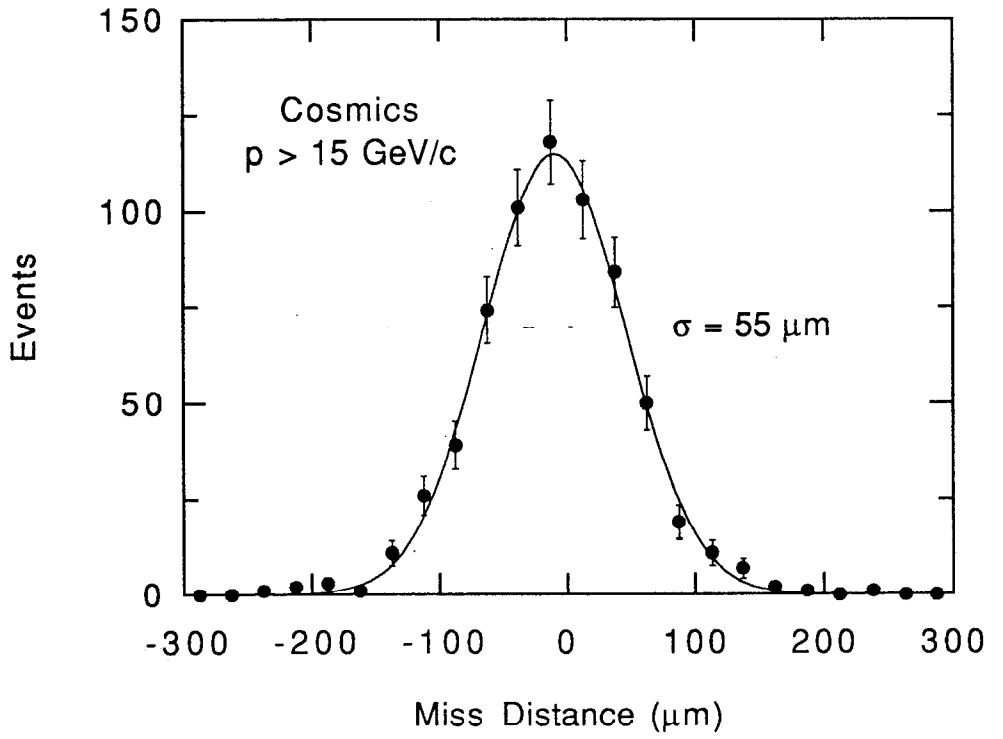

Figure 4–13 The distribution of the miss distance for high momentum cosmic ray events where each half of the track was fit separately. The curve is a Gaussian fit to the data points with a 55 μm width.

described in Section 4.4 and have an extrapolated track error, σ_{TR} calculated to be less than 25 μm. These tracks were chosen as they are virtually unaffected by multiple scattering and provide a well-measured sample of tracks.

The quantity just to study these tracks is the impact parameter significance,

$$S \equiv \frac{b}{\sigma_b}, \tag{4-18}$$

where the form used to calculate the impact parameter resolution for the full tracking system is composed of three terms,

$$\sigma_b \equiv \sqrt{\sigma_{TR}^2 + \sigma_{IP}^2 + (15\ \mu m)^2}. \tag{4-19}$$

As discussed previously, σ_{TR} is the error due to the track fit as extrapolated back to its distance of closest approach to the IP, and σ_{IP} is the error due to uncertainty in the IP position. The third term of 15 μm can be attributed to the remaining uncertainty in the alignment of the SSVD* resulting from the limited statistics

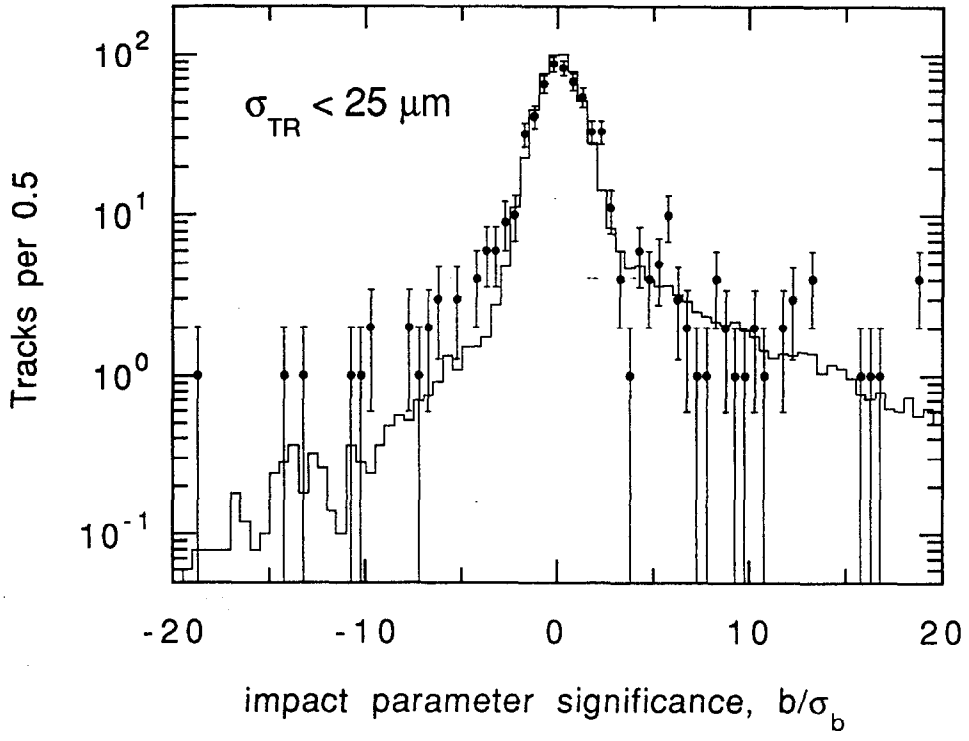

Figure 4–14 The impact parameter significance for data (points) and Monte Carlo (line) tracks with a calculated $\sigma_{TR} < 25$ μm.

available. This value was determined using the Monte Carlo to test the alignment algorithms with many data sets equal in size to our 220 events.

Figure 4–14 shows a comparison of impact parameter significance for the high precision tracks ($\sigma_{TR} < 25$ μm) between the 604 data tracks and a Monte Carlo sample. In this plot and the others in this section, the impact parameter is calculated with respect to a vertex which is determined on an event-by-event basis. In these resolution studies, the interaction point location is fit separately for each track, and in each fit the track in question is omitted from the fit. This is done to reduce correlations resulting from a track being used in the fit for the interaction point location which in turn is used to calculate the impact parameter of that track. Comparing only the left side of these distributions, which will be used to study the resolution fairly independently of the contribution of tracks from B decays, it is clear that the Monte Carlo underestimates the resolution of the detectors.

A concerted effort was made to determine the source or sources of this systematically degraded resolution and despite finding and accounting for

* See Section 2.2.4.4 on page 77 for information on the SSVD alignment.

numerous sources of lower resolution, there remained a notable difference between the observed impact parameter significance distribution and that predicted by the Monte Carlo. It is certainly possible, and indeed likely, that with a larger data set the detector performance would be better understood and the data/Monte Carlo brought into agreement by accounting for the individual sources of lower resolution. However, given as that is not the case, the next best solution is to modify the Monte Carlo track impact parameters after they have been determined to obtain agreement with the data. As described below in more detail, the impact parameters of the Monte Carlo tracks are indeed smeared to better match the data and these b-smeared tracks are used in the subsequent analyses in Chapter 6, "The Branching Fraction to Bottom Quarks" and in Chapter 7, "The Multiplicity of Bottom Quark Events". However, the amount of smearing has only a minor affect on the results of these analyses, with the case of no additional smearing being included in the systematic error determination.

Without a particular systematic effect to explain the difference between the data and Monte Carlo tracking performance, the remaining option was to apply additional smearing to the impact parameters of the Monte Carlo tracks randomly. The form of the additional smearing was the sum of two Gaussian probability functions, P_G, where the second is only applied to a randomly selected subset of the tracks. Mathematically this is

$$\mathrm{b} \rightarrow \mathrm{b} + P_G(\sigma_{core}) + \Theta(\mathrm{f}_{tail}) \cdot P_G(\sigma_{tail}), \tag{4-20}$$

where $\mathrm{f}_{tail} \in [0, 1]$ and $\Theta(x)$ is a random function which is 1 for the fraction x of the samples and 0 otherwise. The first Gaussian function accounts for a slightly broader central core in the Monte Carlo impact parameter significance distribution compared to the data, while the second adjusts the tail region just beyond this central peak.

In order to determine optimal amounts of smearing to add to the Monte Carlo tracks, several methods were investigated for quantifying the comparison between the data and Monte Carlo impact parameter significance distributions. These methods included a fit to a functional form which typically consisted of a Gaussian central core and an additional term to account for the non-Gaussian tails. A particular form which worked quite well was

$$N(S = \mathrm{b}/\sigma_{\mathrm{b}}) \propto (1-f)\, e^{-S^2/(2\alpha^2)} + f e^{-|S|/\beta}. \tag{4-21}$$

The fit parameters, the widths of the Gaussian central core (α), the tail (β) and the tail fraction (f), can then be compared for fits done on distributions from the data and Monte Carlo. Reference [73] contains a thorough analysis of this same data set using this method. Although the results in this reference are consistent with other methods, great care must be taken in fitting low statistics data, where fluctuations and bins with no entries can be problematic for least-squares fits.

A comparison of the data and Monte Carlo distributions can also be made without assuming any particular functional form or binning for the data tracks. To make these comparisons, the negative side of the Monte Carlo impact parameter significance distribution was normalized and used as a probability distribution of tracks having a particular impact parameter significance. To reduce the effects of low statistics in the tails of this Monte Carlo distribution, variable bin sizes were used to ensure that each bin had at least 100 entries.* Thus, the probability of each track in the data having a particular negative impact parameter significance can then be calculated and used to find a total probability for the comparison of the data and Monte Carlo distributions. Two methods of computing a probability were investigated for making this comparison.

- The multinomial probability, an extension of the familiar binomial probability, gives the probability of getting a given distribution for an assumed parent distribution. The multinomial probability has the form,[111]

$$P_{mult}(n_1, n_2, n_3 \cdots ; p_1, p_2, p_3 \cdots) = \frac{N!}{\prod_{bin\ i} n_i} \cdot \prod_i (p_i)^{n_i} \tag{4-22}$$

  where the n_i and p_i are the number of data tracks and the Monte Carlo probability of a track being in bin i, and $N = \Sigma n_i$ is the number of tracks.

- The log-likelihood, $\boldsymbol{L}$, which for a given set of data tracks is given by

$$\log \boldsymbol{L} = \log \prod_{track\ j}^{N} p(S_j) = \sum_{bin\ i} n_i \log p_i \tag{4-23}$$

  where j is the index of the data tracks, i is the index over the bins and p is the Monte Carlo probability.

* Twelve bins were used to cover the range $-20 < b/\sigma_b < 0$, and these had lower edges of –20, –8, –6, –5, –4, –3.5, –3, –2,5, –2, –1.5, –1, –0.5

Both methods yield similar results for the optimal amount of additional impact parameter smearing, and so the latter is chosen as the standard definitions of the confidence intervals for a log-likelihood will be useful later.

A range of different smearing was investigated, employing the core-and-tail smearing as described by Equation (4-20) and varying the width the core and tail smearing Gaussians and the fraction of tracks which are smeared by the tail term. Using the log-likelihood comparison, the combination of smearing which makes the Monte Carlo best match the data is that with the maximum log-likelihood. Table 4–2 shows the resulting log-likelihood differences between the combination of smearing with the maximum log-likelihood and that of the other possible combinations. The best data/Monte Carlo agreement is for an impact parameter smearing of

10 μm to all tracks and 100 μm to 10% of the tracks selected randomly.

Figure 4–15 illustrates the effect of this impact parameter smearing on the high precision tracks used for the data/Monte Carlo comparison. Note that the agreement is significantly improved, particularly in the tail region immediately beyond the central core. Also shown in Table 4–2 are the combinations of smearing which are 1σ and 2σ allowed, namely they are <0.5 and <2.0 units of log-likelihood different than the maximum likelihood point. It should be noted that the other measurements[73] of the optimal additional smearing do indeed fall with the 2σ contour for this analysis.

While working well for most of the tracks, the double Gaussian form as used above to provide additional smearing for the Monte Carlo has little effect on the far tail region of the impact parameter significance (beyond about –10) for the high precision tracks. With the above smearing already applied, a very broad additional Gaussian smearing was applied randomly to a fraction of the tracks to investigate a possible range of the far tail smearing. Using the same techniques as used previously, it was found that a small quantity of additional smearing is allowed, and the limits on this smearing are given in Table 4–3. However, the case of no additional far tail smearing is preferred and thus none of this far tail smearing will be used except for placing systematic limits.

4.5.1.3 Lepton Pair Events

Lepton pair events ($e^+e^- \rightarrow e^+e^-$ or $\mu^+\mu^-$) are particularly useful for studying intrinsic detector performance as the produced leptons have energies very nearly

$\sigma_{TR} < 25$ μm	Fraction of tracks with tail smearing							
Width of tail smearing	0%	5%	10%	15%	20%	25%	30%	35%
	0 μm core smearing							
0 μm	9.72	9.72	9.72	9.72	9.72	9.72	9.72	9.72
25 μm	9.72	8.21	6.67	5.23	4.37	3.72	3.79	
50 μm	9.72	6.35	3.55	2.11	1.45	1.43	1.50	2.57
75 μm	9.72	4.56	1.89	0.65	0.63	1.23	3.49	
100 μm	9.72	3.93	1.41	0.90	1.91	4.21	6.71	
150 μm	9.72	4.46	2.59	3.55	6.20	9.46		
200 μm	9.72		4.13	6.18	9.42			
	5 μm core smearing							
0 μm	8.27	8.27	8.27	8.27	8.27	8.27	8.27	8.27
25 μm	8.27			4.68	3.45	3.70		
50 μm	8.27		2.92	1.47	1.02	1.15	1.55	
75 μm	8.27	3.84	1.51	0.53	0.79	1.932	4.23	
100 μm	8.27	2.72	0.50	0.37	1.78	4.13		
150 μm	8.27	4.98	2.54	3.42				
200 μm	8.27							
	10 μm core smearing							
0 μm	5.06	5.06	5.06	5.06	5.06	5.06	5.06	5.06
25 μm	5.06			2.16	1.95			
50 μm	5.06		1.76	1.15	1.57	1.64		
75 μm	5.06	1.76	0.38	0.32	1.35	2.30		
100 μm	5.06	2.35	0	0.47	2.42			
150 μm	5.06	3.15	2.14	3.96				
200 μm	5.06		4.52	7.23				
	15 μm core smearing							
0 μm	3.24	3.24	3.24	3.24	3.24	3.24	3.24	3.24
25 μm	3.24							
50 μm	3.24		2.18	2.44	3.46			
75 μm	3.24		2.31	1.36				
100 μm	3.24	1.99	1.09	1.72				
150 μm	3.24	2.34	2.25					
200 μm	3.24							

Table 4–2 The difference between the log-likelihood for the combination with the maximum log-likelihood (10 μm of core and 10% of the tracks with 100 μm tail smearing) and that with other combinations. The optimal smearing is shaded, while the 1σ and 2σ allowed combinations are bordered by the thick and thin lines.

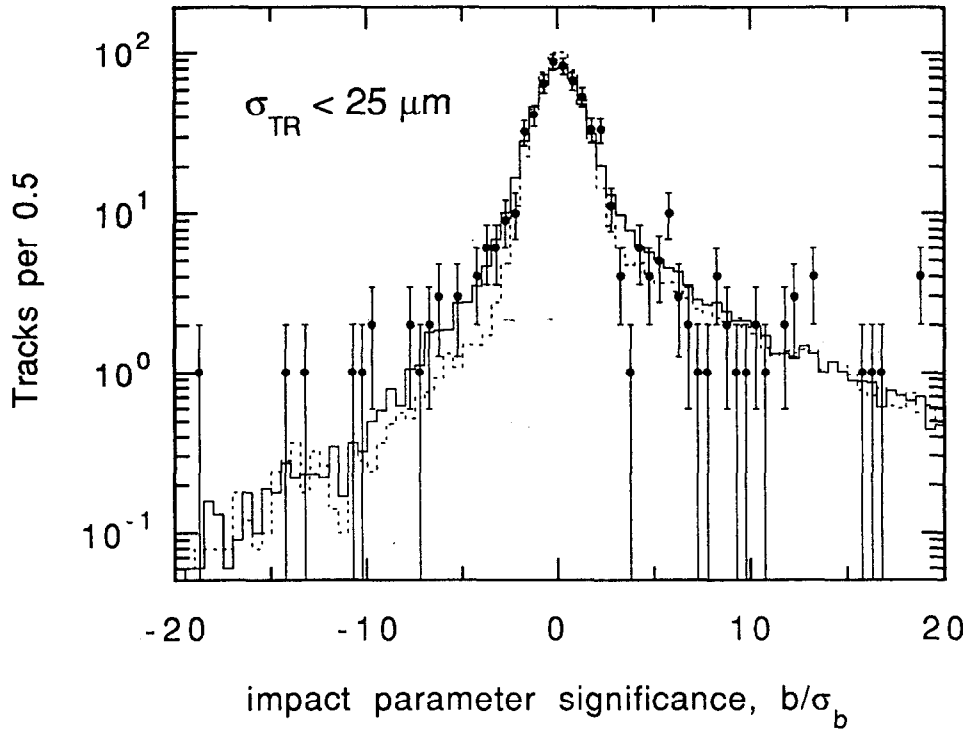

Figure 4–15 The impact parameter significance for the data (points), the unsmeared Monte Carlo (dashed line) and the Monte Carlo with the optimal smearing (solid line) for tracks with a calculated $\sigma_{TR} < 25$ μm.

Width of far tail smearing	maximum allowed fraction of tracks	
	1σ	2σ
250 μm	0.8%	2.2%
500 μm	0.4%	1.3%
1000 μm	0.3%	1.0%
2000 μm	0.3%	0.8%

Table 4–3 Maximum fraction of tracks smeared by a given Gaussian width which are allowed at the level of 1σ and 2σ by the log-likelihood comparison of the data and Monte Carlo tracks with $\sigma_{TR} < 25$ μm.

that of the beam energy, the miss distance measurement is independent of the IP position and the events are free of errors caused by nearby tracks as can be the case

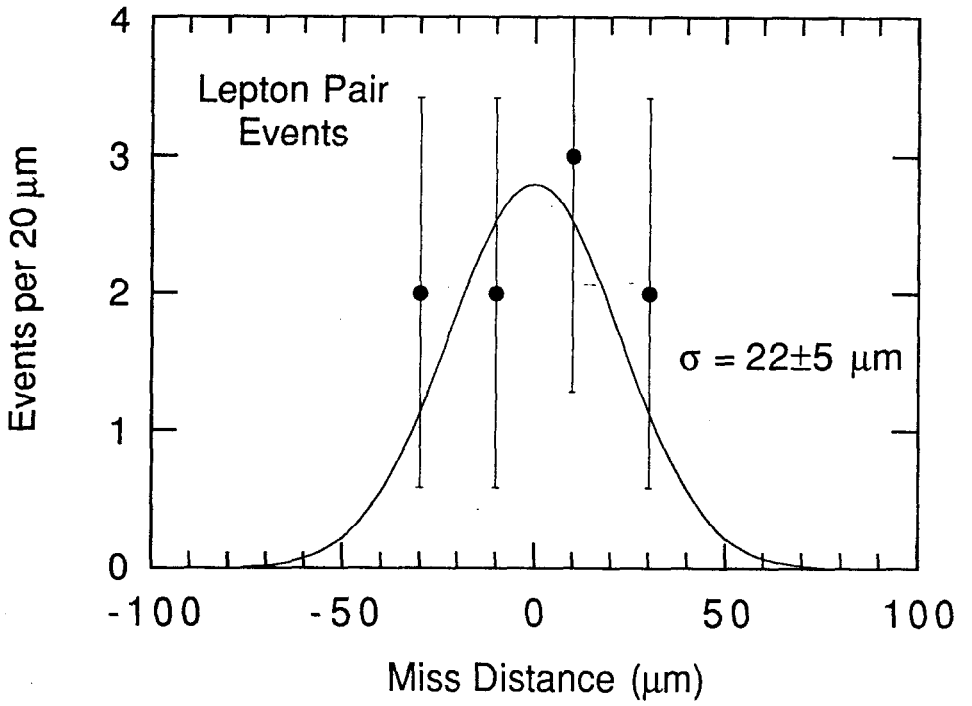

Figure 4–16 The miss distance distribution for the 9 good e or μ pair events.

in hadronic jets. These could, in sufficient number, provide a good measure of the tracking resolution. In the 1991 data sample, there are 21 events which are identified as potential lepton pair events. Applying the standard vertex quality track cuts, as described in Section 4.4, leaves 14 events. In order to remove 1+1 prong τ events, a further requirement is made that each track have a total measured momentum of no less than 3σ below the beam energy. With the Mark II transverse momentum and dip angle resolution, this cut is typically on the order of 35 GeV. A distribution of the miss distance for these 9 remaining lepton pair events is shown in Figure 4–16. The width found by fitting the miss distance distribution to a Gaussian function is 22±5 μm. The default Monte Carlo predicts the width of the miss distance distribution to be 11 μm. With the additional impact parameter smearing as evaluated using high resolution hadronic tracks in the previous section, the Monte Carlo predicts a width of 28 μm, which is consistent with the value observed in the data.

4.5.2 Multiple Scattering-Limited Resolution

The impact parameter resolution for low momentum tracks will be dominated by the amount of scattering material present in the detectors. Thus, proper

Sample of tracks with $100 < \sigma_b < 200$ μm	Gaussian fit σ	standard deviation
MC with Gaussian scattering	1.07	1.56
MC with Molière scattering	1.13	1.67
Data (478 tracks)	1.15±0.05	1.66±0.05

Table 4–4 The fit Gaussian width, σ, and the standard deviation for the Monte Carlo (MC) and data distributions of the impact parameter significance b/σ_b are given for various samples. The Monte Carlo samples were generated using the two methods of applying multiple scattering to the tracks in the detector simulation, a Gaussian distribution and the Molière theory. Note that these were calculated using only the tracks with negative impact parameters.

modeling of the resolution in the multiple scattering-limited regime essentially requires tuning the material in the Monte Carlo to reflect the actual amount of material in the detectors. To do this without being too sensitive to the intrinsic detector resolution or the uncertainty in the IP location, only tracks with a large calculated resolution, $100 < \sigma_{TR} < 200$ μm, were used. Starting with the nominal thicknesses for the various layers, and reasonable estimates of their uncertainties, the thicknesses used in the detector simulation were varied and the resulting distributions of the impact parameter significance distributions, b/σ_b, were compared to those observed in the data.

A major improvement in the agreement between the observed distribution and the Monte Carlo was achieved by implementing Molière Scattering Theory in place of a simpler Gaussian approximation for multiple Coulomb scattering in the detector simulation (see Section 3.4, "Detector Simulation," on page 102). This improvement is reflected in the impact parameter significance distribution of tracks generated using these two methods. As shown in Table 4–4, the results using Molière scattering caused a marked improvement in the data and Monte Carlo agreement compared with the Gaussian formula. Using the Molière scattering in the Monte Carlo generation and the optimally tuned materials, the impact parameter significance distribution for those tracks with $\sigma_{TR} > 25$ μm, namely those not used for the determination of the additional smearing, is shown in Figure 4–17. The agreement for these tracks is also good.

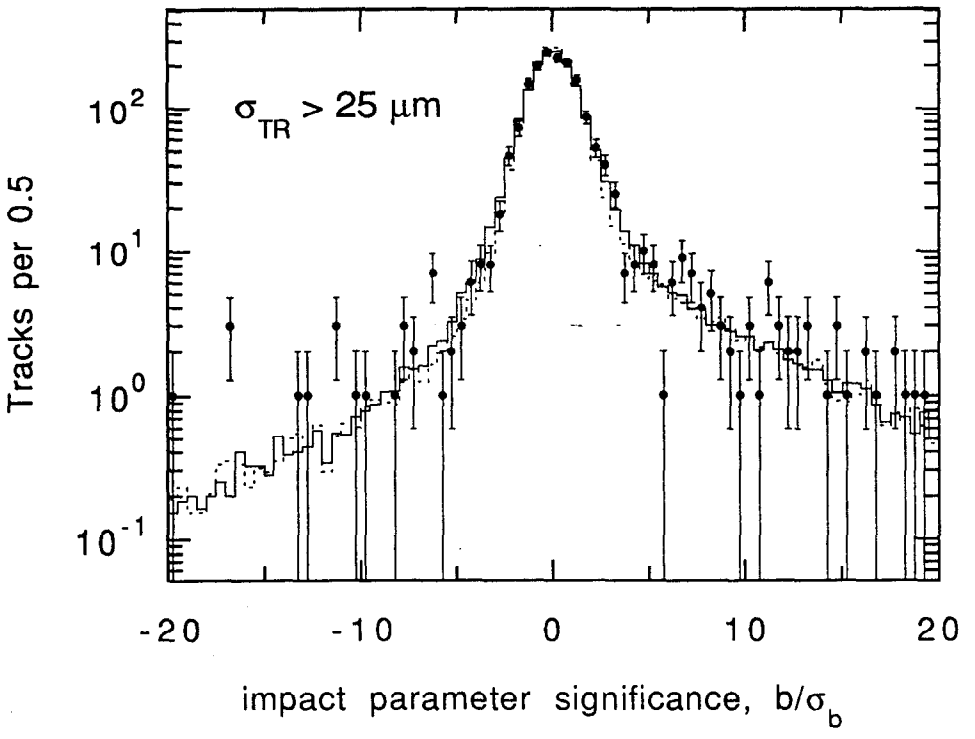

Figure 4–17 The impact parameter significance for the data (points), the unsmeared Monte Carlo (dashed line) and the Monte Carlo with the optimal smearing (solid line) as discussed in Section 4.5.1 for tracks with a calculated σ_{TR} > 25 μm.

4.5.3 Impact Parameter Resolution Checks

In this section, several effects are investigated which have the potential to alter the resolution as measured in the preceding sections. In general, these are effects which will contribute asymmetrically to the impact parameter significance distribution, and because only one side of the distribution (namely that with negative impact parameter tracks) is studied for determining the resolution, asymmetries will not be detected. Applying an algebraic sign to the impact parameter using the thrust axis can cause tracks from long-lived parents to be signed incorrectly for a number of reasons including:

- the Z^0 hadronic branching fraction to $b\bar{b}$,
- the alignment of the thrust axis with the parent B direction, and
- the effects from scattering and particle production in the detector material.

An effect which is of particular concern regarding the asymmetric distribution of positive and negative impact parameter tracks is the variation of the resolution determination due to an incorrect assumption for the value of F_b, the hadronic

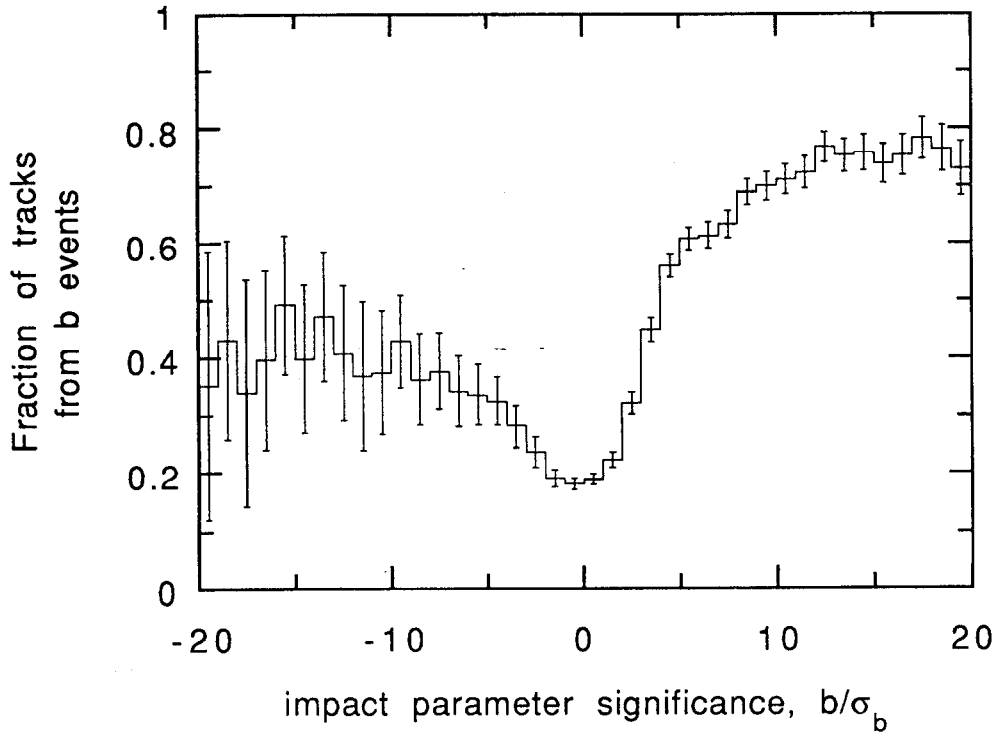

Figure 4–18 Fraction of reconstructed tracks which are from b events as a function of the impact parameter significance.

branching fraction of the Z^0 to $b\bar{b}$ events. This is important because the tracks from B decays will naturally contribute to the impact parameter significance distribution asymmetrically, and the level to which they contribute relative to other presumably symmetric sources can affect the resolution measurement. As F_b is going to be one of the quantities measured in the following analyses, it would also be advantageous for the measured resolution to be insensitive to F_b in order to avoid an iterative solution. It is interesting to note that the reconstructed tracks from $b\bar{b}$ events comprise about 35% of the tracks with large negative impact parameter significance ($b/\sigma_b < -5$), whereas they are only ~23% of the total number of tracks (see Figure 4–18). The level to which the choice of F_b affects the resolution measurement was studied in the Monte Carlo by varying F_b from its nominal value of 0.217 by ±25% and ±50% and repeating the data/Monte Carlo log-likelihood comparison that was used to study the resolution in Section 4.5.1. It is observed that a ±25% variation of F_b does not change the optimal amount of additional required impact parameter smearing (namely 10 μm for all tracks and 100 μm on a random subset of 10% of the tracks) and a ±50% variation changes the optimal smearing within the 1σ allowed region (see Table 4–2 on page 136). Similarly, no

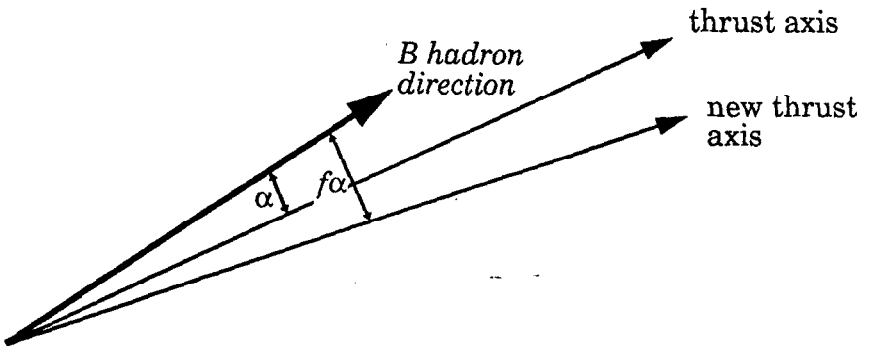

Figure 4–19 Changing the thrust axis by some fixed angular fraction, *f*, from the *B* hadron direction.

change beyond the 1σ region was seen in the amount of far tail impact parameter smearing which is preferred, even with a ±50% change in F_b.

Another mechanism by which the impact parameters can be signed asymmetrically is due to the level at which the thrust axis properly approximates the direction of the *B* hadrons. To investigate this with the Monte Carlo, the angle between the thrust axis and the *B* hadron direction, α, was varied separately for each hemisphere by some fraction, *f*, of the original angle, thus broadening or narrowing the angular distribution (see Figure 4–19). It follows that a value of $f = 1$ leaves the thrust direction unchanged, whereas $f = 0$ causes the *B* hadron direction to be used for signing the track impact parameters. As above, the resulting Monte Carlo impact parameter significance distributions for tracks with $\sigma_{TR} < 25$ μm were then compared to the data and the range of tolerable differences determined using the log-likelihood comparisons as discussed in Section 4.5.1. Table 4–5 shows the results of varying *f* over a broad range, from using the *B* direction to sign the impact parameters to broadening the distribution by a factor of three. The log-likelihood difference is given between the default Monte Carlo thrust axis determination ($f = 1$) and the variously modified thrust axes. The results indicate that the determination of the impact parameter resolution is quite insensitive to how well the thrust axis approximates the *B* direction, as the 1σ range varies almost from the thrust axis perfectly reproducing the *B* direction to the thrust axis approximating the *B* direction twice as poorly as predicted by the Monte Carlo.

It is also possible to generate asymmetric impact parameter distributions for tracks which are scattered or produced in the material of the detectors, through such processes as multiple scattering, pair production, and elastic and inelastic

fractional change in the B-$\hat{T}$ angle (f)	log-likelihood difference $\log(L_{f=1}) - \log(L_f)$
0	0.54
0.5	0.14
1.0	0
1.5	0.10
2.0	0.29
3.0	0.70

Table 4–5 The sensitivity of the resolution determination to the level at which the thrust axis reproduces the *B* hadron direction, given in terms of a log-likelihood comparison of the Monte Carlo with various *B* direction/thrust axis distributions and the data.

nuclear scattering.[73] The mechanism by which these asymmetric tails develop is illustrated in Figure 4–20. Looking along the direction of the track, the half of the scatters that go to the left of the original track (region I) will all be assigned a positive impact parameter according to the algorithm for applying a sign to the impact parameter as described in Section 4.1.2.2. The half of the scatters which go to the right of the original track will predominantly be assigned a negative impact parameter (region II). However, when they scatter at a fairly large angle the impact parameter again becomes positive (region III), and it is this region which can cause an asymmetry.

The use of the high precision tracks ($\sigma_{TR} < 25$ μm) to study the resolution minimizes the contributions to the asymmetry from multiple scattering and pair production tracks. The level of asymmetry is also reduced by the 2 mm impact parameter cut, which means that only tracks which are within 2 mm of the thrust axis as they pass through the scattering material can contribute. For $\sigma_{TR} < 25$ μm tracks, about 49% of the tracks fall within 2 mm of the thrust axis at the radius of the first scatterer, the beam pipe (25 mm). To gauge the level of this effect, note that only 1.7% of all high precision tracks cross the thrust axis beyond 25 mm from the IP.* For better clarity, a cut is used to remove tracks too near the thrust axis, as the angular resolution of these tracks can cause them to cross the thrust axis far from

* In just this one case are the positive impact parameter tracks used in this study of resolution, and here it is only to qualitatively examine the size of these asymmetric tails and *not* to make any determination of the resolution.

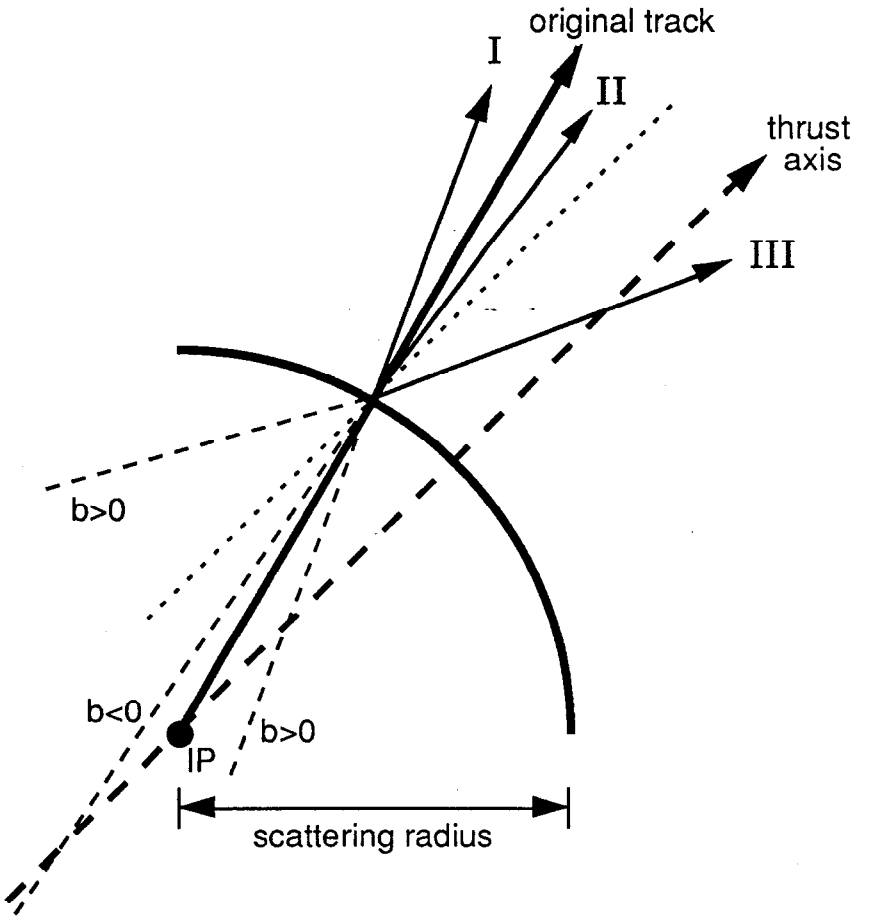

Figure 4–20 The source of an impact parameter sign asymmetry which results from scattering and production mechanisms. The asymmetry will come from region III in which the impact parameter is given a positive sign.

the IP. If a subset of the high precision tracks which fall between 0.15 and 2 mm of the thrust axis at a 25 mm radius are chosen, it is found that now only 2 of these 279 tracks cross the thrust axis beyond a 25 mm radius. The Monte Carlo would predict a consistent value of 1.6 tracks. Finally, even if the impact parameter signing definition is modified to symmetrize tracks from these sources by assigning a negative impact parameter to all of those tracks which cross beyond the beam pipe radius, the resulting optimal impact parameter smearing required for data/ Monte Carlo agreement is unchanged.

4.6 Tracking efficiency

The track finding efficiency of the CDC has been studied extensively in the past[62] and has been measured to be >99% for isolated tracks at PEP and is

estimated to be >95% efficient for tracks with $p_{xy} > 0.15$ GeV/c in hadronic jets at the SLC (see Section 2.2.2, "The Central Drift Chamber," on page 36). The Monte Carlo simulation of the CDC has been tuned to accurately reproduce the hit efficiencies observed in the data and it is believed that within a fiducial volume of $p_{xy} > 0.15$ GeV/c and $|\cos\theta| < 0.8$, the simulation is accurate to within ±1%.

The efficiency with which tracks pass the full vertex quality track cuts (particularly the required number of position measurements in the DCVD and SSVD) is also crucial. As with the CDC, the single hit efficiencies have been tuned in the Monte Carlo to reproduce those observed in the data. In the sample of 196 events which will be used in subsequent analyses, 66.4±1.9% of the 3276 tracks were found by the CDC and passed a set of basic quality cuts: $p_{xy} > 0.15$ GeV/c, $|\cos\theta| < 0.8$, $|z_m| < 15$ mm, $N_{CDC} \geq 25$ and $|b| < 15$ mm.* Of these, 2176 tracks pass the remainder of the vertex quality track cuts (see Section 4.4), which require $N_{DCVD} \geq 15$, $N_{SSVD} \geq 1$, $\sigma_{TR} < 200$ μm, and a tighter impact parameter cut, $|b| < 2$ mm. This corresponds to 66.4±1.9% of the CDC quality tracks passing the additional vertex track requirements. The Monte Carlo predicts an efficiency of 68.3% which is consistent with the data. Thus, the limit to which the efficiency is understood and modelled correctly is the sum in quadrature of the contribution from the CDC track finding efficiency and the uncertainty from the additional constraints of the vertex detector cuts, which yields ±2.3%.

As a check, another way to place limits on the track finding efficiency is by using the well-measured average total charged multiplicity from the Mark II[113] and the four LEP[114][115][116][117] experiments. The average of these multiplicity measurements is 20.94±0.20 tracks per event. The efficiency is measured for two cases,

1. vertex quality track cuts, and
2. CDC only track cuts, as described above.

In order to use the world average measurement of the multiplicity, the reconstructed multiplicity measured in each case must be corrected to the equivalent produced multiplicity using constants determined by the Monte Carlo. Table 4–6 shows the measured and corrected multiplicities for each of the above two cases, and in each case the corrected multiplicity agrees well with the world average multiplicity. The level to which one can limit the track finding efficiency

* These are essentially the same track cuts as used in the $b\bar{b}$ event multiplicity analysis, where it is particularly important to understand the tracking efficiency. (see Section 7.2.1, "Multiplicity Track Quality Cuts," on page 194).

Track Cuts	measured multiplicity	corrected multiplicity
1. vertex quality	11.10±0.31	20.34±0.57
2. CDC only	16.71±0.35	20.90±0.44
World Average		20.94±0.20

Table 4–6 Measured and corrected multiplicities for tracks which pass the vertex quality cuts and a reduced set of cuts which do not require vertex detector information on the track. The corrections applied to our measured multiplicities use the same convention as the world average, so these values can be directly compared. Except for the world average, the errors are statistical only.

using these results depends on the uncertainty in the world average (1.0%) and the uncertainty in the measured multiplicity (2.1% for the CDC only track cuts, and 2.8% for the vertex quality track cuts). Thus the uncertainty can be measured to an accuracy of 2.3% for the CDC only cuts and 2.9% for the vertex quality track cuts. That our corrected values are within these tolerances indicate that our tracking efficiency is indeed correct as modelled by the single hit efficiencies in the Monte Carlo.

4.7 Average Interaction Point

As mentioned in Section 4.2, one can either use an interaction point which is determined for each event separately, as is done in the preceding impact parameter resolution analysis, or use an interaction point which is the average over a series of events. The former approach is used in the majority of this analysis, but use of an average IP provides a useful check.

To determine the average interaction point in the data, only a subset of the events will be used. These events are selected as those with a particularly good vertex fit. To implement this, only tracks which pass the vertex quality cuts (see Section 4.4) are considered when forming the vertex. Then the resulting vertex is required to have:

1. at least 7 vertex quality tracks in the vertex;
2. at least 70% of all vertex quality tracks in the vertex; and
3. a minor axis of the vertex error ellipse of less than 20 μm.

These cuts reject the $b\bar{b}$ events more substantially than *udsc* events, thus reducing the uncertainty from the multi-vertex nature of $b\bar{b}$ events. The Monte Carlo predicts that 84% and 77% of *uds* and $c\bar{c}$ events which passed the event selection cuts will have a vertex fit which meets these criteria, whereas only 44% of $b\bar{b}$ events pass.

The average IP position is then determined for the Z^0 data using the fit vertex position (x_{fit}, y_{fit}) by finding the quantities c_x and c_y which center distributions of

$$(x_{fit} - x_{SLC} - c_x)/\sigma_{x,fit} \text{ and } (y_{fit} - y_{SLC} - c_y)/\sigma_{y,fit}.$$

In the above expressions, $\sigma_{x,fit}$ and $\sigma_{y,fit}$ are the projections of the vertex fit error ellipse onto the x and y axes, and the parameters x_{SLC} and y_{SLC} are information from the SLC instrumentation such as the corrector magnets and beam position monitors which provide information regarding relative shifts of the beam position. To investigate the motion of the beam position, one can use the variable y_T which, as discussed in Section 4.2, is the distance from the fit vertex to the nominal IP in the direction perpendicular to the major axis of the ellipse. This distribution for data events in which the vertex has been well fitted according to the above requirements is shown for the data in Figure 4–21. The Gaussian width of this distribution is 26±1.5 μm, and it lacks any significant non-Gaussian tails.

With the additional impact parameter smearing as discussed in previous sections and no motion of the interaction point, the Monte Carlo predicts a y_T distribution of 17 μm in the width. By adding different amounts of Gaussian motion to the beam position in the Monte Carlo, and assuming this motion to be the same in both the x and y directions, it is found that a Gaussian of width 20±3 μm produces a y_T distribution with the same width as that observed in the data. As a check of possible systematic effects which might result from the various cuts imposed in this study, the above analysis was repeated allowing all tracks, not just the vertex quality tracks, to be fit to the vertex. Furthermore, no vertex quality requirements were applied. In this case, an IP smearing of between 16 and 20 μm was found to provide the best data/Monte Carlo agreement, which is in agreement with the above value.

Instead of comparing the displacements of the fit vertices, one can look directly at the impact parameter significance distributions to determine the motion of the interaction point. To do this, the same log-likelihood comparison techniques were employed as were used previously in the study of the impact parameter resolution (see Section 4.5.1 on page 130). Again using the high precision tracks, namely those

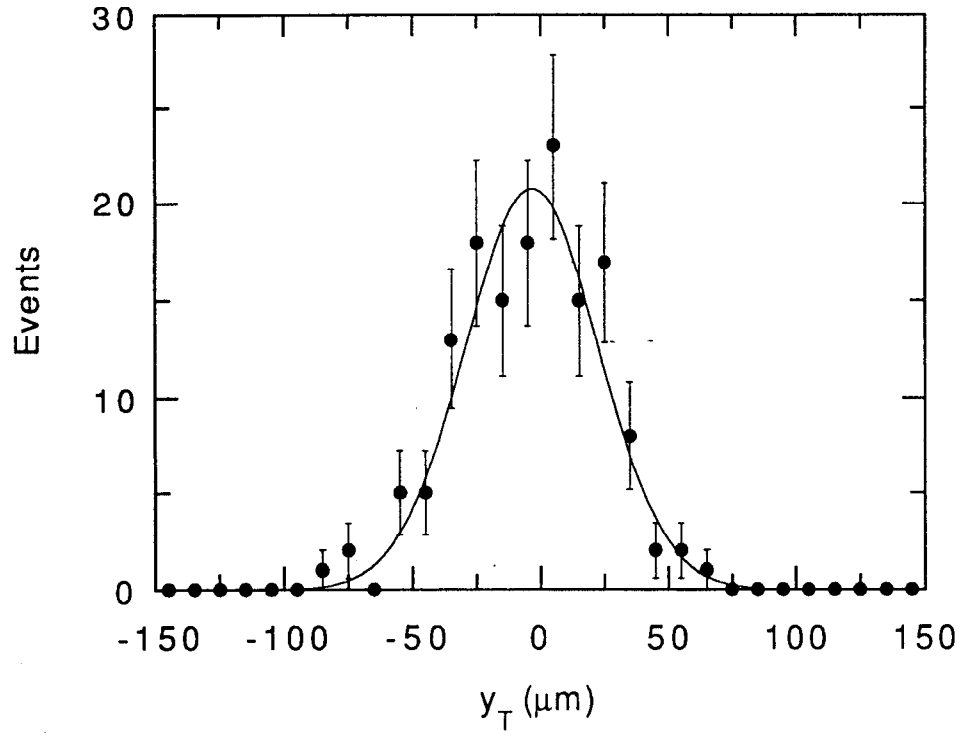

Figure 4–21 The y_T distribution for 145 data events with a well fit vertex (see vertex quality requirements on page 146), and a Gaussian fit to these points. The standard deviation of the data is 28 μm and the fit σ is 26 μm.

with $\sigma_{TR} < 25$ μm, the distribution of b/σ_b observed in the data was compared to the Monte Carlo distribution with different amounts of Gaussian IP motion. The additional impact parameter smearing found necessary in Section 4.5.1 is included in the Monte Carlo impact parameters for this comparison. The data/Monte Carlo comparison indicates that the most favored amount of IP motion is 25 μm and the 1σ and 2σ error on this are ±3 and ±7 μm. The impact parameter significance distributions for the data and the Monte Carlo with no IP motion, and with 25 μm of Gaussian IP motion are shown in Figure 4–22, both for the high precision tracks and the remainder of the tracks, which naturally are less affected by the IP motion.

The two methods of determining the motion of the IP give reasonably consistent results. From studying the y_T distribution it is evident that a Gaussian distribution aptly describes the motion of the IP. Given this, comparing the data and the Monte Carlo distributions of both y_T and b/σ_b demonstrate that a Gaussian distribution with a width of about 20–25 μm adequately describes the observed motion of the interaction point. The uncertainty in the IP motion will be a source of systematic error to measurements which rely on the use of track impact parameters (in the

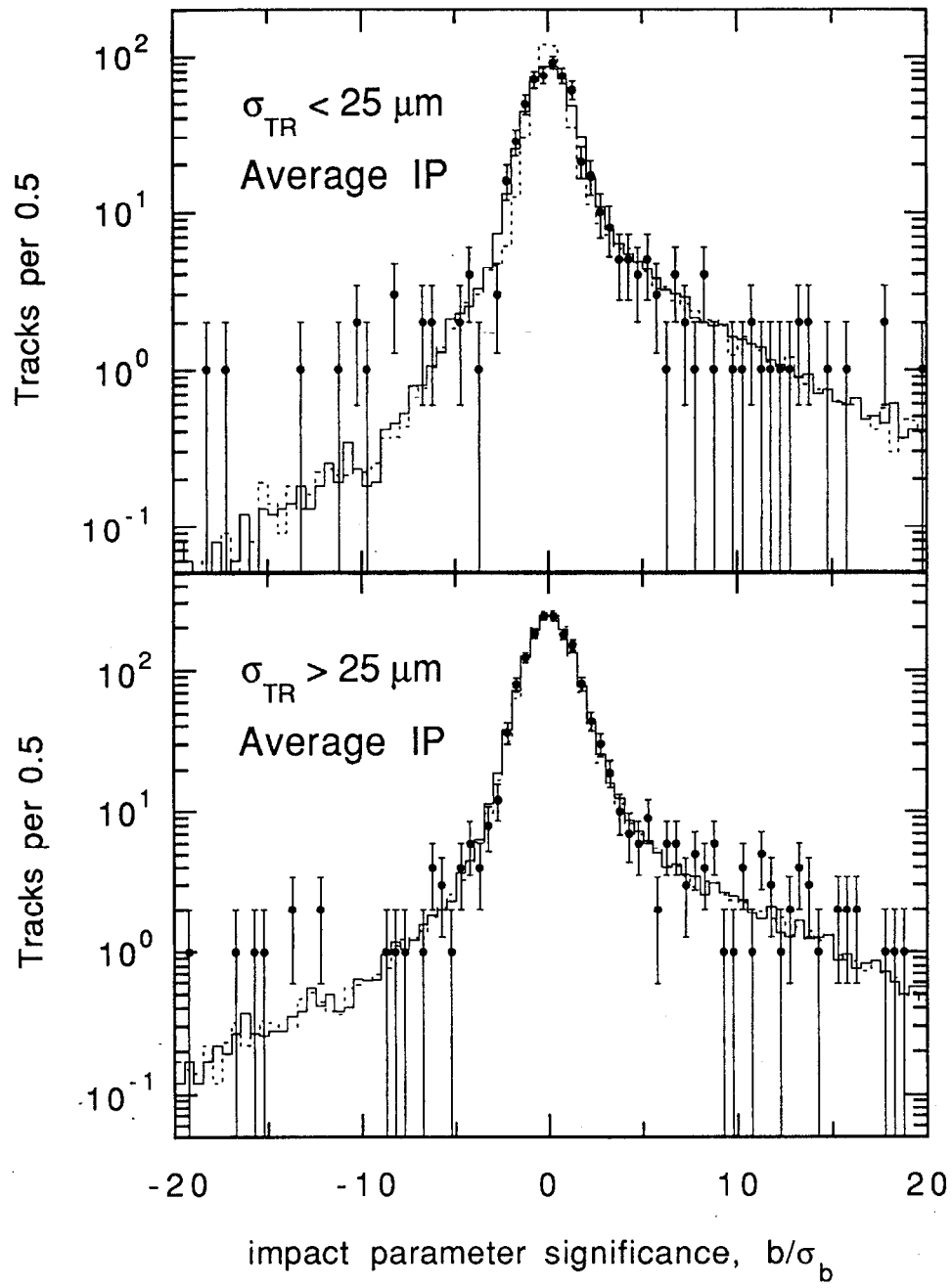

Figure 4–22 Impact parameter significance for the data (points), the Monte Carlo with no IP motion (dashed line) and the Monte Carlo with 25 μm of IP motion (solid line). All Monte Carlo tracks have had their impact parameters smeared by 10 μm for all tracks and 100 μm for 10% of the tracks as discussed in Section 4.5.1.

case of the hadronic branching fraction to $b\bar{b}$ events it would be about ±3%). This can largely be avoided if instead an event-by-event fit vertex is used. In this case, any uncertainties in the primary vertex fitting are accounted for as secondary effects as other sources of error are studied. Furthermore, because the production rate of hadronic events was quite low during the 1990 SLC run, these events are often seperated quite significantly in time. This serves to further reduce the reliability of the of an average IP determination and increase the impetus for the use of an IP determined on an event-by-event basis.

4.8 Tracking System Performance Summary

In this chapter, the performance of the Mark II tracking detector system: the Central Drift Chamber, the Drift Chamber Vertex Detector and the Silicon Strip Vertex Detector, has been evaluated. The Monte Carlo detector simulation has been tuned to reproduce as accurately as possible the observed performance. The parameters of primary importance are the impact parameter resolution and the track finding efficiency.

In studying the impact parameter resolution it was found that even with the detector simulation tuned with the observed single-layer position resolution, the resulting impact parameter resolution of the data is poorer than that of the Monte Carlo. With the small event sample, no systematic source was found which could account for this difference. Consequently, it was decided that to improve the data/ Monte Carlo agreement, the impact parameters of the Monte Carlo tracks should be smeared after the track fitting. The amount of this smearing and its uncertainty was evaluated using the impact parameter significance distribution, as this will be the basic variable used to tag $b\bar{b}$ events as discussed in the next chapter. To minimize the bias of the resolution studies on the resulting measurements, only those tracks with $b < 0$ were used in the resolution study, whereas the tracks of interest, namely those from B decay will primarily have positive impact parameters as a result of signing the impact parameters with the thrust axis.

It must be noted that because this additional impact parameter smearing is applied to tracks on a random basis, it almost certainly is not applied correctly in the sense that no correlations with the unknown source of the degraded resolution could be made. Nonetheless, this is not a major impediment to the subsequent measurements which rely on impact parameter information. This is the case because the correction resulting from this smearing is relatively minor, such that if no smearing were applied, the resulting measurements would change within the

quoted systematic errors. If, however, higher statistics were available, it would be advantageous to reduce the uncertainty associated with the resolution. It is indeed quite possible that the resolution would be better understood with higher statistics, as the search for systematic correlations to explain the degraded resolution was hampered by the small event sample.

The tracking efficiency was also studied and it was determined that the efficiency as modelled in the Monte Carlo appears to be correct to an uncertainty of a few percent. Finally, the position of the interaction was studied and an average interaction point and the motion about this point studied. Using two related techniques, it was found that a Gaussian motion of 20 to 25 μm width appears to adequately describe the motion observed in the data.

Chapter 5

Tagging Bottom Quark Events

This chapter addresses the method used to select a subset of events which is enriched in the fraction of $Z^0 \to b\bar{b}$ events. As discussed in Section 1.4, a number of methods have been used previously, including the most common tag which looks for the high p and p_T leptons from semi-leptonic B decays. With high precision tracking detectors, such as those described in the previous chapter, it is possible to design a fairly simple yet powerful tagging algorithm which is not restricted to the semi-leptonic B decays. In particular, the goal of the tagging algorithm is both to efficiently tag the $Z^0 \to b\bar{b}$ events and to substantially reject $Z^0 \to c\bar{c}$ and $Z^0 \to u\bar{u}, d\bar{d}$, or $s\bar{s}$ events such that the tagged sample will have a high $b\bar{b}$ purity.

5.1 Introduction

In order to tag a sample of events containing a large fraction of B hadrons, one must identify distinctive signatures of these events. Among the possible characteristics of B hadrons, the mean lifetime of ~1.3 picoseconds[102][25] is particularly useful. Furthermore, a bottom-flavored hadron essentially always decays into a charmed hadron,[119] which also has a lifetime between ~0.2 and ~1.0 picoseconds, depending on the particular species.[102] The bottom hadrons from the decay of the Z^0 and the subsequent fragmentation process are produced with a large boost ($\gamma \sim 6$). The mean decay length for the B hadrons is thus about 2 mm. As a consequence of this hard fragmentation, the tracks from B decay will tend to have

both high momentum and because the B hadron is quite massive, a substantial component of this momentum tends to be transverse to the B direction. The result of the long lifetime and the transverse momentum is that the particles resulting from the decay of the B hadrons will have an average impact parameter of about 200 μm. With a tracking system of sufficient resolution, one can then look for these large impact parameter tracks as the signature of the B hadron decay. To account for the accuracy of the impact parameter measurement, which varies widely with the track's momentum, direction and the number of position measurements assigned to the track, the variable used is instead the impact parameter, b, divided by the expected resolution in that quantity, σ_b, which is called the *impact parameter significance*,

$$S \equiv \frac{b}{\sigma_b}. \tag{5-1}$$

A possible tagging algorithm which uses the impact parameter significance for tagging $Z^0 \to b\bar{b}$ events is to require the presence of at least a given number of tracks, n_{min}, either in the entire event or a single jet, which have an impact parameter significance greater than some minimum value, S_{min}. Such a tag was studied in 1984 by K. Hayes.[120] The specific requirements he employed were that there be at least 3 tracks per hemisphere with a minimum significance of 3.0. To further reduce the background from $Z^0 \to c\bar{c}$ events, he also required that the invariant mass of the three or more tagged tracks be at least 1.95 GeV/c^2.

For this analysis, a number of variations of this impact parameter significance algorithm have been investigated, in order to locate that which is optimal for each measurement. As discussed in Chapter 4, the impact parameter resolution is given by the sum in quadrature of three terms:

$$\sigma_b \equiv \sqrt{\sigma_{TR}^2 + \sigma_{IP}^2 + (15\ \mu\text{m})^2}, \tag{5-2}$$

where σ_{TR} is the error due to the track fit as extrapolated back to its distance of closest approach to the IP, and σ_{IP} is the error due to uncertainty in the IP position and the 15 μm is due to the remaining uncertainty in the alignment of the SSVD. With this definition chosen for σ_b, the Monte Carlo prediction of the impact parameter significance distribution for uds, $c\bar{c}$ and $b\bar{b}$ events is shown in Figure 5–1. These distributions were generated with the standard Monte Carlo as described in Chapter 3 and include tracks which passed the vertex track quality cuts (see Section 4.4). It can be seen that the tracks from $b\bar{b}$ events comprise the

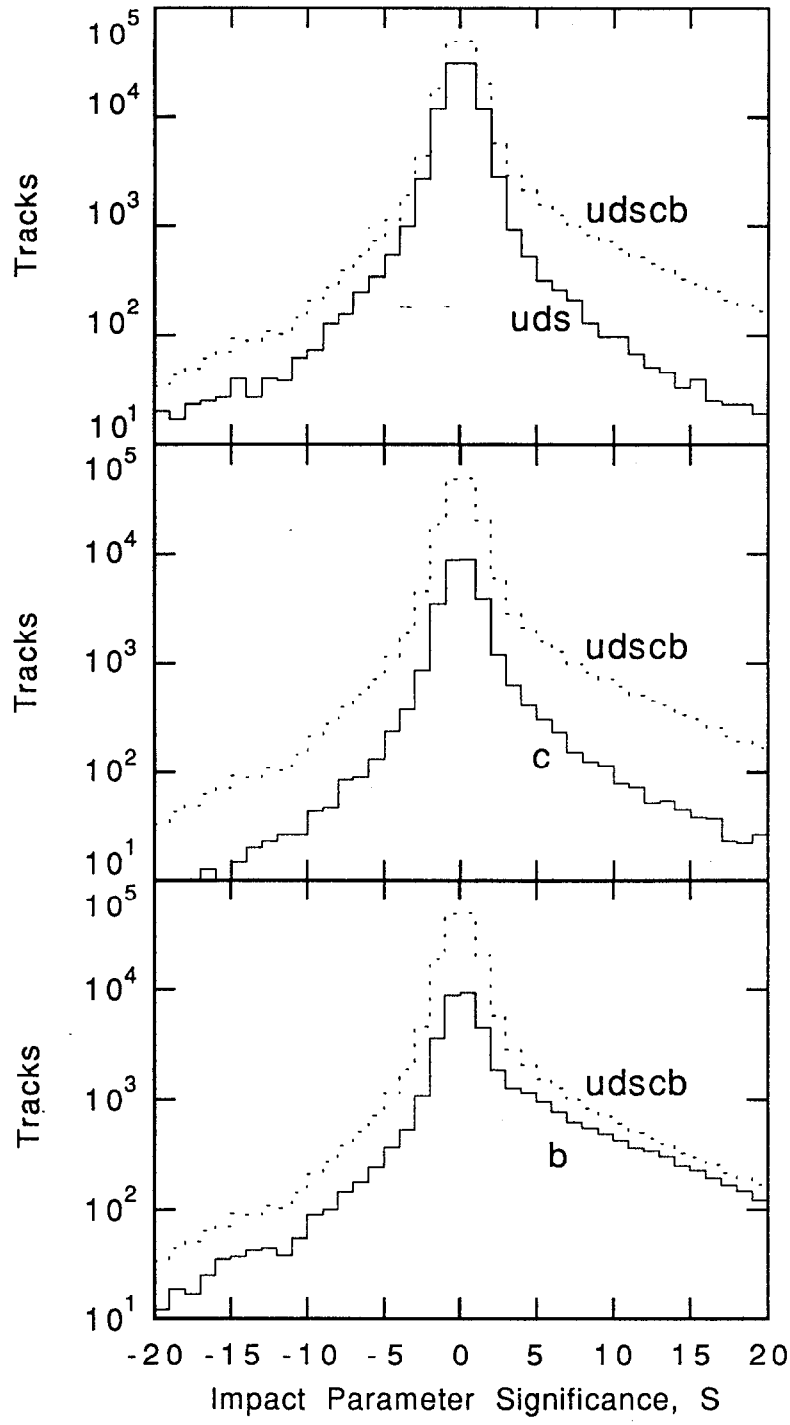

Figure 5–1 Impact parameter significance distributions as predicted by the Monte Carlo for different flavors of events.

majority of the tracks for large values of S. The number of significant tracks (namely those with $S > S_{min}$) per event illustrates the separation of $b\bar{b}$ events which is possible using a tag based on the impact parameter significance, given the resolution of the Mark II tracking detector system. Figure 5–2 shows the distribution of the number of significant tracks per event for a tag with $S_{min} = 3.0$.

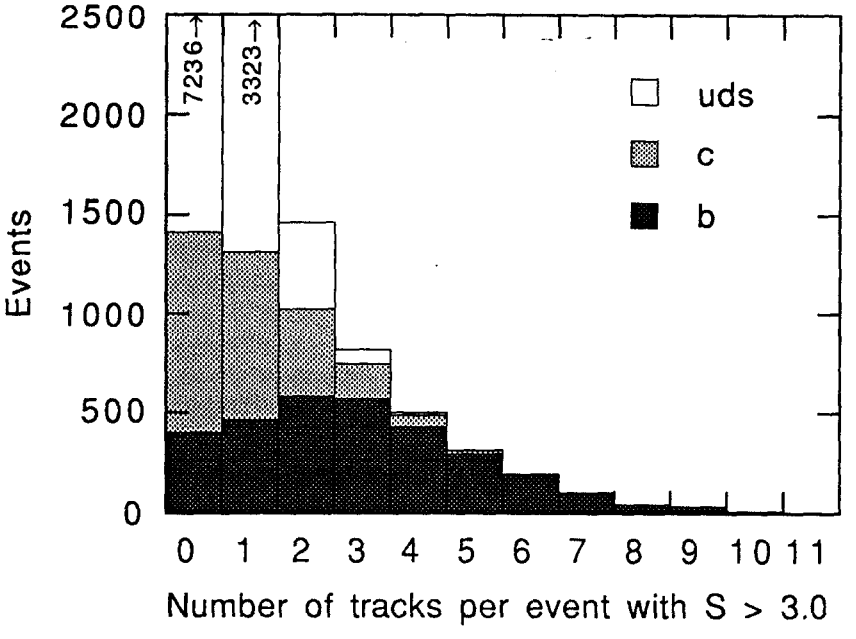

Figure 5–2 The number of significant tracks per event which illustrates the increasing fraction of b events as large numbers of tracks are required. A significant track is defined as one that has passed a minimum impact parameter significance cut, which in this example is S > 3.0.

From this it can be seen that as additional significant tracks per event are required, the events become increasingly dominated by $b\bar{b}$ as expected for the reasons described above.

Clearly one desires a tag which is both efficient in selecting $Z^0 \rightarrow b\bar{b}$ events, yet sufficiently discriminating to reject most other events. We define the efficiency for selecting $b\bar{b}$ events as the ratio of the number of tagged $b\bar{b}$ to the number of $b\bar{b}$ events *after* the hadronic event selection cuts have been applied. (Recall that the

efficiency for these event cuts is ~70%, and this varies only slightly among different flavors of events – see page 158). The $b\bar{b}$ event tagging efficiency is thus,

$$\varepsilon_b = \frac{N_b^{tag}}{h_b \mathrm{F}_b N_{udscb}} \tag{5-3}$$

where,

- N_b^{tag} is the number of tagged $Z^0 \to b\bar{b}$ events,
- N_{udscb} is the total number of produced events,
- h_b is the efficiency of the hadronic event selection cuts for $Z^0 \to b\bar{b}$ events,
- F_b is the $Z^0 \to b\bar{b}$ branching fraction, $\Gamma(Z^0 \to b\bar{b})/\Gamma(Z^0 \to \text{hadrons})$.

Note that in agreement with the above definition of efficiency, the denominator is simply equal to the number of $b\bar{b}$ events which passed the hadronic event selection cuts. Analogously, the efficiency of the tag to select non-$b\bar{b}$ events is

$$\varepsilon_{udsc} = \frac{N_{udsc}^{tag}}{h_{udsc}(1-\mathrm{F}_b)N_{udscb}}. \tag{5-4}$$

The $b\bar{b}$ purity of the tagged sample is then

$$p_b = \frac{N_b^{tag}}{N_b^{tag} + N_{udsc}^{tag}}. \tag{5-5}$$

Note that evaluating the tag $b\bar{b}$ purity necessitates the choice of some value of the $Z^0 \to b\bar{b}$ branching fraction, which is evident when the purity is rewritten in a useful form,

$$p_b = \frac{\varepsilon_b h_b \mathrm{F}_b}{\varepsilon_b h_b \mathrm{F}_b + \varepsilon_{udsc} h_{udsc}(1-\mathrm{F}_b)}. \tag{5-6}$$

While clearly a tag which is more efficient for a given purity (and conversely a tag which is purer for a given efficiency) is more statistically powerful, one must achieve a balance between efficiency and purity, because as the tagging algorithm is tuned for a higher efficiency, the effect is usually to reduce the purity. As will be shown this is in fact the case with the impact parameter significance tag. The optimal tag for a given measurement will however be the tag which yields the lowest possible total statistical and systematic error in the quantity measured. In the case of this analysis, the small data sample essentially simplifies this to finding

the tag with the lowest statistical error. This is addressed separately in the measurement of the $Z^0 \to b\bar{b}$ hadronic branching fraction in Section 6.2 on page 172 and the measurement of the non-leading multiplicity in $Z^0 \to b\bar{b}$ events in Section 7.2.2 on page 195. The remainder of this chapter will give some of the properties of the impact parameter significance tag and compare this tag to other methods.

5.2 Impact Parameter Significance Tag

Starting from the basic impact parameter tag as introduced by K. Hayes, a number of improvements were applied and the resulting tag efficiency and purity analyzed using the Monte Carlo. One of the primary improvements is the use of the physically-signed impact parameter, as described in Section 4.1.2, "Impact Parameter Signing," on page 110. This in and of itself improves the purity substantially as the tracks from light quark events will be spread almost evenly between positive and negative impact parameter while almost all of the tracks from B decay will be assigned a positive impact parameter. Among the broad range of different parameters which were varied in search of improved tag performance, there are

- the minimum track impact parameter significance required (S_{min}) for a track to be considered by the tag;
- the minimum number of significant tracks required (n_{min});
- the choice that the n_{min} tracks be in a single hemisphere, jet or the entire event;
- the use of a mass cut for the jet and hemisphere tags;
- the use of different algorithms to determine the event or jet axes.

A number of different algorithms were investigated for determining the event axis or jet axes, including the thrust axis, sphericity axis, a scaled invariant mass algorithm[101] and a momentum cluster algorithm,[107] as discussed in Section 4.1.2. The difference between these methods, in terms of the tag efficiency and purity was quite small, and when one eventually evaluates the statistical power for a measurement such as the hadronic branching fraction for $Z^0 \to b\bar{b}$, the difference is negligible. The thrust axis is therefore taken as the default.

5.2.1 Event Tags

Using the Monte Carlo with the full detector simulation, including the additional impact parameter resolution degradation found optimal in the previous

chapter the tag efficiencies were calculated. In particular, the event selection cuts and vertex track quality cuts described in Sections 4.3 and 4.4, were applied and tag properties calculated over a range of various S_{min} and n_{min} for *event tags* (namely the n_{min} significant tracks are required in the entire event, not a single jet or hemisphere). The efficiency to select $b\bar{b}$ events and *udsc* events, and the resulting purity of the tagged sample is given in Table 5–1. The purities are calculated using the $b\bar{b}$ tag efficiencies for b and *udsc* events, as well as the Monte Carlo predicted values of the hadronic event selection cut efficiencies, h_b and h_{udsc}, of 0.723±.007 and 0.698±.004 respectively, and the Standard Model prediction of 0.217 for the $Z^0 \rightarrow b\bar{b}$ branching fraction.[13] As shown in Figure 5–3, it is useful to view this information graphically by plotting the efficiency versus the purity for each of the different tags. In this type of plot the best tags from a statistical viewpoint are in the upper right corner. Namely, they select $b\bar{b}$ events with high efficiency, yet reject the *udsc* background well enough to produce a tagged event sample of high $b\bar{b}$ purity.

There are two facts which are immediately evident from this plot: there is a trade-off between achieving high efficiency and high purity. Also, the results from tags requiring different S_{min} and N_{min} primarily tend to fall within a fairly narrow band from high efficiency/low purity to low efficiency/high purity, indicating that they are using the available impact parameter information about equally well. The tag with $S_{min} > 1.0$ does significantly worse than the other tags, as it causes too many *udsc* events to be selected because this low significance cut is well into the central core of the impact parameter significance distribution. Among the other tags, those with a significance requirement of 3.0 or 4.0 appear to perform slightly better than either lower or high significance requirements in terms of achieving both high efficiency and purity.

5.2.2 Hemisphere Tags

One can also apply an impact parameter tag using only tracks in a single thrust hemisphere. A tag which requires that the minimum number of significant tracks be in one of the hemispheres will be referred to as the *hemisphere tag*. A useful feature of this tag is that it leaves the hemisphere opposite the tagged hemisphere unbiased. This facilitates its use in further analyses, such as the B lifetime or the $b\bar{b}$ event multiplicity, the latter of which is discussed in Chapter 7. If instead this is used simply to count events (as is the case in the measurement of the $b\bar{b}$ branching fraction), an event is considered tagged if *either* of the hemispheres are tagged. One

Event Tags		S_{min} 1.0	2.0	3.0	4.0	5.0
		tag efficiency for b events				
	1	0.956±.004	0.913.±005	0.877±.006	0.838±.007	0.793±.007
	2	0.905±.005	0.798±.007	0.723±.008	0.657±.008	0.580±.009
	3	0.822±.007	0.650±.008	0.542±.009	0.456±.009	0.385±.009
	4	0.704±.008	0.479±.008	0.364±.009	0.290±.008	0.224±.007
	5	0.543±.009	0.310±.008	0.222±.007	0.170±.007	0.122±.006
	6	0.402±.009	0.193±.007	0.124±.006	0.085±.005	0.055±.004
		tag efficiency for *udsc* events				
	1	0.860±.003	0.543±.005	0.369±.005	0.290±.004	0.235±.004
	2	0.640±.005	0.226±.004	0.111±.003	0.068±.002	0.047±.002
n_{min} per event	3	0.410±.005	0.080±.003	0.030±.002	0.017±.001	0.010±.001
	4	0.225±.004	0.027±.002	0.007±.001	0.004±.001	0.002±.000
	5	0.110±.003	0.008±.001	0.002±.000	0.001±.000	0.000±.000
	6	0.051±.001	0.002±.000	0.000±.000	0.000±.000	0.000±.000
		b purity of the tagged sample				
	1	0.242±.004	0.326±.005	0.406±.006	0.453±.007	0.492±.007
	2	0.289±.005	0.501±.007	0.653±.008	0.735±.008	0.780±.009
	3	0.365±.006	0.700±.008	0.841±.008	0.885±.008	0.917.007
	4	0.473±.007	0.836±.009	0.937±.007	0.954±.007	0.970±.006
	5	0.586±.009	0.918±.008	0.970±.006	0.980±.005	1.000±.000
	6	0.694±.011	0.965±.006	1.000±.000	1.000±.000	1.000±.000

Table 5–1 Event tag efficiency to tag a b event, a *udsc* event and the b purity of the resulting sample, as calculated by the Monte Carlo. (The associated errors are the statistical errors from the Monte Carlo). The efficiency for tagging a c event is greater than that for a *uds* event, with the factor varying widely depending on the restrictiveness of the tag. For example, the tag which requires at least 3 tracks with a minimum significance of 3.0 has a c (*uds*) efficiency of 0.098 (0.009).

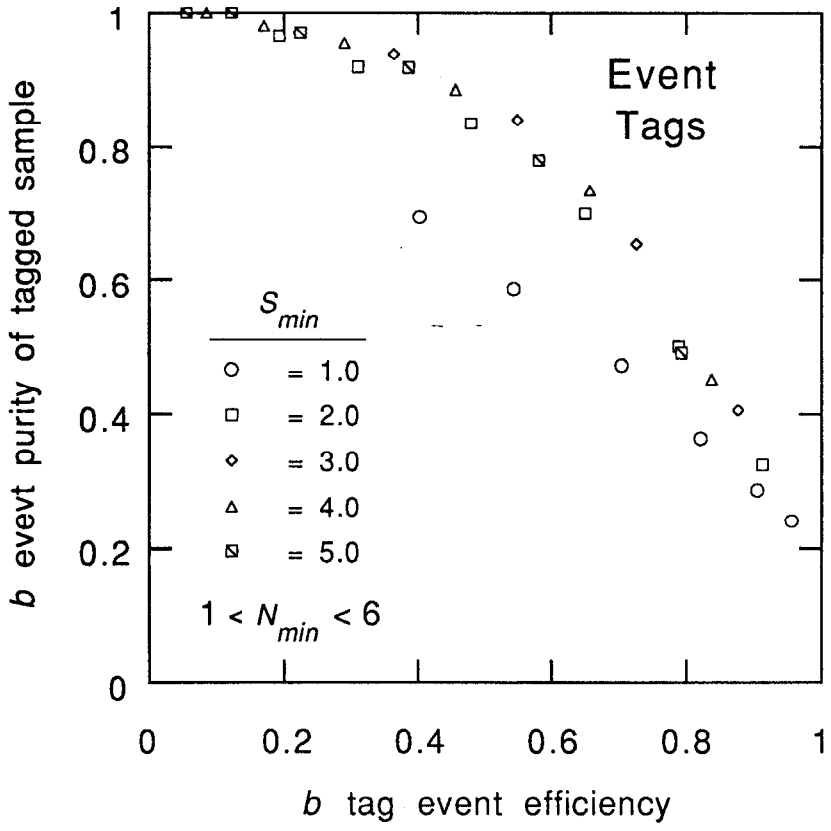

Figure 5–3 The b purity is plotted versus the b efficiency for event tags with a range of S_{min} and N_{min}. For a given S_{min}, there are six entries with different N_{min}, which go from the 1 to 6 from the left to right. These points represent data from Table 5–1.

must note that there are two possible definitions of efficiency for a hemisphere tag: the efficiency to tag a hemisphere, ε_i^{hem}, or the efficiency to tag an event as containing at least one tagged hemisphere, ε_i, where i is the initial quark flavor of the event. If the two hemispheres in an event are assumed to have uncorrelated probabilities of being tagged, then these efficiencies are related by

$$\varepsilon_i = 2\varepsilon_i^{hem} - (\varepsilon_i^{hem})^2. \tag{5-7}$$

Table 5–2 gives the event efficiencies (ε_b and ε_{udsc}) and purities for various hemisphere tags as calculated by Monte Carlo, and Figure 5–4 shows these graphically. From these it can be seen that the hemisphere tags have efficiencies and purities similar in performance to the event tags, and again in the central region, the tags with a significance requirement of 3.0 or 4.0 appear to be superior to either higher or lower significance cuts.

Hemisphere Tags		S_{min} 1.0	2.0	3.0	4.0	5.0
		tag efficiency for b events				
	1	0.956±.004	0.913.±005	0.877±.006	0.838±.007	0.793±.007
	2	0.864±.006	0.740±.008	0.660±.008	0.590±.009	0.516±.009
	3	0.683±.008	0.483±.009	0.391±.009	0.315±.008	0.264±.008
		tag efficiency for *udsc* events				
n_{min} per hemi-sphere	1	0.860±.003	0.543±.005	0.369±.005	0.290±.004	0.235±.004
	2	0.529±.005	0.161±.004	0.062±.002	0.049±.002	0.035±.002
	3	0.231±.004	0.036±.002	0.014±.001	0.008±.001	0.005±.001
		b purity of the tagged sample				
	1	0.242±.004	0.326±.005	0.406±.006	0.453±.007	0.492±.007
	2	0.319±.005	0.569±.008	0.753±.008	0.776±.008	0.809±.009
	3	0.459±.007	0.794±.009	0.889±.008	0.919±.008	0.938±.008

Table 5–2 Hemisphere tag efficiency to tag a b event, a *udsc* event and the b purity of the resulting sample, as calculated by the Monte Carlo. These efficiencies to tag the event by having tagged either of its two hemispheres can be related to the efficiency to tag any given hemisphere by Equation (5-7). (The associated errors are the statistical errors from the Monte Carlo).

As pointed out in K. Hayes' memo, a cut on the invariant mass of the significant tracks in a hemisphere of 1.95 GeV can significantly reduce the background from $c\bar{c}$ events. These events comprise 64% (76%) of the non-$b\bar{b}$ events tagged requiring at least 2 (3) tracks per hemisphere with a minimum significance of 3.0. The efficiencies and purities for these two tags are shown in Figure 5–3. While these cuts do reduce the background, the effect is such a large reduction in the efficiency that a restrictive tag without the mass cut can achieve similar purities, but with better efficiency. Consequently, tags with a mass cut are not pursued further.

5.2.3 Measuring Efficiency with Double Tagging

An advantage of the hemisphere tag as compared to the event tag is that it is possible to *measure* the $b\bar{b}$ tagging efficiency using a double tag technique instead

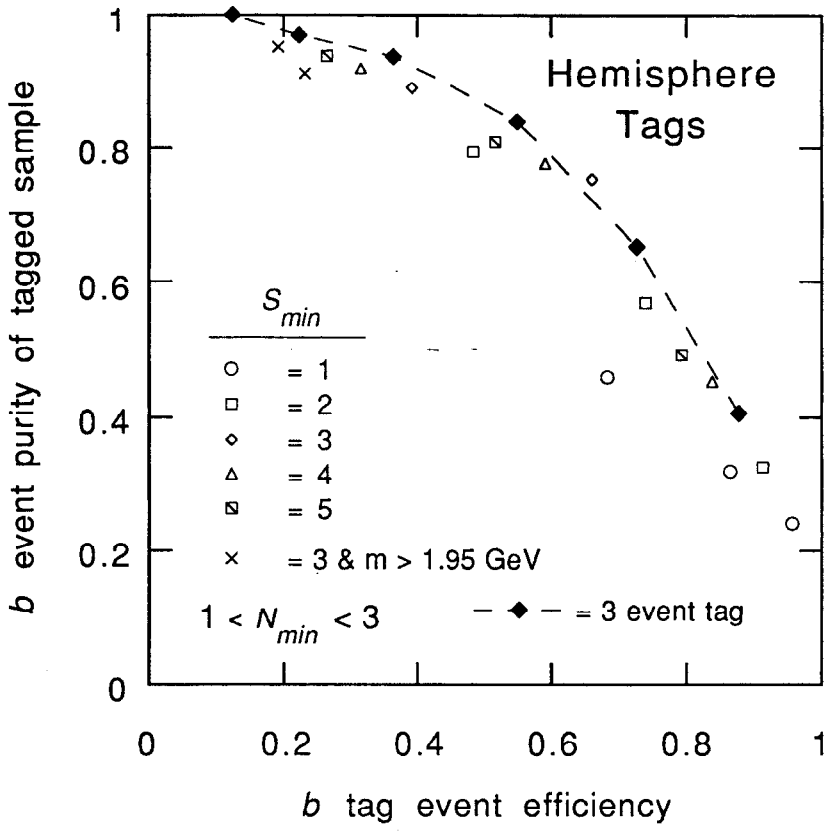

Figure 5–4 The b efficiency is plotted versus the b purity for tagging events by requiring that either hemisphere in the event be tagged with N_{min} tracks of significance S_{min} and N_{min}. For comparison, the event tags with $S_{min} = 3$ is also shown. With the exception of the points with the invariant mass cut, this data is from Table 5–1.

of relying on a Monte Carlo estimate. This involves applying the tag to one hemisphere per event, then applying it again to the opposite hemisphere in events which had a hemisphere tagged in the first pass. In an ideal case in which no *udsc* hemispheres are tagged, the $b\bar{b}$ efficiency is simply

$$\varepsilon_{2b}^{hem} = \frac{N_{2tag}^{hem}}{N_{1tag}^{hem}} \tag{5-8}$$

where N_{1tag}^{hem} and N_{2tag}^{hem} are the number of hemispheres tagged on the first and second passes, respectively.

Of course any tag will have some *udsc* component, and this complicates the situation a bit. In that case, it can be shown that

$$\varepsilon_{2b}^{hem} = \frac{N_{2tag}^{hem}}{N_{1tag}^{hem}} \cdot \left[\frac{1}{2p_{1b}^{hem}} \left(1 + \sqrt{1 - \frac{4\varepsilon_{2udsc}^{hem} p_{1b}^{hem} (1 - p_{1b}^{hem})}{N_{2tag}^{hem} / N_{1tag}^{hem}}} \right) \right] \tag{5-9}$$

where p_{1b}^{hem} is the $b\bar{b}$ purity of the hemispheres tagged on the first pass and $\varepsilon_{2udsc}^{hem}$ is the *udsc* hemisphere tag efficiency of the tag used in the second pass, namely the tag for which ε_{2b}^{hem} is to be determined. (Note that it is not required that the tags used in the two passes be the same). For the hemisphere tag requiring at least 2 (3) tracks on the first pass and at least 2 tracks with a minimum significance of 3.0 on the second pass, the correction term in square brackets is about 1.3 (1.1). Although the correction term is not of a particularly transparent form, it can be seen that in the limit $p_{1b}^{hem} \to 1$, namely no *udsc* hemispheres are tagged by the first pass tag, Equation (5-8) is recovered.

That the size of the correction term can be reduced with a higher tag purity in the first pass implies using a tag of very good purity for that pass, so as to minimize the sensitivity of the efficiency determination on the Monte Carlo estimated values of p_{1b}^{hem} and $\varepsilon_{2udsc}^{hem}$. However, as shown previously, raising the purity is usually done at the cost of lower efficiency. Thus, if limited statistics are a concern, a balance must be achieved between the reliance on statistical power and sensitivity to the Monte Carlo determined constants. The statistical power of the determination of ε_{2b}^{hem} is roughly proportional to $(N_{2tag}^{hem})^{-1/2}$. For our data sample, if we use the hemisphere tag with $S_{min} = 3.0$ and $n_{min} = 2$, 41 hemispheres are tagged on the first pass and only 8 of these are double tagged on the second pass. This corresponds to a statistical uncertainty in ε_{2b}^{hem} of order 35%, which makes this double tag measurement of the hemisphere $b\bar{b}$ tagging efficiency of little value as tighter limits can be placed on ε_{2b}^{hem} using the Monte Carlo with its resulting systematic uncertainties. In the future however, the use of a hemisphere based tag for which the $b\bar{b}$ efficiency is measured holds significant promise for reducing systematic errors.

5.2.4 Tag Dependence on Properties of *B* Hadrons from *Z* Decay

It is interesting to investigate the dependence of the impact parameter significance tag on the various properties of the B hadron. Some of these are illustrated in Figure 5–5, in which the efficiency to tag the hemisphere containing

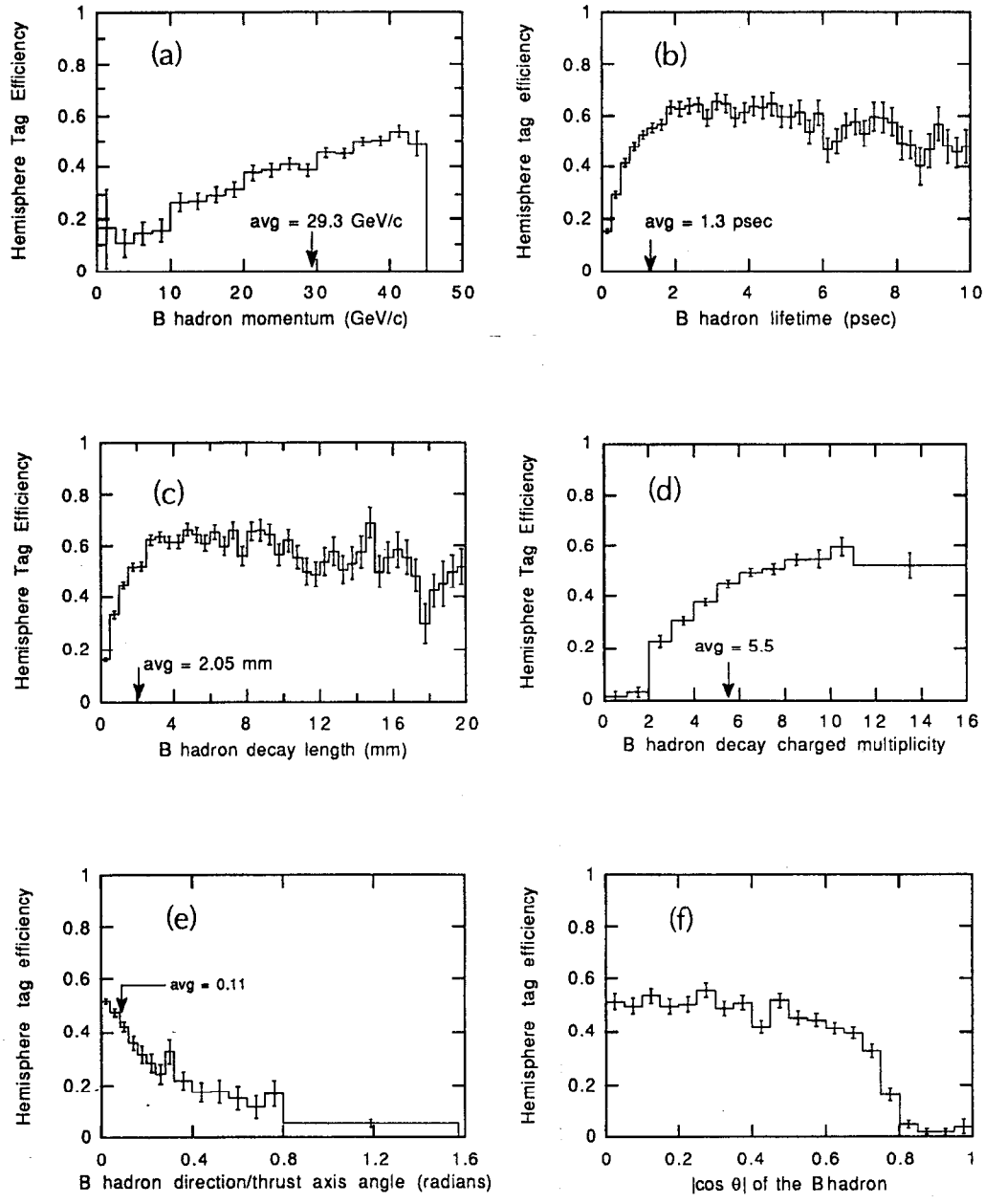

Figure 5–5 The Monte Carlo predictions of hemisphere b tagging efficiencies as a function of several variables related to the produced B hadron. The hemisphere tag efficiencies were calculated for a tag requiring at least 2 tracks per hemisphere with an impact parameter significance of at least 3.0 and only events which pass the event selection cuts were considered. The average b efficiency for this tag is 0.424.

the B hadron in question is plotted versus the property of that hadron. The tag used was to require at least 2 tracks per hemisphere of significance $b/\sigma_b > 3.0$.

As one might expect, the tagging efficiency increases with higher B hadron momentum. This dependence is illustrated in Figure 5–5(a). This is, in part, a consequence of the fact that the impact parameters of the tracks from B decay depend on the B momentum (albeit weakly once the B has a large boost). Compounding this is the use of the impact parameter significance which depends on the impact parameter resolution, σ_b. At low momentum σ_b becomes large as a result of multiple scattering, thus reducing the significance of that track.* Another effect which contributes to the poorer efficiency at low B hadron momentum is that these B's are more likely to have had a hard gluon radiate from the b quark during fragmentation. This will tend to reduce the correlation between the B hadron direction and the thrust axis resulting in more tracks with mis-signed impact parameters.

The impact parameter of a track from B decay is linearly dependent on the lifetime of the decaying B hadron (tracks from B-to-D decays have slightly less dependence and is complicated by the particular lifetime of the D and by the angle of the D with respect to the B) and thus one expects a notable dependence of the tagging efficiency on the B lifetime. From Figure 5–5(b) one can see that with the impact parameter resolution of this tracking detector system, the tagging efficiency essentially levels off around one mean B lifetime (about 1.3 picoseconds) and then gradually decreases at very long lifetimes. This decrease is an artifact of the cut which requires that all tracks have impact parameters of less than 2 mm.† The effects due to lifetime and momentum can be viewed together by studying the decay length of the B hadron. Figure 5–5(c) shows that the efficiency has almost reached a plateau by the average decay length of 2 mm. The gradual decline in the tagging efficiency for very large decay lengths is also due to the $|b| < 2$ mm track cut.

The tagging efficiency also depends on the charged multiplicity of the decaying B hadron as shown in Figure 5–5(d). The impact parameter significance tag is most adept at tagging those hemispheres with high B charged multiplicities simply because the probability of having the requisite number of significant tracks increases as more tracks are produced. However, as more particles are produced, the momenta of these particles in the decaying B's rest frame will tend to decrease.

* The dependence of the impact parameter and the impact parameter resolution on the B hadron momentum is discussed in Section 4.1.1, "Impact Parameter Definition," on page 108 and Section 4.1.3.2, "Multiple Scattering Resolution Term," on page 119, respectively.

† The track cuts are described in Section 4.4, "Vertex Quality Track Cuts," on page 128.

Upon boosting these tracks into the laboratory frame, the component of momentum transverse to the B direction will thus be smaller, resulting in smaller impact parameters for these tracks and reducing the probability to tag the hemisphere.

Figure 5–5(e) demonstrates the level to which the thrust axis approximates the actual B direction is also of importance. As discussed in Section 4.1.2 on page 110, the thrust axis approximates the B direction well in a majority of the cases, although there is a long tail, primarily due to events with substantial hard gluon radiation. This will affect the tagging efficiency through incorrect signing of the impact parameter for tracks from B decay. The probability to tag hemispheres in which the B hadron direction is not well approximated by the thrust axis drops very quickly as the angle between the thrust axis and the B hadron direction increases.

Finally, the tag efficiency is shown as a function of the polar angle in Figure 5–5(f). The efficiency is flat in the central region of the detector and falls off at large $\cos\theta$, primarily because of the event cut which requires that the thrust axis have a $\cos\theta$ of less than 0.7.

5.3 Comparison to Other Tagging Methods

Beside the impact parameter significance tag outlined in the previous section, there are other interesting ideas for tagging $b\bar{b}$ events. A survey of the many variations of tagging algorithms can be found in Chapter 1.

5.3.1 Other Impact Parameter Tags

There are many other possible algorithms for tagging $b\bar{b}$ events using track impact parameters which have different strengths. In particular, one can use the sum of the impact parameters or impact parameter significance as a signal for studying $b\bar{b}$ events. If a sum of impact parameters is made for all of the tracks in an event, it has the desirable characteristic that it will on average be insensitive to uncertainty of the interaction point location which is used to calculate the impact parameters. Varying the IP location along the event axis will simultaneously increase the impact parameters of tracks in one event hemisphere while decreasing the impact parameters in the other. Similarly, moving the IP in a direction perpendicular to the event axis also results in an average cancellation among tracks on each side of the event axis. The disadvantage of a sum of impact parameters is that low momentum tracks can unduly affect the sum. If instead one sums the impact parameter significance, this problem is corrected and some of the insensitivity to the IP location remains. Using either of these sums, or modifications

of them, one can extract information about $b\bar{b}$ events either by tagging them with a requirement that the sum be greater than some threshold cut or fitting the resulting distribution of the sums for all events. The latter provides a more powerful approach for a number of reasons as described below.

B. Schumm has done a detailed analysis along these lines.[121] In this approach, the variable which is calculated for each event is

$$\frac{1}{\sqrt{N}} \sum_{tracks} \frac{b}{\sigma_b}$$

where N is the number of tracks which pass track quality cuts that require they be well measured in the DCVD and SSVD. The factor of $1/\sqrt{N}$ accounts for the statistical uncertainty in the sum due to the number of tracks that pass the track quality cuts, which varies as the square-root of the number of tracks in the sum. It should also be noted that in order to reduce the effects from mis-measured tracks, the tracks with the largest absolute value of the impact parameter was excluded from the sum. The distribution of this variable was then fit to a form which included separate terms for *uds*, $c\bar{c}$ and $b\bar{b}$ events. These were Gaussian terms of the same width for each flavor of events (to account for the impact parameter resolution) and in the case of the heavy quark events, the Gaussian was convoluted with an exponential term, whose width is different for $c\bar{c}$ and $b\bar{b}$ events. A fit to a form such as this is systematically powerful for the determination of the hadronic branching fraction to bottom quarks, as its free parameters allow variation in the impact parameter resolution (through the width of the Gaussians) and the heavy hadron lifetimes (through the exponential tail width). Studies of the statistical power of this tag however indicate that the impact parameter significance tag as previously discussed is statistically stronger, and thus preferred for use when the total error will be dominated by statistical uncertainty. (The statistical power of the impact parameter significance tag will be discussed in more detail later in Section 6.2 on page 172).

5.3.2 Lepton Tag

The high p and p_T lepton tag has been used recently by groups at the SLC and LEP as discussed in Section 1.4.1 on page 19. Table 5–3 shows the efficiency to tag produced $b\bar{b}$ events* and the tagged sample purity for the lepton tags used in previous measurements of $\mathrm{Br}(Z^0 \to b\bar{b})$. These efficiencies and purities are illustrated in Figure 5–6. The purity of the lepton tagged events is between 62 and 75% while the efficiency if the electron and muon samples are combined is still less

Collaboration	p cut (GeV/c)	p_T cut (GeV/c)	$b\bar{b}$ efficiency	$b\bar{b}$ purity
Mark II (e and μ) [27]	> 2.0	> 1.25	10%	72%
ALEPH (e)[22]	> 3.0	> 2.0	4.6%	75%
ALEPH (μ)[22]	> 3.0	> 2.0	3.7%	71%
L3 (e)[23]	> 3.0	>1 & < 6	3.6%	76.7%
L3 (μ)[23]	> 4.0	>1 & < 6	6.9%	62.7%
OPAL (μ)[24]	> 4.5	> 1.0	5.1%	66%

Table 5–3 Efficiency and purity of the high p and p_T lepton tags used at the SLC and LEP. Note that the Mark II efficiency is higher because it is for a combined electron and muon sample.

than ~11%. At similar purities, the impact parameter significance tag has efficiency in the range 40 to 55%. Of course the lepton tag suffers from a combined semi-leptonic branching ratio of the B hadron to electrons and muons ~22%, which provides an ultimate limit for the lepton tag performance. It should be noted that the efficiency of the lepton tag for tagging semi-leptonic events is ~50%. It is clear that the impact parameter significance tagging algorithm is statistically more powerful than the lepton tags. However, the goal is to minimize the total statistical and systematic error, and when high statistics are available the limiting factors will be systematic considerations.

* Note the efficiency used in this section is different than that used previously. This is the probability to tag events in the sample of *produced* $b\bar{b}$ events, whereas elsewhere the efficiency refers to the probability to tag events in the sample of $b\bar{b}$ events *which pass the event selection cuts*.

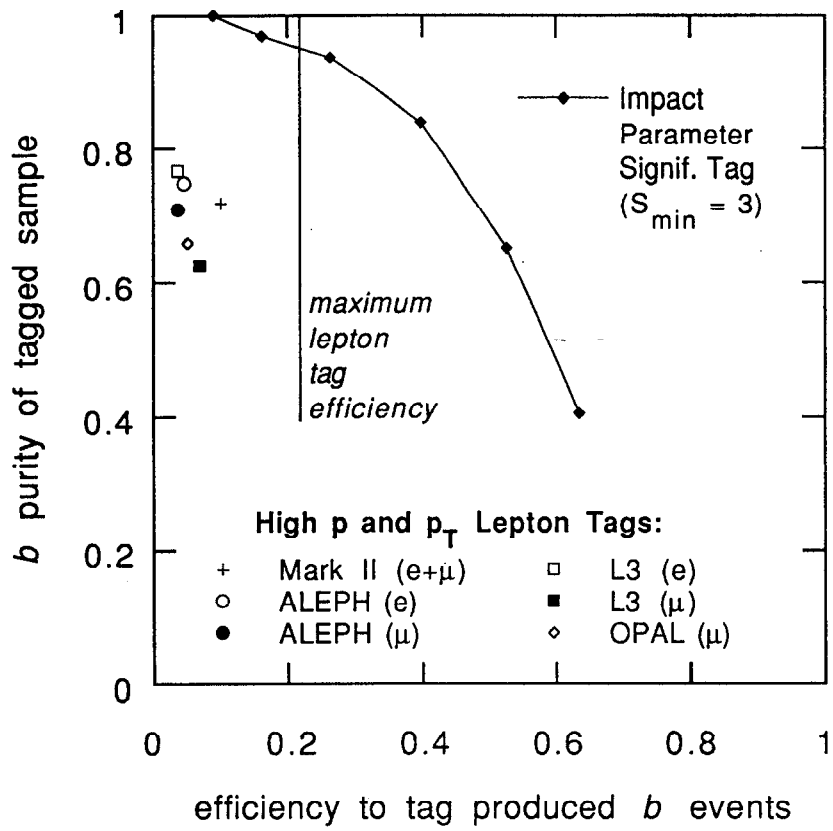

Figure 5–6 Comparison of efficiency and purity for the impact parameter tag and several previously published lepton tags (see Table 5–3). Note that this efficiency is with respect to the number of events *produced*, not the number which pass the event selection cuts as has been used previously.

Chapter 6

The Branching Fraction to Bottom Quarks

The hadronic branching fraction of the Z^0 to bottom quarks is the probability that a Z^0 decayed into a pair of bottom quarks instead of one of the other four flavors of quarks. This branching fraction, F_b, can be expressed as the ratio of partial widths for Z^0 decay,

$$F_b = \frac{\Gamma(Z^0 \to b\bar{b})}{\sum_{q=u,d,s,c,b} \Gamma(Z^0 \to q\bar{q})} , \tag{6-1}$$

assuming that only up, down, strange, charm and bottom quarks are produced in hadronic Z^0 decay. Measurements at LEP have shown that indeed there are only five flavors of quarks. For instance, the total hadronic width of the Z^0 has been measured to be 1.740±0.012 GeV (assuming lepton universality)[122], which is in agreement with the Standard Model prediction of 1.728.[13] As discussed in Chapter 1, this quantity is of theoretical interest first as a check of the Standard Model prediction of the electroweak couplings of the Z^0 to the bottom quarks and with increased precision as an exploratory tool in search of new physics.

6.1 Formalism

The $Z^0 \rightarrow b\bar{b}$ branching fraction can be determined in terms of two observed quantities, the number of events which pass the event selection cuts, N_{evt}, and the number of events which are selected by a particular tag N_{tag}. These quantities are related to the number of produced events, N_{udscb}, by the branching fraction, the efficiencies of the event selection cuts and the tag by the following relations:

$$N_{evt} = N_{udscb}\left[h_{udsc}(1-\mathrm{F}_b) + h_b \mathrm{F}_b\right] \tag{6-2}$$

$$N_{tag} = N_{udscb}\left[\varepsilon_{udsc} h_{udsc}(1-\mathrm{F}_b) + \varepsilon_b h_b \mathrm{F}_b\right]. \tag{6-3}$$

As discussed in the previous chapter, the efficiencies h_{udsc}, h_b, ε_{udsc} and ε_b are determined by the Monte Carlo, so the two unknowns are F_b and N_{udscb}. Solving for F_b yields,

$$\boxed{\mathrm{F}_b = \frac{f_{tag} - \varepsilon_{udsc}}{r_{evt}\varepsilon_b - \varepsilon_{udsc} - (r_{evt}-1) f_{tag}}} \tag{6-4}$$

where $r_{evt} \equiv h_b / h_{udsc}$, and f_{tag} is defined as the fraction of the hadronic cut selected events which are tagged,

$$f_{tag} \equiv \frac{N_{tag}}{N_{evt}}. \tag{6-5}$$

Note that F_b is sensitive only to the ratio of the hadronic event selection efficiencies h_{udsc} and h_b, rather than their absolute values.

6.2 Measurement of $\mathrm{F_b}$

The statistical error is of primary importance, because as will be demonstrated in the following sections, the total error will be dominated by statistical rather than systematic error. This is just a consequence of the small number of events recorded during the 1990 SLC runs. Consequently, the statistical error will guide the choice as to a particular tagging algorithm in an attempt to achieve the smallest possible error.

6.2.1 Statistical Error Formalism

To predict statistical error, we need to ask how the number of tagged events will fluctuate within the sample of events which have passed the event selection cuts. As the events will be divided into two groups, tagged and untagged, the statistical

error in F_b can be estimated using binomial statistics. To do this, first consider the fraction of $Z^0 \rightarrow b\bar{b}$ events in the sample of events which pass the event selection cuts, F_b^{evt}. As can be seen from Equations (6-2) and (6-3), the number of tagged events is related to this by,

$$N_{tag} = N_{evt}\left[\varepsilon_{udsc}(1 - F_b^{evt}) + \varepsilon_b F_b^{evt}\right] \tag{6-6}$$

which using the definition of f_{tag} from Equation (6-5) yields,

$$F_b^{evt} = \frac{f_{tag} - \varepsilon_{udsc}}{\varepsilon_b - \varepsilon_{udsc}}. \tag{6-7}$$

Thus the relative variation in F_b^{evt} as a function of the number of tagged events, N_{tag}, is

$$\frac{\delta F_b^{evt}}{F_b^{evt}} = \frac{f_{tag}}{f_{tag} - \varepsilon_{udsc}}\left(\frac{\delta N_{tag}}{N_{tag}}\right). \tag{6-8}$$

From the variance of the binomial distribution of tagged events, the relative uncertainty in the number of tagged events is

$$\frac{\delta N_{tag}}{N_{tag}} = \frac{1}{\varepsilon_{tag}}\sqrt{\frac{\varepsilon_{tag}(1 - \varepsilon_{tag})}{N_{evt}}}, \tag{6-9}$$

where ε_{tag} is the efficiency to tag any *udscb* event which has passed the event cuts, and is given by

$$\varepsilon_{tag} = \varepsilon_{udsc}(1 - F_b^{evt}) + \varepsilon_b F_b^{evt}. \tag{6-10}$$

Using Equations (6-8) and (6-9), the prediction of the relative statistical error in F_b^{evt} is

$$\left.\frac{\delta F_b^{evt}}{F_b^{evt}}\right|_{stat} = \frac{1}{|\varepsilon_{tag} - \varepsilon_{udsc}|}\sqrt{\frac{\varepsilon_{tag}(1 - \varepsilon_{tag})}{N_{evt}}}, \tag{6-11}$$

where ε_{tag} has been used as the average value for f_{tag}. The fraction of $b\bar{b}$ events in the sample of events which pass the event selection cuts, F_b^{evt}, is related to F_b, the hadronic branching fraction for, $Z^0 \rightarrow b\bar{b}$ as

$$F_b = \frac{F_b^{evt}}{[r_{evt} - (r_{evt} - 1) F_b^{evt}]}, \tag{6-12}$$

yielding a prediction of the relative statistical error of

$$\left.\frac{\delta F_b}{F_b}\right|_{stat} = \frac{r_{evt}}{[r_{evt} - (r_{evt} - 1) F_b^{evt}] |\varepsilon_{tag} - \varepsilon_{udsc}|} \sqrt{\frac{\varepsilon_{tag}(1 - \varepsilon_{tag})}{N_{evt}}}. \tag{6-13}$$

To get a qualitative feel for this function, Figure 6–1 shows contours of constant $\delta F_b/F_b$ on a plot of tag efficiency versus purity for an event sample of 196 events. As had been expected the region of the best statistical power is in the upper right hand corner where a tag must have high efficiency and also good purity. In the lower half of the plot the $\delta F_b/F_b$ contours repeat themselves in the opposite order from the region above. This is a region where the tag is essentially working as an anti-tag by efficiently rejecting $b\bar{b}$ events, which in principle could work equally well for measuring F_b. Finally, the bottom region of the plot is unphysical; the upper boundary of that region corresponds, to tagging all *udsc* events for each given $b\bar{b}$ efficiency, and thus the purity can not get any smaller.

As a check of whether this estimate of the statistical error using binomial statistics is indeed valid, a series of independent Monte Carlo 'experiments' were performed, each with the same number of events as in our data sample, and the statistical fluctuations found by the 68.3% bounds on the distribution of F_b calculated for each of the experiments. The upper and lower bounds for the calculated values of F_b were found to be in good agreement with the binomial estimate of the error. Furthermore, the 68.3% bounds exhibited little asymmetry.

6.2.2 Statistical Error Evaluation and Tag Selection

As our event sample is small, the resulting uncertainty in the measurement of F_b will be limited by statistics and thus necessitates choosing a tag of the highest statistical power. Evaluating the statistical error for each of the event and hemisphere impact parameter significance tags discussed in the previous chapter allows selection of the most statistically powerful combination of the minimum significance, S_{min}, and minimum number of significant tracks, n_{min}. The statistical error for each of the different tags is calculated using the Monte Carlo

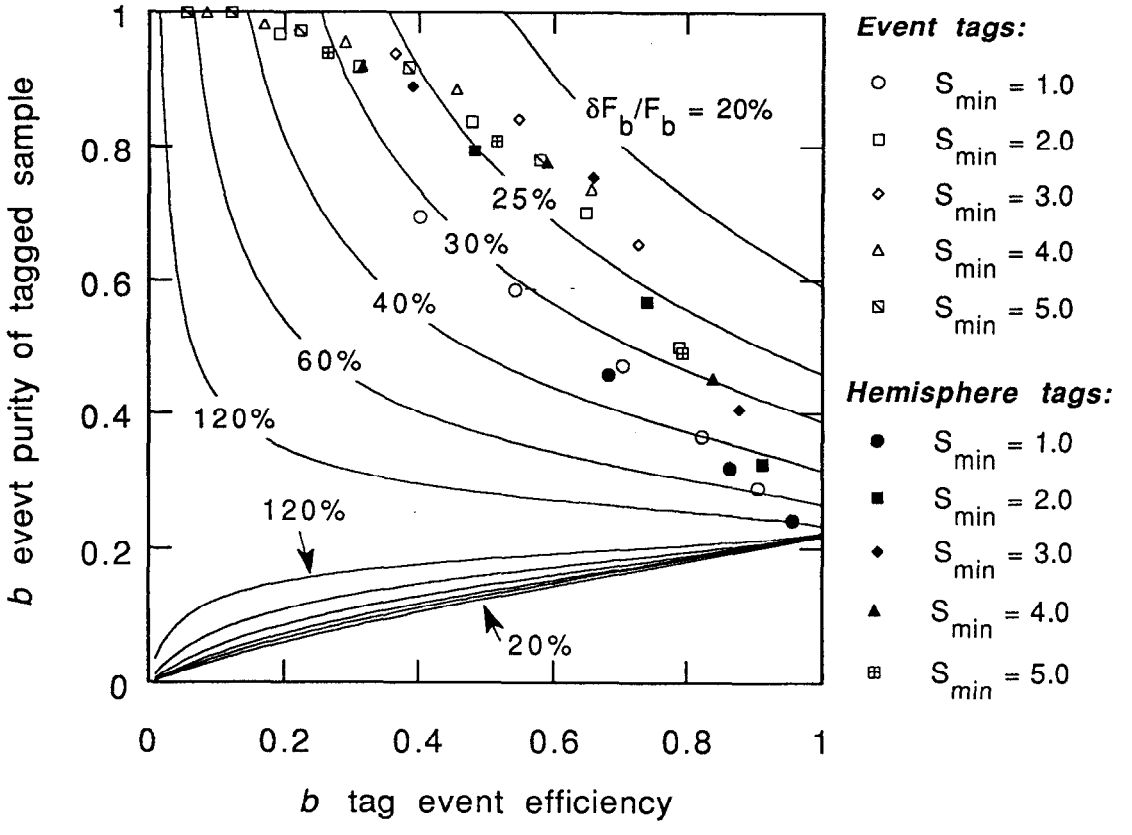

Figure 6–1 Contours of constant statistical error as a function of the b tag efficiency and the purity of the tagged sample assuming 196 events passed the event selection cuts. Also shown are the calculated efficiencies and purities for various event and hemisphere tags, which for a range of S_{min} span n_{min} of 1 to 6 for event tags and 1 to 3 for hemisphere tags. This tag data is from Table 5–1 on page 160 and Table 5–1 on page 160.

predicted efficiencies from Table 5–1 on page 160 and Table 5–1 on page 160, and the ratio for $b\bar{b}$ to $udsc$ hadronic event selection efficiency, r_{evt} = 1.035±0.011, where the uncertainty is the statistical error from the Monte Carlo determination of this value. Figure 6–1 shows the efficiencies and purities for various event and hemisphere tags with the contours of constant statistical error in F_b shown. The specific values of the statistical error for these tags is tabulated in Table 6–1 and Table 6–2 for the event and hemisphere tags, respectively. From these tables it can be seen that there is a fairly shallow minimum for the event tags around S_{min} from 3 to 5, and n_{min} around 2 or 3. Similarly, the minimum for the hemisphere tags is around the same S_{min} and n_{min} values. As the region of minimum statistical error is fairly broad, a tag near the minimum is chosen as the nominal tag. Aside from

Event Tags		S_{min}				
		1.0	2.0	3.0	4.0	5.0
		predicted fractional statistical error in F_b				
n_{min} per event	1	1.08	0.42	0.32	0.29	0.28
	2	0.56	0.27	0.22	0.22	0.22
	3	0.39	0.23	0.22	0.23	0.25
	4	0.31	0.23	0.25	0.28	0.32
	5	0.30	0.28	0.31	0.36	0.42
	6	0.30	0.34	0.42	0.51	0.63

Table 6–1 Event tag fractional statistical error in F_b, as calculated using Equation (6-13). This assumes 196 events pass the event selection cuts and the Standard Model value for F_b.

Hemisphere Tags		S_{min}				
		1.0	2.0	3.0	4.0	5.0
		predicted fractional statistical error in F_b				
n_{min} per hemi-sphere	1	1.08	0.42	0.32	0.29	0.28
	2	0.47	0.25	0.21	0.22	0.23
	3	0.33	.024	0.25	0.27	0.30

Table 6–2 Hemisphere tag fractional statistical error in F_b, using the same assumptions as in Table 6–1.

the requirement that an event pass the event selection cuts, in order to tag the event it is required that it have

> at least 3 tracks per event (n_{min} = 3) with an impact parameter significance of at least 3.0 (S_{min} = 3.0).

where only those tracks which pass the vertex quality track cuts are used.* Some of the other tags will be used in the next section as a systematic check on the resulting F_b calculated with the nominal tag.

6.2.3 Calculation of F_b

Using this nominal tag on the 196 events in the 1990 data sample, 30 of these events are tagged. With the event selection efficiency ratio $r_{evt} = 1.035 \pm 0.011$, and tag efficiencies ε_b and ε_{udsc} of 0.549 ± 0.009 and 0.030 ± 0.002 respectively, the resulting value for the hadronic branching fraction of the Z^0 to bottom quarks, as given by Equation (6-4), is $F_b = 0.234$. The errors on the above efficiencies are the statistical error from their determination by the Monte Carlo.

To evaluate the statistical error on this measurement, we use formalism similar to that developed in the previous sections, where the statistical error was predicted given only the efficiencies and the size of the event sample for each tagging algorithm. With a measured number of tagged events, it is now more rigorously correct to ask "what are the values of F_b which are 1σ allowed given the measured number of tagged events."[118] To evaluate this, Equation (6-2) and Equation (6-3) can be combined to yield an expression for the predicted number of tagged events for an assumed F_b:

$$N_{tag}(F_b;\varepsilon_b,\varepsilon_{udsc},r_{evt}) = N_{evt}\frac{[\varepsilon_{udsc}(1-F_b)+\varepsilon_b r_{evt}F_b]}{[(1-F_b)+r_{evt}F_b]}. \qquad (6\text{-}14)$$

A 1σ statistically-allowed region on a plot of F_b versus N_{tag} is then bounded by $N_{tag}(F_b+\delta F_b)$ and $N_{tag}(F_b-\delta F_b)$ where δF_b is prediction of the statistical error for a given F_b as determined by Equation (6-13). The statistical error on the value of F_b as determined by the number of events tagged is then determined as illustrated in Equation Figure 6–2. Thus the resulting value for the hadronic branching fraction, and its statistical error is

$$F_b = 0.234^{+0.053}_{-0.045}.$$

Systematic effects will be discussed in the next section.

As a check of this result for F_b, it can be compared with results calculated using the impact parameter tagging method except with other combinations of S_{min} and n_{min}. To determine the significance of the difference between F_b calculated with

* See Section 4.3 on page 127 and Section 4.4 on page 128 for more information on the event selection and vertex quality track cuts.

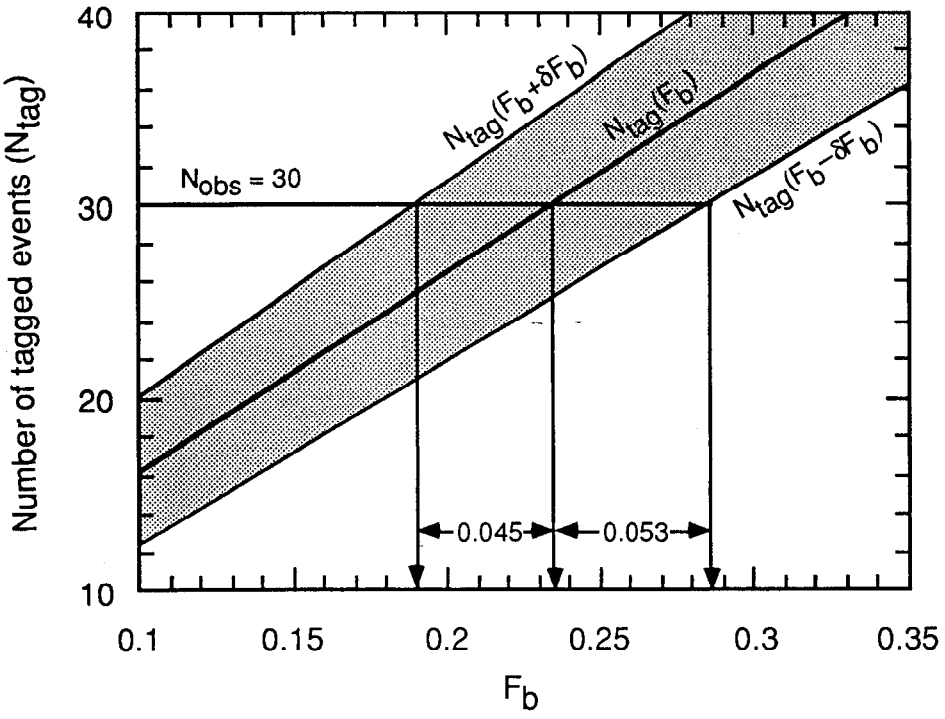

Figure 6–2 Determination of the statistical error in F_b using the nominal tag which selected 30 events. The central diagonal line the relationship between the number of events tagged and the resulting value of F_b as given by Equation (6-4). The shaded area is the 1σ allowed region. The statistical error is determined by finding the values of F_b which are 1σ allowed for the particular measured value of N_{tag}.

the nominal tag and F_b calculated with these other tags, the difference was calculated for 72 independent samples of Monte Carlo data, each with the same number of events as in the actual data sample. The expected difference between the two tags is then the central 68.3% of the distribution of the differences calculated in each MC sample. The differences in the branching fraction as observed in the data using the different tags, and the expected differences are shown in Table 6–3. Of the 14 event and hemisphere tags investigated, only 5 of those are outside of the 1σ of expected difference, and only 1 is beyond 2σ. For a normal distribution, one would expect 4.4 and 0.6 events to be outside the 1σ and 2σ limits, respectively.

Another check is to compare the above value of F_b, which was calculated using an interaction point (IP) determined on an event-by-event basis, with the result using an average IP location as discussed in Section 4.7 on page 146. This is interesting to consider because the IP position will not be not pulled by the presence

Comparison Tag		Number of events tagged	$F_b^{comp} - F_b^{nom}$	
S_{min}	n_{min}		Observed difference	Expected 1σ difference
2.0	2/event	65	–0.049	0.052
2.0	3/event	38	–0.037	0.031
2.0	4/event	27	0.007	0.029
3.0	2/event	48	–0.022	0.036
3.0	4/event	20	0.028	0.030
4.0	2/event	41	0.002	0.030
4.0	3/event	28	0.048	0.021
4.0	4/event	17	0.051	0.040
2.0	2/hemi.	51	–0.065	0.044
2.0	3/hemi.	30	0.024	0.033
3.0	2/hemi.	41	0.008	0.031
3.0	3/hemi.	22	0.023	0.031
4.0	2/hemi.	36	0.011	0.028
4.0	3/hemi.	21	0.084	0.042

Table 6–3 The number of events tagged for a variety of comparison tags with different S_{min} and n_{min} requirements is given along with the observed and expected difference between F_b as measured with the nominal tag ('*nom*') which requires S_{min} = 3.0 and n_{min} = 3 per event, and a comparison tag ('*comp*'). The 1σ limit on the difference in F_b is from the central 68.3% of the F_b difference calculated in 72 Monte Carlo event samples of the same size as the actual data sample. The *b* and *udsc* efficiencies used to calculate these F_b differences are from Table 5–1 on page 160 and Table 5–1 on page 160 and the ratio of *b* to *udsc* event cut efficiency is r_{evt} = 1.035±0.011.

of a high momentum tracks as is the case when the IP is determined for each event separately. As a consequence, the high precision tracks will tend to have larger impact parameters and thus contribute more significantly to tagging events. The event tagging efficiencies for the average IP tag which requires at least 3 tracks per event with S_{min} = 3.0 are 0.526±0.009 and 0.024±0.001 for $b\bar{b}$ and *udsc* events, respectively. In the 196 events of the data sample, 30 events are tagged by this tag.

Of these, 28 are tagged by the event-by-event IP tag. With these efficiencies, the value for the hadronic branching fraction to $b\bar{b}$ c events is found to be $F_b = 0.250 \pm 0.047$, which is consistent with the event-by-event IP result.

6.3 Systematic Error

The systematic errors in the branching fraction arise from two distinct sources, those which are due to the uncertainties in relevant physical constants and processes (lifetimes, branching fraction, fragmentation, *etc.*), and those which are due to the uncertainty in our understanding of the detectors (impact parameter resolution, efficiencies, *etc.*) In the following, all of the systematic errors are calculate for the nominal $n_{min} = 3$ / $S_{min} = 3.0$ event tag.

6.3.1 Average B Hadron Lifetime

The average lifetime of the produced mixture of different B hadrons, $\tau_{\langle B \rangle}$, has been measured by many experiments. The Particle Data Group average of measurements before 1990 is 1.18±0.11 picoseconds.[8] Subsequent measurements have also been made by the experiments at LEP,[25] which increase the world average to 1.31±0.07 psec. Using this value for placing systematic limits on F_b results in a systematic error of ±1.5% and a correction of +1.5% to F_b in order to account for the value of 1.24 psec used for the average B lifetime in the Monte Carlo. Studies have shown that two effects determine the dependence of the uncertainty in F_b on the uncertainty in $\tau_{\langle B \rangle}$. The first of these is a saturation effect which occurs when a tag becomes very efficient and consequently a change in $\tau_{\langle B \rangle}$ will cause a relatively smaller change in the number of tagged events (see Figure 5–5 on page 165). The other effect is due to tracks from $B \rightarrow D \rightarrow X$, whose impact parameters will be somewhat less affected by changes in $\tau_{\langle B \rangle}$ than will tracks directly from the B decay (whose impact parameter will just be proportional to the B lifetime).

There is also some question about the lifetime difference between different species of B hadrons, as is observed in the D system. By assuming the semi-leptonic partial widths for the charged and neutral B mesons to be the same, CLEO[123] and ARGUS[124] have made indirect measurements of the B lifetime ratio. Most recently[127] they have reported measurements of $[\tau(B^+)/\tau(B^0)] \cdot [f(B^+)/f(B^0)]$ to be 0.89±0.19±0.13 and 1.00±0.18±0.12, respectively, where f is the fraction of each B meson produced at the $\Upsilon(4s)$. A direct measurement has been made at 29 GeV by the Mark II[125] which found $\tau(B^0) = 1.20^{+0.52\ +0.16}_{-0.36\ -0.14}$ psec

Experiment	Method	$\tau_{\langle B \rangle}$ (psec)
Particle Data Group	various	1.18±0.11
ALEPH	high p and p_T e and μ impact parameters	1.29±0.06±0.10
DELPHI	high p and p_T μ and hadronic track impact parameters	1.28±0.10
L3	high p and p_T e and μ impact parameters	1.32±0.08±0.09
OPAL	high p and p_T e and μ impact parameters	1.37±0.07±0.06
OPAL	$J/\psi \rightarrow e^+e^-$, $\mu^+\mu^-$ decay length to vertex	$1.32^{+0.31}_{-0.25}$±0.15
Average		1.31±0.07

Table 6–4 List of the measurements of the average B hadron lifetime. If two errors are quoted, they are statistical and systematic, respectively. If only one error is quoted, it is the total error. The average was made accounting for the common systematics such as uncertainty about charm sector parameters and, when applicable, the physics functions used.

and at LEP by ALEPH[126] which has measured $\tau(B^+)/\tau(B^0) = 0.96^{+0.69}_{-0.44}$. However, E653[127] has measured $\tau(B^+)/\tau(B^0) = 4.0^{+2.9}_{-1.8}$. To investigate the effects of a potential lifetime difference on F_b, consider the case of the largest lifetime difference, in which the lifetimes of all neutral B hadrons are changed to 0.6 psec and that for all charged B hadrons to 2.4 psec. The resulting change in the tagging efficiency for $b\bar{b}$ events is –0.02 which corresponds to a 4% lower measurement of F_b. However, the majority of the above experimental evidence indicates that both the charged and neutral B meson lifetimes are consistent with being the same. Furthermore, because of the large mass of the B, the theoretical expectations are for much lower lifetime differences than the D system.[128] Consequently, the contribution to the systematic error from this source is based on the majority of the measurements that indicate nearly equal lifetimes, and yields <1% variation in F_b.

6.3.2 Charm Hadron Lifetimes

The lifetimes of several different species of charmed hadrons have been well measured, and the average values tabulated by the Particle Data Group.[8] Varying the D^0, $D^{\pm}$, D_s and Λ_c lifetimes within the limits of the Particle Data Group causes a systematic error in F_b of less than 1%.

6.3.3 Bottom Fragmentation

The track impact parameters exhibit a weak dependence on the momentum of the bottom hadron, (see Figure 4–2 on page 110), and thus the tag efficiencies will depend on the mean energy carried away by the bottom hadron during the fragmentation process. This mean energy fraction can be parameterized as $\langle x_E \rangle_b = E_B/E_{beam}$ and has been measured by several groups at LEP. These measurements are summarized in Table 6–5. The average of the measurements is

Experiment	Method	$\langle x_E \rangle_b$
ALEPH[22]	high p and p_T e and μ	$0.67^{+0.04}_{-0.03}$
L3[23]	high p and p_T e and μ	0.686±0.006±0.016
OPAL[24]	high p and p_T μ	0.726±0.007±0.022
Average		0.697±0.017

Table 6–5 The measurement of the energy fraction carried from fragmentation by the B hadron. The errors are statistical and systematic, respectively, if both are given, or the total error if a single value is quoted. Different effects were included by the various collaborations in determining the systematic error and the above error is an attempt to remove common effects.

$\langle x_E \rangle_b = 0.697 \pm 0.017$. Varying $\langle x_E \rangle_b$ over this range corresponds to an error on F_b of ±2%. Furthermore, the standard Monte Carlo used for determining the tagging efficiencies had $\langle x_E \rangle_b = 0.676$ and the Monte Carlo shows that F_b should be lowered by 2.0% in order to correct for the difference between this and the average value from LEP.

The shape of the fragmentation distribution has been measured by L3[23] which has shown that the x_E-distribution can be fit reasonably well to the Peterson functional form. While the rigorously correct variable to use in the Peterson function is z, not x_E,[42][43] the L3 plot implies that the Peterson shape is probably

not a bad choice, and thus no additional systematic error is applied based on the shape of the fragmentation distribution.

6.3.4 Charm Fragmentation

The average energy carried off by charmed hadrons, $\langle x_E \rangle_c$, will affect the *udsc*-event tagging efficiency and thus F_b. The average of 0.515±0.011 is the result of measurements by ALEPH and OPAL (see Table 6–6). Varying $\langle x_E \rangle_c$ over this range introduces a systematic effect of less than 1% in F_b.

Experiment	Method	$\langle x_E \rangle_c$
ALEPH[22]	high p and p_T e and μ	$0.52^{+0.16}_{-0.15}$
ALEPH[94]	$D^{*+} \rightarrow K^-\pi^+\pi^+$	$0.504^{+0.013}_{-0.017} \pm 0.008$
OPAL[95]	$D^{*+} \rightarrow K^-\pi^+\pi^+$	0.52±0.03±0.01
Average		0.515±0.011

Table 6–6 The measurement of the energy fraction carried from fragmentation by the charmed hadron as determined by fitting various momentum spectra. The errors are statistical and systematic, respectively, if both are given, or the total error if a single value is quoted.

6.3.5 Charm Production

The hadronic branching ratio to charm quark pairs, $Br(Z^0 \rightarrow c\bar{c})$ has been well measured using a high p_T lepton tag at ALEPH[22] and a D^* tag at DELPHI[129] and OPAL.[95] The average of these measurements is 0.171±0.029. Varying the fraction of charm events in the MC over this range corresponds to a systematic error in F_b of ±2%.

The ratio of the production of D to D^* mesons is also important as the neutral D^* always decays into a D^0, whereas the charged D^* decays 55±4% of the time into D^0 and the remainder into $D^{\pm}$.[102] Thus, a higher initial production of D^* versus D mesons will change the ratio of D^0 to $D^{\pm}$, and as their lifetimes differ by roughly a factor of 2,[102] the tagging efficiencies of $Z^0 \rightarrow c\bar{c}$ events will also change. ALEPH has measured the production of charm from two exclusive decay channels,[94] and has made some initial estimates of the D to D^* production fraction, but with the limited statistics of reconstruction the exclusive channels and the uncertainties regarding higher mass charm hadrons, this measurement is of little use for placing a systematic limit in the measurement of F_b. To span the entire range of

possibilities, the ratio of D to D^* production was varied from 0 to 100% and this led to an uncertainty in F_b of ±0.4%.

6.3.6 *B* Hadron Decay Properties

As the majority of the exclusive B hadron decay channels remain unmeasured, one must rely on inclusive measurements of tracks from B hadron decays to constrain the properties of these particles in the Monte Carlo. In particular, the momentum and multiplicity distributions of tracks from B decay will effectively constrain hadronic decays. CLEO[130] and ARGUS[131] have measured the mean multiplicity at the $\Upsilon(4s)$ to be 10.81±0.05±0.23 and 10.99±0.06±0.29 respectively. The average of these values taking into account an estimate of the common systematics is 10.88±0.20.* Furthermore, the variance of the multiplicity as measured by CLEO[132] is 2.3±0.2, in agreement with our Monte Carlo, which predicts a value of 2.1. The momentum of tracks from B decay is commonly measured using the variable $x = p_B/m_B$, where m_B is the B hadron mass and p_B is the momentum of the tracks from B decay in the B hadron rest frame. The distribution of x has also been measured by CLEO.[133] While these distributions measured at the $\Upsilon(4s)$ only include the decays of $B_{u,d}$ mesons, the expectation is that B_s should behave very similarly, and even the B baryons, which are expected only to be perhaps 10% of the B hadrons at high energy, are not expected to decay vastly differently. Thus the $\Upsilon(4s)$ B decay data is used to constrain the mixture of B hadrons produced at the Z^0 resonance.

The qualitative effects of these two variables, x and multiplicity, on the impact parameter tag can be easily described. When a track is produced with lower momentum in the rest frame of the B hadron, then when it is boosted into the lab frame, it will tend to have lower momentum transverse to the B direction and hence a smaller impact parameter, b. Furthermore its total momentum will be less which raises the impact parameter error, σ_b. The consequence of both of these effects is to lower the impact parameter significance b/σ_b when the B decay momentum spectrum is softened. By the same argument, a harder B decay momentum spectrum will increase the impact parameter significance. The B decay multiplicity spectrum also affects the results of the impact parameter significance tag, as there will be a larger number of tracks which have the required minimum significance.

* A correction to this $B_{u,d}$ multiplicity to include estimates of the effects from B_s and B baryons can be performed, but the remaining error is essentially unchanged. See Section 7.5, "b Event Total and Non-leading Multiplicities," on page 214 for a detailed discussion of this correction.

Note the B decay momentum distribution and the multiplicity distribution can be varied independently because the fraction of charged energy is not constrained.

To investigate the effects of the x and multiplicity distributions, an event reweighting scheme was used. Events were assigned weights depending on the charged energy fraction of the B hadron decay products (in the rest frame of the B hadron) or the number of tracks from the B decay. In order to vary the x distribution independently of the multiplicity, ad-hoc weighting functions were used. Using this scheme, it is seen that a 2% uncertainty on the mean B decay multiplicity corresponds to a systematic uncertainty of ±1.7% in F_b. To place a limit on the allowable variation in x, the region of very low momentum, $x < 0.04$ is used. This region, which contains about 20% of the tracks, is entirely unconstrained by Reference [133]. However, in order measure the charged multiplicity, CLEO and ARGUS made this extrapolation, and thus the uncertainty on the multiplicity can be used to place a limit on the tracks in this region. This method produces an uncertainty of ±2.9% in F_b.

Finally, the ratio of B hadrons which decay to D^0 or $D^{\pm}$ is also of importance, owing to the very different lifetimes of the charged and neutral charm mesons. CLEO[134] has measured this ratio to be

$$\frac{Br(B \to D^0 X)}{Br(B \to D^{\pm} X)} = 2.3 \pm 0.7.$$

Changing this ratio in the Monte Carlo over the above limit produces an uncertainty of 0.9% in F_b. Adding the above three sources of systematic error in quadrature yields a combined error 3.5% from the uncertainty in the B hadron decay properties.

6.3.7 Total Charged Multiplicity

The total hadronic multiplicity has been well measured at the Z^0 resonance by Mark II[113] and all four LEP[114][115][116][117] experiments. The average of these measurements is $\bar{n}_{had} = 20.94 \pm 0.20$ tracks per event. As the decay multiplicity of the bottom and charm hadrons is fixed in the Monte Carlo generation to the results of independent measurements, any variation in $\bar{n}_{had}$ can be considered to arise from *uds* events and the tracks produced by fragmentation in $b\bar{b}$ or $c\bar{c}$. By reweighting events based upon the number of tracks not from the decay of heavy hadrons, the uncertainty of ±0.20 tracks in the multiplicity corresponds to ±1% in F_b. The Monte Carlo total charged multiplicity is 21.93 tracks per event which is

significantly higher than the world average. Correcting F_b using the same reweighting scheme used to place the systematic limit lowers the measured value of F_b by 1.3%.

6.3.8 Non-hadronic Contamination

The initial Mark II hadronic decay analysis estimated the non-hadronic background to be 0.42 events in the sample of 398 hadronic events.[62] For the 1991 data sample of 196 hadronic events, with slightly more stringent hadronic event selection cuts, this corresponds to a contamination of less than 0.2 events. In the worst possible case, if the non-hadronic events were tagged — which is quite unlikely — it would cause a systematic error of <1% in F_b. and so will be ignored.

6.3.9 Intrinsic Impact Parameter Resolution

In Chapter 4, the impact parameter resolution of the combined tracking system was studied and it was found that additional impact parameter smearing was required in the Monte Carlo in order to reproduce the impact parameter distributions observed in the data. Comparing the data and Monte Carlo led to a choice of an optimal amount of additional smearing as well as 1σ and 2σ allowed regions as shown in Table 4–2 on page 136. The 2σ allowed region is chosen to determine the uncertainty in F_b because of the additional uncertainties regarding the source of the degraded resolution and the potential correlations with track parameters that are not taken into account when adding the additional smearing to the Monte Carlo tracks. Determining the efficiencies for each of these values yields a systematic error in F_b of +9%/–6%. A limited amount of very broad impact parameter smearing (the 'far tail') is also allowed (see Table 4–3 on page 137), and using the 2σ allowed far tail smearing leads to only a –4% variation in F_b.

It is important to mention the affect of the additional impact parameter smearing that was determined necessary in Chapter 4. If this smearing were not added, F_b would be 9.5% higher, which is only ~1σ of the systematic error due to the uncertainty in the impact parameter resolution. Thus adding this additional smearing, though probably the proper approach given the knowledge of the impact parameter resolution, does not alter the determination of F_b beyond its assigned errors.

6.3.10 Multiple Coulomb and Nuclear Scattering

The implementation of multiple Coulomb and nuclear scattering in the Monte Carlo detector simulation is discussed in Section 3.4 on page 102. Systematic

uncertainties can arise due to the imperfect knowledge of the amount and distribution of scattering material in the detectors, as well as the limitations of the models employed in the simulation. For example, the modification of the detector simulation to incorporate the Molière scattering theory significantly improved the accuracy of the simulation compared with the earlier Gaussian-based method. Additionally, although elastic nuclear scattering is modelled in the Monte Carlo, inelastic scattering was modelled only as removing the inelastically scattered track in the default Mark II detector simulation. To investigate the effects of tracks produced by inelastic nuclear scattering, a nuclear interaction generator was written and employed.

To study the amount of material in the detectors and the effects of multiple Coulomb and elastic nuclear scattering from within this material, tracks with extrapolated errors $\sigma_{TR} > 25$ μm were employed. These tracks were chosen because these lower momentum tracks will be more sensitive to multiple scattering effects. The amount of scattering material which most affects the impact parameter resolution, the beam pipe and SSVD, can be constrained using these tracks to ±3% given the available statistics. The material further outside, the DCVD and CDC, is more difficult to study but less important for the impact parameter resolution. Varying the amount of scattering material in the inner scattering layers by ±3% results in a change in F_b of ±1%.

As mentioned above the default Mark II detector simulation did not produce tracks from inelastic nuclear scattering, but instead just terminated the scattered track. A crude nuclear interaction generator was written which was based on data from nuclear scattering experiments.[135] This generator makes conservative assumptions throughout and is intended only to set an upper limit on the effects of these tracks, not to apply a correction. With this generator installed, it is found that an average of approximately 0.04 tracks per event whose origin was an inelastic nuclear interaction passed the vertex quality cuts. Furthermore, only half of these have a significance larger than 3.0 and only 3% of events have more than one nuclear interaction track which passed the vertex track quality cuts. The consequence is that the effect of inelastic nuclear scattering is small, producing an uncertainty in F_b of less than ±1%.

6.3.11 Tracking Efficiency

As discussed in Section 4.6 on page 144, the uncertainty in the track finding efficiency for the vertex quality track cuts is ±2.3%. By adding this amount of

additional tracking uncertainty to the Monte Carlo simulation, it is found that this uncertainty in the tracking efficiency corresponds to an uncertainty in F_b of ±4%.

6.3.12 Monte Carlo Statistics

The determination of the event selection efficiency ratio r_{evt}, and the tagging efficiencies, ε_{udsc} and ε_b, used a Monte Carlo sample of approximately 20,000 hadronic events. The finite size of this sample results in a statistical uncertainty in these efficiencies. The values and their uncertainties from the Monte Carlo efficiency ratio and tagging efficiencies, and their statistical uncertainties are $r_{evt} = 1.035 \pm 0.011$, $\varepsilon_{udsc} = 0.030 \pm 0.002$ and $\varepsilon_b = 0.549 \pm 0.009$, respectively. This corresponds to a systematic error of ±2% in F_b.

6.4 Hadronic Branching Fraction to Bottom Quarks

Table 6–7 shows a summary of the various contributions to the relative systematic error in F_b as described in the preceding sections. Adding these contributions in quadrature yields +11%/–9%. It is interesting to note the sources of the systematic errors. About ±6% is due to uncertainties in various physical measurements, within which the B decay properties and $\mathrm{Br}(Z^0 \to c\bar{c})$ are the largest sources, and it is probable that at least the latter will be reduced by measurements at LEP in the near future. The remainder of the error, +10%/–7%, is due to the uncertainties related to the knowledge of the tracking detector system. As discussed later, this second source of error can be substantially reduced with higher statistics as one is able to study the detectors more thoroughly.

Thus, including the small systematic corrections to correct for the most recent measurements of the total charged multiplicity (+2.0%), the average B hadron lifetime (–1.5%) and $\langle x_E \rangle_b$ (–1.5%), the hadronic branching fraction for $Z^0 \to b\bar{b}$ is measured to be

$$F_b = 0.232^{+0.053}_{-0.045}\ (\mathrm{stat})\ ^{+0.025}_{-0.021}\ (\mathrm{syst}).$$

This value for F_b is, within its uncertainty, in agreement with the Standard Model prediction of 0.217.[13] Comparison can also be made with the various previous measurements of F_b. Table 6–8 shows the previously measured values of F_b and shows an excellent agreement between this measurement and previous measurements, whose average was calculated in Section 1.5 to be 0.212±0.003±0.011.

Source of Systematic Error	Range	Systematic Error on F_b
Physics-related errors:		
average B hadron lifetime	1.24 – 1.38 psec	±2%
charm hadron lifetimes	PDG limits	<1%
b fragmentation	0.680 – 0.714	±2%
c fragmentation	0.504 – 0.526	<1%
$\mathrm{Br}(Z^0 \to c\bar{c})$	0.142 – 0.200	±2%
B decay properties	CLEO & ARGUS data (see text)	±4%
total charged multiplicity	20.74 – 21.14	±1%
Detector-related errors:		
non-hadronic events	<0.1% contamination	<1%
impact parameter resolution	2σ allowed region of b smearing	+9/–6%
multiple scattering	±3%	±1
nuclear scattering	(see page 187)	<1%
tracking efficiency	±2.3%	±4%
Monte Carlo statistics	20,000 MC events	±2%
Total Systematic Error on F_b		+11/–9%

Table 6–7 A summary of the systematic errors on F_b. The sources for each of these limits is given in the relevant section of text.

The impact parameter significance tagging algorithm used in this analysis demonstrates the strength of using a tagging method based on impact parameters as measured by high resolution tracking detectors. In the future, methods such as this should serve as important check on the lepton tag methods, as they are largely independent of the semileptonic B decay branching fraction. Furthermore, it should be possible to significantly reduce the systematic error, particularly as high statistics are available to study the impact parameter resolution of the detectors.

Experiment	F_b
Mark II	$0.23^{+0.10+0.05}_{-0.09-0.04}$
ALEPH	0.220±0.016±0.024
L3*	0.221±0.004±0.012
OPAL*	0.193±0.006±0.015
DELPHI	0.209±0.030±0.031
this measurement	$0.230\pm0.045^{+0.025}_{-0.021}$

Table 6-8 Values for F_b from previous experiments and this measurement. Those marked with an asterisk have been converted from related measurements as described in Section 1.5 on page 22.

Chapter 7

The Multiplicity of Bottom Quark Events

The average charged multiplicity of $Z^0 \to b\bar{b}$ events ($\bar{n}_b$) can be measured by making use of the impact parameter tag to select a sample composed primarily of $b\bar{b}$ events. The primary purpose of this measurement is a qualitative check of QCD phenomenology. Within the framework of QCD, non-leading particle production is governed by gluon fragmentation, triggered by the disruption of the vacuum by the color charge, and thus is expected to be independent of the flavor of the initial quarks. It has been suggested[37][38] that this expectation can be tested by measuring $\bar{n}_b$, subtracting off the well-known average B meson decay multiplicity, and comparing the resulting *non-leading* multiplicity to the multiplicity of e^+e^- annihilation at the center-of-mass energy equal to the average energy available to the non-leading system in $Z^0 \to b\bar{b}$ events, essentially $E_{nl} = E_{cm}(1 - \langle x_E \rangle_b)$. Conversely, if this expectation is taken as a given, then the non-leading multiplicity in $Z^0 \to b\bar{b}$ events may be used to extract $\langle x_E \rangle_b$, the average energy fraction carried off by the hadron system in e^+e^- annihilation.

In this chapter, both approaches are taken. The $b\bar{b}$ event multiplicity is determined by measuring the difference in multiplicity between $b\bar{b}$ and all hadronic events, which significantly reduces the systematic error of the measurement. The multiplicity comparison checking the flavor independence is then made between the non-leading multiplicity and the total multiplicity at a center-of-mass energy equal to E_{nl}. Finally, the flavor independence is assumed and a value for $\langle x_E \rangle_b$ measured.

7.1 Approach and Formalism

In the Mark II measurement of the total hadronic multiplicity at the Z^0,[113] the systematic error was dominated by a contribution of ±0.8 tracks due to uncertainty in the detector efficiency. In this measurement of $\bar{n}_b$, this systematic error is reduced by measuring

$$\delta\bar{n}_b \equiv \bar{n}_b - \bar{n}_{had} \tag{7-1}$$

with our data, and then adding back in the world average $\bar{n}_{had}$, which is now known to about ±0.2 tracks. This also has the effect of reducing the systematic error from several important sources as will be discussed below.

Given a perfectly efficient detector, and a $Z^0 \to b\bar{b}$ tag with sample purity P_t and no multiplicity bias effects, we can write the measured multiplicities of the hadronic events and the tagged subset, ($\bar{m}_{had}$ and $\bar{m}_{tag}$), as

$$\bar{m}_{had} = (1-P_h)\,\bar{n}_{udsc} + P_h\bar{n}_b \tag{7-2}$$

$$\bar{m}_{tag} = (1-P_t)\,\bar{n}_{udsc} + P_t\bar{n}_b \tag{7-3}$$

where P_h is the $b\bar{b}$ purity of the event sample which passed the event selection cuts (see Section 4.3 on page 127), and the $\bar{n}_i$'s are the 'true' average multiplicities for *udsc* and *b* events. As is now standard, we use the following definition of the true charged multiplicity:

> The true multiplicity includes any prompt track or decay product of a parent particle with a mean lifetime less than 3×10^{-10} sec.

Thus, decay products of K_s^0 and Λ are included in the true multiplicity.

In general, there are inefficiencies and biases, so we must introduce *reconstruction constants* $C_{i,j}$ relating the true multiplicities $\bar{n}_i$ to the measured multiplicities $\bar{m}_i$

$$\bar{m}_{had} = C_{h,\,udsc}\,(1-P_h)\,\bar{n}_{udsc} + C_{h,\,b}P_h\bar{n}_b \tag{7-4}$$

$$\bar{m}_{tag} = C_{t,\,udsc}\,(1-P_t)\,\bar{n}_{udsc} + C_{t,\,b}P_t\bar{n}_b. \tag{7-5}$$

However, the B hadron decay multiplicity $\bar{n}_B$ has been independently measured, so the measurement of $\delta\bar{n}_b$ is only sensitive to the size of the non-leading multiplicity $\bar{n}_{nl}$. Since the B decay products are stiffer and more collimated than the non-leading particles, the reconstruction constant $C_{i,b}$ is different for leading and non-

leading particles. Thus, to avoid having $C_{i,b}$ itself depend on $\delta\bar{n}_b$, thereby necessitating an iterative solution for $\delta\bar{n}_b$, the constants $C_{i,b}$ must be broken up into two separate sets of constants $C_{i,B}$ and $C_{i,nl}$, and so

$$\bar{m}_{had} = C_{h,\,udsc}(1-P_h)\bar{n}_{udsc} + C_{h,B}P_h\bar{n}_B + C_{h,nl}P_h\bar{n}_{nl} \tag{7-6}$$

$$\bar{m}_{tag} = C_{t,\,udsc}(1-P_t)\bar{n}_{udsc} + C_{t,B}P_t\bar{n}_B + C_{t,nl}P_t\bar{n}_{nl} \tag{7-7}$$

Finally noting that $\bar{n}_{had} = (1-\mathrm{F}_b)\bar{n}_{udsc} + F_b\bar{n}_b$, we can substitute into Equation (7-1) which yields

$$\delta\bar{n}_b = (1-\mathrm{F}_b)\,(\bar{n}_B + \bar{n}_{nl} - \bar{n}_{udsc}) \tag{7-8}$$

where $\bar{n}_{nl}$ and $\bar{n}_{udsc}$ are the solutions to the above two simultaneous equations. Solving these equations yields

$$\delta\bar{n}_b = \frac{(1-\mathrm{F}_b)}{\eta}\left[\bar{m}_{tag}\chi_{had} - \bar{m}_{had}\chi_{tag} + \bar{n}_B(\eta + C_{t,B}P_t\chi_{had} - C_{h,B}P_h\chi_{tag})\right] \tag{7-9}$$

where,

$$\eta = C_{t,\,udsc}C_{h,\,nl}(1-P_t)P_h - C_{t,\,nl}C_{h,\,udsc}(1-P_h)P_t$$

$$\chi_{had} = C_{h,\,udsc} + (C_{h,\,nl} - C_{h,\,udsc})P_h$$

$$\chi_{tag} = C_{t,\,udsc} + (C_{t,\,nl} - C_{t,\,udsc})P_t$$

In the above solution, the B hadron decay multiplicity, $\bar{n}_B$, is obtained primarily from $\Upsilon(4s)$ data, the $C_{i,j}$'s are constants determined from the Monte Carlo, and F_b is the $Z^0 \to b\bar{b}$ branching fraction. The B hadron decay constants $C_{i,B}$ are determined by inclusive decay properties measured at the $\Upsilon(4s)$, while the light decay constants $C_{i,udsc}$ are constrained by the OPAL tuning of Lund 7.1 to hadronic data.[102] The non-leading constants $C_{i,nl}$, on the other hand, are not tightly constrained by existing data, and so must be constrained by more general arguments in order to preserve the model dependence of the measurement. The uncertainty introduced by these considerations will be addressed later.

A slight simplification of Equation (7-9) lends particular insight to the behavior of $\delta\bar{n}_b$. In the case where all of the constants $C_{i,j}$ are equal to the same number C (which is roughly true in actuality) the solution for $\delta\bar{n}_b$ becomes

$$\delta\bar{n}_b = \frac{(1-F_b)}{(P_t - P_h)}\,\frac{(\bar{m}_{tag} - \bar{m}_{had})}{C} \tag{7-10}$$

Here one can clearly see the advantage of measuring $\delta\bar{n}_b$ rather than the total multiplicity: systematic fluctuations which similarly affect the hadronic event sample and the tagged event sample multiplicities will tend to cancel. In particular, this avoids potentially large systematic errors due to tracking efficiency, photon conversions, and nuclear scattering. However, some remnant of systematic uncertainty will still result from these sources. This is because the actual formula for $\delta\bar{n}_b$ is Equation (7-9) and the reconstruction constants used in this formula are slightly different from each other, such that $\bar{m}_{tag}$ and $\bar{m}_{had}$ do not enter this equation as symmetrically as they do in Equation (7-10).

7.2 Measurement of Multiplicity Difference

This section describes the track cuts used to select a well-understood set of reconstructed tracks for the multiplicity determination, the tags used to select a $b\bar{b}$-enriched sample, the biases these tags induce on the multiplicity, the determination of the various constants, and a value for $\delta\bar{n}_b$.

7.2.1 Multiplicity Track Quality Cuts

Within the selected sample of events (the hadronic events and those tagged as $b\bar{b}$ events), a subset of the tracks is selected for inclusion in the measured multiplicities $\bar{m}_{had}$ and $\bar{m}_{tag}$. The track cuts employed are similar to the cuts used to select vertex-quality tracks for selecting $b\bar{b}$ events except for the requirements of DCVD and SSVD information. An important aspect of this analysis is that the vertex detector information is used only to tag $b\bar{b}$ events, while the multiplicity tracks are selected using the well-understood CDC.

The multiplicity track cuts are as follows.

1. The calculated angle of the track with respect to the beam axis must satisfy $|\cos\theta| < 0.8$ such that the tracks are well inside the active regions of the tracking detectors.
2. The projection of the track's momentum into the plane perpendicular to the beam axis, p_{xy}, must be greater than 0.150 GeV/c.
3. The distance of closest approach in the z-direction of the track to the nominal interaction point must satisfy $|z_m| < 15$ mm.
4. The number of hits associated with the track in the CDC tracking must be at least 25 of the 72 possible.
5. The impact parameter of the track, with respect to an interaction point which is fit on an event-by-event basis, must satisfy $|b| < 15$ mm.

Table 7–1 gives the fraction of tracks remaining after each cut is applied in order, as estimated by the Monte Carlo. Extensive studies have been done to ensure that the

track cut	% passed
1. $\|\cos\theta\| < 0.8$	94.3%
2. $p_{xy} > 0.15$ GeV	88.6%
3. $\|z_m\| < 15$ mm	80.8%
4. $N_{CDC} \geq 25$	80.6%
5. $\|b\| < 15$ mm	78.9%

Table 7–1 The fraction of the reconstructed tracks passing each of the multiplicity track quality cuts in events which pass all of the hadronic event selection cuts.

Monte Carlo is modelling these values sufficiently. This also allows systematic limits to be placed on the calculated value of $\delta\bar{n}_b$ which result from uncertainties associated with these cuts. (This will be addressed in detail in Section 7.3.11 on page 208).

In order to get some insight as to the relationship between the generated true multiplicity tracks (namely, the tracks to be counted in the multiplicity according to the definition on page 192) and those actually reconstructed in the detector, the generated and detected tracks were matched in the Monte Carlo. Of the reconstructed tracks, 90.5% are true multiplicity tracks, while the remaining 9.5% are due to conversions. (The effects of these conversion tracks on the determination of $\delta\bar{n}_b$ is addressed in Section 7.3.9 on page 207). On the other hand, of the generated true multiplicity tracks, 70.8% are properly reconstructed, 20.2% are outside the detector acceptance in $|\cos\theta|$ or p_{xy}, 6.5% are decays in flight from parents of lifetimes longer than the requisite 3×10^{-10} sec and the remainder are due to detector inefficiencies. Thus the corrections to the measured multiplicity are not large.

7.2.2 Impact Parameter Tags and Biases

As for the $Z^0 \to b\bar{b}$ branching fraction measurement, $Z^0 \to b\bar{b}$ candidates were selected by requiring that the event have at least a certain number of tracks, n_{min}, with a physically-signed impact parameter significance b/σ_b of at least some minimum value S_{min}.* Of the many variations of this tag using different

combinations of n_{min} and S_{min}, three tagging algorithms were investigated further, based on their statistical power for measuring the non-leading multiplicity. Each of these tags used S_{min} = 3.0.

7.2.2.1 Impact Parameter Tag Properties

The three significant track event tag ('EV3') was found, based on Monte Carlo studies, to have less statistical power than a two track event tag ('EV2'). One can remove much of the multiplicity bias introduced by the tag by restricting the tag to one hemisphere (as defined by the plane perpendicular to the thrust axis), and counting only the multiplicity in the hemisphere opposite to the tagged hemisphere. Thus, we included in the study a hemisphere-only tag ('HE2') requiring two or more significant tracks. The relevant properties of these three tags, as well as the event cut, are summarized in Table 7–2. Because there are very significant correlations

Tag Property	Event Selection	EV2 Tag	EV3 Tag	HE2 Tag
minimum impact parameter significance, S_{min}	—	3.0	3.0	3.0
minimum number of significant tracks, n_{min}	—	2/event	3/event	2/hemi.
$b\bar{b}$ efficiency (MC)	0.723±.007	0.723±.008	0.542±.009	0.423±.006
$b\bar{b}$ sample purity (MC)	0.227±.002	0.653±.008	0.841±.008	0.753±.007
Number of events tagged	196	48	30	49
$\delta\bar{n}_b$ statistical error	—	$^{+1.78}_{-1.86}$	$^{+1.97}_{-1.85}$	$^{+2.05}_{-2.00}$

Table 7–2 The properties of the event selection cuts and the three tags used for this multiplicity measurement. The tag efficiency for the tags is given with respect to the number of events which have already passed the hadronic event cuts and is that predicted by the full detector simulation Monte Carlo. The number of events tagged is what is observed in our data sample. The statistical errors are the result of a Monte Carlo study.

between the hadronic event multiplicity, the sample multiplicity and the sample purities, the statistical error was calculated using a Monte Carlo method. Specifically, it was calculated by using 72 Monte Carlo samples of identical size to the data sample and calculating $\delta\bar{n}_b$ in each. The spread in the resulting values of

* See Chapter 5 for more information on using the impact parameter significance tag to select $b\bar{b}$ events.

$\delta\bar{n}_b$ for all of these experiments indicates the statistical precision of the measurement. The 1σ range of $\delta\bar{n}_b$ was chosen as the central 68.3% of the values found in the 72 data samples. As will be discussed in a later section, the systematic error in the $Z^0 \to b\bar{b}$ multiplicity measurement is relatively small, and so we chose the EV2 tag for the measurement based solely on its statistical power. The other two tags will be used as checks on the multiplicity result.

7.2.2.2 Multiplicity Biases Introduced by the Impact Parameter Tags

Biases introduced by the tags, to the extent that they are modelled by the Monte Carlo, are taken into account naturally in the Monte Carlo-derived reconstruction constants $C_{i,j}$ described in Section 7.1. In order to have confidence that the Monte Carlo is correctly accounting for tag biases, it is helpful to understand the source of all biases which affect the result by more than a fraction of the statistical error.

A tag can alter the relationship between reconstructed and true multiplicity in two ways: either via correlations with the event multiplicity (e.g. events with high multiplicity B hadron decays are more likely to be tagged), or via correlations with the reconstruction efficiency. To study these effects, one can define two quantities: the *raw bias* and the *reconstructed bias*. The raw bias for a given set of tracks, j, (where $j \in udsc$, $b\bar{b}$ non-leading, or B decay tracks) is given by the following ratio of the Monte Carlo generated multiplicities $\bar{n}^{\,j}_{gen}$ for the sample of b-tagged events and for all of the hadronic events:

$$B^j_{raw} = \frac{\bar{n}^{\,j}_{gen}\ \text{(tagged events)}}{\bar{n}^{\,j}_{gen}\ \text{(all hadronic events)}}. \tag{7-11}$$

This raw bias is a measure of the correlation between the tagging efficiency and the multiplicity of the events tagged. The reconstructed bias is similarly given by ratio of multiplicities of tracks reconstructed by the tracking detectors after the Monte Carlo detector simulation, $\bar{m}^{\,i}_{recon}$:

$$B^j_{recon} = \frac{\bar{m}^{\,j}_{recon}\ \text{(tagged events)}}{\bar{m}^{\,j}_{recon}\ \text{(all hadronic events)}}. \tag{7-12}$$

where again the multiplicity sample i is that of subset f the tracks such as the $udsc$, $b\bar{b}$ non-leading, or B decay tracks. A value of 1.0 corresponds to no bias.

In the case of the hemisphere tag HE2, which is expected to be relatively free of bias, the raw bias is 0.989±.008 (1.016±.016) and the reconstructed bias 1.036±.009 (1.056±.015) for $Z^0 \to b\bar{b}$ ($Z^0 \to udsc$) events. The $1-2\%$ raw biases correspond to

less than 0.5 tracks, and are statistically consistent with 1.0. The reconstructed biases are significant, and are found to be due to the back-to-back correlation introduced by recoiling jets: the HE2 tag preferentially tags central events (namely those with $\cos\theta_{thrust} \sim 0$) due to the higher average reconstructed multiplicity, and since the untagged jets used to measure the multiplicity is recoiling against the tagged jet, it carries the preference towards events with a larger reconstruction fraction into the multiplicity measurement. If the sample is restricted to central events only ($|\cos\theta_{thrust}| < 0.6$), the reconstructed bias is reduced to 1.016±.011 (1.013±.019) for $Z^0 \rightarrow b\bar{b}$ ($Z^0 \rightarrow udsc$) decays. This is consistent with no bias. The removal of 3-jet events from the sample, which also might be expected to introduce significant hemisphere-to-hemisphere correlations, produces very little change in the HE2 tag bias. Nevertheless, it has been demonstrated that, for the HE2 tag, the 6% tag bias is understood in terms of effects well modelled by the Monte Carlo.

For the EV3 tag, where the biases are expected to be the largest,* the raw and reconstructed biases are given in Table 7–3 for $Z^0 \rightarrow b\bar{b}$ and $Z^0 \rightarrow udsc$ decays. The biases are given with the standard event cuts and after restricting the sample to central 2-jet events as above. The sources of this bias will be investigated separately for the $b\bar{b}$ and *udsc* events below.

Event Cuts	$Z^0 \rightarrow b\bar{b}$		$Z^0 \rightarrow udsc$	
	raw bias	recon. bias	raw bias	recon. bias
standard cuts	0.985±.008	1.005±008	1.060±.016	1.143±.017
2-jet events & $\|\cos\theta_{thrust}\| < 0.6$	1.012±.010	1.031±.010	1.090±.019	1.113±.020

Table 7–3 Raw and reconstructed biases for the EV3 tag.

Although the $Z^0 \rightarrow b\bar{b}$ reconstructed bias of 1.031 looks small, it is so only because of a cancellation between the biases for leading and non-leading tracks (1.061 *vs.* 0.995). However it is expected that significant biases may be present for an event tag. The possible sources of this bias include the B energy from fragmentation and the B decay multiplicity. The bias due to the B hadron energy can arise from the fact the impact parameter tag is more efficient for a higher B energy† and if the B has much of the energy, less is available for the non-leading

* By requiring that a given event have more significant tracks, the EV3 tag will more strongly bias the measured multiplicities than the less restrictive EV2 tag.

system to form additional particles. To examine this source of bias, events were selected in which both B hadrons have $x_E < 0.5$, $0.5 < x_E < 0.75$ or $x_E > 0.75$. The resulting biases in these event samples were found to still be statistically inconsistent with unity, indicating that the B hadron energy is not the dominant source of bias. In fact, the B hadron energy spectrum for the B hadrons in events tagged by the EV3 tag has virtually the same mean as that for all produced B hadrons, which indicates that this should not cause a bias. The B decay multiplicity is also a potential source of bias because a larger B decay multiplicity raises the tagging efficiency and also the multiplicity of the entire event. To investigate the bias due to the B decay multiplicity, the sample of events was binned by the number of tracks from the decays of both B hadrons in the event. Both the raw and reconstructed biases for the leading and non-leading tracks were found to be statistically equal to 1.0 within each of these bins, indicating that it is the B decay multiplicity which is the major source of bias for the event tag in $b\bar{b}$ events.

For $Z^0 \rightarrow udsc$ events the source of the remaining bias is also straight forward: it is simply due to the tendency of high multiplicity events to more often have the requisite number of significant tracks to be tagged. A simple calculation can demonstrate this for *uds* events. If one assumes that the significant tracks in such an event are uncorrelated, then binomial statistics can be used to estimate the *uds* bias. Two inputs are used from the full Monte Carlo: the probability of a track in a *uds* event having $b/\sigma_b > 3$ and a hadronic reconstructed multiplicity distribution. With this, the average reconstructed multiplicity of the tagged sample can be determined and the bias calculated. The results are that reconstructed biases for the EV3 (EV2) tag are 1.18±0.03 (1.13±0.01) using the full Monte Carlo and 1.24 (1.15) with this model. For $Z^0 \rightarrow c\bar{c}$ events, the effect of correlated heavy quark decay tracks is not large enough to significantly change the generally uncorrelated behavior seen with $Z^0 \rightarrow uds$ events.

Thus the source of the bias introduced by the different tags has been resolved for effects modelled by the Monte Carlo. For the hemisphere tag it results primarily from the back-to-back correlation between recoiling jets. For the whole event tags, the bias in $Z^0 \rightarrow b\bar{b}$ events results from the correlation with the high multiplicity and the large impact parameters of tracks from the decay of the heavy quark. For $Z^0 \rightarrow udsc$ events the bias simply arises from correlation between multiplicity and the likelihood of having two uncorrelated tracks with significantly mis-measured

† See Figure 5–5 on page 165 for information on the sensitivity of the impact parameter tag to certain B hadron properties.

impact parameters. In all cases, we are confident that these effects are either well modelled in the Monte Carlo, or will be properly addressed in the section on systematic errors (e.g. B decay kinematics, uncorrelated impact parameter smearing). Of course, there is always the possibility that there are biasing effects which the Monte Carlo knows nothing about. For these, we have only the consistency between the whole-event tags and the relatively unbiased hemisphere tag to indicate that the biases are properly modelled.

7.2.3 Calculation Parameters and Results

In order to derive $\delta\bar{n}_b$ from the measured multiplicity of the hadronic and the tagged events, the sample b-purities and reconstruction constants introduced in Section 7.1 must be determined. The purities P_h and P_t are determined by counting the number of b and $udsc$ events in the hadronic and tagged Monte Carlo samples. The reconstruction constants, $C_{i,j}$, are given by the Monte Carlo ratio of the reconstructed to generated multiplicity for all events in the categories specified by the indices i and j (*i.e.* tagged/un-tagged and $udsc$/B-decay/non-leading $b\bar{b}$). The values of these parameters for the event cuts and the three tags described in the previous section are shown in Table 7–4. The B decay multiplicity used to calculate

Tag Property	Hadronic Event Cuts	EV2 Tag	EV3 Tag	HE2 Tag
C_{udsc} (MC)	0.804	0.878	0.889	0.819
C_B (MC)	0.848	0.917	0.959	0.879
C_{nl} (MC)	0.749	0.745	0.731	0.776
tag b purity (MC)	0.227	0.653	0.841	0.753
mean multiplicity (data)	16.71	18.52	19.37	18.66
$\delta\bar{n}_b$ (data)	—	2.11	2.73	2.76

Table 7–4 The constants and multiplicities used to calculate the difference between the b event and total hadronic multiplicity. The reconstruction constants $C_{i,j}$ and the purity were determined by the Monte Carlo. The mean multiplicities are those observed in the data (see Figure 7–1) Note that the statistical error on the multiplicity difference is not calculated from the errors on the above quantities, but rather using the Monte Carlo method described on page 202.

$\delta\bar{n}_b$ was given by the average of the CLEO[130] and ARGUS[131] $B_{u,d}$ meson

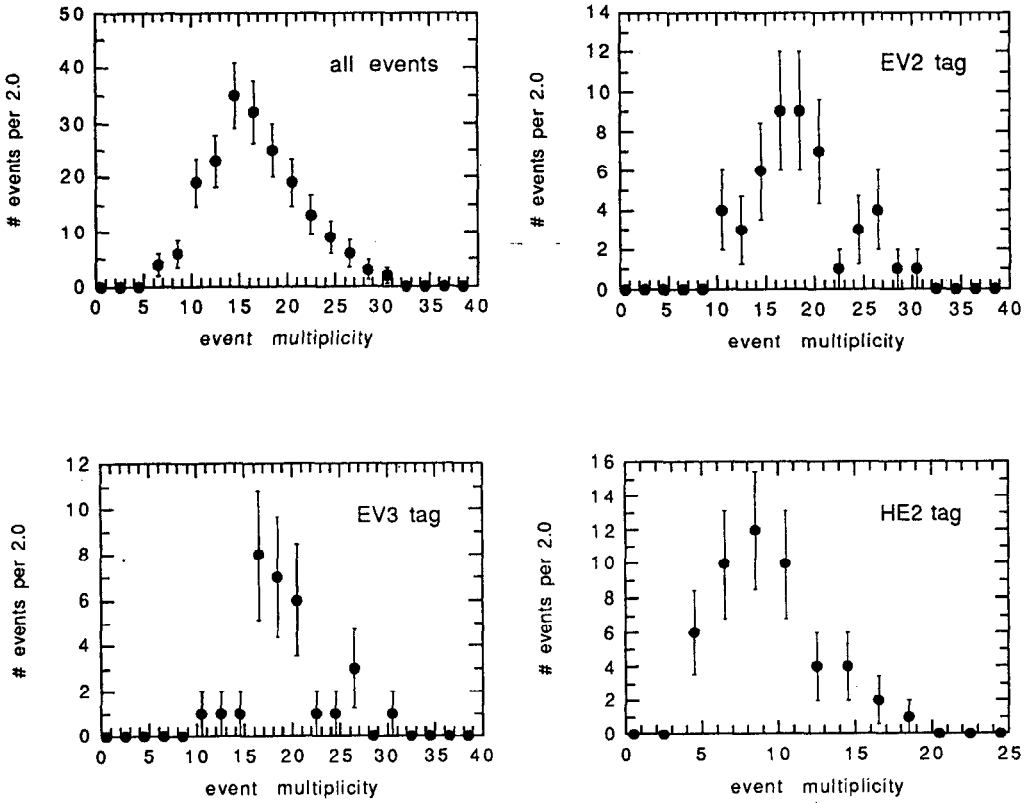

Figure 7–1 Multiplicity distributions for all events after the event selection cuts and for the events which passed each b-tag.

multiplicities measurements, 5.44, with a correction determined using the Lund Monte Carlo of 0.13 tracks per event to account for the decays of the other B hadrons ($B_{s,c}$ and B baryons). The resulting event multiplicity due to B-decay was thus $\bar{n}_B = 11.01$. This Monte Carlo correction for the heavier B species is described in more detail in Section 7.5 on page 214. For the $Z^0 \to b\bar{b}$ branching fraction, F_b, the standard model value of 0.217 was assumed.[13]

The measured multiplicity distributions for the hadronic sample and the three tagged samples are shown in Figure 7–1. Using the means of these multiplicity distributions, the values of $\delta\bar{n}_b$ for each of the three tags was calculated and is given in Table 7–4. To determine whether the three different tags yield consistent values for $\delta\bar{n}_b$, a technique similar to that used for determining the statistical errors was employed (see page 196). For 72 different Monte Carlo, $\delta\bar{n}_b$ was calculated using each of the three tags and the *difference* between $\delta\bar{n}_b$ calculated by each tag was recorded. The width of the resulting $\delta\bar{n}_b$ difference distribution yields

the level of difference one might expect to see in the data. The 1σ differences among these three tags were determined by the central 68.3% of these samples. Table 7–5

Tag	measured difference in $\delta\bar{n}_b$	expected 1σ difference in $\delta\bar{n}_b$
EV2 – EV3	–0.62	1.06
EV2 – HE2	–0.65	1.34
HE2 – EV3	0.03	1.59

Table 7–5 Comparison between multiplicity difference calculated using the three different tags.

shows the measured differences among the various combinations of the three tags with the expected 1σ difference. From this it is seen that all three values are consistent. Thus using the EV2 tag as the standard, the nominal result is,

$$\delta\bar{n}_b = 2.11^{+1.78}_{-1.86} \tag{7-13}$$

where this error is statistical only.

As another check, the reconstruction constants for the hadronic event cut sample, $C_{h,j}$, can be combined into a single constant and multiplied by the measured mean multiplicity in the hadronic sample of 16.71±0.35, to yield a corrected multiplicity for the 1991 data set of 20.89±0.44 (statistical error only). This value is close to the world average total multiplicity of 20.94±0.20 and provides an independent check that our method of extracting the 'true' multiplicity from the measured multiplicity is sensible. Furthermore, if the reconstruction constants are entirely ignored by using Equations (7-2) and (7-3), the result for $\delta\bar{n}_b$ is 4.13. This would cause a difference of less than 20% in the resulting value of the non-leading multiplicity in $b\bar{b}$ events, compared to the value calculated using the fully corrected equations. This difference is the full effect of the biases and variations among the individual reconstruction constants.

7.3 Systematic Errors in the Multiplicity Difference

A broad range of effects which can systematically affect $\delta\bar{n}_b$, either through the tagging purities or the reconstruction constants, were investigated. The sources of error due to uncertainties in various physics parameters include the ability to

properly model events in the three classes (*udsc*, *B*-decay and non-leading tracks in $b\bar{b}$ events) and heavy quark production and decay properties (branching ratios, fragmentation, lifetimes). Other errors result from uncertainties in the detectors. These include track finding efficiency, tracks from photon conversions, multiple Coulomb and nuclear scattering, track selection cuts, and impact parameter resolution. The final source of systematic error is that due to the finite number of tracks used in the Monte Carlo data sample.

The principle sources of error for this measurement are:

- the uncertainty in modelling the momentum and polar angle distributions of the non-leading tracks in $b\bar{b}$ events;
- the uncertainty in the impact parameter resolution function;
- the statistics in the number of Monte Carlo events generated.

All of the significant sources of systematic error are discussed below and values are given for the EV2 tag. A summary of the results can be found in Table 7–8 on page 213. The total systematic error in $\delta\bar{n}_b$ is significantly smaller than the statistical error.

7.3.1 Modelling of $Z^0 \rightarrow$ *udsc* Decays

Since the acceptance of the Mark II detector is not perfect, there will be a dependence of the reconstruction constants $C_{i,j}$ on the modelling of hadronic events due to acceptance limits in $\cos\theta$ and p_{xy}. In the case of *udsc* events, the distributions of these variable are well constrained by the existing measurements of the exclusive properties of hadronic decays.

All reconstruction constants were initially derived using the Lund 6.3 Parton Shower tuned primarily to Mark II data from PEP, as discussed in Chapter 3. For *udsc* events, the reconstruction constants were then corrected to those corresponding to a more recent tuning of Lund done at the Z^0 by OPAL.[102] This was accomplished by comparing the two models in $\cos\theta$ and p_{xy} at the generator level, after applying a cut equivalent to the event cut applied after full detector simulation. For all three tags, the correction to the light quark reconstruction constants were less than 0.1%.

The uncertainty in $\delta\bar{n}_b$ introduced by the uncertainty in the light quark reconstruction constants was studied by varying the Lund Parton Shower parameters within the range constrained by the OPAL tuning, and calculating the resulting change in the reconstruction constants. The corresponding uncertainty in $\delta\bar{n}_b$ was found to be less than ± 0.05 tracks. There is also uncertainty due to the

model-dependent extrapolation below $|\cos\theta| = 0.8$ and $p_{xy} = 0.15$ GeV/c, which is outside the acceptance of all experiments. To be conservative, an ALEPH estimate is used of the uncertainty associated with this extrapolation. Using a somewhat larger p_{xy} cut of 0.2 GeV/c, they estimated this to be ±0.1 tracks.[114] Combining these two effects, the total uncertainty in $\delta\bar{n}_b$ due to the uncertainty in the modelling of udsc events is taken as ±0.10.

7.3.2 Modelling of Non-leading Particle Production in *b* Events

In the case of non-leading tracks from $Z^0 \to b\bar{b}$ decays, there is no data available to constrain the $\cos\theta$ and p_{xy} distributions, and in particular the fraction of these tracks which fall outside of the detector acceptance of $|\cos\theta| < 0.8$ and $p_{xy} > 0.15$ GeV/c . Consequently, an approach based on more general principles is warranted.

Within the Lund Parton Shower Model, the various parameters control the stiffness of the momentum spectrum and the spread of the event around the jet axis (*e.g.* the vector to pseudovector ratio, strangeness and baryon production, fragmentation and shower cut-off energies) have been varied over wide ranges. In addition, the Matrix Element generator has been substituted for the Parton Shower routine and Feynman-Field fragmentation has been substituted for the Lund String fragmentation for light quarks. None of these effects changed $\delta\bar{n}_b$ by more than 0.25 tracks.

In addition to the above, the momentum spectrum of the non-leading tracks was rescaled so that the fraction of the non-leading energy in the form of charged tracks varied between 2/3, corresponding to pure isospin 1 (pion-like) production, and 1/2, corresponding to pure isospin 1/2 (kaon-like) production. This is an extremely conservative constraint: if instead this range is changed by varying the level of mass suppression, or the relative population of SU(3) multiplets, the variation in the charged energy fraction is less than half of this size. In any case, varying the non-leading charged energy fraction from 0.50 to 0.67 (our default Lund Monte Carlo gives 0.59), yields, an error in $\delta\bar{n}_b$ of ±0.4 tracks. In the interest of preserving the model independence of this measurement, this conservative estimate is taken as the systematic error.

7.3.3 *B* Decay and Modelling of Leading Particle Properties

The measurement of $\delta\bar{n}_b$ is sensitive to the modelling of the B hadron decay properties, such as the multiplicity and momentum spectrum, through the leading reconstruction constants $C_{i,B}$ and the tag purity. These properties are constrained

primarily by CLEO and ARGUS measurements at the $\Upsilon(4s)$.[130][131][133] A reweighting technique was used to conform to the CLEO and ARGUS data, and to study the uncertainty in $\delta\bar{n}_b$ introduced by the uncertainty in these constraints, as was used in the $Z^0 \to b\bar{b}$ fraction measurement in Section 6.3.6 on page 184. The largest effect, the uncertainty in the B decay multiplicity, was found to introduce an uncertainty of ±0.05 tracks in $\delta\bar{n}_b$. The variation in $\delta\bar{n}_b$ associated with the softening of the Lund generated momentum spectrum to agree with the CLEO data was negligible.

7.3.4 3-Jet Rate

The dependence of the 3-jet rate was explored through the use of a reweighting scheme which preserved $\langle x_E \rangle_b$ while varying the 3-jet rate (at $y_{min} = 0.08$) over a very conservatively large range between 0.12 and 0.22.[136] The resulting change in $\delta\bar{n}_b$ was ±0.04 tracks.

7.3.5 Non-hadronic Contamination

For the initial Mark II hadronic decay measurements, the non-hadronic background was estimated to be 0.42 events in the sample of 398 hadronic events.[62] For the 1991 data sample of 196 hadronic events, with slightly more stringent hadronic event selection cuts, this corresponds to a contamination of less than 0.2 events. In the worst possible case, if this 0.2 events has 7 tracks (the minimum allowed by the event selection cuts) and is tagged (unlikely), it causes an uncertainty of 0.05 tracks in $\delta\bar{n}_b$.

7.3.6 Bottom and Charm Hadron Production and Lifetimes

The result for $\delta\bar{n}_b$ will depend on the branching ratio of the Z^0 to bottom and charm quarks, the energy carried off by the heavy hadron during fragmentation and lifetime of the heavy hadrons, primarily through their effects on the purity of the tagged event samples. For more information on the limits chosen here, see Section 6.3 on page 180.

7.3.6.1 Z^0 Branching Fraction to Bottom Quarks

All four LEP experiments have measured $\mathrm{Br}(Z^0 \to b\bar{b})$ and as discussed in Section 1.5 on page 22, the average value is 0.212±0.011. Varying the fraction of $b\bar{b}$ events by ±0.011 in the Monte Carlo will change $\delta\bar{n}_b$ by ±0.05 tracks.

7.3.6.2 Z^0 Branching Fraction to Charm Quarks

Similarly, $\mathrm{Br}(Z^0 \to c\bar{c})$ has been well measured using both a high p_T lepton tag at ALEPH[22] and D^* tags at DELPHI[129] and OPAL.[95] The average of these

measurements is 0.171±0.029. Varying the fraction of charm events in the Monte Carlo similarly yields a systematic error in $\delta\bar{n}_b$ of ±0.10 tracks.

7.3.6.3 Bottom Fragmentation

The mean energy carried away by the bottom hadron, $\langle x_E \rangle_b = E_B/E_{beam}$, will affect $\delta\bar{n}_b$ both through the reconstruction constants and the tag purity. The energy carried away by the B hadron determines how much energy is left to produce the non-leading particles, and in this way the value of $\langle x_E \rangle_b$ will affect the non-leading reconstruction constants. The track impact parameters also have a weak dependence on $\langle x_E \rangle_b$ (see Figure 4–2 on page 110), and thus the tag efficiency and purity will also depend on the stiffness of the fragmenting process. The average of the measurements by ALEPH,[22] L3,[23] and OPAL[24] is $\langle x_E \rangle_b = 0.697 \pm 0.017$ corresponds to an error on $\delta\bar{n}_b$ of ±0.03 tracks. Note that care must be taken to hold the non-leading multiplicity constant while $\langle x_E \rangle_b$ is varied. This was achieved using a reweighting scheme which depended on both the $\langle x_E \rangle_b$ of the two B hadrons in an events and the non-leading multiplicity. As discussed in Section 6.3.3 on page 182, no attempt is made to account for uncertainty in the shape of the fragmentation function.

7.3.6.4 Charm Fragmentation

The average energy carried off by charmed hadrons, $\langle x_E \rangle_c$, will affect the reconstruction constants and tag purities as in the case of the bottom hadrons. The average of 0.515±0.011 is the result of measurements by ALEPH[22] and OPAL.[95] Using this uncertainty to provide a systematic limit on $\delta\bar{n}_b$ yields an error of ±0.03 tracks.

7.3.6.5 Bottom Hadron Lifetime

The average lifetime of the B hadrons is well measured[102][25] and as discussed in Section 6.3.1 on page 180, has an average value of 1.31±0.07 picoseconds. This uncertainty corresponds to an uncertainty in $\delta\bar{n}_b$ of ±0.03 tracks.

7.3.6.6 Charm Hadron Lifetime

The lifetimes of each of the charm hadrons have been independently measured. Varying the D^0, $D^{\pm}$, D_s and Λ_c within the Particle Data Group limits[102] produces an uncertainty in $\delta\bar{n}_b$ of ±0.02 tracks. Additionally, if the ratio of D^0 to $D^{\pm}$ production is varied from 0–100% vector (D^*) production leads to uncertainty of ±0.05 tracks in $\delta\bar{n}_b$.

7.3.7 Intrinsic Impact Parameter Resolution

As discussed in Section 6.3.9 on page 186, additional impact parameter smearing is required in the Monte Carlo in order to reproduce the impact parameter distributions observed in the data. Making the same conservative choice as before by using the 2σ allowed region of different amounts of smearing, and determining the reconstruction constants for each of these values yields a systematic error in $\delta\bar{n}_b$ of ± 0.15 tracks. A limited amount of very broad impact parameter smearing (the 'far tail') is also allowed (see Table 4–3 on page 137), and using the 2σ allowed far tail smearing leads to an additional error on $\delta\bar{n}_b$ of ± 0.02 tracks. Thus the total systematic error on $\delta\bar{n}_b$ due to the uncertainty in the intrinsic impact parameter resolution is ± 0.15 tracks.

7.3.8 Multiple Coulomb and Nuclear Scattering

Using methods as described in Section 6.3.10 on page 186, systematic limits can be placed on $\delta\bar{n}_b$ which result from multiple Coulomb scattering and both elastic and inelastic nuclear scattering. The amount of scattering material which most affects the impact parameter resolution, namely that in the beam pipe and SSVD, can be constrained to $\pm 3\%$ with our statistics. Varying the amount of scattering material in the inner scattering layers by this amount results in a change in $\delta\bar{n}_b$ of ± 0.04 tracks. Although the material in the DCVD and CDC is more difficult to study using tracking information, it is less important for the impact parameter resolution. This material is, however, quite relevant for photon conversions as will be discussed in the next section. Using the inelastic nuclear scattering generator, it was found a conservative systematic limit of ± 0.10 tracks can be placed on $\delta\bar{n}_b$.

7.3.9 Photon Conversions

The Monte Carlo predicts that 9.3% of the reconstructed tracks which pass the multiplicity track cuts arise from photon conversions. Hence it is important that these be well modelled so their effect is properly accounted for in the reconstruction constants, $C_{i,j}$. Two approaches were taken to verify our modelling of these conversion tracks. The first check is a rough estimate based on the Monte Carlo generated photon spectrum. It has been estimated that the conversion probability is $P_c = 7/9\,(L/L_R)$, where L/L_R is the number of radiation lengths.[137] Making use of the generated photon spectrum and the nominal material thicknesses in the Monte Carlo, this estimates that conversions should be between 9 and 11% of all of the reconstructed charged tracks, thus confirming the more rigorous result from the detector simulation.

The second check investigated how well the conversion tracks are modelled in comparison to our data. This uses the fact that according to the detector simulation, greater than 60% of the conversion tracks originate in the DCVD outer wall and the CDC inner wall. Thus the addition of a track cut which requires track information to be found in the DCVD will substantially reduce the number of conversions. If at least 15 out of 32 possible position measurements in the DCVD are required the detector simulation predicts that the fraction of tracks from conversions should be reduced from 9.3% to 3.7%. When $\delta\bar{n}_b$ is determined using the additional track cut and the EV2 tag, the result differs by 0.27 tracks from the nominal result. The significance of the difference is determined as above using the 72 Monte Carlo data samples of 220 events, and it is found that the expected 1σ difference between the determination with and without the requirement of DCVD information on the tracks is 0.83 tracks, thus indicating that the observed difference of 0.27 is well within the expected range.

Given the consistency of these two checks and the accuracy of the *a priori* knowledge of the amount of material present in the detectors (particularly the DCVD/CDC interface region which is not well constrained by the impact parameter resolution studies of the previous section) a very conservative limit of ±20% is placed on the number of conversion tracks. This corresponds to a systematic error in $\delta\bar{n}_b$ of ±0.05 tracks.

7.3.10 Track Finding Efficiency

The track finding efficiency has been studied as described in Section 4.6 on page 144, and is understood to within ±1% for the multiplicity track cuts (which do not use the vertex detector information). This corresponds to a systematic error in $\delta\bar{n}_b$ of ±0.04 tracks. It is interesting to note that this uncertainty would be much larger (>0.2 tracks) if instead of $\delta\bar{n}_b$, the total multiplicity had been measured.

7.3.11 Track Cuts

Differences between the effects of the multiplicity track cuts on the data and the Monte Carlo are also a possible source of systematic error. (See Section 7.2.1 on page 194 for a description of these cuts.) Exclusive distributions* of the quantities used in the multiplicity track cuts are shown in Figure 7–2 for all of the events which pass the hadronic selection cuts, and in Figure 7–3 for the events which were tagged by the EV2 tag. As an initial check, each of the cuts was separately varied

* In this usage, 'exclusive distribution' means that when looking at the distribution of one variable used in the track cuts, the other cuts have already been applied.

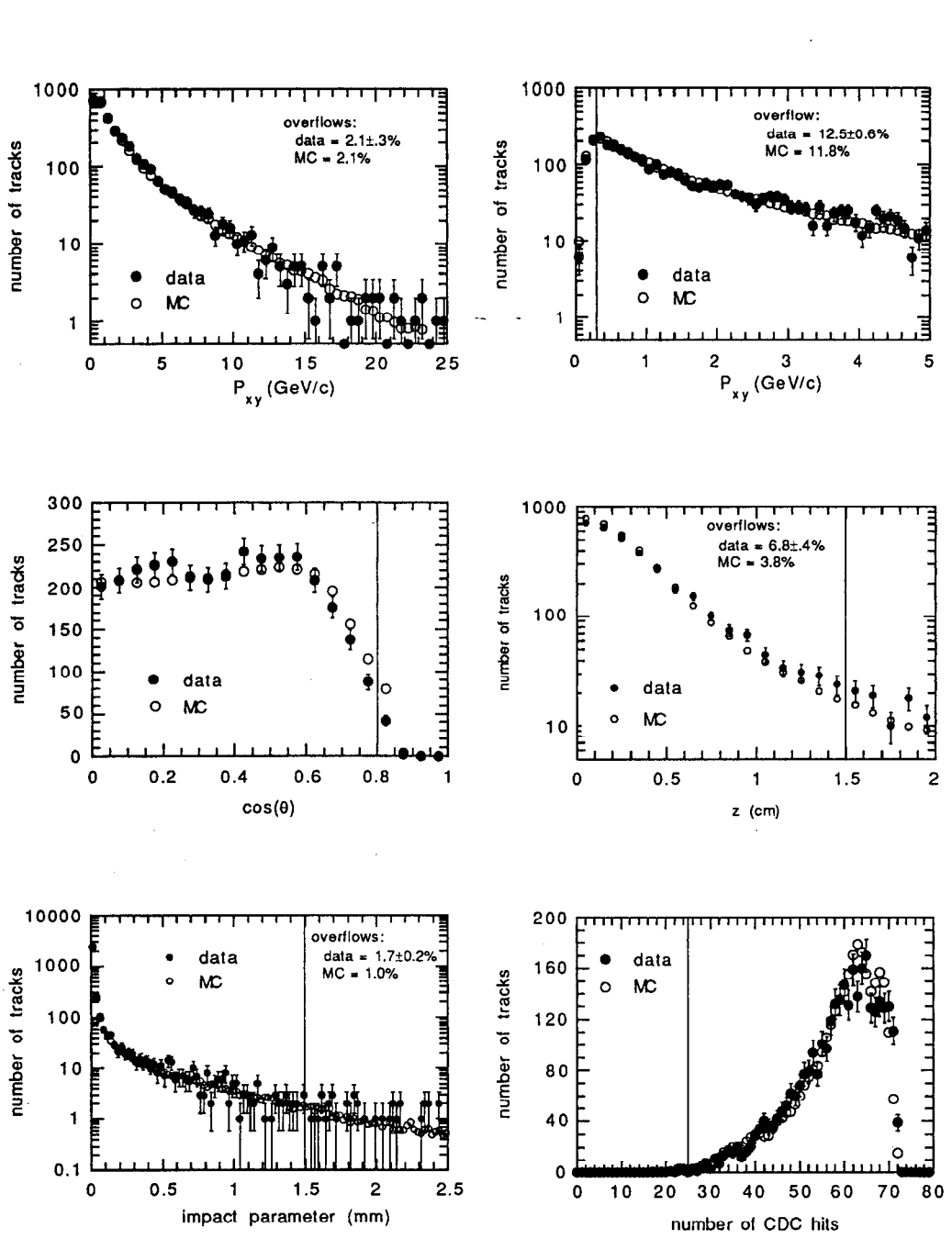

Figure 7–2 Exclusive track distributions of the variables used for the multiplicity track cuts for all events. The apparent discrepancy in the cos θ distribution actually is just a result of a slightly lower fraction of events in the data at values of large |cos θ| probably resulting from a statistical fluctuation. Specifically, in the data we see 81±11% as many tracks in the region $0.6 < |\cos\theta| < 0.8$ as are predicted by the Monte Carlo.

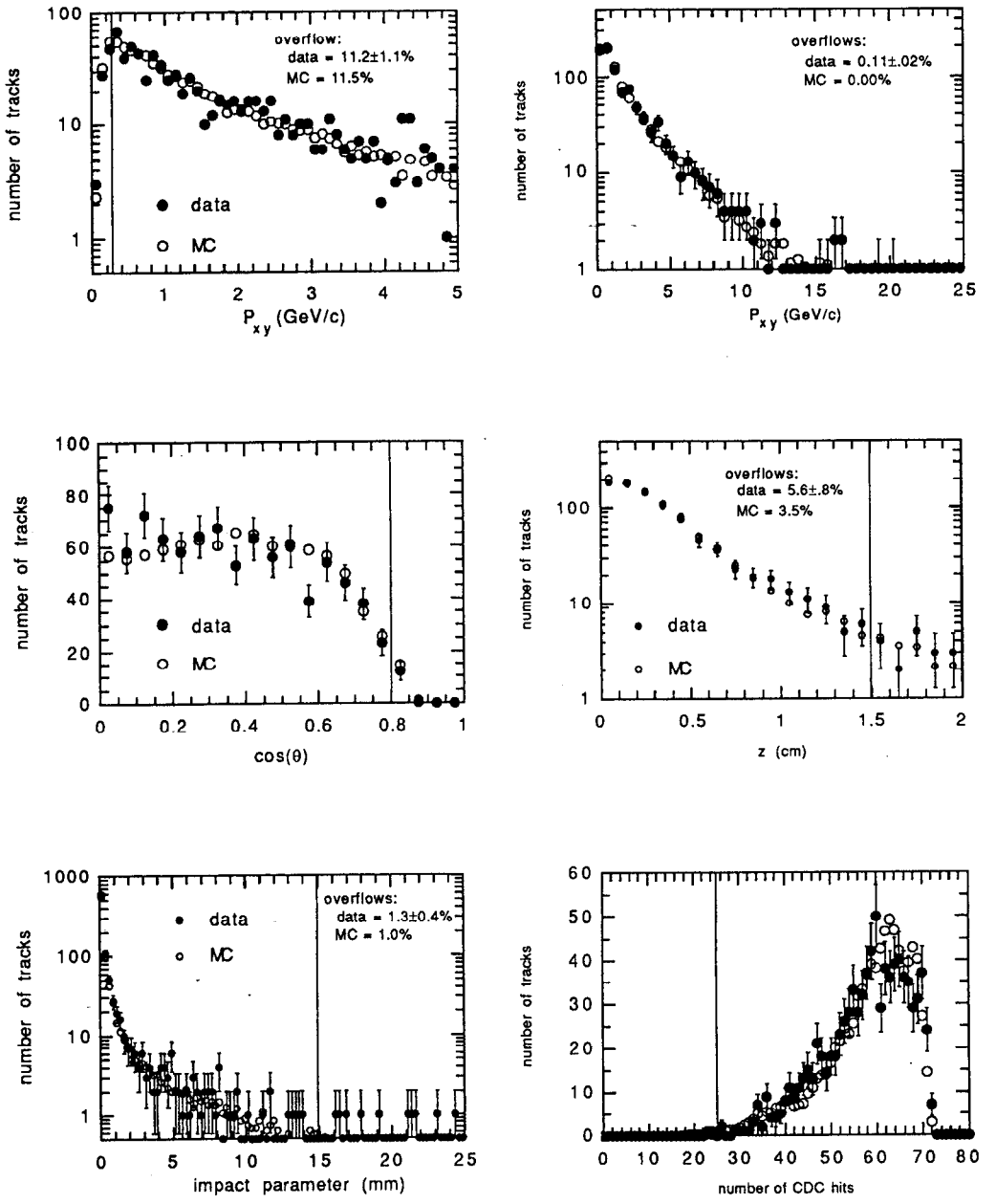

Figure 7–3 Exclusive track distributions of the variables used for the multiplicity track cuts for events which were selected by the EV2 tag.

Original cut	Modified cut	measured difference in $\delta\bar{n}_b$	expected 1σ difference in $\delta\bar{n}_b$
$\lvert\cos\theta\rvert < 0.8$	< 0.6	0.756	1.502
	< 0.7	0.604	0.587
$p_{xy} < 0.15$ GeV/c	< 0.25 GeV/c	–0.401	0.306
	< 0.50 GeV/c	–0.453	0.814
$N_{CDC} \geq 25$	≥ 15	0.004	0.058
	≥ 35	0.084	0.222
$\lvert z_m \rvert < 15$ mm	< 10 mm	0.060	0.263
	< 20 mm	0.162	0.212
$\lvert b \rvert < 15$ mm	< 10 mm	0.060	0.156
	< 20 mm	–0.032	0.125

Table 7–6 The difference between multiplicity difference $\delta\bar{n}_b$ calculated with the original multiplicity track cuts and the case when one of the multiplicity track cuts at a time is changed. In only 2 of the 10 cases does the measured difference exceed one standard deviation.

and a value for $\delta\bar{n}_b$ calculated with this new cut. To gauge the significance of the difference between the result with the original and the modified cuts, the same method used above was employed. In this method the values of $\delta\bar{n}_b$ are calculated for 72 Monte Carlo event samples of the same size as the data sample. The standard deviation of the differences in $\delta\bar{n}_b$ calculated with the original and modified cuts for the 72 samples thus provides an estimate of the expected difference in $\delta\bar{n}_b$. Table 7–6 shows the results of this test. Of the 10 trails in which a particular cut value was varied, the difference of $\delta\bar{n}_b$ was greater than one standard deviation in only 2 of them.

To obtain some quantitative estimate of the systematic error, the differences between the fraction of tracks outside the cuts in the data and Monte Carlo was interpreted as an uncertainty in the reconstruction efficiency. This approach is very conservative, as the cuts are designed to remove regions where the detector modelling is suspected to be poor. The data/Monte Carlo differences are given for

multiplicity track cut	fraction fail: data	fraction fail: MC	fraction fail: data – MC	effect on $\delta\bar{n}_b$
$\|\cos\theta\| < 0.8$	1.33±.20%	2.48%	-1.15%	±0.03
$p_{xy} < 0.15$ GeV/c	1.33±.20%	1.71%	-0.38%	±0.01
$N_{CDC} \geq 25$	0.21±.08%	0.22%	-0.01%	±0.00
$\|z_m\| < 15$mm	8.97±.48%	5.46%	3.51%	±0.06
$\|b\| < 15$ mm	2.79±.28%	2.04%	0.75%	±0.01
Total Systematic Error on $\delta\bar{n}_b$ due to multiplicity track cuts:				±0.07

Table 7–7 A data/Monte Carlo (MC) comparison of the fraction of tracks failing each track cut. The differences are used to set a conservative limit on the multiplicity difference.

each cut in Table 7–7 along with the effective uncertainty this introduces in $\delta\bar{n}_b$, as measured by the EV2 tag. The sum of the effects in quadrature yields ±0.07 tracks which will be taken as the systematic uncertainty due to the uncertainty in the effect of the track cuts.

7.3.12 Monte Carlo Statistics

Since the reconstruction constants and purities were determined using the Monte Carlo, there will be an uncertainty due to the finite statistics of the Monte Carlo sample of 20,000 hadronic events with full detector simulation. The effect of this level of statistics is a systematic error of ±0.30 tracks in $\delta\bar{n}_b$.

7.3.13 Full Result for the Multiplicity Difference

Table 7–8 has a summary of the contributions to the systematic error $\delta\bar{n}_b$ for the EV2 tag. The sum of these systematic errors in quadrature is ±0.57 tracks and thus the full result for the difference between the multiplicity of $b\bar{b}$ events and all flavors of hadronic events is

$$\delta\bar{n}_b = 2.11 \pm 1.82\,(\text{stat}) \pm 0.57\,(\text{syst})\,.$$

Source of Systematic Error	Range	Systematic Error on $\delta\bar{n}_b$
MC Model: *udsc* tracks	see text	±0.10
MC Model: non-leading tracks from $b\bar{b}$ events	see text	±0.40
MC Model: B decay tracks	see text	±0.05
3-jet fraction	0.12 – 0.22 (at y_{min} = 0.08)	±0.04
non-hadronic events	0–0.2 in 196 events	±0.05
b fragmentation	0.680 – 0.714	±0.04
c fragmentation	0.504 – 0.526	±0.03
average bottom hadron lifetime	1.24 – 1.38 psec	±0.03
average charm hadron lifetime	PDG limits	±0.05
$\mathrm{Br}(Z^0 \to b\bar{b})$	0.201 – 0.223	±0.05
$\mathrm{Br}(Z^0 \to c\bar{c})$	0.142 – 0.200	±0.10
conversion tracks	±20%	±0.05
multiple scattering	±3%	±0.03
nuclear scattering	see text	±0.10
impact parameter resolution	see text	±0.15
track finding efficiency	±1%	±0.04
multiplicity track cuts	see text	±0.07
Monte Carlo statistics	20000 MC events	±0.30
Total Systematic Error on $\delta\bar{n}_b$		±0.57

Table 7–8 A summary of the systematic errors on the difference of b and *udscb* multiplicity.

7.4 Center-of-Mass Energy

The average center-of-mass energy for the 1990 running has been measured with the distribution of energy spectrometer readings from runs with Small Angle Monitor Bhabha events to be

$$\langle E_{cm} \rangle = 90.93 \pm 0.01 \pm 0.04 \text{ GeV}$$

with a roughly Gaussian distribution of width 0.2 GeV.[50] In certain cases, in order to make a proper comparison with lower energy data, this value must be corrected for the effect of initial state radiation, which is small near the Z^0 resonance. For example, the corrections, as given by the standard Lund initial state radiation routine, at the Z^0 mass and 400 MeV below and above it are –0.20, –0.21 and –0.41 GeV, respectively. The correction for the data sample, most of which lies between 90.7 and 91.2 GeV, is approximately –0.20 GeV. Thus the average center-of-mass energy for the 1990 run, corrected for initial state radiation, is

$$\langle E_{cm}^{\text{isr corr.}} \rangle = 90.7 \text{ GeV}.$$

7.5 *b* Event Total and Non-leading Multiplicities

To extract the value of the average non-leading multiplicity, we recall that $\delta\bar{n}_b = \bar{n}_b - \bar{n}_{had}$. The $Z^0 \to b\bar{b}$ event multiplicity, $\bar{n}_b$, can be written as the sum of the B hadron decay multiplicity and the non-leading multiplicity, $\bar{n}_B + \bar{n}_{nl}$. Substituting this into the above equation for $\delta\bar{n}_b$ and solving for the non-leading multiplicity yields,

$$\bar{n}_{nl} = \delta\bar{n}_b + \bar{n}_{had} - \bar{n}_B. \tag{7-14}$$

As shown in Table 7–9, the total hadronic multiplicity, $\bar{n}_{had}$ has been well measured at the Z^0 resonance by Mark II and all four LEP experiments. The average $\bar{n}_{had} = 20.94 \pm 0.20$ tracks per event. Adding this value to $\delta\bar{n}_b$ gives a $b\bar{b}$ event multiplicity of

$$\bar{n}_b = 23.05 \pm 1.82 \text{ (stat)} \pm 0.60 \text{ (syst)}.$$

To determine the non-leading multiplicity in $b\bar{b}$ events, the B decay multiplicity is required. The multiplicity of $B_{u,d}$ meson decays has been well measured at the $\Upsilon(4s)$. CLEO[130] and ARGUS[131] have measured the multiplicity at the $\Upsilon(4s)$ to be 10.81±0.05±0.23 and 10.99±0.06±0.29 respectively. The average of these values

experiment	total charged multiplicity
ALEPH[114]	20.85±0.02±0.24
OPAL[115]	21.40±0.02±0.43
DELPHI[116]	20.71±0.04±0.84
L3[117]	20.70±0.02±0.70
Mark II[113]	20.10±1.00±0.90
Average	20.94±0.20

Table 7-9 The previous measurements of the total charged multiplicity at the Z^0 and weighted average. The average accounts for the correlated systematic errors among the experiments.

taking into account an estimate of the common systematics is 10.88±0.20. At energies higher than the $\Upsilon(4s)$ however, there are contributions to the B hadron decay multiplicity from other B mesons and B baryons. The Lund Monte Carlo calculates that the B hadron multiplicity for all B species is 0.13 tracks per event higher than for $B_{u,d}$ only. A summary of the production fractions and multiplicities as predicted by Lund are given in Table 7–10. Adding this to the CLEO and ARGUS

B hadron species	production fraction	average multiplicity per event
$B_{u,d}$	0.79	10.88
B_s	0.12	11.34
B baryon	0.09	11.74
average B hadron multiplicity per event		11.01

Table 7-10 Production fractions and decay multiplicities used for the different B hadron species. The production fractions are those predicted by the Lund Monte Carlo. The decay multiplicities for $B_{u,d}$ and B baryons are also predicted by the Lund Monte Carlo and scaled to the average of the CLEO and ARGUS values for the $B_{u,d}$ decay multiplicity.

average multiplicity gives a value for the combination of all B hadron species of

11.01 tracks per event. Of course this number is somewhat sensitive to the specific assumptions in the Monte Carlo regarding the decay multiplicities of the B_s and B baryons and production fractions of the different B species. Although no experimental information on B_s and B baryon multiplicities exists, and theoretical information is of little help, one expects that because of the high Q^2 of the decays, the differences between the decays of the $B_{u,d}$ are reasonably well handled by standard approaches, such as that implemented by the Lund Monte Carlo, in which the difference is simply provided by the change in the phase space.

There is however some information available about the production fractions of the different B hadrons. Although the information on the B baryon production fraction is limited,* one can constrain the B_s production fraction, $P(b \to B_s)$, using the present measurements of $B\bar{B}$ mixing. This is done using a Standard Model places a constraint on the relative mixing strengths of B_d and B_s, which results from the unitarity of the Kobayashi-Maskawa (KM) matrix (see Appendix A). The $b \to B_s$ fraction is found in this manner to be 0.18±0.10, assuming a B baryon production fraction of 0.1±0.1. This is consistent with the Lund prediction of 0.12.

Using the $b \to B_s$ fraction found above and 0.1±0.1 as the B baryon production fraction, this adds an uncertainty of ±0.04 tracks to the 0.13 track correction to the B decay multiplicity which accounted for the non-$B_{u,d}$ hadrons. Thus the B decay multiplicity at the Z^0 is taken as

$$\bar{n}_B = 11.01 \pm 0.20.$$

Thus with the value for $\delta\bar{n}_b$ as found in Section 7.3.13, the world average value for the total hadronic charged multiplicity at the Z^0 resonance from Table 7–9 and this value of the B decay multiplicity modified to include all of the B hadron species, the non-leading multiplicity is calculated at the initial-state radiation corrected center-of-mass energy of E_{cm} = 90.7 GeV to be

$$\bar{n}_{nl} = 12.04 \pm 1.82\ (\text{stat}) \pm 0.63(\text{syst}).$$

* ALEPH has done a presently-unpublished analysis of Λ_b production. They use a fairly standard lepton tag to measure the quantity $P(b \to \Lambda_b) \cdot Br(\Lambda_b \to l + \Lambda + X)$. The size of the errors and the fact that this will not constrain the production of the other weakly-decaying B baryons (the Σ_b^+ and Σ_b^-) limits the usefulness of this measurement for our purpose. For more information on this measurement, see Reference [127].

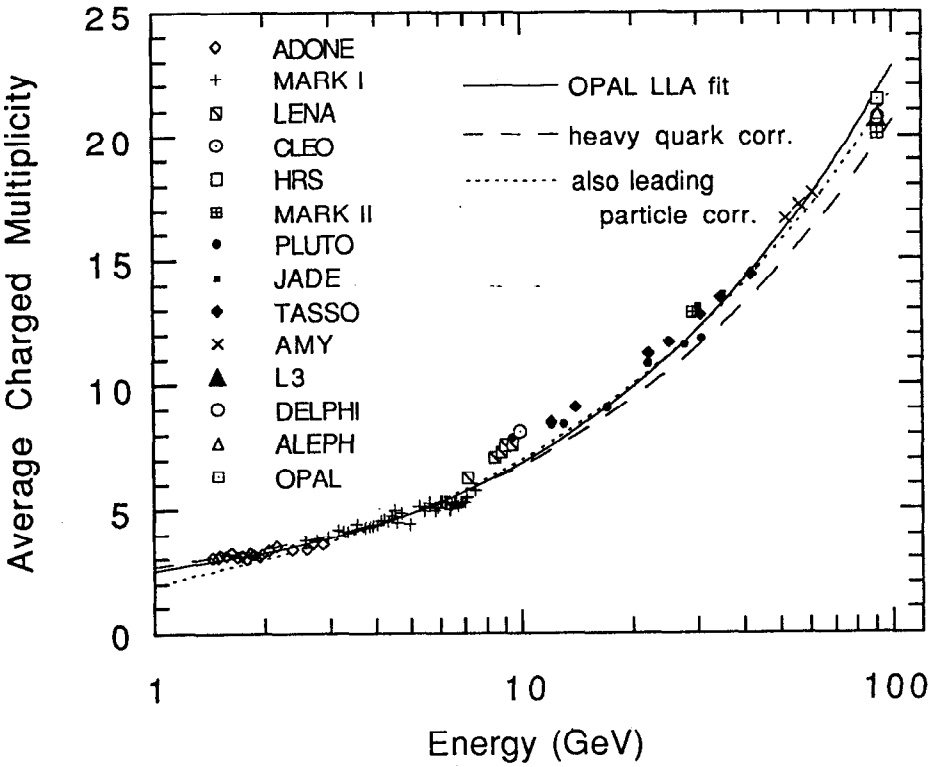

Figure 7–4 World sample of e^+e^- annihilation charged multiplicity data versus E_{cm}. Each of the fits is based on the leading log approximation-inspired form. The OPAL fit corresponds to the constants given in Reference [115]. The heavy quark corrected fit removes the effects of c and b production, as discussed in Section 7.6.1. The third fit has removed the leading particle effects, in addition to the heavy quark correction (see Section 7.6.3). The data comes from References [97], [114], [115], [116], [117] and [138].

7.6 Comparison with Data at Lower C.M. Energy

Figure 7–4 shows the world sample of non-resonant mean charged multiplicity data versus the center-of-mass energy, E_{cm}, for e^+e^- annihilation. The solid line in the figure is a fit to the multiplicity data using the leading-logarithm approximation (LLA) inspired form,[139]

$$\bar{n}_{had} = a + b \cdot \exp\{c\sqrt{\ln E_{cm}}\}, \tag{7-15}$$

where a, b, and c are the constants determined by the fit and E_{cm} is in GeV. For this fit, done by OPAL, the constants have the values $a = 2.418$, $b = 0.113$ and $c = 2.421$.[115] While the LLA inspired form provides a general description of the

data over a wide range of energies, there are some regions where the agreement is not very good. In particular, the fit is significantly lower than the data in the region around the bottom threshold, where one would expect that the LLA inspired shape would not hold. There is probably a similar problem at the charm threshold, obscured by the large systematic uncertainty of the Mark I data. Clearly, one should use caution in making such global fits to the multiplicity. To make the comparison between the non-leading multiplicity and this data more meaningful, several corrections were studied.

7.6.1 Heavy Quark Correction

In the total multiplicity measurements of Figure 7–4, there is a significant contribution from heavy quark ($c\bar{c}$ and $b\bar{b}$) production, which is almost entirely absent in the non-leading production process, and thus must be removed from the total multiplicity measurements. At 29 GeV, we find that the heavy quark event multiplicities are[37][39][40]

$$\bar{n}_{c\bar{c}} = 13.4\pm0.7 \text{ and } \bar{n}_{b\bar{b}} = 15.7\pm0.6,$$

and from all PEP and PETRA measurements near 29 GeV[140] the multiplicity for all flavors of hadronic events is

$$\bar{n}_{udscb} = 12.41\pm0.21.$$

Combining these yields a correction to the total multiplicity to account for the presence of heavy quarks of

$$\bar{n}_{udscb} - \bar{n}_{uds} = 1.20\pm0.50.$$

To extend this to other center-of-mass energies, the Lund Monte Carlo was employed with the parameter settings determined by Chrin,[42] (taking care to evolve ε_c and ε_b in the manner outlined in that article) tuned to the above multiplicity difference at 29 GeV.

With the multiplicity data corrected in this fashion, it was re-fit to the LLA-inspired form with the result

$$\bar{n}_{had} = 2.554 + 0.1252 \cdot \exp\{2.317\sqrt{\ln E_{cm}}\}.$$

Figure 7–5 shows the corrected data and the fit. With the heavy quark contributions removed, the LLA form provides a much better description of the data. The worst agreement is in the region between 3 and 7 GeV, which is nevertheless within the common systematic error of 0.9 tracks of the Mark I data in that region. This fit is

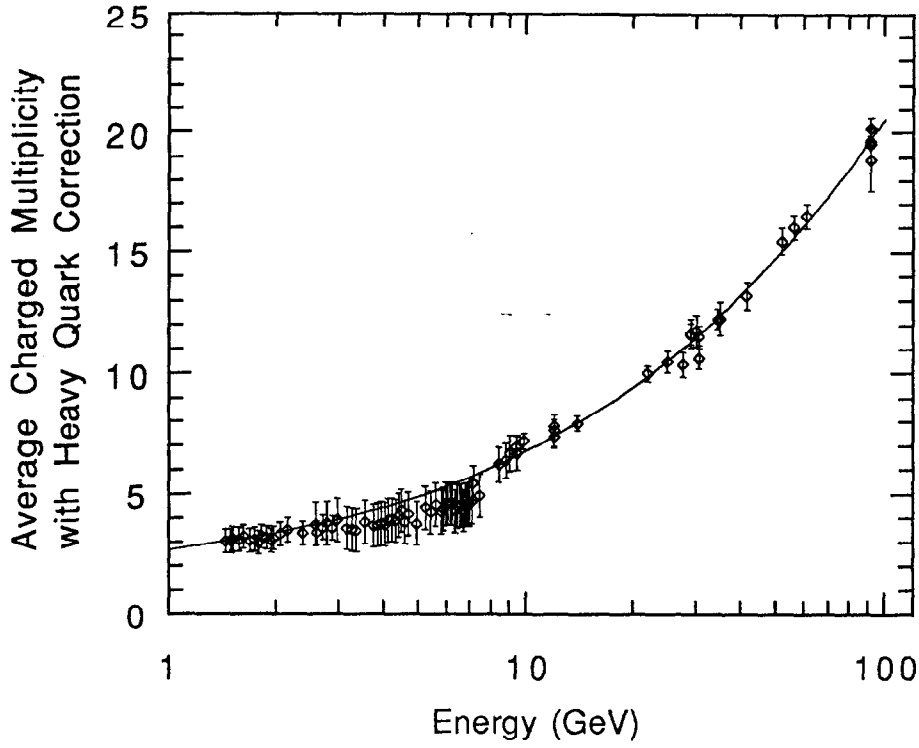

Figure 7–5 World sample of charged multiplicity data, corrected to remove the effects of heavy quark production. The line is a fit of the LLA-inspired form to this data.

also shown as the dashed line in Figure 7–4, where it lies below the *udscb* data points.

It should be noted that, in basing this correct on measurements of the $c\bar{c}$ and $b\bar{b}$ multiplicities at 29 GeV, we have introduced an additional systematic error of ±0.5 tracks in the multiplicity comparison. While this is small compared to the statistical error in the non-leading multiplicity, it is nevertheless one of the largest systematic errors, and thus may possibly determine the degree of accuracy with which this comparison can be made in the high-statistics limit. It may well be that this uncertainty could be reduced by considering the measurements of the *difference* between $c\bar{c}$, $b\bar{b}$ and *udscb* multiplicities, rather than considering the measurements separately as has been done before.

7.6.2 Non-leading Energy and x_E-distribution Bias

Because the x_E distribution is not a δ-function, but is instead a rather broad function presumably related to the Peterson function, and because the relationship between the average multiplicity and E_{cm} is not linear, the mean non-leading multiplicity expected for a given $\langle x_E \rangle$ is not quite equal to the mean total

multiplicity measured at a lower center-of-mass energy equal to average non-leading energy,

$$\langle E_{nl} \rangle = E_{cm}(1 - \langle x_E \rangle). \tag{7-16}$$

Mathematically, this accounts for the fact that the non-leading multiplicity measures the multiplicity at a distribution of energies is given by

$$\langle \bar{n}(E_{nl}) \rangle = \int \bar{n}(E_{nl}) P(E_{\bar{n}l}) dE_{nl}, \tag{7-17}$$

whereas the multiplicity at $\langle E_{nl} \rangle$ is

$$\bar{n}(\langle E_{nl} \rangle) = \bar{n}[\int E_{nl} P(E_{nl}) dE_{nl}] \tag{7-18}$$

where $\bar{n}$ is the function which relates center-of-mass energy to the mean total multiplicity and $P(E_{nl})$ is the normalized non-leading energy distribution which is given by a convolution of the $1 - x_E$ distributions for the two B hadrons in the event. In the following comparisons between the non-leading multiplicity and lower energy total multiplicity data, this is accounted for by the application of a correction to the non-leading energy. The corrections used are given in Table 7–11. These

E_{cm} (GeV) and heavy quark type	$\langle x_E \rangle$ (no ISR)	x_E dist. corr. (GeV)	$\langle E_{nl} \rangle$ (GeV)
29 GeV ($c\bar{c}$)	0.562	–0.24	12.46
29 GeV ($b\bar{b}$)	0.751	–0.10	7.12
35 GeV ($b\bar{b}$)	0.740	–0.35	8.75
42.1 GeV ($b\bar{b}$)	0.727	–0.45	11.04
90.9 GeV ($b\bar{b}$)	0.697	–1.50	26.05

Table 7–11 The non-leading energies and the associated x-distribution correction at which the previous measurements of the non-leading multiplicity were done.

corrections have been calculated assuming a Peterson fragmentation function. The values for $\langle x_E \rangle$ at PEP/PETRA energies were calculated using the values and prescription as described by Chrin,[42] except with initial state radiation (ISR) off. This is because multiplicities are customarily quoted at the nominal E_{cm} and are corrected to remove ISR.

The non-leading energies used for comparison to the total multiplicity data, for this measurement as well as for the PEP and PETRA measurements, are shown in Table 7–12, along with the non-leading multiplicity values. It should be pointed out

experiment and heavy quark type	E_{cm} (GeV)	$\bar{n}_b$ or $\bar{n}_c$	$\bar{n}_{nl}$	$\langle E_{nl} \rangle$ (GeV)
Mark II $(b\bar{b})$[37]	29	16.1±1.1	5.1±1.1	7.12
Mark II $(c\bar{c})$[37]	29	13.2±1.0	8.1±1.0	12.46
DELCO $(b\bar{b})$[39]	29	14.32±0.92	3.31±1.20	7.12
TPC $(b\bar{b})$[40]	29	16.7±1.0	5.7±1.0	7.12
TPC $(c\bar{c})$[40]	29	13.5±0.9	8.4±0.9	12.46
TASSO $(b\bar{b})$[41]	35	15.96±1.43	4.95±1.44	8.75
TASSO $(b\bar{b})$[41]	42.1	17.02±1.98	6.01±1.99	11.04
this meas. $(b\bar{b})$	90.9	23.05±1.92	12.04±1.93	26.05

Table 7–12 The b or c event multiplicities, corresponding non-leading multiplicities and corrected non-leading energies are given with their total statistical and systematic error for previous experiments and this measurement. The b non-leading multiplicities were calculated using an average B decay multiplicity of 11.01±0.20 (see Section 7.5). The c non-leading multiplicities were calculated assuming 5.1±0.3 tracks for the average charm hadron decay multiplicity, as used in these measurements.

that the PEP and PETRA experiments have chosen to take initial state radiation into account by correcting their measured $b\bar{b}$ multiplicity back to the nominal beam energies. On the other hand, $\langle x_E \rangle_b$ is quoted in terms of the *uncorrected* beam energy, and so initial state radiation must be added back into E_{cm} before multiplying by $\langle x_E \rangle_b$ to get the non-leading energy. Since events with very energetic initial state radiation will fail hadronic cuts, this effect is detector dependent. The average energy lost to initial state radiation at PEP and PETRA energies has been estimated to be 1.0±0.5 GeV. This correction has been applied to the PEP and PETRA energies, and the uncertainty included. For our measurement at the Z^0 uncorrected beam energy of 90.9 GeV is used as a starting point.

7.6.3 Leading Contribution in Light Quark Decay

One might expect that the comparison with the non-leading multiplicity from heavy quark decays at higher energy might be most properly done with only the non-leading portion of the light quark decays at lower energy. Again, the Lund Monte Carlo can be used to derive a correction to the multiplicity data, although in this case the correction is somewhat model dependent since it can not be tied to an independent measurement, as can the heavy quark correction. This correction, from the multiplicity in *uds* decays to the non-leading multiplicity in *uds* decays, has the form

$$\delta_{\bar{n}} = a' + b' \cdot \log_{10}(E_{cm})$$

where $a' = -0.724$, $b' = 0.970$ and E_{cm} is in GeV. At 30 GeV, for instance, the size of this correction is +0.71 tracks. The correction is derived by removing the leading (most energetic) particle, or its decay products, in each hemisphere from both the multiplicity sum and the center-of-mass energy. The result of this correction is plotted as the dotted line in Figure 7–4.

The correction for the effects of the leading particles should be interpreted as a check of the dependence of the multiplicity comparison and later, in the opposite fashion, the extraction of $\langle x_E \rangle_b$, on the theoretical uncertainty in the underlying assumptions. These assumptions include those regarding the process of non-leading particle production, and specifically the relationship of the non-leading particle multiplicity and the non-leading energy. Nonetheless, that the difference of approximately 0.7 tracks between this leading particle-corrected multiplicity function and the multiplicity function with only the heavy quark correction is on the same order as the total systematic error indicates that the overall approach is robust. This illustrates that this is another area (along with the non-leading reconstruction constant and heavy quark correction) which could benefit from additional theoretical study. Consequently, for the final results derived in the following sections only the heavy quark and the x_E-distribution corrections are used.

7.6.4 Multiplicity Comparison

Figure 7–6 shows the world sample of multiplicity data, and the heavy quark-corrected multiplicity fit (see Section 7.6.1 for a description of this correction). Plotted over this are the non-leading multiplicity points from Table 7–12, which include the x_E-distribution correction described in the previous section. To the level

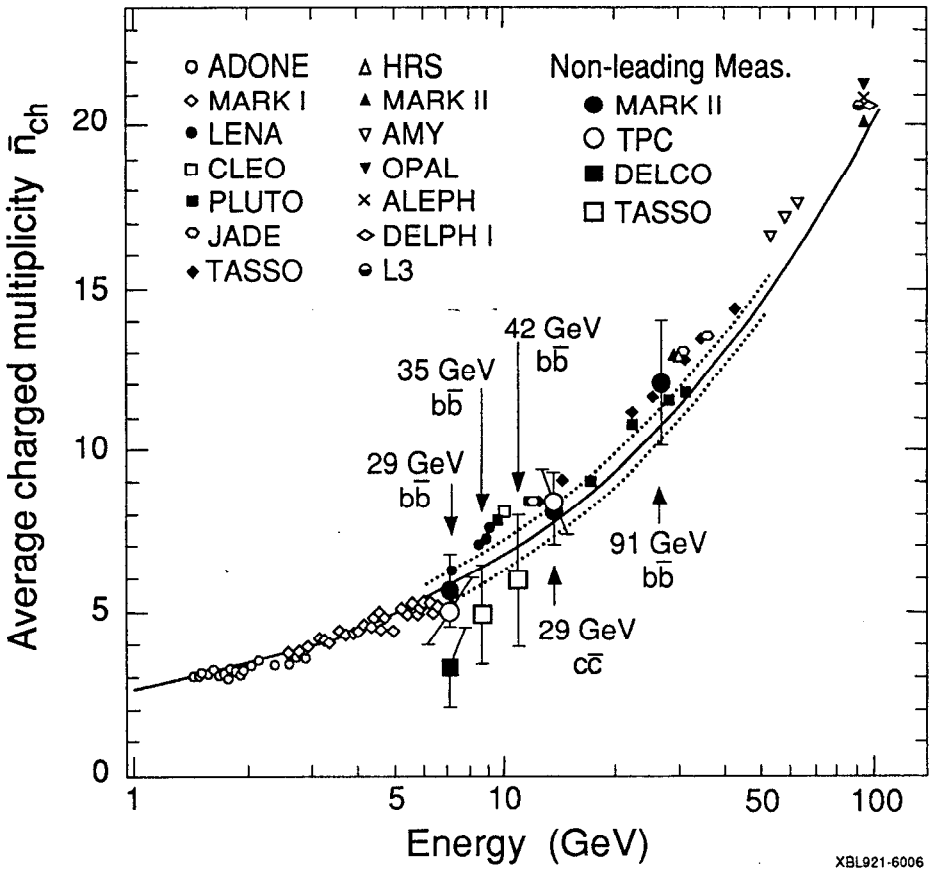

Figure 7–6 World sample of charged multiplicity data, without error bars, and the heavy quark corrected fit from Figure 7–4 and Figure 7–5. The dotted line is the ±0.5 track uncertainty resulting from the normalization of the heavy quark correction to PEP and PETRA data. Also shown are the non-leading multiplicity measurements from previous experiments and this analysis, plotted at the appropriate x_E-distribution corrected non-leading energy, as listed in Table 7–12. (The effects from the leading quark in *uds* events are not included as discussed in Section 7.6.3). The assumption of flavor independence for the fragmentation process predicts that the non-leading data should fall on the solid line.

of experimental accuracy available, that the points lie on the corrected multiplicity curve, represented by the solid line, confirms the prediction of the flavor independence of the fragmentation process on the initial quark flavor. The highest energy point, from this study, serves to strengthen the quality of the check available from the lower energy measurements alone.

Finally, should this measurement be pushed at LEP, and an effort made to better understand the theoretical underpinnings of the measurement, it should be pointed out that there is a limit to the accuracy of the comparison imposed by the uncertainty in the measurement of $\bar{n}$ at lower energy. This is most likely a hard limit, since there are no plans for more running at intermediate energies (around 30 GeV). Fortunately, the centroid of the non-leading energy distribution for $Z^0 \rightarrow b\bar{b}$ decay falls in a region, where $\bar{n}$ has been well measured by five of the PEP and PETRA collaborations. Correcting for the small energy differences and combining the five measurements closest to 30 GeV[140] gives an uncertainty in $\bar{n}$ of ± 0.21 tracks, with a $\chi^2 = 7.0$ for 4 degrees of freedom. Thus, depending on how much the various systematic problems mentioned above can be brought under control, it will soon be possible to push this test to an accuracy 4 to 10 times greater than presented here.

7.7 Extraction of the Average x_E

If it is instead assumed that the non-leading fragmentation is indeed independent of the flavor of the leading quarks, it is possible to estimate $\langle x_E \rangle_b$ from the non-leading multiplicity, essentially by reading off the non-leading energy from the $\bar{n}$ versus E_{cm} plot. For $\langle x_E \rangle_b \sim 0.7$, the relevant range of E_{cm} for this measurement is between 15 and 45 GeV. The value of $\langle x_E \rangle_b$ is determined by the value of $\bar{n}$ at the central value of $E_{cm} \sim 30$ GeV, while the uncertainty in $\langle x_E \rangle_b$ will be given by the slope of the $\bar{n}$ dependence upon E_{cm}, which in this range is given by the low energy PETRA data and the TRISTAN data. Figure 7–7(a) shows the fit to the LLA inspired form as discussed previously,

$$\bar{n}_{had} = a + b \cdot \exp\{c\sqrt{\ln E_{cm}}\} \tag{7-19}$$

with $a = 4.684$, $b = 0.511$ and $c = 2.736$. Figure 7–7(b) shows the residuals from this fit as a function of energy. All corrections discussed previously, the heavy quark correction, removing the effects of the leading particles and the x_E-distribution corrections, can then be applied to the results of this fit, although none have been included in Figure 7–7(a). The value of $\langle x_E \rangle_b$, with errors, is then found by solving the above equation, with the desired correction included, for the center-of-mass energy corresponding to the measured non-leading multiplicity. As a correction to the charged multiplicity, rather than a correction to the energy, the x_E-distribution correction has the approximate form $\delta\bar{n} = -141 \cdot E_{cm}^{-1.80}$, such that at 30 GeV, it is

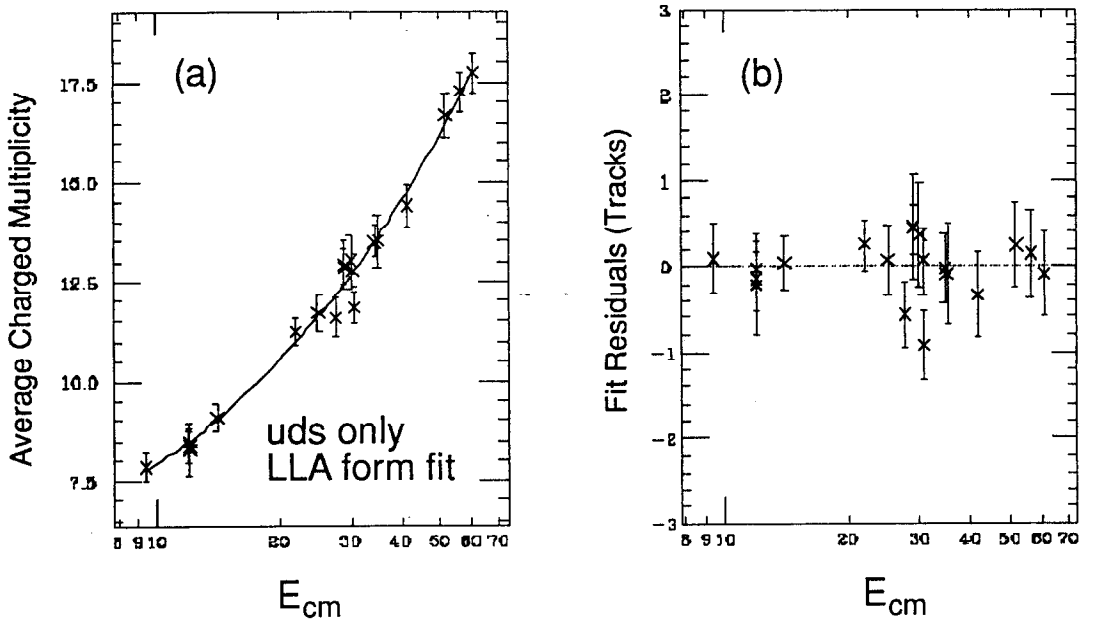

Figure 7–7 (a) Data and fit to the LLA-inspired form for total multiplicity restricted to the data from PEP, PETRA, and TRISTAN, for extraction of the mean x_E. (b) Residuals from the fit.

–0.31 tracks. For example, with the heavy quark and x_E-distribution corrections applied, the corrected fit is

$$\bar{n}_{had} = 3.484 + 0.511 \cdot \exp\{2.736\sqrt{\ln E_{cm}}\} - 141 \cdot E_{cm}^{-1.80}. \qquad (7\text{-}20)$$

Table 7–13 shows the results for $\langle x_E \rangle_b$, including statistical error only, for each of the three tags. In addition to systematic effects enumerated in the previous

tag	no correction	add x_E distribution correction	also add heavy quark correction	also add non-leading, correction
EV2	$0.701^{+.095}_{-.103}$	$0683^{+.082}_{-.097}$	$\mathbf{0.619^{+.096}_{-.107}}$	$0.659^{+.085}_{-.096}$
EV3	$0667^{+.098}_{-.120}$	$0.650^{+.092}_{-.114}$	$0.583^{+.102}_{-.124}$	$0.627^{+.089}_{-.111}$
HE2	$0.665^{+.105}_{-.124}$	$0649^{+.098}_{-.119}$	$0.581^{+.110}_{-.130}$	$0626^{+.096}_{-.117}$

Table 7–13 The values of $\langle x_E \rangle_b$ calculated with the different corrections as described in text. The EV2 value with the x_E-distribution and heavy quark corrections is taken as our final result.

section, the systematic error must include a contribution of 0.5 tracks due to the

uncertainty in the heavy quark correction. For the fit with the heavy quark and x_E-distribution corrections, which is taken as the final measurement, the resulting total systematic error of ±0.80 tracks yields

$$\langle x_E \rangle_b = 0.619^{+.096\ +.043}_{-.107\ -.046}.$$

where the errors are statistical and systematic, respectively. Thus, to its rather limited level of statistical accuracy, this approach provides a result in agreement with the current LEP average of 0.697±0.013,[22][23][24] and thus has provided an important independent check of the $\langle x_E \rangle_b$ measurements which use the lepton momentum spectrum.

In the future, the LEP experiments should be able to exceed the systematic error limit quoted here. This should provide a very meaningful check of the B hadron fragmentation energy, which is a critical parameter in the measurement of various parameters associated with $Z^0 \to b\bar{b}$ decays (branching fraction, lifetimes, exclusive branching fractions, *etc.*)

Appendix A

Limits on B_s Production at the Z from B Mixing Measurements

It is useful in the measurement of the non-leading multiplicity in $Z^0 \to b\bar{b}$ events, to place a limit on the production of the various bottom hadron species. Though little direct information on the production fractions exists, one can limit the B_s production fraction, $P(b \to B_s)$, using the present measurements of $B\bar{B}$ mixing and assuming a constraint from the Standard Model. The strength of the mixing can be parameterized as[141]

$$\chi \equiv \frac{N(BB) + N(\bar{B}\bar{B})}{N(b\bar{b})}, \tag{A-1}$$

which is the ratio of the number of mixed events to the total number of produced $b\bar{b}$ events. If the B-mixing is large enough that the meson could mix many times before the B decays ('full mixing'), then χ tends toward 0.5. To determine the level of B_s mixing, one notes that the Standard Model places a constraint on the relative mixing strengths of B_d and B_s, resulting from the unitarity of the Kobayashi-Maskawa (KM) matrix, that

$$\frac{|V_{td}|^2}{|V_{ts}|^2} > 0.21. \tag{A-2}$$

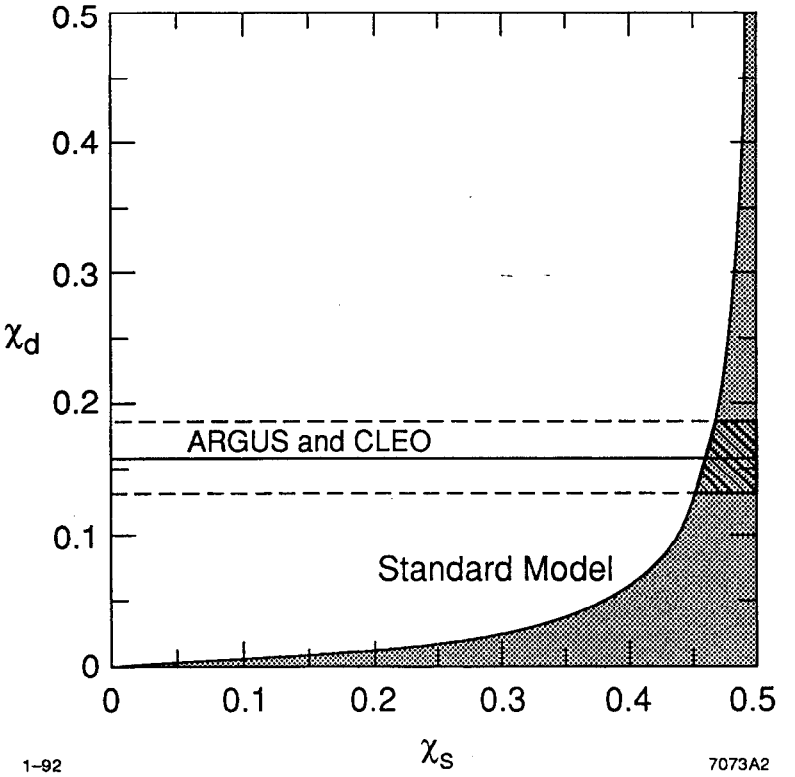

Figure A–1 The allowed regions for B_d mixing from the CLEO and ARGUS experiments[126] and the constraint from the standard model are shown. The combination of these indicates that B_s mixing is nearly maximal.

The ratio of the B_d to B_s mixing rates (x_d/x_s) will then, to within small uncertainty, be proportional to this ratio of KM elements and x_i is then related to χ_i by

$$x_i = \sqrt{\frac{2\chi_i}{1-2\chi_i}}. \qquad \text{(A-3)}$$

The mixing of the B_d has been measured by CLEO and ARGUS at the $\Upsilon(4s)$, where no B_s is produced, and yields an average value of $\chi_d = 0.155 \pm 0.043$.[126] Using the Standard Model constraint in conjuction with the CLEO and ARGUS measurement of χ_d, it can be seen in Figure A–1 that B_s must be almost fully mixed, namely $0.45 < \chi_s < 0.5$.

At the Z^0, the mixing will be a linear combination of the B_d and B_s mixing strengths,

$$\chi(Z^0) = f_d\chi_d + f_s\chi_s, \tag{A-4}$$

where f_d and f_s are the B_d and B_s fractions, with

$$f_u + f_d + f_s + f_{B\ baryon} = 1. \tag{A-5}$$

The LEP experiments have measured the mixing to be $\chi(Z^0) = 0.143 \pm 0.023$.[126] To place a limit on f_s, Equations (A-4) and (A-5) can be solved to yield,

$$f_s = \frac{2\chi(Z^0) - (1 - f_{B\ baryon})\chi_d}{2\chi_s - \chi_d} \tag{A-6}$$

with the assumption that $f_u = f_d$. Using the above values for χ_d and χ_s, and assuming that $f_{B\ baryon} = 0.1 \pm 0.1$, the $b \rightarrow B_s$ fraction is found to be 0.18±0.10, which is consistent with the Lund value of 0.12.

Appendix B

DCVD Gas and Temperature Control Systems

The operation of the DCVD in the unsaturated regime placed stringent constraints on the gas parameters such as its composition and temperature. This appendix discusses the apparatus used to investigate and maintain the required gas properties.

B.1 Gas Properties Overview

The gas used in the DCVD was a mixture of 92% CO_2 and 8% C_2H_6. The nominal gas pressure during the 1990 operation at the SLC was 2 atmospheres (absolute), although the chamber ran at 3 atm for much of its check-out prior to installation. At either operating pressure, the nominal reduced drift field, E/P, was 0.77 kV/cm/atm. With this field, the drift velocity is typically about 5.7 μm/ns. The drift velocity in this regime is unsaturated, which means that it depends acutely on the environmental conditions. This dependence can be expressed as

$$v_d \propto \frac{\mathrm{E}}{\mathrm{P}} f(\mathrm{T}, \text{gas composition}) .$$

The drift velocity depends linearly on the reduced electric field, and will also have a non-trivial dependence on the gas temperature and composition. Furthermore, because the drift velocity is so low and the maximum drift distance fairly long

(about 5 cm), the electronegative impurities in the gas must be kept to a minimum in order to maintain a minimum loss of signal during the electron drift. In order to minimize the influence of these environmental properties on the drift velocity and hence the time-distance relation, the goal was to control these parameters adequately to maintain a drift velocity variation of less than 0.05%. As discussed in Section 2.2.3.3 on page 56, the electric field strength was maintained within the required tolerances by the DCVD high voltage system.

B.2 Gas Delivery System

The gas delivery system for the DCVD was designed to handle a number of responsibilities. Specifically, it was required that the gas delivery system

- supply gas as free of impurities as possible,
- monitor and maintain a constant gas composition, and
- monitor and control the gas pressure.

The entire gas system appears reasonably complex, in part because it was designed to be flexible enough to work with a variety of gas quality control and monitoring devices. A diagram of the system can be found in Figure B–1. The system does not re-circulate the gas, but just vents the gas after passing through the chamber.

B.2.1 Mechanical Assembly

The mechanical assembly of the plumbing for the gas panel used 0.25 inch diameter oxygen-free high-conductivity (OFHC) copper tubing, which was cleaned in a solvent to remove any oils and then fired in a hydrogen furnace to remove any remaining volatile compounds. The connections were made with brass Swagelok compression fittings,* which were cleaned with an ultrasonic cleaner before use. All valves were brass Nupro H-Series bellows valves and were ordered fully cleaned. These valves contained no non-metal seals which could potentially contaminate the gas. The bulk of the gas delivery system shown in Figure B–1 was mounted on a large gas panel and was located next to the Mark II counting house.

To ensure the integrity of the system when it was fully assembled and connected to the DCVD, a helium mass-spectrometer leak detector was used. It was found that these fittings could routinely achieve full vacuum leak-tightness when properly tightened. Furthermore, no leaks could be detected from any of the pressure seals on the DCVD itself.

* The Swagelok fittings and Nupro valves are manufactured by the Crawford Fitting Company of Solon, Ohio.

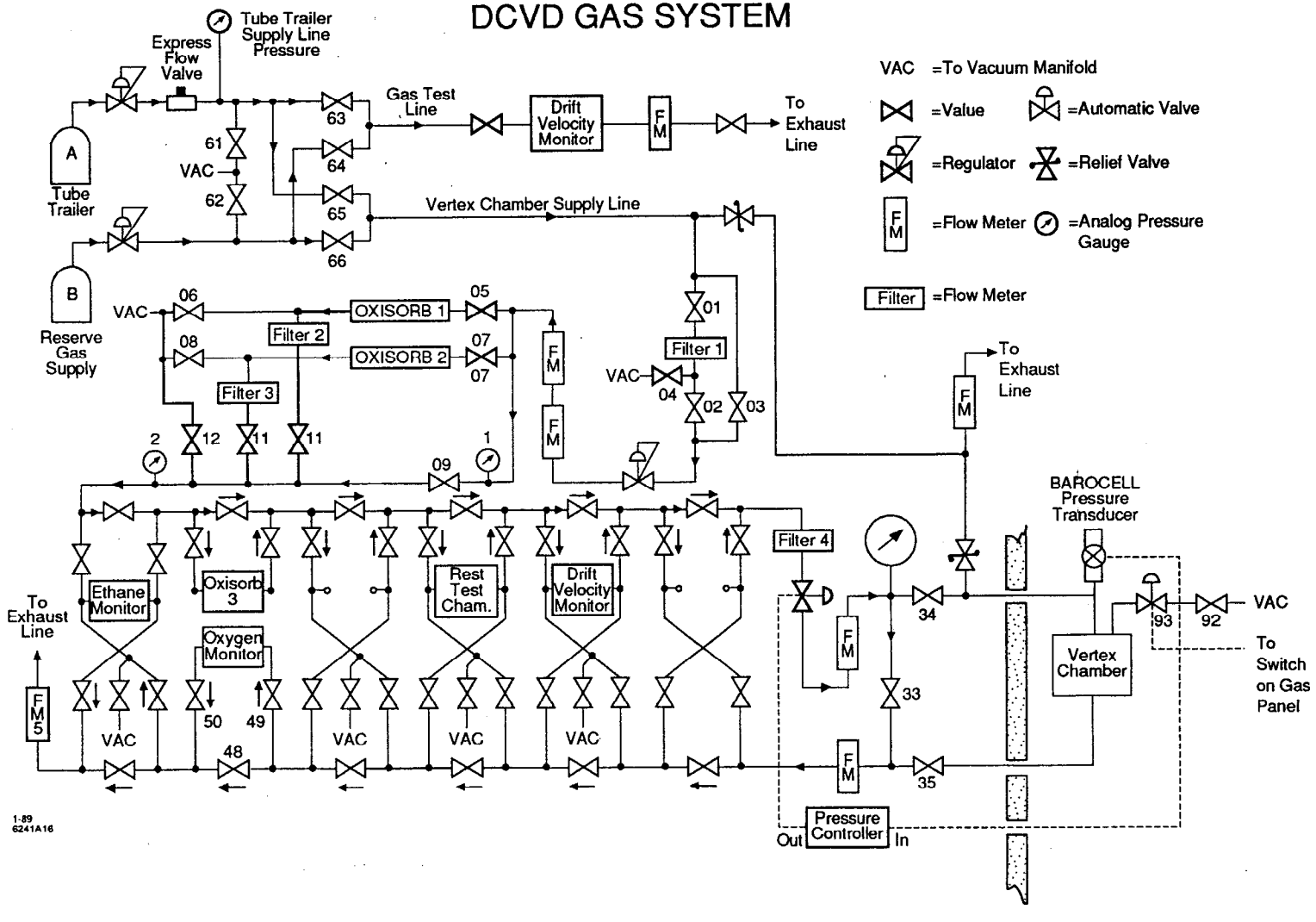

Figure B–1 A schematic diagram of the gas system for the DCVD.

Because the DCVD could be pumped to a vacuum, a 0.875 inch diameter vacuum manifold went from a mechanical vacuum pump placed by the gas panel, out to the Mark II magnet iron, about 15 feet from the chamber. A pneumatically controlled vacuum valve was located there to seal the chamber from the vacuum manifold. The final 15 feet of vacuum manifold was comprised of 0.5 inch OFHC copper tubing, as this was in constant contact with the gas in the chamber.

B.2.2 Gas Source

The gas supply for the 1990 run was two large tube trailers containing the CO_2/C_2H_6 gas mixture. The gas was mixed commercially by the Liquid Carbonic Company and required to meet purity specifications. It was standard to also test the gas locally using our gas monitoring equipment, as discussed later. Typical gas shipments would contain as much as 3 ppm of oxygen as the primary electronegative contaminant. Contamination of other organic compounds, as measured by the supplier, were usually less than 100 ppm. Using the tube trailers was particularly advantageous, as it ensured a constant gas composition for extended periods. At the nominal gas flow rates of 1–2 scfh, a tube trailer would last for at least six months of operation. The gas pressure of the tube trailer when supplied was about 500 lbs, which is below the pressure at which the CO_2 would liquify. The gas pressure was regulated down to about 80 psi for the transfer line to the gas panel. Mounted on each tube trailer was an excess flow valve, designed to close automatically should the flow rate get too large (as in the case of a broken supply line, *etc.*)

B.2.3 Elements of the Gas System

At the gas panel, the gas was routed through a pair of Oxisorb units which remove virtually all of the trace amount of oxygen in the gas. Two units were used because the small units tended to last only about two weeks, depending on the oxygen level in the incident gas. Several particulate filters were used to ensure that the chamber was not contaminated by any solid material. The specifications for the Oxisorb units stated that they would lower the oxygen level to less than 0.1 ppm when the inlet gas is not greater than 15 ppm. This performance is consistent with the observations made with our monitoring equipment.

The last item on the gas panel before the supply line to the chamber was an electronically controlled regulator valve for active pressure control. The pressure in the chamber was measured by a Barocell Pressure Transducer, mounted on the end of the 0.5 inch vacuum manifold, about 15 feet from the chamber. This transducer

was connected to a Datametrics Type 1501 Pressure Controller. The controller incorporated an electronic feedback system and would adjust a regulator valve placed on the gas panel just prior to the supply line to the chamber. The desired pressure was set with a dial switch on the controller.

After the chamber, the gas would flow through some of the gas monitoring equipment such as the Drift Velocity Monitor (DVM), the oxygen monitor and the ethane monitor. The DVM was a device for monitoring the drift velocity and electron lifetime of the gas, and is discussed below in Section B.4.1. It was not operated continuously, as were the other monitors, but rather was used for studies of gas properties and for verifying the quality of new gas shipments.

The oxygen level in the gas was measured by a Model 316 Oxygen Analyzer produced by Teledyne Analytical Instruments. This device uses a fuel cell to electrochemically measure the concentration of oxygen in a gas. It can measure levels from a few parts per million up to 21%. Although intended to be calibrated with air, the cell type which was required for use in CO_2 had a very long recovery time until it would again be sensitive on the few ppm level. Consequently, we employed a standard reference bottle of CO_2 with about 80 ppm O_2 to provide at least a very good relative oxygen determination. This unit was used continuously as a warning device of possible problems during the 1990 data runs.

The percentage of ethane in the gas was measured by a Teledyne Model 235 Thermal Conductivity Analyzer. This analyzer determines the fraction of C_2H_6 by comparing the thermal conductivity of the sample gas to that of a reference sample of pure CO_2. The accuracy of this device is 0.01% ethane.

The pressure measurement, oxygen level and ethane fraction were read out through a 14-bit CAMAC analog-to-digital converter to the VAX host computer. The Mark II environmental monitoring routine, which recorded information for all the various Mark II systems would record the gas monitoring information to the data tape every four minutes. This program would also check that the various values were within preset limits and alert the physicists on shift of a potential problem. The pressure measurement was also connected to a hardware DCVD alarm interlock which would trip the DCVD high voltage should the gas pressure drop too low.

The gas system data recorded by the VAX can be used to characterize the long term performance of the gas system. The oxygen and ethane levels were virtually constant throughout the entire running. Typically the pressure would be held constant to better than 0.01 psi (0.03%) over periods of weeks, although some shifts

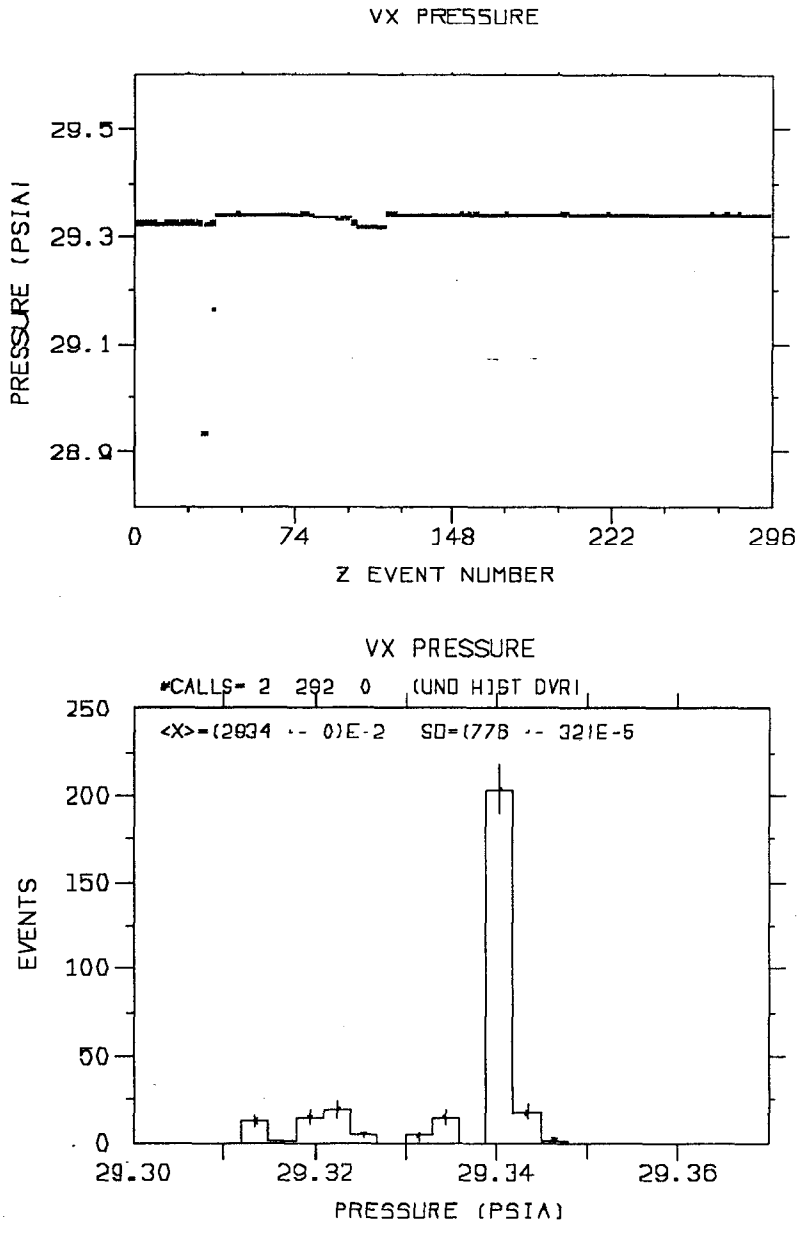

Figure B–2 Measured DCVD pressure for all of the 294 triggered Z events. The two low points we during periods when the pressure control malfunctioned.

were seen on the order of 0.02 psi at a few points during the run. The pressure which was recorded closest to each recorded Z trigger is shown in Figure B–2. Neglecting two very low points when the pressure control was malfunctioning, the rms pressure is 0.007 psi over all of the Z events.

B.3 Temperature Control System

The temperature of the DCVD was monitored and controlled by a computer controlled feedback system which circulated water around the outside of the chamber. The goal of this system was to achieve temperature stability and uniformity within the chamber.

B.3.1 Temperature Measurement

The temperature of the DCVD was measured by a series of 48 thermistors placed in and around the chamber. These thermistors were individually calibrated with respect to a reference thermistor to correct for relative offsets. Over the typical temperature ranges of 25 to 35° C, the temperature response was not significantly different among thermistors to require more than a single offset correction. The average offset correction was equivalent to less than 0.05° C. After the thermistors were installed in the DCVD, the entire chamber was placed inside of a foam container and allowed to equilibrate thermally. Further, generally small, offset corrections were made from this test.

The thermistors on the chamber were placed in a number of locations. These included:

- on the outer surface of the inner and outer shells
- on the aluminum supports for the Macor wire-foundations, which are inside the gas volume
- on the pressure heads
- in the high voltage faraday cages
- in the air outside of the DCVD
- on the CDC inner core
- in the water lines which circulate water around the DCVD

The best measurement of the internal chamber temperature came from the thermistors mounted on the aluminum supports for the Macor foundations, as these are the most de-coupled from surfaces with the temperature control water lines.

The thermistor resistances were converted to a voltage signal using custom electronics containing 64 thermistor channels. These temperature signals were read out to the VAX host computer via the same CAMAC ADC's as used for the pressure system. The temperature signals were read in every 12 seconds and corrected in software to account for the individual thermistor calibrations. These temperatures

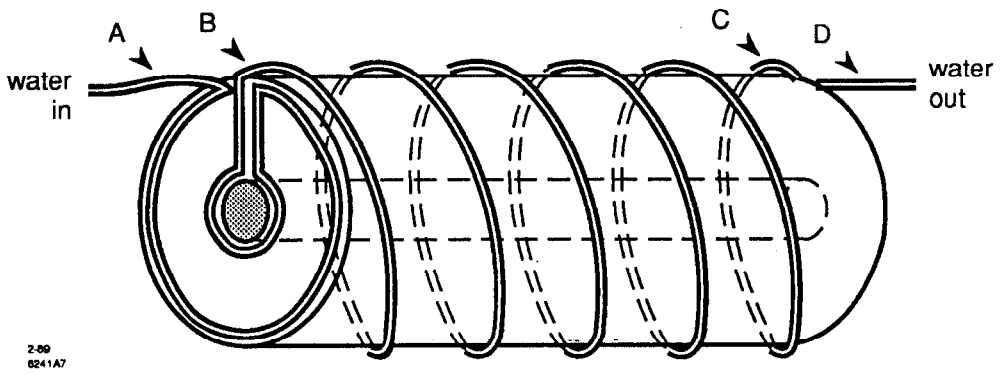

Figure B–3 Water tubing around the pressure heads and the outer shell of the DCVD. The letters indicate the positions of the thermistors in the water supply lines.

were recorded to the data tape every four minutes and were used for the active temperature control discussed in the next section.

B.3.2 Temperature Control

The temperature of the DCVD was controlled by circulating water from a temperature-controlled reservoir around the DCVD. The water would first go around the pressure head on the inner and outer radius, then around the outer shell in a helical pattern and finally around the pressure head on the other end of the chamber, as shown in Figure B–3.

The system to circulate the water to the DCVD is shown schematically in Figure B–4. The temperature controlled reservoir was a Haake N2-R Digital cryostat. It was comprised of a 15 liter reservoir, which contained a compressor for a constant rate of cooling, and a control unit mounted atop the reservoir which handled the temperature control by use of a heating coil. The specifications for this unit claim a temperature control of ±0.1° C with their internal hardware feedback circuit.

The water from this reservoir was pumped out to the chamber using a Liquiflo 3 gallon per minute (gpm) gear pump. The maximum output pressure of the pump was 100 psi. Typically, the flow rate out to the DCVD would be about 1 gpm, a value which was chosen so that the flow through the 0.25 inch tubing would be on the onset of turbulence for better heat transfer. The supply and return lines to and from the chamber were 0.5 inch insulated aluminum tubing to reduce the pressure drop in these lines. To keep the water in the closed system clean, a UV sterilizer, a de-ionizer and several particulate filters were employed. A hardware alarm system

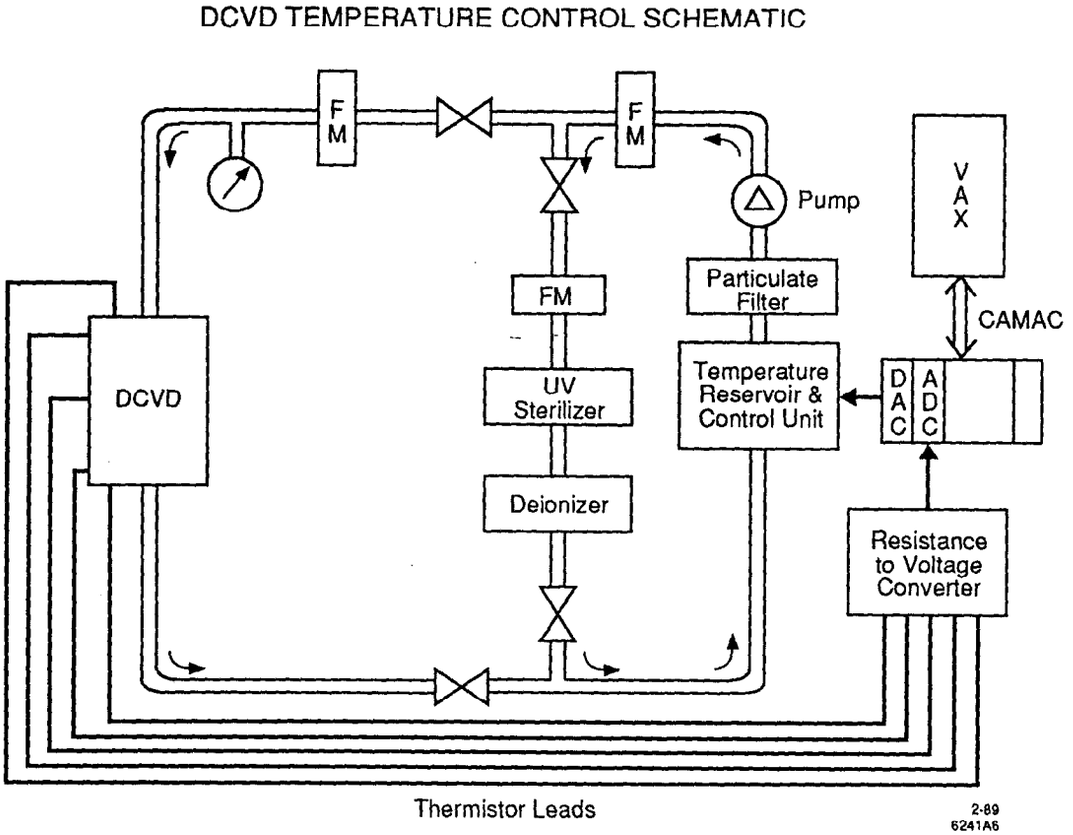

Figure B–4 A schematic diagram of the water circulating temperature control system for the DCVD. The devices labelled FM are flowmeters.

monitored the pressure in the supply line to the chamber and the water level in the reservoir. If an out of tolerance condition was detected, this system would trip an interlock which supplied power to the pump.

The active temperature control was achieved by software which interacted with the Mark II environmental monitoring. Both routines ran on the VAX host computer. With each 12 second interval, the new temperatures would be analyzed and the temperature of the water circulating out to the DCVD appropriately adjusted. This adjustment was made using a 16-bit DAC to which the temperature control unit was adjusted.

The algorithm used to maintain a constant temperature used the two thermistors in the water lines just before and just after the outer shell (thermistors B and C in Figure B–3). The variable to which the temperature feedback system reacted was the average of these two thermistors. These were chosen because the outer shell has the largest surface area in the chamber exposed to the gas volume,

and thus would most substantially affect the gas temperature. The feedback algorithm was quite straightforward. If a temperature adjustment was required, it would vary the temperature voltage signal sent to the temperature controller by the amount of the desired change and then wait for a time period to allow the system to come to thermal equilibrium. This time period would depend on the temperature change which was requested. The hardware alarm system would also check that the voltage signal generated by the DAC corresponded to a reasonable temperature range. If this were not the case the alarm system would substitute a default safe voltage and notify the persons on shift. As the check of last resort, this system also used a thermistor to check the temperature of the water being sent to the DCVD, and if it were out of range the pump interlock would be activated, shutting off water circulation to the chamber.

B.3.3 Temperature Stability and Uniformity

The performance achieved by this system during the 1990 run was quite good. The thermal environment in which the DCVD ran is illustrated in Figure B–5 which shows the temperature outside the chamber yet still inside the central core of the CDC. It is seen that during the 1990 run, the temperature variation spanned a full range of almost 4° C due to external environmental factors. There are clear diurnal variations of about 0.25° C if this temperature is plotted as a function of

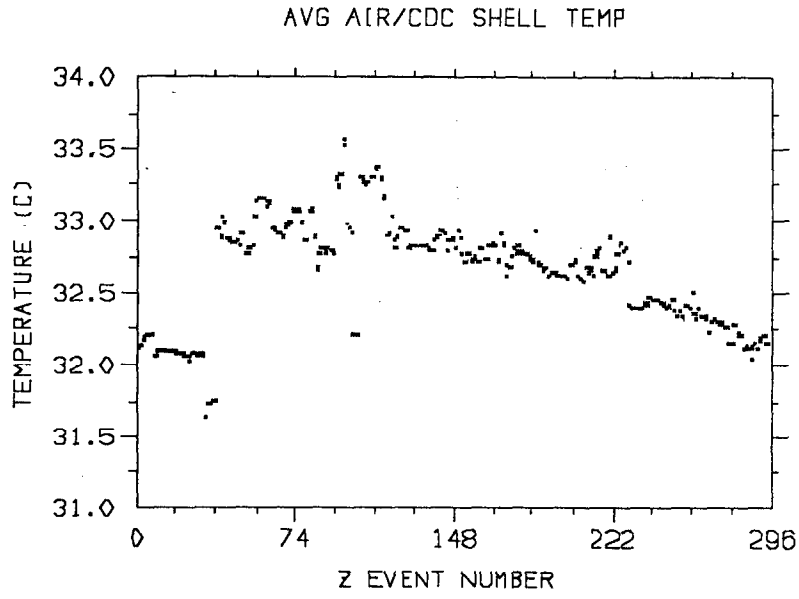

Figure B–5 Temperature in region inside the CDC but outside of the DCVD.

time as well as larger variations corresponding to various systems turning on and off (these systems include the Mark II solenoid, the DCVD high voltage and the SSVD). The chamber temperature as measured by the average of three thermistors placed on the aluminum support for the Macor foundations is shown in Figure B–6. The width of the central peak can be characterized as having an rms width of about 0.02° C. Outside this central peak there are a number of spurious points which were caused by known malfunctions in the temperature control system.

The temperature of the other major surfaces in the chamber, the outer shell and the inner core are shown in Figure B–7. The outer core temperature was very stable, which is expected because the water tubing was connected directly to this surface and the temperature control algorithm used the thermistors before and after the shell for temperature determination. The inner core was not actively temperature controlled and consequently exhibits significant temperature variation. There is virtually no diurnal variation in the inner core. However, temperature changes of ~0.3° C would occur when the SSVD was turned on and off, indicating that, as one might expect, the SSVD is the dominant contributor to the inner core temperature.

Finally there is the question of the temperature uniformity inside the chamber. Figure B–8 illustrates the temperature difference between the ends of the chamber and the temperature difference from the inner core to the outer cylinder. The temperature difference between the ends of the chamber, as measured by the thermistors mounted on the aluminum supports for the Macor wire-foundations, is about 0.12° C with a variation of less than 0.02° C for closely spaced events. This temperature difference is just a consequence of the water temperature warming as it passed from one pressure head to the other due to the heat load of the chamber. The radial temperature difference is larger. Typically the inner core was about 0.5° C warmer than the outer cylinder. Furthermore, as noted previously this temperature difference will vary because the inner cylinder had no active temperature control. This is the largest temperature difference and corresponds to about 0.17%. However, over local blocks of events the variation in this temperature difference is only about 0.1° C.

B.4 Gas Property Studies

A series of studies were done to measure some properties of the CO_2-based gas mixtures. In particular, these investigated the drift velocity dependence on the temperature and the electron lifetime with various chamber additives such as

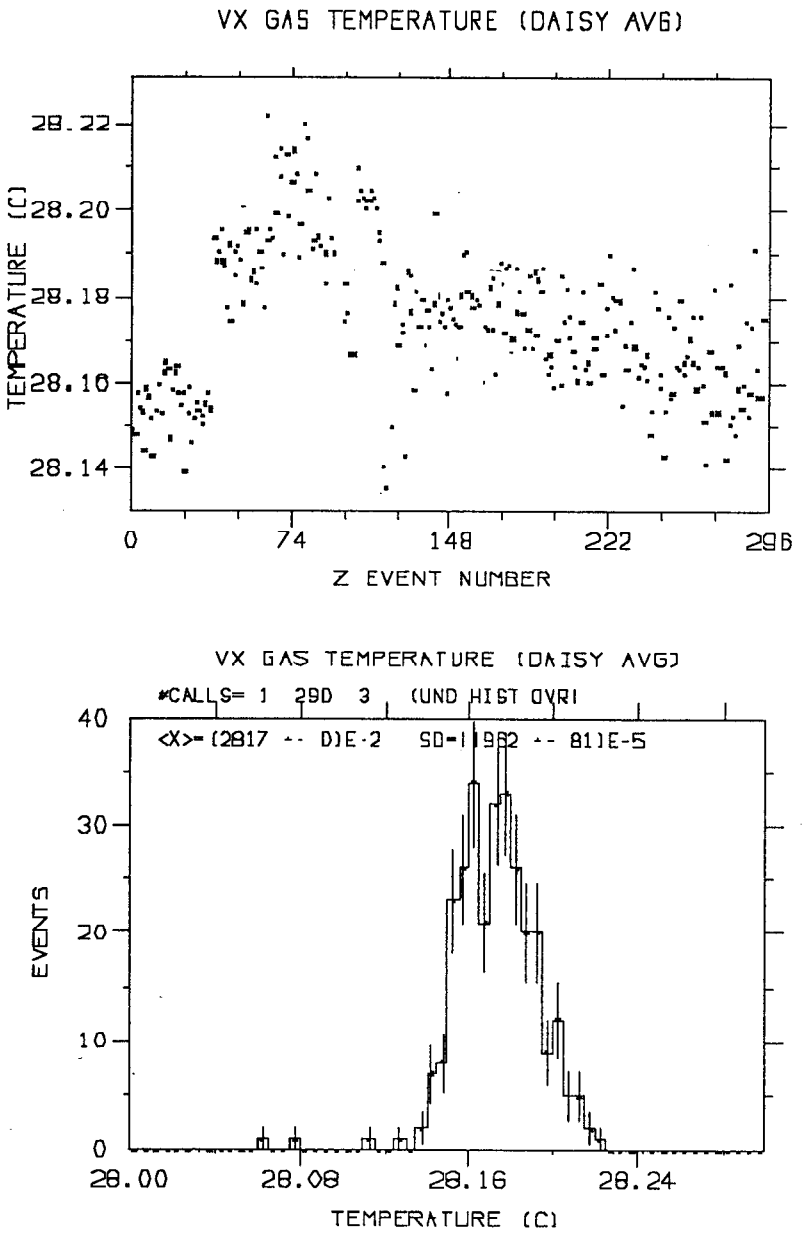

Figure B–6 The nominal temperature inside the DCVD as measured by thermistors placed on the aluminum support for the Macor foundations (the "daisy").

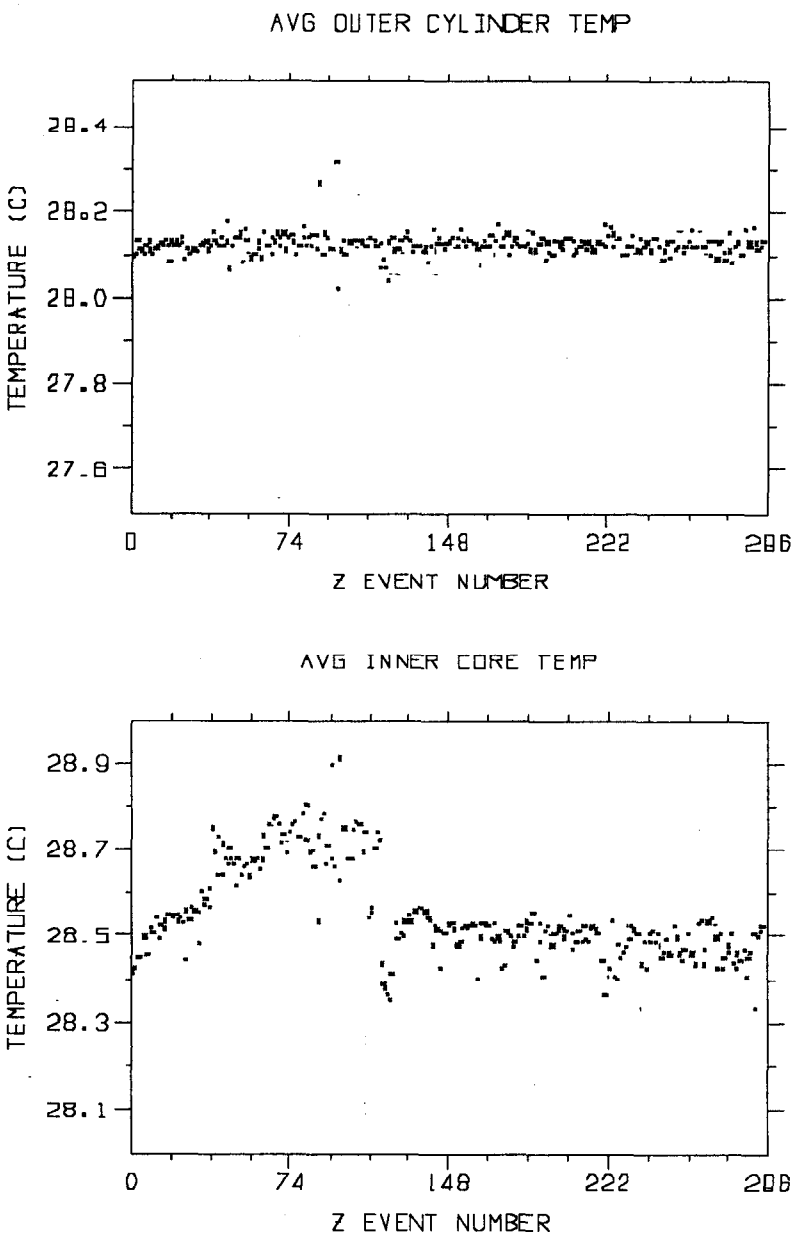

Figure B–7 Temperatures of the outer cylinder and inner core as determined by an average of the thermistors mounted on these surfaces.

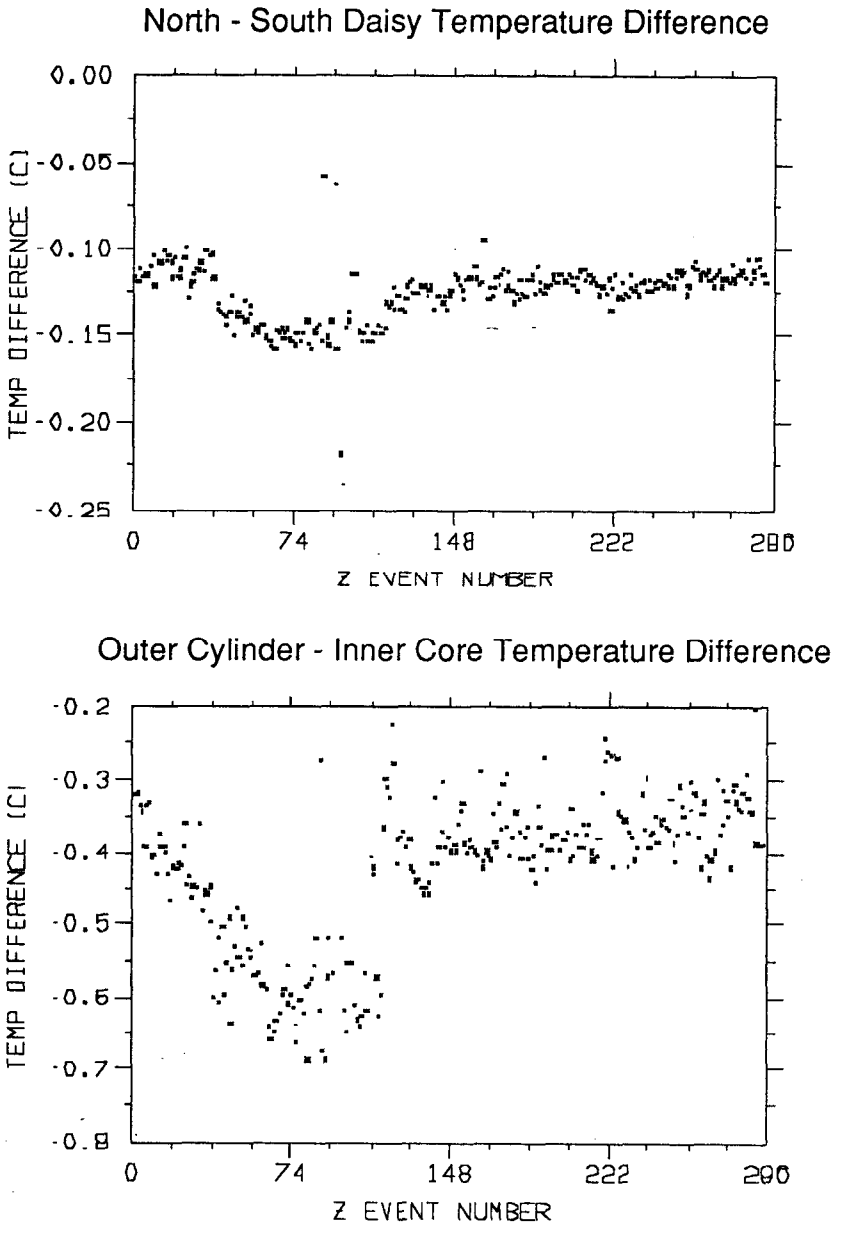

Figure B-8 Temperature differences between the aluminum supports for the Macor on each end of the chamber and between the inner core and outer cylinder.

isopropanol, and most importantly, oxygen. These studies were carried out largely with a small chamber called the Drift Velocity Monitor (DVM). Tests were also done on the tolerance of the gas to radiation. These tests were done in another device, the Radiation Test Chamber (RTC).

B.4.1 Drift Velocity Monitor

The DVM consists of a single 5.08 cm long drift cell, bordered by edge field wires with graded voltages to maintain a uniform electric field in the drift region (see Figure B–9). Electrostatic simulation indicated that the field is uniform to within 0.25% at the center of the cell. Two 1.0 mCi ^{106}Ru were placed within collimators to produce thin beams of 39.4 keV β^-. The β's would produce ionization at two fixed distances from the sense wire and the drift velocity could be obtained from the time difference between their known spatial separation.

The data acquisition electronics for this chamber were quite simple. The pulse from the photomultiplier fed into a discriminator then through a gate-and-delay generator. This signal was then sent to the start input on a Lecroy Model 3001 Multichannel Analyzer ('qVt'), operating in the t-mode. This particular qVt was

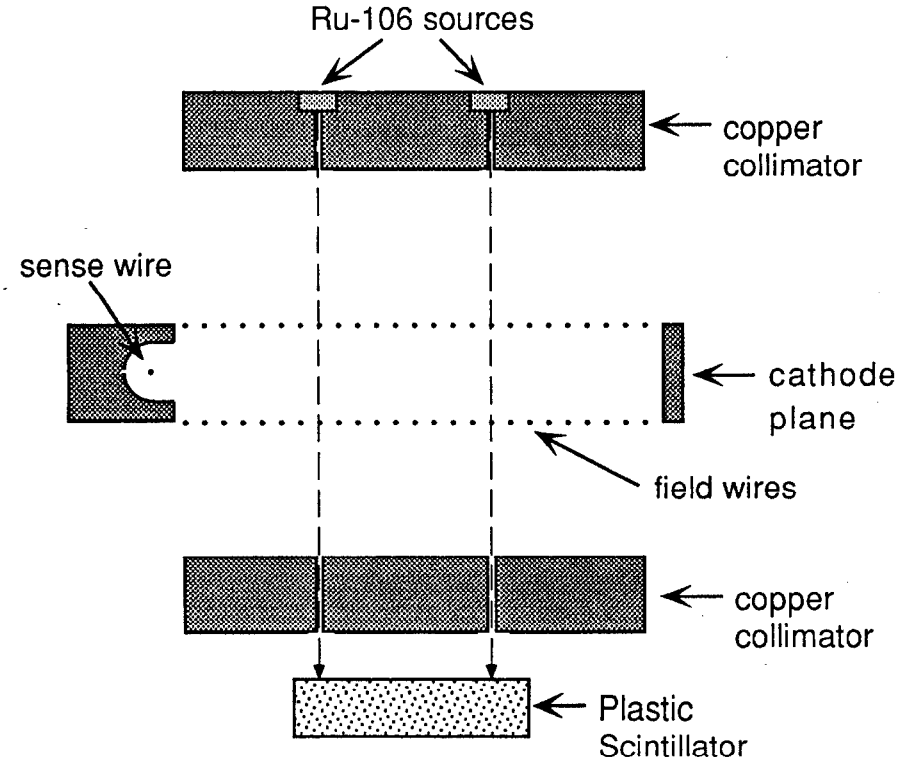

Figure B–9 A schematic illustration of the Drift Velocity Monitor. The paths of the 39.4 keV β^- are shown by the dotted lines.

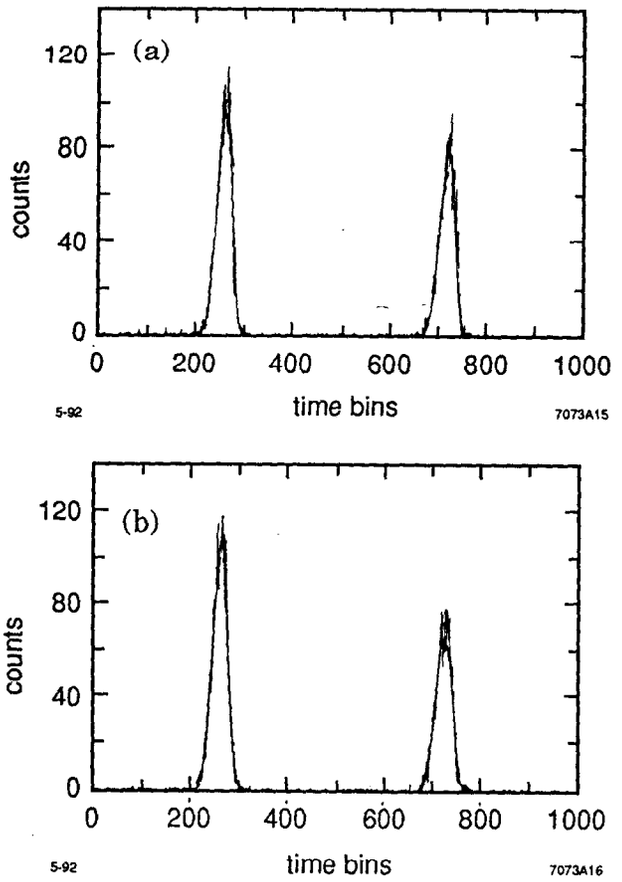

Figure B–10 Drift time spectra recorded on the qVt. Each LeCroy time bin is equivalent to 0.0187 μs. These plots are with different amounts of oxygen in the gas: (a) 0.2 ppm, and (b) 3.4 ppm. The ratio of the areas under the later to earlier peak is 0.80 and 0.70, respectively.

modified to increase the maximum time scale to about 18 μs. The signal from the sense wire of the drift cell was fed through a preamplifier, a 10X amplifier, a discriminator and finally into the stop input of the qVt. Both discriminators were set quite low to minimize the effect from time slewing due to the pulse heights. The qVt was read out via CAMAC to a VAX computer using a LeCroy Model 2301 CAMAC Interface.

Typical time distributions are shown in Figure B–10. The time spectrum is fit with a 8-parameter double Gaussian plus linear background function. The fit Gaussian means are used to determine the drift velocity. Comparing these spectra, recorded with different levels of oxygen in the gas, illustrate how the DVM is sensitive to the electron lifetime of the gas by looking at the ratio of the area in the

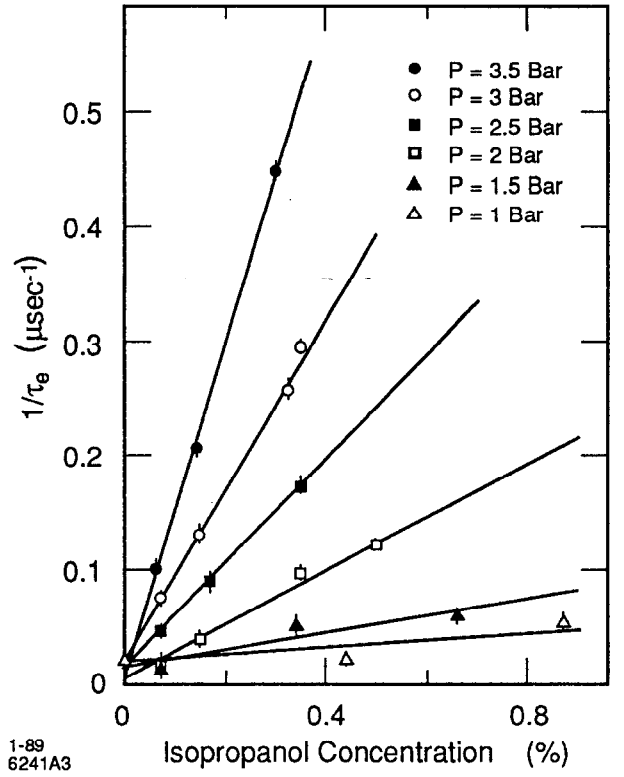

Figure B–11 The electron lifetime in the nominal CO_2/C_2H_6 gas with a small admixture of isopropanol.

earlier and later peaks. Note that the ^{106}Ru sources were not necessarily the same strength, so this also was taken into account, which can be done, for instance, by exchanging the positions of the two sources.

The electron lifetimes in the gas were measured by the DVM for the nominal CO_2/C_2H_6 gas mixture with different amounts of isopropanol, a common proportional chamber gas additive which has the effect increasing the radiation tolerance of a gas, as discussed in the following section. The isopropanol was mixed into the gas using a bubbler which was held at a constant temperature to control the isopropanol vapor pressure. The resulting electron lifetimes are shown in Figure B–11. With a drift velocity of about 5.7 mm/μs and a maximum drift length of about 50 mm in the DCVD, the maximum drift time is about 9 μs. Thus an electron lifetime of 30 μs corresponds to a 25% loss in pulse height, and at an operating pressure of 2 atm this limits the amount of isopropanol which should be used to less than ~0.1%.

The electron lifetime was also measured as a function of the oxygen level in the gas. This was done simply by using gas bottles supplied by the commercial gas

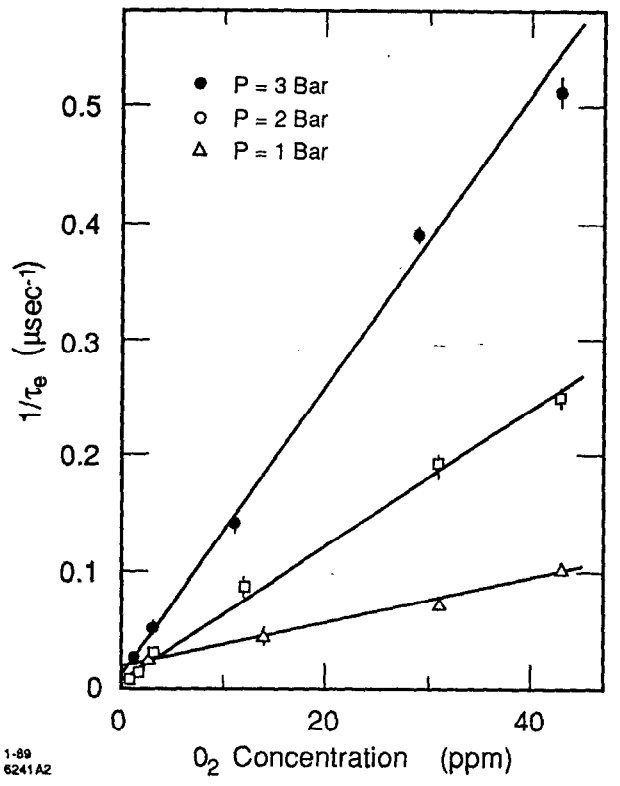

Figure B–12 Electron lifetimes as a function of the oxygen concentration in the standard CO_2/C_2H_6 gas mixture.

vendor which (unintentionally) had high levels of oxygen present. The gas sources were as high as 35 ppm of O_2. The electron lifetimes as a function of the oxygen concentration are shown in Figure B–12 and demonstrate that a very low oxygen level is required to produce reasonable electron lifetimes. These levels were routinely achievable in the actual system by keeping the system very leak-tight and by the use of Oxisorb to remove virtually all of the oxygen from the gas just prior to sending it into the chamber (see Section B.2.3). It is also interesting to note that these measurements of the electron lifetime confirm that the process of electron attachment is a three-body process, namely

$$O_2 + X + e^- \rightarrow O_2^- + X + \text{energy}.$$

In Reference [142] it is shown that the electron attachment frequency, $\nu_a = 1/\tau_e$, is given for a 2-body process ($O_2 + e^- \rightarrow O_2^- + \text{energy}$) by:

$$\nu_a = k_2 [O_2] \text{ (2-body)},$$

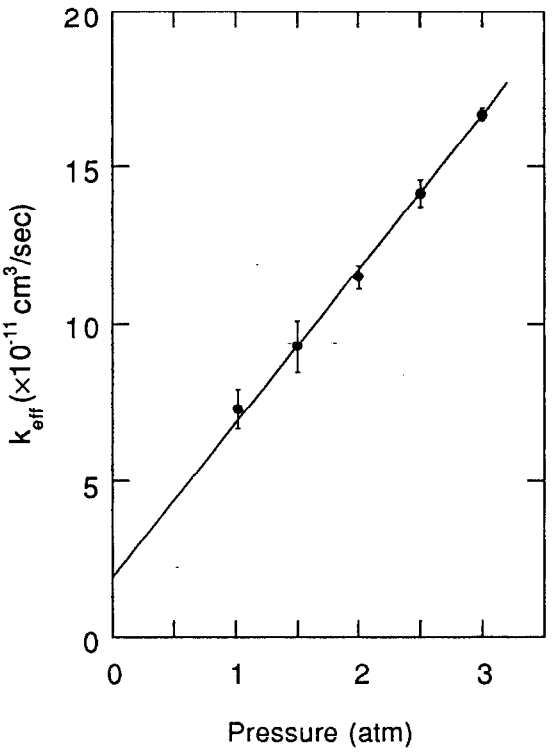

Figure B–13 k_{eff} as a function of the pressure of the CO_2/C_2H_6 mixture, demonstrating that the electron attachment process in this gas is a 3-body process.

where $[O_2]$ is the oxygen concentration and k_2 is the 2-body coefficient. For a 3-body process, the relation becomes,

$$\nu_a = k_3 [O_2] [X] \text{ (3-body)},$$

where [X] is the concentration of the other component in the gas (in our case CO_2), and k_3 is the coefficient for this process. If one forms the quantity

$$k_{eff} = \nu_a / [O_2] = 1/\tau_e [O_2],$$

then as a function of the concentration or pressure of the main component of the gas, k_{eff} can distinguish between the 2 and 3-body processes. A two body process will not exhibit any pressure dependence (since $k_{eff} = k_2$), whereas a three body process will have a linear dependence (because $k_{eff} = k_3 [X]$). The result, shown in Figure B–13, clearly demonstrates the three body nature of the interaction in our gas mixture.

The drift velocity dependence on temperature was also investigated using the DVM. The pressure chamber for the DVM had the same type of 0.25 inch tubing

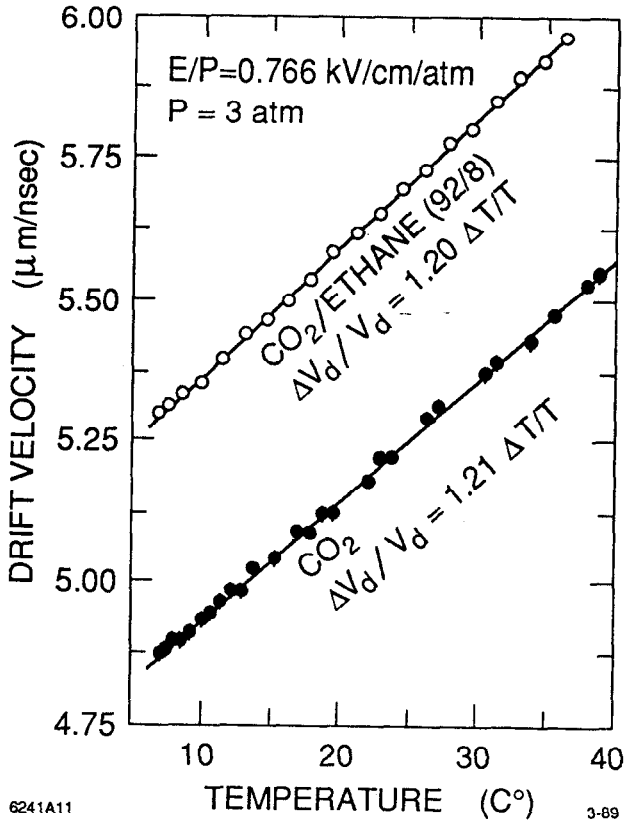

Figure B–14 The drift velocity dependence on temperature for CO_2/C_2H_6 and pure CO_2.

wound around it, as did the outer shell of the DCVD (see Figure B–3), which allowed active temperature control of the DVM. Using a prototype version of the temperature control routines used in the DCVD, the DVM was stepped through a range of temperatures, pausing to measure and read out the drift velocity through the CAMAC interface to the qVt module. The results are shown in Figure B–14. The temperature dependence of the drift velocity was characterized phenomenologically by $v_d \propto T^{\alpha}$. The dependence appears to be slightly stronger than a linear dependence, with a value of α which is about 1.2 for the CO_2/C_2H_6 gas mixture and for a pure CO_2 sample.

B.4.2 Radiation Test Chamber

Radiation damage to wire chambers has received a substantial amount of study, but this is still an imprecise science at best. Nonetheless, there are many ideas about the various mechanisms which contribute to the radiation damage.[143] Carbon dioxide and most nobel gases require the use of a gas additive (*quencher*) to absorb the copious number of photons emitted during the electron avalanche at the

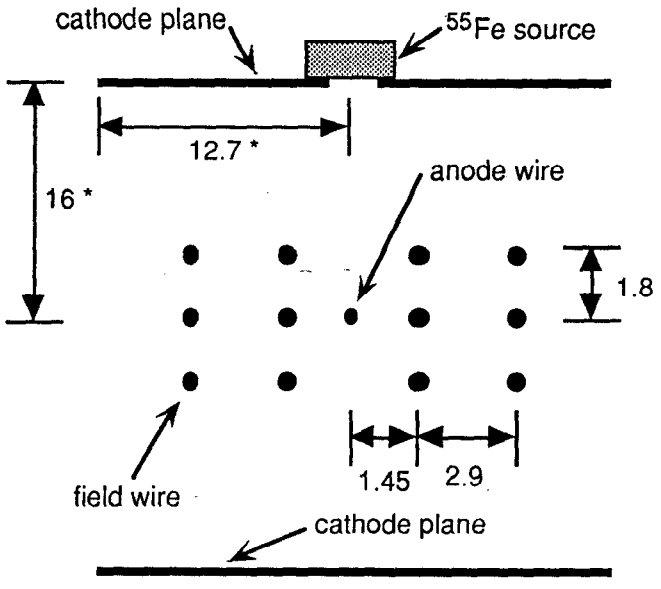

Figure B–15 Radiation Test Chamber cell design.

anode. Typically, organic gases such as ethane or isobutane, have been used. Without these quenchers, the photons tend to produce effects such as photoemission of electrons from the cathode. During the avalanche process, these quencher molecules can be dissociated into radical molecules which typically have a large dipole moment and are thus attracted toward the anode surface. These radicals can then polymerize and form deposits on the electrodes. In later avalanches, these polymers can receive a positive charge and drift toward the cathode. On the anode, these deposits can appear as gain loss, whereas on the cathode these can lead to the production of dark current (Malter Effect). One way to reduce this polymerization is to add a non-polymerizing gas, such as an alcohol, with a lower ionization potential. A very efficient charge transfer mechanism will cause the alcohol to neutralize the polymerizable molecules, thus reducing the organic deposits.

A very simple test cell was built to study the radiation damage for various gases and gas mixtures.[144] The cell design used in the last series of tests is shown in Figure B–15. To irradiate the cell, a ^{55}Fe source (either 300 or 1000 μCi) was used to provide 0.59 keV x-rays from the electron capture process. The gain in the cell was measured by the output voltage from the anode wire, after an RC integrating circuit. The gain as a function of the radiation exposure is illustrated in

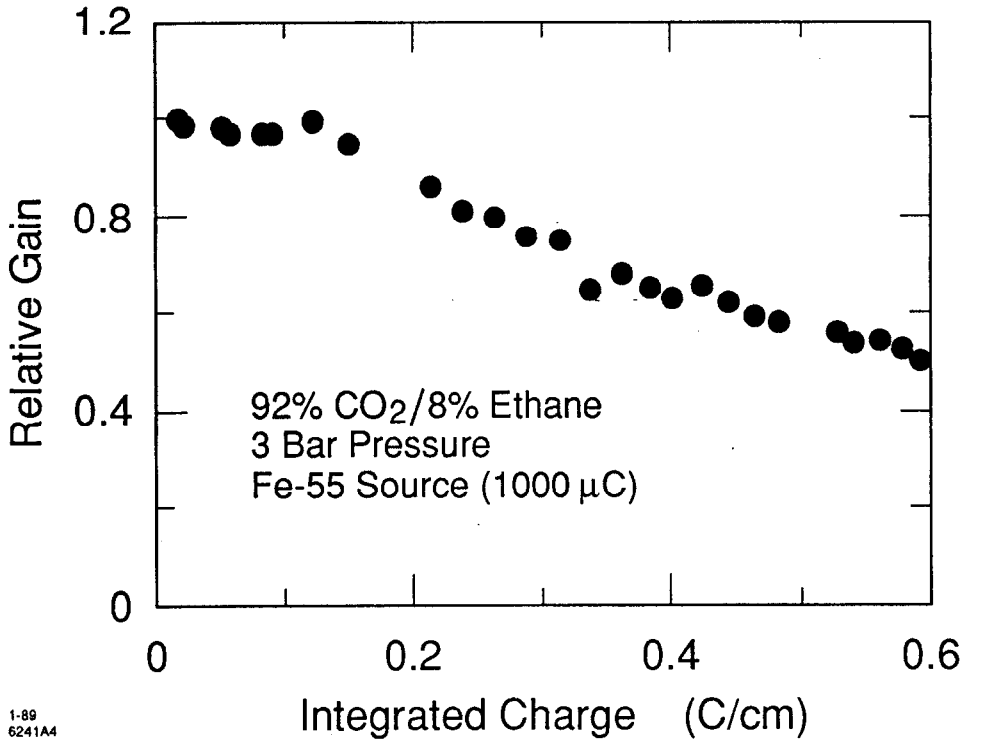

Figure B–16 Relative gain as a function of the total integrated charge for the nominal CO_2/C_2H_6 gas mixture.

Figure B–16 for the standard 92%/8% CO_2/C_2H_6 gas mixture. The summary of the tests on several gas mixtures are given below.

1. 92%/8% CO_2/iso-C_4H_{10}: The observed gain loss was minimal (similar to the CO_2/C_2H_6) except that very high current draw began and the test had to be terminated after about 0.2 C/cm of integrated charge. A possible explanation for this behavior is the Malter Effect, whereby an insulating material builds up on a field or cathode wires. After some irradiation this layer becomes charged and tends to emit electrons spontaneously. A potential cause of the low lifetime with this gas is that the gas used was not of the highest quality, and consequently could have contained impurities which were responsible for the development of the Malter Effect symptoms.
2. 92%/8% CO_2/C_2H_6: The radiation tolerance with this gas mixture was observed to be quite good. The gain was reduced only to about half after an integrated charge of 0.6 C/cm and no excess current draw developed. Upon the conclusion of the test, the anode wire was analyzed using x-ray spectroscopy and the deposits were found to contain silicon. The potential sources of this silicon include the G-10 wire frame, and to this

end a cell was made using Macor. This cell, however, repeatedly suffered premature high current draw and was never operated beyond 0.15 C/cm during which it behaved similar to the previous tests.

3. 92%/8% CO_2/C_2H_6 + 0.1% isopropanol: The addition of some alcohol was done in the hope of improving the tolerance to radiation. No difference was discernible from the CO_2/C_2H_6 test. Of course if the deposits on the anode which cause the gain loss are due to silicon impurities from components in the cell, it is unlikely that the alcohol would have any affect.

4. 50%/50% Ar/C_2H_6: This gas was observed to have a poor radiation lifetime in our tests, with the gain being reduced by half before an integrated charge of 0.15 C/cm. It has been suggested that our results were the consequence of using gas of insufficient purity, because other tests have observed much better lifetimes.[145] The purity in our gas was not known. Another possibility is that Ar/C_2H_6 gas mixtures perform better in chambers without grid or cathode wires, but rather only cathode surfaces, such as a straw chamber.[146] This is the case because the lack of grid and cathode wires would make the chamber much less susceptible to the development of Malter Effect problems.

B.5 Summary

This appendix has described the systems used to very accurately control the environmental conditions in the DCVD during its operation. With only sporadic exceptions due to various malfunctions, these systems performed adequately, maintaining a pressure stability of better than 0.01 psi and temperature stability of 0.02° C. The temperature differences inside the chamber were 0.12° C from end to end and 0.5° C from the inner to outer shells.

Some studies done on the properties of the 92%/8% $C0_2/C_2H_6$ gas mixture, as well as some related gas mixtures, were also presented. These studies measured the sensitivity of the electron lifetime to the presence of isopropanol and oxygen, the temperature dependence of the drift velocity and the radiation tolerance of the gas.

References

Chapter 1

[1] F. Close, Michael Marten and Christine Sutton, *The Particle Explosion*, Oxford University Press (1987);
J. E. Dodd, *The Ideas of Particle Physics*, Cambridge University Press, Cambridge (1984);
D. H. Perkins, *Introduction to High Energy Physics*, Addison-Wesley, Menlo Park, California (1987);
F. Halzen and A. D. Martin, *Quarks and Leptons: An Introductory Course in Modern Particle Physics*, John Wiley & Sons, New York, 1984.

[2] S. L. Glashow, "Partial-Symmetries of Weak Interactions", *Nucl. Phys.* **22** (1961) 579;
A. Salam and J. C. Ward, "Electromagnetic and Weak Interactions", *Phys. Lett.* **13** (1964) 168;
A. Weinberg, "A Model of Leptons", *Phys. Rev. Lett.* **19** (1967) 1264.

[3] G. Arnison *et al.* (UA1 Collaboration), "Experimental Observation of Isolated Large Transverse Energy Electrons with Associated Missing Energy at $\sqrt{s}$ = 540 GeV", *Phys. Lett.* **B122** (1983) 103;
M. Banner *et al.* (UA2 Collaboration), "Observation of Single Isolated Electrons of High Transverse Momentum in Events with Missing Transverse Energy at the CERN $p\bar{p}$ Collider", *Phys. Lett.* **B122** (1983) 476;

G. Arnison *et al.* (UA1 Collaboration), "Experimental Observation of Lepton Pairs of Invariant Mass around 95 GeV/c^2 at the CERN SPS Collider", *Phys. Lett.* **B126** (1983) 398;
M. Banner *et al.* (UA2 Collaboration), "Evidence for $Z^0 \to e^+e^-$ at the CERN $p\bar{p}$ Collider", *Phys. Lett.* **B129** (1983) 130.

[4] S. Schael, "Measurements of $\sin^2\theta_W$ from the Charge Asymmetry of Hadronic Events at the Z^0 Peak", Talk presented at the Lepton Photon Symposium, Geneva, Switzerland, 1991, IEKP-KA/91-12.

[5] M. Kobayashi and T. Maskawa, "CP Violation in the Renormalizable Theory of Weak Interaction", *Progress of Theoretical Physics* **49** (1973) 652.

[6] J. F. Kral, "Measurement of the Z-Boson Branching Fraction into Hadrons Containing Bottom Quarks", LBL-29485, Ph.D. Thesis (1990).

[7] J. Schwinger, *Particles and Fields, Volume II*, Addison-Wesley, New York (1973);
J. Jersak, E. Laermann and P. M. Zervas, "QCD Corrected Forward-Backward Asymmetry of Quark Jets in e^+e^- Annihilation", *Phys. Lett.* **B98** (1981) 363;
T. H. Chang, K. J. F. Gaemers and W. L. van Neerven, "QCD Corrections to the Mass of the Intermediate Vector Bosons", *Nucl. Phys.* **B202** (1982) 407.

[8] J. J. Hernandez *et al.* (The Particle Data Group), "Review of Particle Properties", *Phys. Lett.* **B239** (1990) 1.

[9] B. A. Kniehl and J. H. Kühn, "QCD Corrections to the Axial Part of the Z Decay Rate", *Phys. Lett.* **B224** (1989) 229;
M. Dine and J. Sapirstein, "Higher-Order Quantum Chromodynamic Corrections in e^+e^- Annihilation", *Phys. Rev. Lett.* **43** (1979) 668;
S. G. Gorishny, A. L. Kataev and S. A. Larin, "Next-Next-to-Leading $O(\bar{\alpha}_s^3)$ QCD Correction to $\sigma_{tot}(e^+e^- \to \text{hadrons})$: Analytical Calculation and Estimation of the Parameter $\Lambda_{\overline{MS}}$", *Phys. Lett.* **B212** (1988) 238;
B. A. Kniehl and J. H. Kühn, "QCD Corrections to the Z Decay Rate", *Nucl. Phys.* **B329** (1990) 547.

[10] W. J. Marciano and D. Wyler, "W-production via Z-decay", *Z. Phys.* **C3** (1979) 181;
D. Albert, W. J. Marciano, Z. Parsa and D. Wyler, "Decays of Intermediate Vector Bosons, Radiative Corrections and QCD Jets", *Nucl. Phys.* **B166** (1980) 460.

[11] D. C. Kennedy and B. W. Lynn, "Electroweak Radiative Corrections with an Effective lagrangian: Four Fermion Processes", *Nucl. Phys.* **B322** (1989) 1.

[12] W. Beenakker and W. Hollik, "The Width of the Z Boson", *Z. Phys.* **C40** (1988) 141.

[13] W. Hollik, "Radiative Corrections in the Standard Model and Their Role for Precision Tests of the Electroweak Theory", *Fortschr. Phys.* **38** (1990) 165–260.

[14] A. A. Akhundov, D. Yu. Bardin and T. Riemann, "Electroweak One-Loop Corrections to the Decay of the Neutral Vector Bosons", *Nucl. Phys.* **B276** (1986) 1.

[15] A. Djouadi *et al.*, "$b\bar{b}$-Production on the Z-Resonance: A Challenge to the Standard Model", *Nucl. Phys.* **B349** (1991) 48.

[16] M. Boulware and D, Finnell, "Radiative Corrections to $B\,(Z \to b\bar{b})$ in the Minimal Supersymmetric Standard Model", *Phys. Rev.* **D44** (1991) 2054.

[17] See, for example, B. Boudjema, F. M. Renard and C. Verzennassi, "A Selection Rule for Genuine New Physics in Combined High-Precision Measurement", *Nucl. Phys.* **B314** (1989) 301.

[18] C. Albajar *et al.* (UA1 Collaboration), "Studies of Intermediate Vector Boson Production and Decay in UA1 at the CERN Proton-Antiproton Collider", *Z. Phys.* **C44** (1989) 15;
R. Ansari *et al.* (UA2 Collaboration), "Search for Exotic Processes at the CERN $p\bar{p}$ Collider", *Phys. Lett.* **B195** (1987) 613;
T. A. Fuess (for the CDF Collaboration), "Search for W' and Z' at CDF", *Proc. of the Vancouver Meeting Particles and Fields '91*, Vancouver, B. C., Canada, August 18–22, 1991, p. 349.

[19] See, for example, M. C. Gonzalez-Garcia and J. W. F. Valle, "Constraints on Additional Z' Gauge Bosons from a Precise Measurement of the Z Mass", *Phys. Rev.* **D41** (1990) 2355.

[20] See, for example, B. W. LeClaire, "A Search for Supersymmetric Electrons with the Mark II Detector at PEP", SLAC-REPORT-321, Ph. D. Thesis October 1987; V. D. Barger and R. J. N. Phillips, Collider Physics, Addison-Wesley, Redwood City, California (1987).

[21] J. Carter (ALEPH, DELPHI L3 and OPAL Collaborations), in *Proc. EPS-High Energy Physics Conf. 91*, Geneva, July, 1991.

[22] D. Decamp *et al.* (The ALEPH Collaboration), "Heavy Flavor Production in Z Decays", *Phys. Lett.* **B244** (1990) 551.

[23] B. Adeva *et al.* (The L3 Collaboration), "Measurements of $Z^0 \to b\bar{b}$ Decays and the Semileptonic Branching Ratio $BR\,(b \to l + X)$", *Phys. Lett.* **B261** (1991) 177.

[24] M. Z. Akrawy *et al.* (The OPAL Collaboration), "A Study of heavy flavour production using Muons in Hadronic Z^0 Decays", *Phys. Lett.* **B263** (1991) 311.

[25] D. Decamp *et al.* (The ALEPH Collaboration), "Measurement of the B Hadron Lifetime", *Phys. Lett.* **B257** (1991) 492;
P. Abreu *et al.* (The DELPHI Collaboration), "Measurement of the Average Lifetime of B Hadrons", CERN-PPE/91-131, submitted to *Z. Phys.* **C**;
B. Adeva *et al.* (The L3 Collaboration), "Measurement of the Lifetime of B-Hadrons and a Determination of $|V_{cb}|$", L3 Preprint #32, *Phys. Lett.* **B270** (1991) 111.
P. D. Acton *et al.* (The OPAL Collaboration), "Measurement of the Average B Hadron Lifetime in Z^0 Decays", CERN-PPE/91-201, submitted to *Phys. Lett. B*;
G. Alexander *et al.* (The OPAL Collaboration), "Observation of the J/ψ Production in Multihadronic Z^0 Decays", *Phys. Lett. B*, **B226** (1991) 485.

[26] R. Fulton *et al.* (The CLEO Collaboration), "Observation of B-Meson Semileptonic Decays to Noncharmed Final States", *Phys. Rev. Lett.* **64** (1990) 16;
H. Albrecht *et al.* (The ARGUS Collaboration), "Reconstruction of Semileptonic $b \to u$ Decays", Phys. *Lett.* **B255** (1991) 297.

[27] J. F. Kral *et al.* (The Mark II Collaboration), "Measurement of the $b\bar{b}$ Fraction in Hadronic Z Decays", *Phys. Rev. Lett.* **64** (1990) 1211.

[28] W. Braunschweig *et al.* (The TASSO Collaboration), "Measurement of the Average Lifetime of B Hadrons", *Z. Phys.* **C44** (1989) 1.

[29] P. Abreu *et al.* (The DELPHI Collaboration), "A Measurement of the Partial Width of the Z^0 Boson to b Quark Pairs", CERN-PPE/90-118, *Phys. Lett.* **B252** (1990) 140.

[30] P. Weber, "Separated Vertex Search and Measurement of the B hadron Lifetime in e^+e^- Annihilation at $\sqrt{s}$ = 29 GeV", Ph. D. Thesis, University of Colorado, 1990.

[31] W. Braunschweig *et al.* (The TASSO Collaboration), "A Study of Jets from b Quarks Produced in e^+e^- Annihilations at $\sqrt{s}$ = 35 GeV", *Z. Phys.* **C42** (1989) 17.

[32] P. Henrard *et al.* (The ALEPH Collaboration), presented at the 4th Symposium on Heavy Flavour Physics, Orsay, June 1991;
P. Henrard *et al.* (The ALEPH Collaboration), presented at the Workshop on Neural Networks in High Energy Physics, Isola d'Elba, June 1991.

[33] C. De la Vaissiere and J. Palma-Lopez *et al.*, (The DELPHI Collaboration), CERN 89–5 PHYS 5 (Geneva 1989).

[34] C. Bortolotto, *et al.*, (The DELPHI Collaboration), presented at the Workshop on Neural Networks in High Energy Physics, Isola d'Elba, June 1991.

[35] B. Adeva *et al.* (The L3 Collaboration), "Measurement of Electroweak Parameters from Hadronic and Leptonic Decays of the Z^0", *Z. Phys.* **C51** (1991) 179.

[36] K. R. Schubert, in "Review of B-Meson Decay Results, 1989 International Symposium on Heavy Quark Physics", editors P. S. Drell and D. L. Rubin, AIP Conf. Prod., Vol. 196 (American Institute of Physics, New York, 1989) p. 79.

[37] P. C. Rowson *et al.*, (The Mark II Collaboration), "Charged Multiplicity of Hadronic Events Containing Heavy-Quark Jets", *Phys. Rev. Lett.* **54** (1985), 2580, and P. C. Rowson "Properties of Heavy Quark Jets Produced by e^+e^- Annihilation at 29 GeV", LBL-20463, Ph.D. Thesis, October 1985.

[38] A. V. Kisselev, V. A. Petrov and O. P. Yushchenko, "Average Charged Multiplicities in $Q\overline{Q}$ events $(Q = c, b, t)$ at LEP Energies", *Z. Phys.* **C41** (1988) 521.

[39] M. Sakuda *et al.*, (The DELCO Collaboration), "Properties of Bottom Quark Jets in e^+e^- Annihilation at 29 GeV", *Phys. Lett.* **B152** (1985) 339.

[40] H. Aihara *et al.*, (The TPC Collaboration), "Pion and Kaon Multiplicities in Heavy Quark Jets from e^+e^- Annihilation at 29 GeV", *Phys. Lett.* **B184** (1987) 299.

[41] W. Braunschweig, *et al.*, (The TASSO Collaboration), "A Study of Jets from b Quarks Produced in e^+e^- Annihilations at $\sqrt{s} = 35 - 46$ GeV", *Z. Phys.* **C42** (1989) 17.

[42] J. Chrin, "Upon the Determination of Heavy Quark Fragmentation Functions in e^+e^- Annihilation", *Z. Phys.* **C36** (1987) 163.

[43] C. Peterson, D. Schlatter, I. Schmitt and P. M. Zerwas, "Scaling Violations in Inclusive e^+e^- Annihilation Spectra", *Phys. Rev.* **D27** (1983) 105.

Chapter 2

[44] R. B. Neal (General Editor), "The Stanford Two-Mile Accelerator", W. A. Benjamin, Inc., New York, 1968.

[45] The Nobel Lectures in Physics for 1990 are good sources for information on the deep inelastic scattering experiments are:
R. E. Taylor, "Deep Inelastic Scattering: The Early Years", *Rev. Mod. Phys.* 63 (1991) 573;
H. W. Kendall, "Deep Inelastic Scattering: Experiments on the Proton and

Observation of Scaling", *Rev. Mod. Phys.* 63 (1991) 597;
J. I. Friedman, "Deep Inelastic Scattering: Comparisons with the Quark Model", *Rev. Mod. Phys.* 63 (1991) 615.

[46] J. E. Augustin *et al.*, (The Mark I Collaboration), "Discovery of a Narrow Resonance in e^+e^- Annihilation", *Phys. Rev. Lett.* **33** (1974) 1406.

[47] M. L. Perl *et al.*, (The Mark I Collaboration), "Evidence for Anomalous Lepton Production in $e^+ - e^-$ Annihilation", *Phys. Rev. Lett.* **35** (1975) 1489.

[48] John Rees, "The Stanford Linear Collider", Sci. Am. **261** no. 4 p. 8 (1989).
"SLAC Linear Collider Conceptual Design Report", SLAC Report No. 229, June 1990.

[49] B. Richter, "Very High Energy Electron-Positron Colliding Beams for the Study of Weak Interactions", *Nucl. Instr. and Meth.* **136**, 47 (1976).

[50] S. Hong *et al.*, internal Mark II memo (28 January 1991).

[51] G. Abrams, *et al.* (The Mark II Collaboration), "The Mark II detector for the SLC", *Nucl. Instr. and Meth.* **A281**, (1989) 55.

[52] G. Hanson, "The New Drift Chamber for the Mark II Detector at the SLAC Linear Collider", *Proc. of the Wire Chamber Conference*, Vienna, Austria, February 25-28, 1986.

[53] R. Fernow, "Introduction to Experimental Particle Physics", Cambridge University Press, Cambridge (1986);
W. R. Leo, "Techniques for Nuclear and Particle Physics Experiments", Springer-Verlag, Berlin (1987);
G. Charpack and F. Sauli, "High Resolution Electronic Particle Detectors", An. Rev. Nucl. Part. Sci. **34** (1984) 285.

[54] F. Sauli, "Principles and Operation of Multiwire Proportional and Drift Chambers", CERN 77-09 (1977).

[55] D. Briggs *et al.*, "The SLAC Mark II Upgrade Drift Chamber Front End Electronics", *IEEE Trans. on Nucl. Sci.*, **NS-32**, No. 1 (1985) 653.

[56] A. Peisert and F. Sauli, "Drift and Diffusion of Electrons in Gases: A Compilation", CERN 84-04, 13 July 1984; See Figure 63 for gas mixtures similar to HRS gas.

[57] D. Bernstein *et al.*, Proc. of Nucl. Sci. Symposium, San Francisco, 1985, SLAC-PUB-3806.

[58] H. Brafman *et al.*, "The SLAC Scanner Processor: A Fastbus Module for Data Collection and Processing", *IEEE Trans. on Nucl. Sci.*, **NS-32**, No. 1 (1985) 336.

[59] J. Perl *et al.*, "Track Finding with the Mark II/SLC Drift Chamber", *Nucl. Instr. and Meth.* **A252** (1986) 616.

[60] The definitive descriptions of the Mark II track fitting routines are:
A. D. Johnson and G. H. Trilling, "Orbit reconstruction Program for SPEAR Mark II Detector: ARCS", LBL Memo TG-301, September 15, 1978;
G. H. Trilling, "Tracking with PARC6, ADDTC, PARCV", LBL Memo TG-360, December 8, 1982.

[61] R. L. Gluckstern, "Uncertainties in track Momentum and Direction due to Multiple Scattering and Measurement Errors", *Nucl. Instr. and Meth.* **24** (1963) 381.

[62] K. F. O'Shaughnessy, "Properties of Hadronic Decays of the Z Boson", SLAC-360, Ph.D. Thesis, June 1990.

[63] R. J. Van Kooten, "Searches for New Quarks and Leptons in Z Boson Decays", SLAC-367, Ph.D. Thesis, June 1990.

[64] J. Alexander *et al.*, "Prototype results of a High Resolution Vertex Drift Chamber for the Mark II SLC Upgrade Detector", SLAC-PUB-3889, *Proc. of the Wire Chamber Conference*, Vienna, Austria, February 25–28, 1986.

[65] J. P. Alexander *et al.*, "The Mark II Vertex Drift Chamber", SLAC-PUB-4852, *Proc. of the Wire Chamber Conference*, Vienna, Austria, February 13–17, 1989.

[66] D. Durrett *et al.*, "Calibration and Performance of the Mark II Drift Chamber Vertex Detector", SLAC-PUB-5259, *Proc. of Vth International Conference on Instrumentation for Colliding Beam Physics*, Novosibirsk, USSR, March 15–21, 1990.

[67] L. Barker, "A FASTBUS Flash ADC System for the Mark II Vertex Chamber", SLAC-PUB-4757, Presented at the *Nuclear Science Symposium*, Orlando, Florida, November 9–11, 1988.

[68] The development and testing of the DCVD hit finding algorithms was done primarily by Bruce Schumm.

[69] The first stage of the track finding algorithm was developed by Don Fujino and added to the original track finder, now the second stage, developed by Bill Ford. For more information on the former algorithm, see Don Fujino's Ph.D. thesis, to be published as a SLAC Report.

[70] The detailed studies of the DCVD time-distance relation were done by Jim Smith and Bill Ford, and are discussed in detail in Reference [66].

[71] M. T. Elford, "The Drift Velocity of Electrons in Carbon Dioxide at 293° K", *Aust. J. Phys.* **19** (1966) 629;

R. A. Sierra, H. L. Brooks and K. J. Nygaard, "Electron Drift Velocities in N_2, CO_2 and N_2+CO_2) Laser Mixtures", *Appl. Phys. Lett.* **35** (1979) 764.

[72] C. Adolphsen *et al.*, "The Mark II Silicon Strip Vertex Detector", *Nucl. Instr. and Meth.* **A313** (1992) 63.

[73] R. G. Jacobsen, "A Measurement of the Branching Ratio of the Z Boson to Bottom Quarks Using Precision Tracking", Ph.D. Thesis, SLAC-Report-381, July 1991.

[74] J. Walker *et al.*, "Development of High Density Readout for Silicon Strip Detectors", *Nucl. Instr. and Meth.* **266** (1984) 200.

[75] M. Briendenbach *et al.*, "Semiautonomous Controller for Data Acquisition: The Brilliant ADC", SLAC-PUB-2032 and *IEEE Trans. Nucl. Sci.*, **NS-25**, No. 1 (1978) 706.

[76] A. Breakstone *et al.*, "Design of a Capactitive Displacement-Measuring System for Vertex Detectors at Colliding Beam Machines", *Nucl. Instr. and Meth.* **A 281** (1989) 453;
A. Breakstone, "Performance of the capactitive Displacement Measuring System of the Mark II Detector at the SLC", *Nucl. Instr. and Meth.* **A305** (1991) 39.

[77] C. Adolphsen *et al.*, "An Alignment Method for the Mark II Silicon Strip Vertex Detector Using an x-ray Beam", *Nucl. Instr. and Meth.* **A228** (1990) 257.

[78] C. Field *et al.*, "A Compact Beam Profile Probe Using Carbon Fibers", *Nucl. Instr. and Meth.* **A281** (1989) 453.

[79] J. Kent *et al.*, "Precision Measurements of the SLC Beam Energy", SLAC-PUB-4922, Presented at the *IEEE Particle Accelerator Conference*, Chicago, IL, March 20-23, 1989.

[80] R. Aleksan *et al.*, *Proceedings of the International Conference on the Impact of Digital Microelectronics and Microprocessors on Particle Physics*, World Scientific (1988) 38.

Chapter 3

[81] S. Komamiya *et al.* (The Mark II Collaboration), "Determination of α_s from a Differential-Jet-Multiplicity Distribution in e^+e^- Collisions at $\sqrt{s}$ = 29 and 91 GeV", *Phys. Rev. Lett.* **64** (1990) 987.

[82] A. Ali *et al.*, "QCD Predictions for Four-jet Final States in e^+e^- Annihilation", *Nucl. Phys.* **B167** (1980) 454;
K. Fabricius *et al.*, "Higher Order Perturbative QCD Calculation of Jet Cross Sections in e^+e^- Annihilation", *Z. Phys.* **C11** (1982) 315.

[83] T. Sjöstrand, "Status of Fragmentation Models", *Int. J. of Mod. Phys.* **A 3** (1988) 751;
T. Sjöstrand, "QCD Generators", CERN 89-08 Vol. 3, 21 September 1989 (the final report of the Workshop on Z Physics at LEP);
B. Foster, "Electron-Positron Annihilation Physics", Adam Hilger, Bristol, England (1990).

[84] T. Sjöstrand, *"The Lund Monte Carlo for Jet Fragmentation in e^+e^- Physics – JETSET Version 6.2", Comput. Phys. Commum.* **39** (1986) 347;
T. Sjöstrand and M. Bengtsson, *"The Lund Monte Carlo for Jet Fragmentation in e^+e^- Physics – JETSET Version 6.3 – An Update", Comput. Phys. Commum.* **43** (1987) 367.

[85] M. Bengtsson and T. Sjöstrand, "A Comparative Study of Coherent and Non-coherent Parton Shower Evolution", *Nucl. Phys.* **B289** (1987) 810.

[86] M. Bengtsson and T. Sjöstrand, "Coherent Parton Showers Versus Matrix Elements – Implications of PETRA / PEP Data" *Phys. Lett.* **B185** (1987) 435.

[87] G. Altarelli and G. Parisi, "Asymptotic Freedom in Parton language", *Nucl. Phys.* **B 126** (1977) 298.

[88] B. Andersson *et al.*, "Parton Fragmentation and String Dynamics", *Phys. Rep.* **97** (1983) 31.

[89] B. Andersson *et al.*, "A Model for Baryon Production in Quark and Gluon Jets", *Nucl. Phys.* **B197** (1982) 45.

[90] B. Andersson *et al.*, "Baryon Production in Jet Fragmenation and Υ-Decay", *Phys. Scripta* **32** (1985) 574.

[91] B. Andersson *et al.*, "A General Model for Jet Fragmentation", *Z. Phys.* **C20** (1983) 317.

[92] M. Suzuki, "Fragmentation of Hadrons from Heavy Quark Partons", *Phys. Lett.* **B71** (1977) 139;
J. D. Bjorken, "Properties of Hadron Distributions in Reactions Containing Very heavy Quarks", *Phys. Rev.* **D17** (1978) 171.

[93] S. Bethke, "Experimental Studies on the Heavy Quark Fragmentation Functions", *Z. Phys.* **C29** (1985) 175.

[94] D. Decamp *et al.* (The ALEPH Collaboration), "Production and Decay of Charmed Mesons at the Z Resonance", *Phys. Lett.* **B266** (1991) 218.

[95] G. Alexander *et al.* (The OPAL Collaboration), "A Study of $D^{*\pm}$ -Production in Z^0 Decays", *Phys. Lett.* **B262** (1991) 341.

[96] C. Peterson *et al.*, "Scaling Violations in Inclusive e^+e^- Annihilation Spectra", *Phys. Rev.* **D27** (1983) 105.

[97] A. Petersen *et al.* (The Mark II Collaboration), "Multihadronic Events at $E_{c.m.}$ = 29 GeV and Predictions of QCD Model from $E_{c.m.}$ = 29 GeV to $E_{c.m.}$ = 93 GeV", *Phys. Rev.* **D37** (1988) 1.

[98] G. S. Abrams *et al.* (The Mark II Collaboration), "Measurement of Charged-Particle Inclusive Distributions in Hadronic Decays of the Z Boson", *Phys. Rev. Lett.* **64** (1990) 1334.

[99] G. Marchesini and B. R. Webber, "Simulation of QCD Jets Including Soft Gluon Interference", *Nucl. Phys.* **B238** (1984) 1.
B. R. Webber, "A QCD Model for Jet Fragmentation Including Soft Gluon Interference", *Nucl. Phys.* **B238** (1984) 492.

[100] T. D. Gottschalk and D. A. Morris, "A New Model for Hadronization and e^+e^- Annihilation", *Nucl. Phys.* **B288** (1987) 729.

[101] W. Bartel *et al.*, (JADE Collaboration), "Experimental Studies on Multijet Production in e^+e^- Annihilation at PETRA Energies", *Z. Phys* **C33**, 23 (1986); S. Bethke, Habilitationschrift, University of Heidelberg (1987) (unpublished).

[102] M. Z. Akrawy *et al.* (The OPAL Collaboration), "A Measurement of Global Event Shape Distributions in the Hadronic Decays of the Z^0", *Z. Phys.* **C47** (1990) 505.

[103] See p. III.14 of Reference [8] for information of multiple scattering.

[104] G. Molière, *Z. Naturforschung* **2a** (1947) 133; **3a** (1948) 78;
H. A. Bethe, "Molière's Theory of Multiple Scattering", *Phys. Rev.* **89** (1953) 1256;
W. T. Scott, "The Theory of Small-Angle Multiple Scattering of Fast Charged Particles", *Rev. Mod. Phys.* **35** (1963) 231;
J. B. Marion and B. A. Zimmernam, "Multiple Scattering of Charged Particles", *Nuc. Instr. and Meth.* **51** (1967) 93.

[105] T. Lindelof, editor. "CERN Program Library", 1987 .03.01, page 6.537.

Chapter 4

[106] E. Fahri, "Quantum Chromodynamics Tests for Jets", *Phys. Rev. Lett.*, **39** (1977) 1587.

[107] T. Sjöstrand, "The Lund Monte Carlo for e^+e^- Jet Physics", *Comput. Phys. Commum.* **28** (1983) 227.

[108] B. Rossi and K. Greisen, "Cosmic Ray Physics", *Rev. Mod. Phys.* **13** (1941) 240.

[109] V. L. Highland, "Some Practical Remarks on Multiple Scattering", *Nuc. Instr. and Meth.* **129** (1975), 497.

[110] G. R. Lynch and O. I. Dahl, "Approximations to Multiple Coulomb Scattering", LBL-28165-Rev (November 1990).

[111] R. K. Bock *et al.* (editors) "Formulae and Methods in Experimental Data Evaluation with Emphasis in High Energy Physics", published by the European Physical Society, Volume 1, page 136 (January 1984).

[112] The development of the interaction point finding algorithm used in this analysis and the study of the interaction point motion in the data was done by Steve Wagner.

[113] G. S. Abrams *et al.* (The Mark II Collaboration), "Measurements of Charged-Particle Inclusive Distributions in Hadronic Decays of the Z^0", *Phys. Rev. Lett.* **64** (1990) 1334.

[114] D. Decamp *et al.* (The ALEPH Collaboration), "Measurement of the Charged Particle Multiplicity Distribution in Hadronic Z Decays", CERN-PPE/91-159.

[115] P. D. Acton *et al.* (The OPAL Collaboration), "A Study of Charged Particle Multiplicities in Hadronic Decays of the Z^0", CERN-PPE/91-176.

[116] P. Abreu *et al.* (The DELPHI Collaboration), "Charged Particle Multiplicity Distributions in Z^0 Hadronic Decays", *Z. Phys.* **C50** (1991) 185.

[117] B. Adeva *et al.* (The L3 Collaboration), "Measurement of the Inclusive Production of Neutral Pions and Charged Particles on the Z^0 resonance", *Phys. Lett.* **B259** (1991) 199.

Chapter 5

[118] The fine-point was brought to my attention by Morris Swartz.

[119] R. Fulton *et al.* (The CLEO Collaboration), "Observation of B-Meson Semileptonic Decays to Noncharmed Final States", *Phys. Rev. Lett.* **64** (1990) 16;
H. Albrecht *et al.* (The ARGUS Collaboration), "Observation of Semileptonic Charmless B Meson Decays", *Phys. Lett.* **234** (1990) 409;
H. Albrecht *et al.* (The ARGUS Collaboration), "Reconstruction of Semileptonic $b \rightarrow u$ Decays", *Phys. Lett.* **255** (1991) 297.

[120] K. Hayes, "B Tagging at the SLC", Mark II/SLC Note #73, May 8, 1984.

[121] B. A. Schumm, "High Precision Tracking and the Measurement of $B(Z \rightarrow b\bar{b})/B(Z \rightarrow hadrons)$ with the Mark II at the SLC", LBL-30709, to be published in the proceedings of the 26th Recontre de Moriond, Les Arcs, France, March 10-17, 1991.

Chapter 6

[122] The LEP Collaborations (ALEPH, DELPHI, L3 and OPAL), "Electroweak Parameters of the Z^0 Resonance and the Standard Model", *Phys. Lett.* **B276** (1992) 247.

[123] A. Bean, *et al.* (The CLEO Collaboration), "Limits on $B\overline{B}$ Mixing and τ_{B^0}/τ_{B^+}", *Phys. Rev. Lett.* **58** (1987) 183.

[124] H. Albrecht *et al.*, (The ARGUS Collaboration), "A Measurement of $\tau(B^+)/\tau(B^0)$ from Lepton and Dilepton Rates in $\Upsilon(4s)$ Decay", DESY 91-056, June 1991.

[125] S. Wagner *et al.* (The Mark II Collaboration), "Measurement of the B^0 Meson Lifetime", *Phys. Rev. Lett.* **64** (190) 1095.

[126] M. Danilov, "Heavy Flavour Physics (Non-LEP)", Talk presented at the Lepton Photon Symposium, Geneva, Switzerland, 1991.

[127] P. Roudeau, "Heavy Flavour Physics at LEP", LAL 91-49, November 1991 (presented at the Lepton Photon Symposium, Geneva, Switzerland, 1991).

[128] R. Morrison and M. Witherell, "D Mesons", UCSB-HEP-89-01, to appear in Annual Review of Nuclear and Particle Science, Volume #39.

[129] P. Abreu *et al.* (The DELPHI Collaboration), "Measurement of the Partial Width of the Decay of the Z^0 into Charm Quark Pairs", *Phys. Lett.* **B252** (1990) 140.

[130] B. Gittelman and S. Stone, "*B* Meson Decay", published in A. Ali and P. Söding (editors), "High Energy Electron Positron Physics", World Scientific Publishing Co., (1988) 273.

[131] H. Albrecht *et al.*, (The ARGUS Collaboration), "Measurement of R and Determination of the Charged Particle Multiplicity at $\sqrt{s}$ around 10 GeV", DESY-91-092, August 1991.

[132] M. S. Alam *et al.* (The CLEO Collaboration), "Charged Multiplicities in *B*-Meson Decay", *Phys. Rev. Lett.* **49** (1982) 357.

[133] M. S. Alam *et al.*, CLNS-81-513 (1981) 14;
P. Drell and D. Besson for the CLEO Collaboration, private communication.

[134] D. Bertoletto, *et al.* (The CLEO Collaboration), "Inclusive *B*-Meson Decays to Charm", *Phys. Rev.* **D35** (1987) 19.

[135] A full discussion of this nuclear scattering generator can be found in the Mark II/SLC Memo No. 268 by Bruce Schumm (9 July 1991).

Chapter 7

[136] M. Z. Akrawy *et al.*, "A study of Jet Production rates and a Test of QCD on the Z^0 Resonance", *Phys. Lett.* **B235** (1990) 389.

[137] See p. III.15 of Reference [102] for information on estimating the photon conversion cross section.

[138] C. Bacci *et al.* (The ADONE Collaboration), "Total Cross Section for Hadronic Production by e^+e^- Annihilation in the Total CM Energy range 1.42–3.09 GeV", *Phys. Lett.* **B 86** (1979) 234;
L. Siegrist *et al.* (The Mark I Collaboration), "Hadronic Production by e^+e^- Annihilation at Center-of-Mass Energies between 2.6 and 7.8 GeV. I. Total Cross Section, Multiplicities and Inclusive Momentum Distributions", *Phys. Rev.* **D26** (1982) 969;
B. Niczyporuk *et al.* (The LENA Collaboration), "Charged Hadron Production in e^+e^- Annihilation in the Υ and Υ' Region", *Z. Phys.* **C 9** (1981) 1;
M. S. Alam *et al.* (The CLEO Collaboration), "Charged-Particle Multiplicities in the B-Meson Decay", *Phys. Rev. Lett.* **49** (1982) 357;
Ch. Berger *et al.* (The PLUTO Collaboration), "Multiplicity Distribution in e^+e^- Annihilations at PETRA Energies", *Phys. Lett.* **B95** (1980) 313;
W. Bartel *et al.* (The JADE Collaboration), "Charged Particle and Neutral Kaon Production in e^+e^- Annihilations at PETRA", *Z. Phys.* **C20** (1983) 187;
M. Althoff *et al.* (The TASSO Collaboration), "Jet Production and Fragmentation in e^+e^- Annihilation at 12-43 GeV", *Z. Phys.* **C22** (1984) 307;
M. Derrick *et al.* (The HRS Collaboration), "Study of Quark Fragmentation in e^+e^- Annihilations at 29 GeV: Charged Multiplicity and Single Particle Rapidity Distributions", *Phys. Rev.* **D34** (1986) 3304;
H. Aihara *et al.* (The TPC Collaboration), "Charged Hadron Production in e^+e^- Annihilation at 29 GeV", *Phys. Rev. Lett.* **52** (1984) 577;
H. W. Zheng *et al.* (The AMY Collaboration), "Charged-Particle Multiplicities in e^+e^- Annihilations at $\sqrt{s}$ = 50-61,4 GeV", *Phys. Rev.* **D42** (1990) 737.

[139] For more information on the LLA-inspired form for the multiplicity dependence on center-of-mass energy, see for example,
A. H. Mueller, "On the Multiplicity of Hadrons in QCD Jets", *Phys. Lett.* **B104** (1981) 161; "Multiplicity and Hadron Distribution in QCD Jets, (II.) A General Procedure for all Non-leading Terms", *Nuc. Phys.* **B228** (1983) 351.

[140] The PEP and PETRA collaborations which have measured the total charged multiplicity measurements around 30 GeV are the Mark II (see Reference [97]) and PLUTO, JADE, TASSO and HRS (see Reference [138]).

Appendices

[141] For general information on $B\overline{B}$ mixing, see for example,
H. Schröder, "$B\overline{B}$ Mixing", DESY 91-139, November 1991. To be published in S. Stone (editor) "B Decays", World Scientific, Singapore;
I. I. Bigi, "B°-$\overline{B}^{\circ}$ Mixing – A Theoretical Evaluation After ARGUS", Proceedings of the Fifteenth SLAC Summer Institute, (SLAC Report 328), August 1987

[142] H. S. W. Massey, *Electronic and Ionic Impact Phenomena, Volume II*, Oxford University Press (1969), p. 1009.

[143] For example, see J. Kadyk (Workshop Organizer), *Proceedings of the Workshop on Radiation Damage to Wire Chambers*, LBL-21170, Lawrence Berkeley Laboratory, University of California, Berkeley, California, January 16-17, 1986; Two particularly good overviews contained the above proceedings are:
F. Sauli, "When Everything Was Clear", and
J. Va'vra, "Review of Wire Chamber Aging".

[144] These tests were initiated by P. Drell and carried on by S. Wagner, J. Smith and myself. Some of P. Drell's results are summarized in the workshop proceedings of Reference [143].

[145] J. Kadyk, personal communication.

[146] S. Wagner, personal communication.